Electronic identification systems for asset management

McWilliam, Richard

How to cite:

McWilliam, Richard (2003) *Electronic identification systems for asset management*, Durham theses, Durham University. Available at Durham E-Theses Online: http://etheses.dur.ac.uk/3697/

Electronic Identification Systems for Asset Management

Richard McWilliam, MEng.

Submitted in Partial Fulfilment of the Degree of
Doctor of Philosophy

University of Durham

2003

Declaration

I declare that the work carried out in this thesis, unless otherwise stated, was carried out by the candidate, that it has not previously been submitted for any degree and that it is not currently being submitted for any other degree.

R. McWilliam, March 2003

Statement of Copyright

Contents

4 Shield Effects on RFID Systems 61

Acknowledgements

I would like to thank my supervisor Prof. A. Purvis for his advice and administrative support during my studies. I would also like to thank Jim Wallace and Rob Kevan for their willingness to discuss matters regarding safety testing at Seaward Electronic Ltd.

This work was funded by the Engineering and Physical Sciences Research Council and Seaward Electronic Ltd., to whom I am very grateful.

Abstract

Electronic identification is an increasingly pervasive technology that permits rapid data recovery from low-power transponders whenever they are placed within the vicinity of an interrogator device. Fundamental benefits include proximity detection not requiring line-of-sight, multiple transponder access and data security. In this document, electronic identification methods for asset management are devised for the new target application of electrical appliance testing. In this application mains-powered apparatus are periodically subjected a prescribed series of electrical tests performed by a Portable Appliance Tester (PAT). The intention is to enhance the process of appliance identification and management, and to automate the test process as far as possible.

Three principal methods of electronic identification were designed and analysed for this application: proximity Radio Frequency Identification (RFID), cable RFID and power-line signalling. Each method relies on an inductively coupled mechanism that utilises a signalling technique called direct-load modulation. This is particularly suited to low-cost passive transponder designs. Physical limitations to proximity RFID are identified including coil size, orientation and susceptibility to nearby conducting surfaces. A novel inductive signalling method called cable RFID is then described that permits automatic appliance identification. This method uses the appliance power cable and inlet filter to establish a communication channel between interrogator and transponder. Prior to commencing the test phase, an appliance is plugged into the PAT and identified automatically via cable RFID. An attempt is made to extend the scope of cable RFID by developing a novel mains power-line signalling method that uses direct-load modulation and passive transponders.

Finally, two different implementations of RFID interrogator are described. The first takes the form of an embeddable module intended for incorporation into electronic identification products such as RFID enabled PAT units. Software Defined Radio (SDR) principles are applied to the second interrogator design in an effort to render the device reconfigurable.

1 Introduction

Electronic identification is becoming an increasingly pervasive technology in our modern world because it enables commercial or personal items to be located quickly and accurately, minimising human intervention. This document investigates two principal forms of electronic identification, the established inductive proximity identification method and a new automatic identification method. The two methods are closely related by the physical coupling mechanism utilised between interrogator and transponder, but differ in other respects, particularly with regard to operational constraints, range and physical placement.

An introduction to current methods of electronic identification is given in chapter 2. Particular attention is given to the method of Radio Frequency Identification (RFID), which is a broad term describing the family of low-power and low-cost identification transponders that form the main focus of this thesis. A description of the target application, namely electrical safety testing, is also found in chapter 2. By the use of electronic identification this application benefits in two fundamental ways. First, automation of the test routine is possible; the operator is no longer required to determine the Device Under Test (DUT) prior to programming the test routine. Furthermore, automatic initialisation of the test routine is possible and test data may be stored in the electronic transponder attached to the DUT. The second benefit is automation of asset management. Electrical safety testing performs the dual role of device testing and device tracking because unique identifiers that are pertinent to safety testing are stored in the transponder and may be used to locate items that have been tested. Since it is common practice to test any item brought into the commercial work place, all electrical items are assigned unique identifiers. A goal of this thesis is to find means by which item tracking is possible by recognising unique identifiers according to location.

Inductive proximity RFID technology is investigated in chapters 3 and 4 with the objective of defining critical factors that influence performance given constraints imposed by the application. The factors considered in chapter 3 were maximum range as a function of antenna dimensions and sensitivity to orientation. It was necessary to minimise the interrogator coil size, a factor that is critical in determining the range of such identification systems, without sacrificing useable range. An analytical approach is taken to visualise the effective "near-field beam pattern" of the inductive loop, revealing significant regions in which zero or little coupling between interrogator and transponder exist. A system of mutually orthogonal transmitting and receiving loop coils is modelled with the intention of eliminating failures in communication and the resulting coupling patterns are visualised. It is shown that, for the antenna geometry assumed, communication failures can eliminated by two means. The first is to use three orthogonal receiving coils whose individual Electromotive Forces (EMF) can be rectified and summed. The second is to employ orthogonal coils (and a single transponder coil) and to ensure that only one coil is active at a given time. The second method is preferable for low-cost identification applications because alteration of the transponder coil (which forms an appreciable fraction of the transponder cost) is not required.

It was found during the course of this work that limited information is available regarding the shielding effect of metallic (conducting) surfaces when placed close to inductive proximity RFID interrogators and transponders. These effects are critical for many RFID applications that use the inductive field because eddy currents are easily induced in foreign conducting surfaces by the magnetic flux established between the interrogator and transponder. An analysis was conducted in chapter 4 to determine if the dependency of coil impedance (including inductance and equivalent resistance) on shield proximity could be modelled by equations found in the literature. These equations were originally developed to determine shield effectiveness, that is the attenuation of cross talk between two coils by inserting a shield between them, but may be adapted to the current problem to predict the change of coil impedance in the presence of conducting surfaces. It is shown that changes in coil impedance may be modelled with good accuracy, except for losses within thin shields. This is due to the assumption of uniform current distribution throughout the shield depth. In addition, the analytical approach does not consider the effect of shielding material possessing relative permeability greater than unity. Some common materials such as steel and iron were characterised to reveal that the change of inductance is positive or negative depending on frequency. The effect of conducting surfaces on RFID performance was gauged by determining the behaviour of interrogator and transponder circuits under the influence of changing coil impedance.

In chapter 5 a new automatic identification method is described that utilises the power cable of the device under test (DUT) to form an electrical signal path that passes through the mains inlet filter. An interrogator resides within the Portable Appliance (PAT) device and is activated when the DUT is plugged into the test socket. A pulsed carrier-current is passed through the power cable, energising an inductive coupler that is placed around the live or neutral wire and to which a passive transponder IC is attached. This forms an inductive transponder that does not require galvanic connection to the power cable. In either case, communication is established between the interrogator and transponder by a direct-load modulation method, causing perturbations in the total impedance of the power cable that are sensed by the interrogator detection circuit. The system permits retrieval of important information such as the unique DUT identification number, test codes and test history data. The recovered data is then processed by the PAT and the most appropriate electrical test routine configured without requiring user intervention. Test results may then be written to the transponder for reference. In chapter 8 a two-wire coupler design is investigated that is placed around the entire cable assembly without any need for separating live and neutral wires. Limitations on conductor spacing, core permeability and core shape are identified.

In chapter 6 the power cable and inlet filter are analysed from the perspective of inductive load modulation communications as they constitute the electrical circuit formed between the interrogator and transponder. The transponder (comprising inductive coupler and IC) is modelled in terms of a coupled impedance that appears in the power cable circuit. Interaction between this coupled impedance other circuit elements are then characterised. Two main types of inlet filter were analysed to determine effects of filter resonance on load modulation sensitivity and power transfer between interrogator and transponder. As the length of the power cable increases, resonant modes are encountered that alter transponder operating conditions. It was important that these be understood because it was anticipated that destructive interference in the standing wave pattern that is established along the cable would lead to failure of the communication system. It was also important to determine the effect of transponder position along the cable for applications in which position is determined by the most convenient location. The method is extended in chapter 9 to facilitate signalling between interrogator and transponder across the live power-line. Properties are analysed in the context of passive load modulation operation and limitations are suggested following a simulation. It is demonstrated that under favourable power-line conditions, direct-load modulation is possible even when using passive transponders. However, variations in channel impedance caused by loads attached to the power-line and non-deterministic noise sources that modulate the power-line impedance pose a great challenge to this communication method. These difficulties are common to all power-line communication methods, but are accentuated for the relatively low-power, low-complexity method described here.

Finally, chapters 7 and 10 are concerned with RFID interrogator design. A new embedded Read-Write Device (RWD) was designed for use with proximity RFID products developed at Seaward Electronic Ltd. that are able to communicate with RFID transponders. The design and evaluation of this device is covered in chapter 7. In chapter 10 a novel design approach is taken that seeks to implement the interrogator radio functionality in the digital domain. The approach was motivated in part by the observation that there is a strong need for reconfigurable interrogator devices in the electronic identification market. This is due to the existence of multiple standards, protocols and frequency bands within this market. A case is made for the adoption of a Software Defined Radio (SDR) architecture for RFID interrogator design that has the potential to fulfil the above requirements. Another motivation for this approach is reduction of external (primarily analogue) interrogator components that would improve suitability for embedded applications. A novel transmitter implementation is described that requires only three external components in order to establish interrogator-transponder communication. For the receiver section, direct conversion of the carrier is possible for low-frequency (125 kHz) RFID, again using minimal external components, which permits the implementation of demodulation and detection operations in the digital domain. Work is ongoing to determine whether this is also feasible at higher frequency bands.

2 *Electronic Identification for Asset Management*

2.1 Introduction

Over the next few years, electronic identification will revolutionise the retail product chain by enabling automatic identification of goods at each critical location in the supply chain [Alexander]. Electronic identification is now commonplace in key public sector applications such as smart cards [Fancher], baggage handling [Ealing] road-tolling [Frenzel] and transport/logistics [Davie]. However each target application requires careful study to determine the most applicable identification technology if value and functionality are to be maximised. With this in mind, a brief overview of electronic identification methods is presented in this chapter, followed by a description of the asset management application of interest in this thesis, namely, electrical safety testing.

2.2 Electronic Identification Systems

An electronic identification system consists of an interrogator, or base unit, and at least one transponder (figure 2.1). In this document we consider identification methods that operate over short-range wireless links, typically separated by less than one metre. These devices are collectively referred to *proximity devices*. The common goal of these systems is to allow automatic recognition of the transponder whenever it is placed within the vicinity of the interrogator. Several methods of electronic identification have appeared since the barcode was first adopted more than two decades ago. Each has helped to extend the boundaries of technology available at the time. For example, the introduction of the smartcard has encouraged significant developments in the areas of low-resource operating systems, biometrics and secure encryption methods [Praca], [Domingo], [Noore], [Dettmer]. Several further proximity methods that are currently in use are listed in table 2.1 for comparison.

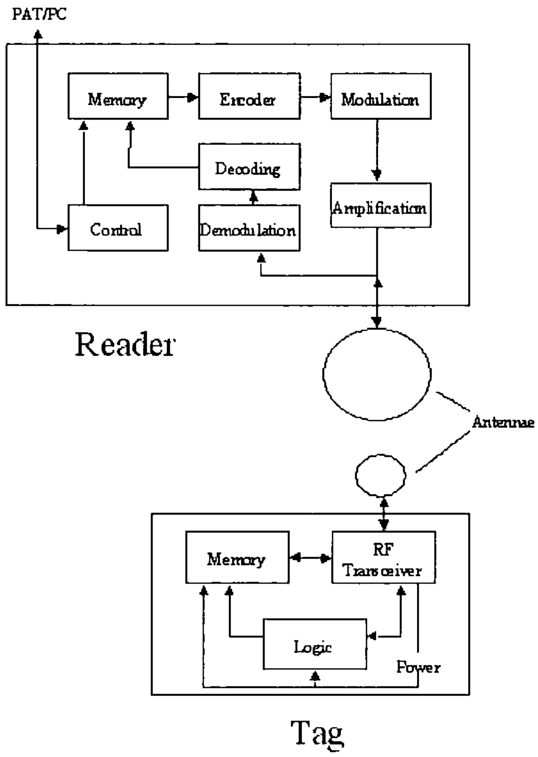

Figure 2.1 Elements of the proximity interrogator and transponder

Electronic Article Surveillance (EAS) transponder systems are utilised in anti-theft applications, in which a one-bit transponder is used to trigger an alarm when the object to which it is attached is removed from the consumer store. EAS detection may be implemented in several ways. Possible methods include detecting field dampening, hysteresis effects or harmonics generated by the transponder when in close proximity to the interrogator. For more information, see [Finkenzeller].

Technology	Description
Electronic Article Surveillance (EAS)	Very low-cost, high volume; high detection rate.
Radio Frequency Identification (inductive)	Low cost and complexity; rapid identification of "tagged" object by ID number; passive operation supported in the inductive near-field.
Radio Frequency Identification (radiation)	High-speed identification transponder; corresponding high chip complexity and cost. Operates using backscatter (passive) or two-way radio link (active).
Smartcard	Secure Identification method supporting encryption and multiple embedded operating systems. Direct-contact and proximity coupling interfaces.
Wireless Sensors	Two-way radio link usinglow-cost transceivers. Often uses proprietary protocols.
Bluetooth	Point-point radio link with discovery protocol for identifying new devices. Relatively complex radio system and software stack; active transceivers required.

Table 2.1 Summary of electronic identification methods in use, ordered approximately by cost of identification transponder (lowest to highest).

Bluetooth is an example of a low-powered radio system that may be suitable for electronic identification. The communication protocol support ad-hoc connections and device profiles which are suitable for establishing communication between an interrogator and unknown transponder. The specification [Bluespec] uses frequency hopped spread-spectrum that would permit identification of multiple transponder within the vicinity. The cost is comparatively high at present, but suitable embedded applications have already been identified [CIE00], [Leen]. Power consumption is still a problem for low-powered applications [Jones], not least due to the requirement of the active transponder design.

2.3 Inductively-Coupled Mechanism for Radio Frequency Identification

By the year 2002 the RFID market was estimated to be worth $964.5 million, including hardware, software and services [Liard1]. This included sales of around 295.4 million transponder ICs [Liard2] at an average of $0.26 each (not including antenna and packaging). The uptake of RFID has increased as the benefits it offers over barcode technology have become better understood by potential adopters. (For a discussion of business issues involving transition from barcode technology to RFID, see [Chartier]). Market expansion will be further driven by reductions in transponder cost and the emergence of several global standards (see section 2.5), leading to a projected value of $2.7 billion by the year 2007.

Inductively coupled communication circuits have been considered for several applications, such as animal tracking [Sowell], implantable medical devices [Matsuki], in-car communications [Bunzel01] and personal area communications [Neaves]. These applications benefit from inductive communications in different ways. In [Matsuki], inductive coupling is used to supply up to 20 W of power to an artificial heart system and electrical stimulation system without requiring wires. In [Sowel], [Neaves] and [Bunzel] the near-field restriction of inductive coupling is exploited to provide personal communications within a small zone surrounding the user. This reduces the possibility of interference from other radio systems and indeed other inductive communication systems. This method has the potential to become a viable alternative to current low-powered radio systems such as Bluetooth due to the following benefits:

- Low-power required for proximity communication;
- Complexity of radio modules is comparatively low;
- Less prone to fading effects that can occur in radio communication.

Radio Frequency Identification (RFID) systems operate in the near-field (inductive) or far-field (radiation), depending on the operational frequency (figure 2.2). For electrically small antennas the transition point between near and far fields occurs at a distance of approximately $\lambda/2\pi$ [Balanis]. The most common operational frequencies are listed in table 2.2. For further information on inductively coupled RFID, see [Finkenzeller].

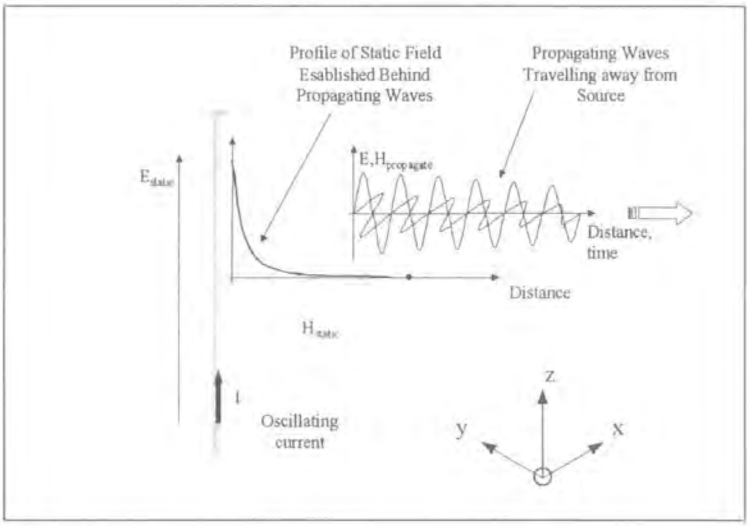

Figure 2.2 Transition from magnetostatic field (near-field) to propagating wave (far-field).

Carrier Frequency	**Typical Bandwidth**	**Dominant Coupling Mechanism**
125 kHz / 134 kHz	4 kHz (typical)	Inductive
13.56 MHz	14 kHz (typical)	Inductive
868-870 MHz (Europe)	400 kHz (maximum permitted)	Propagating EM wave
2.45 GHz	83 MHz (maximum permitted)	Propagating EM wave

Table 2.2 The most common ISM (license-free) frequency bands used in RFID.

2.3.1 Transponder

The fundamental element of RFID systems is the transponder. The transponder must be fixed to the object or individual that it identifies and, at the most basic level, must be capable of communicating a code that uniquely identifies the object or individual. A wide variety of transponders are available on the market, ranging from read-only variants that fulfil the minimum requirement of storing a unique identification number, to high capacity transponders that offer reading and writing to memory. In appendix A, a comparison between common commercial transponder IC's is given. The internal architecture of a typical passive transponder is discussed at length in [Schuermann].

Transponders may also be classified by antenna design; as discussed earlier there are several RFID bands in operation, each requiring different optimal antenna designs. Inductive antennas range from large, bulky, wound coils for low frequencies (figure 2.3(a)), to planar coils created by etching or printing processes for high frequencies (figure 2.3(b)). Induced EMF is proportional to frequency from the relation $EMF = j\omega MI$ where M is the mutual inductance between interrogator and transponder coils and I is the current flowing through the interrogator coil. Increased losses and winding capacitance preclude high coil inductance at higher frequencies.

(a) (b)

Figure 2.3 Examples of commercial RFID transponders, using (a) low-frequency (125 kHz) wound coil and (b) high-frequency (13.56 MHz) printed / etched coil.

Reducing the total manufacturing cost of transponders is the current focus of researchers in high-volume RFID. By targeting high-frequency inductive RFID, primary cost reductions have been made in the coil printing process and assembly of the coil and transponder IC [Gengel].

2.3.2 The RFID Interrogator

The RFID interrogator must detect the presence of transponders placed within the local vicinity and recover at least a unique identification number. In applications were passive transponders are used, the interrogator must receive data by detecting variations imposed on the energising carrier by the transponder. This technique is called direct-load modulation.

The interrogator may also be capable of storing data that relates to objects that have been "tagged". By using the transponder identification number as an index look-up, the relevant information can be accessed. Alternatively, information about the tagged object may be stored in the transponder itself. This means that data remains accessible by any compatible interrogator. A discussion of which method is most appropriate for a given application can be found in [IDtech].

2.4 Standardisation of Radio Frequency Identification Technology

Global standardisation is currently lacking in the RFID industry, which has dissuaded many potential adopters from implementing the technology. Three major standards are currently under development that may assist in harmonising the industry. The first is the ISO/IEC18000 physical standard, called "Information Technology — Radio Frequency Identification (RFID) for Item Management" [ISO18000]. This standard seeks to define air interface methods for all RFID frequency bands. The second standard is called Global Tag (GTAG™) and is concerned with high specification transponders for demanding applications such as pallet tracking [GTAG]. It currently defines several sophisticated requirements such as active transponder operation and anti-collision protocols. The third emerging standard is called the Electronic Product Code (ePC) and was initiated by the Auto-ID Center[1], Massachusetts Institute of Technology. It seeks to define an extremely low-cost means of electronic tagging that is suitable for the general supply chain [Aston], [Stajano]. To achieve this, every aspect of the technology must be optimized with the aim of reducing cost whilst guaranteeing reliability. The main aim of ePC is to provide a means of identifying every product in the supply chain by a unique 96 bit number that is partitioned into three sections: manufacturer, product type and product serial number. The interrogator must be capable of recognizing several ePC tags in the vicinity and may be multi-band and multi-protocol [Reynolds].

2.5 A New Target Application

A new application for electronic identification was identified that requires recognition of mains-powered devices prior to electrical safety testing. In this section a brief description of the adopting company, Seaward Electronic Ltd, and the strategy adopted is given.

2.5.1 Sponsoring Company

Seaward Electronic Ltd. is a developer and manufacturer of Portable Appliance Testing (PAT) equipment. PAT equipment is used to check the electrical integrity of mains approved appliances. Establishments typically require that all equipment be subjected to a series of electrical tests that are designed to ensure safe operation with respect to the

---

[1] See http://www.theautoidcenter.org.

user. By passing these, tests an appliance conforms to safety standards such as EN 61010-1 "Safety Requirements for Electrical Equipment for Measurement, Control and Laboratory Use". The PAT unit is designed to perform the required tests automatically with minimal user intervention. Efficiency is important when considering the task of commissioning a new site with new equipment, all of which must be safety checked before use. Furthermore it is important to keep track of all electrical equipment in a building, such as an office block or a hospital, to ensure that tests are performed regularly, and records updated accordingly.

2.1.1 Motivation

A project was outlined that aimed to investigate the potential for automatic identification as part of the electrical safety testing procedure. The intention was to enhance the process of appliance testing and item management by using electronic identification transponders. A market study was contracted by Seaward Electronic with the aim of identifying existing markets in which RFID has been adopted. It was found that RFID had been exploited in relatively few markets due to fragmented standards, lack of awareness of the technology and a lack of direct expertise among small SME companies in RFID technology.

2.1.2 An Overview of Portable Appliance Testing

The purpose of appliance testing is to establish whether an electrically-powered device is safe for general use. The general procedure requires that the Device Under Test (DUT) is plugged directly into a test socket located on the Portable Appliance Tester (PAT). Following a visual inspection, the relevant test routine must be programmed into the PAT. Possible tests include earth bond, insulation, earth leakage, flash and load. Selection of the appropriate test routine can be automated by the use of barcodes which are fixed to the DUT and, when read by a scanner, indicate the class of device. The PAT may then construct an individual test routine for the DUT.

2.1.3 Strategy

A strategy was devised to explore new automatic identification techniques pertinent to electrical safety testing, and the integration of conventional proximity systems within the test product range. Existing limitations of proximity coupling techniques were investigated including size/range trade-offs, sensitivity to orientation and effects of metallic surfaces, with the aim of improving overall performance. The project was split into three main areas: an inductive proximity system, an automatic identification concept and a power-line signalling method.

2.1.3.1 Proximity System

The first stage involved the design of an inductively coupled proximity reader and transponder system (figure 2.4). Inductive coils were designed for both interrogator and transponder. Third party transponder IC's (Hitag 1, manufactured by Philips Semiconductors) and interrogator modules are currently being used, but a new interrogator module design is being completed (see chapter 7). Transponders are attached to the Equipment Under Test (EUT) as an identification label, enabling test information to be read and written to the transponder. The added value of this system is that electronic data is stored in the electronic transponder and may be recovered by proximity coupling, a method that offers non-line of sight and multiple simultaneous access. It was intended that the integration of proximity transponders within the electronic test product range of Seaward Electronic would bring increased functionality and value. By choosing to operate at low-frequency (125 kHz), stable performance was established in metallic environments by minimising the surface area of interrogator and transponder coils (chapter 4).


(a) (b)

Figure 2.4 Proximity reader developed for safety test market. Slide (a): portable appliance tester (right) and proximity reader (left). Slide (b): two proximity reader models shown with low-frequency transponders. Components are manufactured by Seaward Electronic Ltd., including transponder assembly.

2.1.3.2 Automatic Identification System

End users would be more likely to use an automatic identification system if identification were performed in a seamless fashion as part of the existing test procedure. With this in mind, research into an innovative use of proximity technology by modifying the electromagnetic interface was undertaken, with the aim of providing a more convenient identification procedure for the user. The use of existing transponder technology was encouraged in order to maintain low cost. This created the need to study direct modulation and power requirements for the new design such that existing transponder ASIC's could be used. A suitable interface was therefore required between the coupler and transponder, and the effects of line impedance, coupler loading, leakage inductance and other parameters on performance were studied. The resulting system enables rapid identification of the DUT immediately upon attaching it to the PAT (figure 2.5). An interrogator device is embedded into the PAT with serial interface (figure 2.5) to manage transponder communication.

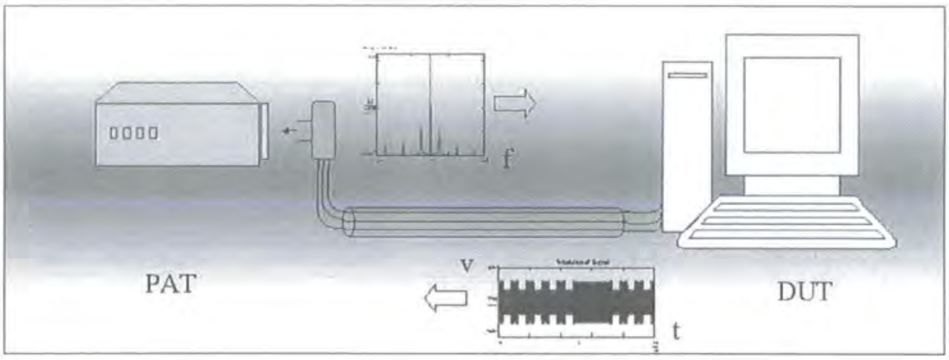

Figure 2.5 Elements of an automatic identification system for safety testing, including PAT unit, appliance power cable and DUT.

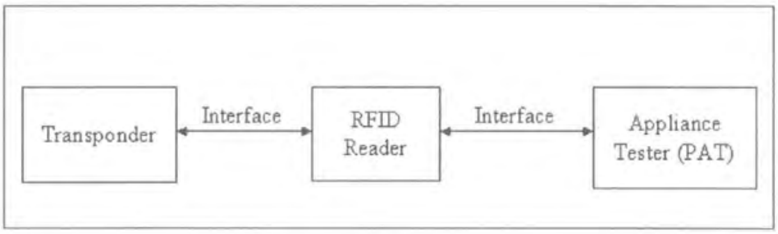

Figure 2.6 Relationship between automatic identificaiton and appliance testing technology.

In a novel variation, the coupler assembly is miniaturised such that it may be placed within the electrical fuse. This would allow retro-fitment of transponders into any appliance by replacing the fuse. In chapter 8 it is shown that a coupler placed around both live and neutral cannot source sufficient power for the passive transponder ASIC unless the wires are spaced a considerable distance apart. Integration within the fuse provides convenient access to the live wire.

2.1.3.3 Power-Line Signalling

The automatic identification concept was to be extended such that signalling takes place between an interrogator and transponder across the live power-line. This facility would enable remote appliance checking from a central location, or at least within the local branch to which the interrogator is attached. The concept differs from existing power-line communication procedures in that direct-load modulation is established between the interrogator and transponder. Furthermore, an entirely passive transponder is used so that all energy is sourced from the interrogator.

2.2 Summary

In this chapter an introduction to electronic identification technology was given with emphasis on passive Radio Frequency Identification (RFID), which is the main focus of this thesis. A new prospective application was described that requires enhanced identification of electrical appliances. The application benefits from automatic identification and item management abilities inherent to electronic identification. An outline of the strategy adopted to explore new automatic identification possibilities for the application were given.

3 *Enhancing the performance of Inductively Coupled RFID*

3.1 Introduction

In this chapter we inspect the electromagnetic properties of inductive coupling and identify the fundamental performance constraints for proximity RFID. The specific area of focus lies in the relative positioning of transponder and transmitter coils which affects the mutual coupling between them. Relative transmitter-source orientation and relative coil dimensions for a given distance of operation are the fundamental performance factors that will be considered here.

Field equations for circular coils are used to investigate the problem of coil size optimisation and to derive an expression for the quality of coupling between coplanar and coaxial coils. It is then shown that when a single source coil is moved around the vicinity of a single receiving coil, regions of zero mutual coupling exist. The transponder output is therefore extremely sensitive to its orientation relative to the source coil due to the highly directive nature of the inductive near-field. A well designed RFID system—or any magnetic inductive system—would apparently perform poorly in applications where the transponder and interrogator coils are not suitably aligned.

With this in mind, the problem is expanded to the use of multiple source loops in an attempt to eliminate the occurrence of nulls within the near-field region. This is achieved by three coils orientated in each of the x, y and z planes, thus forming an orthogonal set. This technique has been employed in the past for position tracking systems [Raab] and more recently for near-field magnetic induction network devices [Bunzel].

It is found that when the three orthogonally disposed transmission coils are simultaneously active, nulls persist when a single receiving coil is used regardless of its orientation. However these nulls may be eliminated by switching on each transmitter coil separately such that their fields do not interact. Similarly, a three coil transponder could work at any orientation to single transmitter coil, provided that the signals from each transponder coil were rectified and summed before applying to the chip. A three-coil transponder is therefore viewed as being less beneficial than a three-coil interrogator due to the need for extra coils and additional electronics which increases the transponder bulk and cost. An interesting outcome of this study was the ability to change the location of the point of strongest field by changing the phase of each orthogonal source coil by 180 degrees, thus forming a primitive beam steering mechanism that operates within the near-field region.

3.2 Inductive Coupled Mechanism

In order to enable communication between reader and transponder, a coupled RFID system requires an energy field into which transponders are placed. By convention, the energy field is generated by some manner of electrically small antenna, whose dimensions are optimised to maximise the reactive near-field. Such coils are referred to as *Inductive Loop Coil Transmitters* when the circumference is less than one quarter of the wavelength [Balanis]. Planar coils are most often used since they possess strong flux densities along the coil's axis and, if made electrically small, have low radiation resistance in comparison to their copper loss. As a result, these coils have poor radiation characteristics; energy is stored in the near-field around the coil, providing the energy field required to activate transponders.

3.2.1 Magnetic Field Equations

The magnetic field equations for circular loop antennas are considered. We assume electrically small loops, that is, loops whose sizes are considerably less than the electrical wavelength. The most common frequency bands used by RFID are the 125 kHz and 13.56 MHz ISM bands. The corresponding wavelengths in free space are 2400m and 22.12m, therefore most practical loops used in RFID are considered to be electrically small. With this assumption, the general electromagnetic field equations for an electrically small loop may be expressed in spherical form as [Balanis]:

$$H_r = j\frac{k_p a^2 I\cos\theta}{2r^2}\left[1+\frac{1}{jk_p r}\right]e^{-jk_p r} \quad \text{[A/m]} \qquad (1)$$

$$H_\theta = -\frac{(k_p a)^2 I\sin\theta}{4r}\left[1+\frac{1}{jk_p r}-\frac{1}{(k_p r)^2}\right]e^{-jk_p r} \quad \text{[A/m]} \qquad (2)$$

$$H_\phi = 0 \qquad (3)$$

where a is the loop radius, r the radial distance, $k_p=\omega\sqrt{(\mu\varepsilon)}$ is the propagation constant. These equations describe the field created around a small circular loop lying in the x-y plane which is sufficiently small that the current distribution I is uniform around the loop. The sinusoidal oscillation term $exp(j\omega t)$ is assumed and therefore not included in equations 1 and 2. Near-field conditions are of interest here, in which case $k_p r<<1$. In addition, the phase term $exp(-jk_p r)$ may be written as $exp(-j2\pi r/\lambda)\rightarrow 1$ provided $r<<\lambda$. Applying these assumptions to equations 1, 2 and 3 results in the following equations:

$$H_r = \frac{a^2 I}{2r^3}\cos\theta \quad \text{[A/m]} \qquad (4)$$

$$H_\theta = \frac{a^2 I}{4r^3}\sin\theta \qquad \text{[A/m]} \qquad (5)$$

From equations 4 and 5, we see that the magnetic field strength comprises a radial component, H_r, and tangential component, H_θ. The radial component reaches its maximum value at an elevation angle of $\theta=0$ along the loop axis, while the tangential component reaches a maximum value at an elevation of $\theta=\pi/2$. Furthermore, the maximum radial component is twice the maximum tangential component. A simulation of the resulting flux pattern produced by a 20 mm coil with 10 turns of copper is shown in Figure 3.1. Because the loop is assumed to be very small, the radial field component along the loop axis tends towards infinity as $r \to 0$ (i.e. at the centre of the loop). Actual loops have an appreciable surface area through which flux passes, creating an approximately uniform field close to the loop. By integrating the Biot-Savart equation around the loop, an alternative expression for H_r can be derived that takes into account the finite radius of the loop [Dugdale]:

$$H_r = \frac{Ia^2}{2\left(r^2 + a^2\right)^{3/2}} \qquad \text{[A/m]} \qquad (6)$$

There are three restrictions that must be adhered to when using this equation: it is only valid for at a single point of observation positioned along the z-axis; it is valid only within the inductive near-field; and is, in the strict sense, a quasi-magnetostatic solution. With respect to the last point, the equation is valid for the frequencies considered (<125 kHz) provided we remain well within the inductive near-field region and that the current displacement term may be ignored. The denominator of equation 6 includes a radial term which causes H_z to approach the value $I/2a$ at the centre of the loop. Note that by reducing the coil radius ($a \to 0$) the field strength at the centre of the loop tends towards infinity, which agrees with equation 4. Indeed, equation 6 is identical to equation 4 when $r \gg a$. For situations in which the field strength close to the loop is needed, equation 6 is therefore used to investigate the near-field around an electrically small loop along its axis. Equations 4 and 5 are used when the loop diameter is much smaller than the observation distance, and the loop may be regarded as a magnetic dipole. Note that the field solution is not limited to the z-axis when using equations 4 and 5; the field is computed around the whole region surrounding the loop.

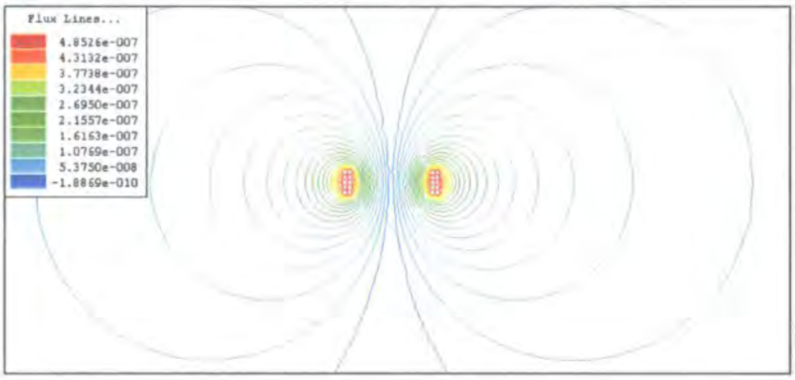

Figure 3.1 Simulation showing lines of flux produced by a 20 mm coil having 10 turns of 1 mm diameter copper wire, current of 100 mA, f = 125 kHz.

3.2.2 Maximum field strength for fixed distance

Since single loop coils are used in most proximity RFID applications, it is important to understand the effect this has on performance. Simple loops are used in order to keep cost to a minimum. However, it will be shown that this results in limited range and a high sensitivity to orientation.

By use of equation 6 the field characteristics along the z-axis may be investigated as a function of distance and coil size. As an example, the field strength versus distance is plotted in figure 3.2 for three different coil sizes. A flat region exists close to the coil centre, but as the distance increases beyond a threshold distance, the field strength decreases. In the decay region, the field reduces by 60 dB per decade which agrees with the inverse-cube profile described by equation 4. The threshold distance is a function of coil size, which may be found by differentiating equation 6 with respect to a, to give [Finkenzeller]:

$$\frac{\partial H_z}{\partial a} = \frac{2a}{\left(r^2 + a^2\right)^{3/2}} - \frac{3a^3}{\left(r^2 + a^2\right)^{5/2}} \tag{7}$$

Setting (7) equal to zero gives the relationship:

$$a = r\sqrt{2} \tag{8}$$

Equation 8 indicates the point of maximum field strength when the coil size varies at a fixed distance. It also represents the point at which the field strength begins to decrease as the distance is varied for a given loop size, as depicted in figure 3.2 by the straight dotted line.

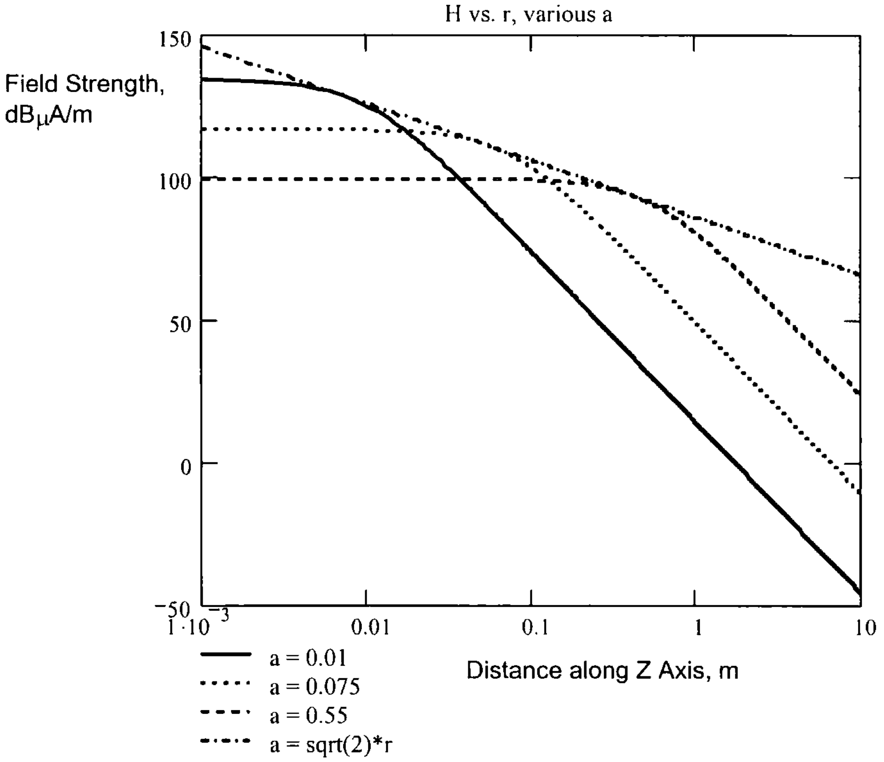

Figure 3.2 Field strength versus distance for three coil sizes (I = 1 mA, N = 100). Straight dotted line represents threshold distance, the distance at which field strength falls rapidly for a given coil radius.

We may use this result to determine the optimal coil size for a specified field strength and range by plotting the product of distance and field strength, as shown in figure 3.3. Peaks in distance×field strength are clearly seen coinciding with the straight dotted line, which represents the maximum possible value for a given *NI* product when a is specified as $r\sqrt{2}$ in (6). Furthermore, these peaks occur at the points along the x-axis when:

$$r = \frac{a}{\sqrt{2}} \qquad (9)$$

For example, figure 3.3 indicates that a coil whose radius is 0.01 m delivers the maximum distance-field strength product at around 0.007 m, beyond which a decay of 60 db per decade can be expected.

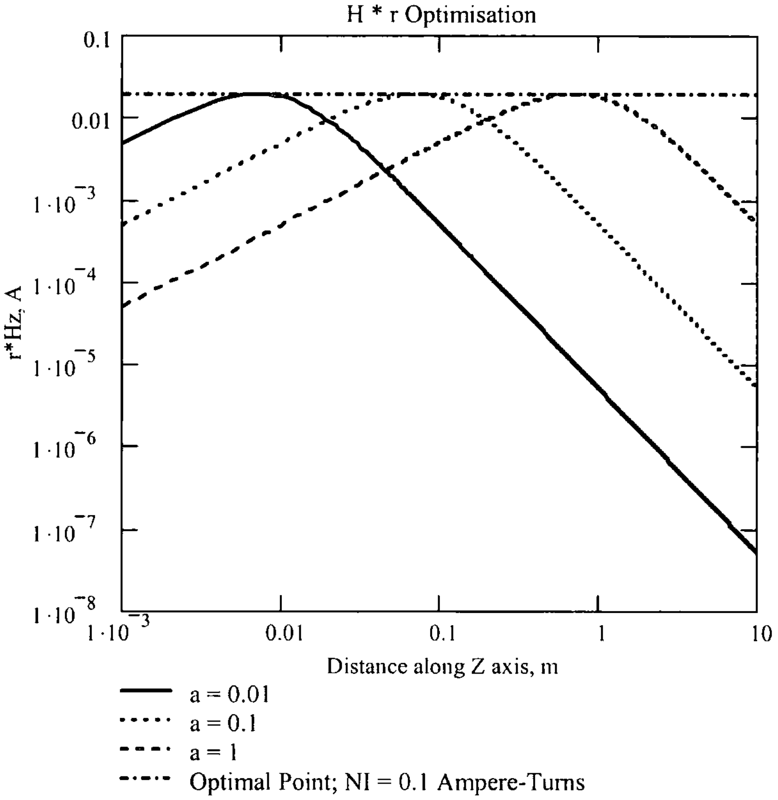

Figure 3.3 Graph showing r*H_Z versus distance, showing maximum possible value of r*H_Z for a given coil radius, *a*.

3.2.3 Self Inductance

Self inductance is defined as the flux produced per unit current:

$$L_1 = \frac{n_1 \phi_1}{I_1} \tag{10}$$

L_1 is the coil self inductance, ϕ is the flux passing through the inner diameter of the coil, n is the number of coil turns. It is a measure of the effectiveness with which current produces magnetic flux.

In most RFID applications it is desirable to maximise the reader and transponder coil inductance. This results in the highest mutual inductance, as discussed in section 3.3. Size restrictions limit the available winding area, so the design procedure normally progresses by obtaining the highest ampere-turns within the available area. This must take into account copper loss, which increases inversely with the wire cross-section area due to the skin effect. Each coil is normally made to resonate in either series or parallel fashion, and therefore each has an associated quality factor which is partially determined by copper loss[2]. Formulas for coil inductance are usually preferred to exact calculation due to the complexity involved and are described in [Grover]. A degree of approximation and refinement is therefore required when designing coils to a specification.

3.3 Mutual coupling Constrained to Coaxial, Coplanar Coils

In this section the mutual coupling between interrogator and transponder coils that are coplanar and coaxial is analysed. This arrangement is most commonly described in RFID literature to indicate performance.

---

[2] For coils with magnetic core (such as ferrite), the loss tangent of the core material also contributes towards the overall quality factor.

3.3.1 Assumptions

Two assumptions are made in this section: *Uniformity*; the lines of flux are uniform across the area of the coil, and *Normality*; the lines of flux are perpendicular to the plane of the transponder coil.

3.3.2 Characteristics of Inductive Mutual Coupling

Mutual coupling occurs when the flux produced by one coil links with another coil. Referring to figure 3.4, when the coupling between source and receiving coils is strong, mutual coupling may be expressed as the induced open-circuit voltage, V_{oc}, in loop 2 due to the current, I_1, flowing in loop 1:

$$V_{oc} = j\omega M I_1 \tag{11}$$

M is the mutual inductance between loop 1 and loop 2 given by:

$$M = k\sqrt{L_1 L_2} = \frac{n_1\phi_1}{I_2} = \frac{n_2\phi_2}{I_1} \tag{12}$$

where k is the coupling factor, a dimensionless parameter that indicates the degree of flux linkage. k may take any real value between 0 (no flux linkage) and 1 (total coupling). Inspection of equation 12 reveals that mutual inductance can be determined by geometry alone (since the coupling coefficient depends on the relative position and orientation of the loops) and that inductance is also a function of geometry. However we may also define mutual inductance similarly to equation 10 i.e., the ratio of flux passing through the receiving coil to the current passing through the source coil. Given that parallel resonance is typically employed to increase transponder chip voltage, M may be used to estimate the transponder chip voltage and hence determine whether the transponder is likely to activate.

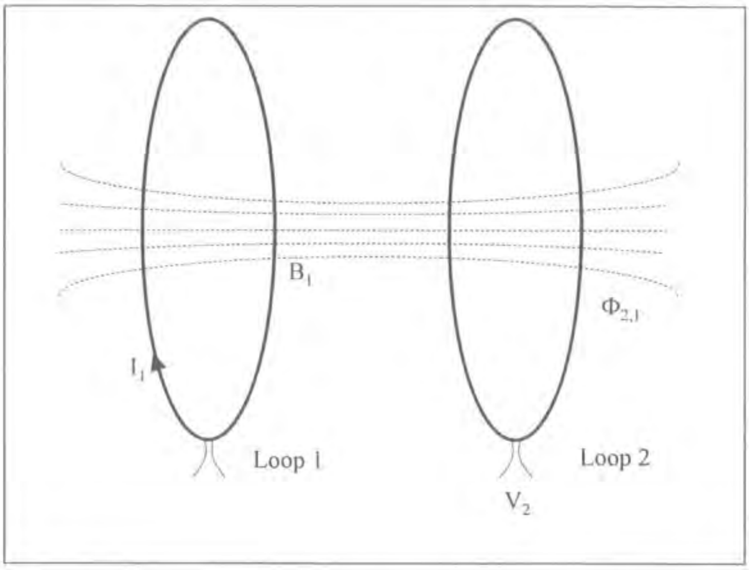

Figure 3.4 Mutual coupling between two loops

Evaluating the mutual inductance at distances comparable to the loop radii requires that we assume one coil, named *coil 1*, is larger than the other coil, *coil 2*. This allows us to further assume that flux passing through *coil 2* is reasonably uniform, in which case we may write:

$$M = \frac{n_2 \phi_2}{I_2} = \frac{n_2 \pi a_2^2 B_1}{I_2} = \frac{\mu n_1 n_2 a_1^2 a_2^2}{2\left(d^2 + a_1^2\right)^{3/2}} \qquad (a_1 > a_2) \qquad (13)$$

where d is the distance between coil 1 and 2, and n_1, n_2 are the number of turns for each coil. If $a_1 < a_2$, then equation 13 becomes:

$$M = \frac{\mu n_1 n_2 a_1^2 a_2^2}{2\left(d^2 + a_2^2\right)^{3/2}} \qquad (a_1 < a_2) \qquad (14)$$

the only change being in the denominator. We may use 13 and 14 to evaluate the mutual inductance between two coils. a_1 represents the radius of an interrogator coil and a_2 the radius of a transponder coil. We assume that each coil has a constant number of turns, and therefore that inductance varies only with radius a_1. The mutual inductance was calculated as a function of separation distance for three different interrogator coil radii, as shown in figure 3.5. The transponder coil radius is 0.01 m. The graphs are similar to the field strength plot of figure 3.2, possessing a flat region at small separation distances and a rapid decay of 60 dB per decade at larger separation distances. The transition point indicated in figure 3.5 occurs when the separation distance is equal to the interrogator coil radius. Substituting this condition into equation 14 gives the transition point related to the transponder coil radius

$$M = \frac{a_2^2}{4\sqrt{2}d_{trans}} = \frac{a_2^2}{4\sqrt{2}a_1} \qquad (15)$$

Equation 15 indicates that by increasing the size of the interrogator coil the transition distance d_{trans} increases, extending the flat region. However for separation distances less than the transition distance, the maximum mutual inductance is achieved when the coils are of equal radius as given by the solid line in figure 3.5. The decision of interrogator coil radius therefore depends on both transponder coil size and the separation distance likely to be encountered. For long range applications the interrogator coil must be considerably larger than the transponder coil if the flat region is to be maximised. However, the trade-off incurred is weaker coupling at close range.

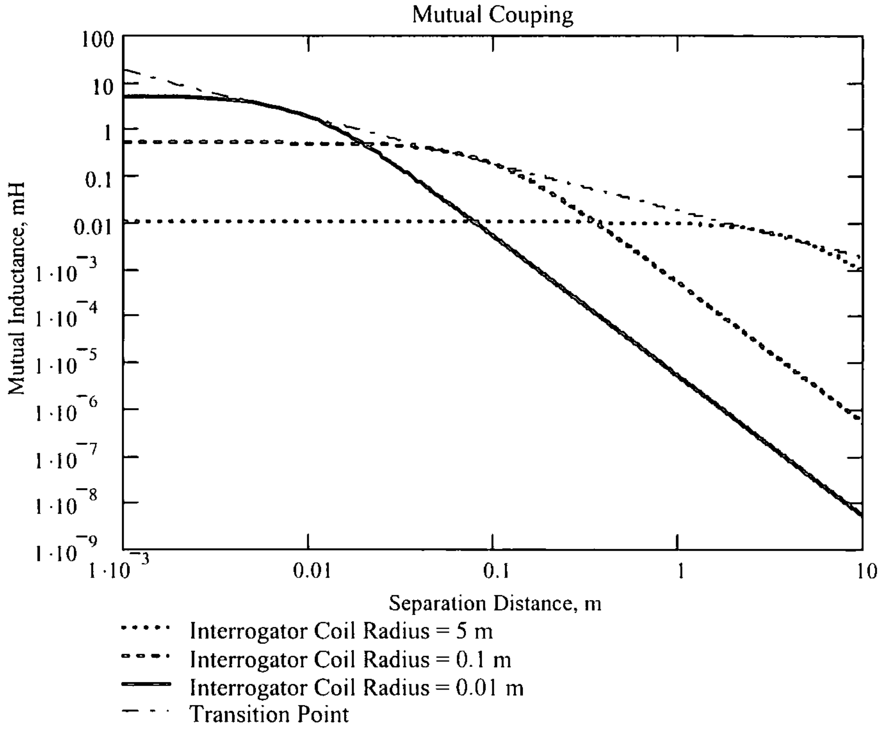

Figure 3.5 Mutual inductance as a function of separation distance. Transponder coil radius = 0.01 m.

If mutual inductance must be maximised for a given distance, then the interrogator coil size should be determined by a different approach. In figure 3.6, equations 13 and 14 were combined to produce a plot of mutual inductance as a function of interrogator coil radius for various separation distances. A fixed transponder coil radius of 0.01m is assumed. This graph shows that the maximum value of mutual inductance occurs at a particular interrogator coil radius depending on the separation distance. When the separation is zero, this condition occurs when both coils have the same radius. This is due to the fact that the same flux passes through both coils resulting in a coupling coefficient of unity. This condition also represents the highest possible mutual inductance for a given radius. If the interrogator coil is made smaller or larger than the transponder coil, the maximum obtainable mutual inductance decreases, and a larger interrogator coil is required to achieve maximum coupling. The condition for optimum coupling is found by differentiating equation 13 (or 14) with respect to a_1 and equating to zero, which results in the relationship

$$a_1 = d\sqrt{2} \tag{16}$$

This condition is analogous to that for maximum magnetic field strength from a single coil, which was given by equation 8. Equation 16 is independent of a_2 provided that $a_2 \le a_1\sqrt{2}$. Therefore to achieve optimum coupling we must ensure that the transmitter coil radius satisfies equation 16.

When the interrogator coil is larger than the optimal size given by equation 16, mutual inductance decreases from its maximum value, causing the transponder voltage to drop. Note how each curve in figure 3.6 tends towards the same straight line showing that increasing the interrogator coil radius brings no further benefit in this region. If however the interrogator coil is smaller than the optimum size, then the field strength may be increased by adding more turns (at the expense of increasing the copper losses) or by increasing the current amplitude. Note that while adding turns to the interrogator coil generally increases the mutual inductance, it does not affect the condition for maximum mutual inductance; the maximum possible mutual inductance for a given coil radius is not a function of the number of turns.

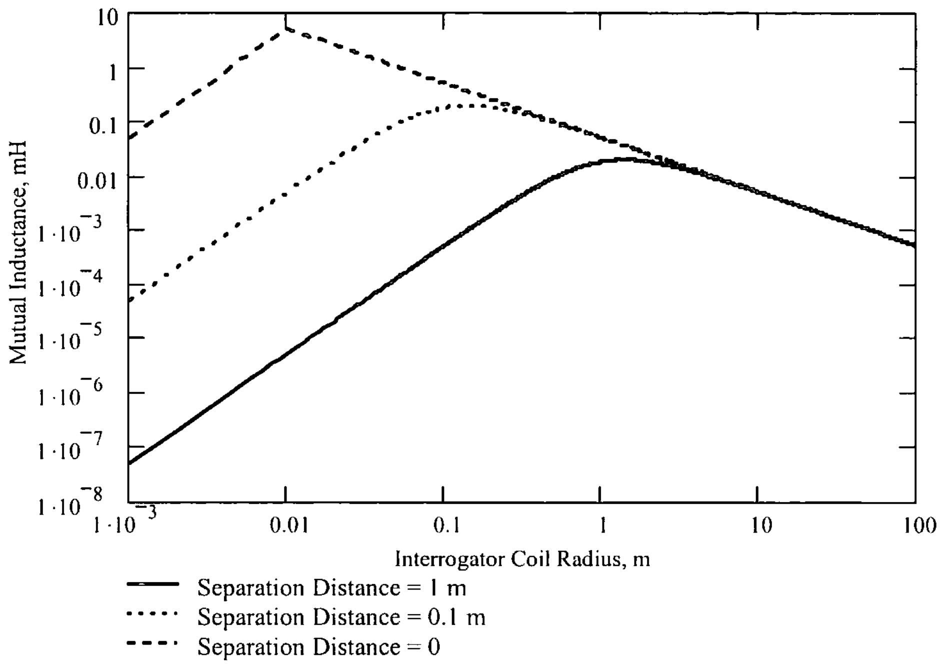

Figure 3.6 Showing the variation of mutual inductance with interrogator coil size and separation distance. Transponder coil radius was 0.01 m.

3.3.3 Characteristics of Coupling Coefficient, *k*

In equation 12 the quantity *k* was used in defining mutual inductance. *k* is a dimensionless quantity determined by the division between flux that is mutual to inductances L_1 and L_2, and that which is exclusive. Approximate expressions for *k* may be derived assuming circular coils:

$$k = \frac{a_1^2 a_2^2}{\sqrt{a_1 a_2}\left(d^2 + a_1^2\right)^{3/2}}\cos(\theta) \qquad (17)$$

The derivation of equation 17 can be found in appendix B. The assumptions described in the appendix are repeated below to illustrate the approximations incurred when calculating mutual inductance by equation 12:

a) Only the radial field component of B is considered because the tangential component has little effect when considering coaxial coils ($\theta = 0$);

b) The effects of winding geometry were ignored. Equation 17 is valid only when the coil's winding height and depth are small compared to the radius;

c) The field is assumed to be uniform across the cross-sectional area of each coil;

d) Copper losses in the wires was ignored. By making L_1 and L_2 complex quantities that represent the inductance and ESR (Equivalent Series Resistance) of the coil, copper loss could be included.

The effect of assumptions a)-d) becomes apparent when the coupling between two real coils is measured and compared with the theoretical calculation. Two nearly identical coils were constructed, each having 70 turns of SWG 32 enamelled wire, a radius of 4.75cm and inductance of approximately 1 mH. A more detailed specification can be found in section 4.3.3, chapter 4 (see coil A). For an *ideal* transformer (k = 1), the voltage ratio is related to the inductance ratio by the following equation [MacFayden]

$$\frac{V_{primary}}{V_{\sec ondary}} = \sqrt{\frac{L_{primary}}{L_{\sec ondary}}} \qquad (18)$$

For a *non-ideal* transformer this ratio must include k as a constant of proportionality. Since the coils were roughly identical, the inductance ratio is unity and k may approximated by measuring the voltage ratio as given by the right-hand side of equation 18. The resulting profile of k versus separation distance d is shown in figure 3.7. The measurement was conducted at the standard frequency of 125 kHz and additionally at 10 kHz to ensure that self-resonance effects had no effect on the measured voltages. A further measurement was taken having attached an op-amp to the receiving coil. This was done to remove any probe-loading effects that may have occurred. All three variations gave similar values between 10 mm (the minimum separation due to winding geometry) and 200 mm. Although the measured k is appreciably lower than the theoretical *k*, there is good agreement with regard to the decay rate which theoretically tends to 60 db per decade at separation distances greater then either coil radius.

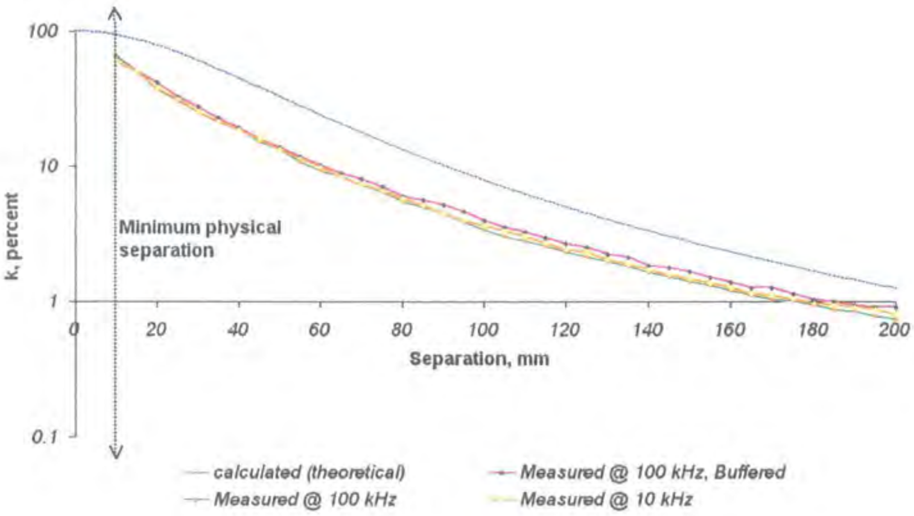

Figure 3.7 Measured and analytical *k* compared.

3.4 General Orientation of Source and Receiving Coils

In this section we consider the general case of coil position and orientation. The transmitting coil was fixed at a frame of reference and the sensing coil located at any position on the surface of a unit sphere surrounding the transmitting coil as indicated in figure 3.8. Spherical coordinates are therefore used to describe the sensor's position by azimuthal, α, and elevation, β angles. Sensor orientation is described by angular rotation from a reference orthogonal axis according to azimuthal ψ, elevation, θ and roll, ϕ angles.

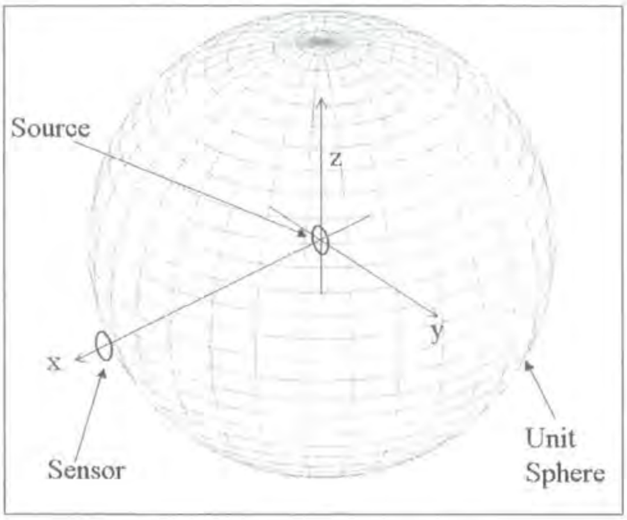

Figure 3.8 Showing placement of sensor on unit sphere around source

The radial and tangential field equations 4 and 5 were used to describe the transmitter field, for which we must assume $r^2 >> a^2$. In this case we may gather constant terms and rewrite the equations as:

$$H_r = \frac{M}{r^3}\cos\theta; \qquad H_\theta = \frac{M}{2r^3}\sin\theta; \qquad M = \frac{a^2 I}{2}$$

where M is a constant. In addition, if we assume a unit sphere then the separation distance, r, is always 1, we the see that the radial and tangential components differ only by a factor of 0.5. By inspecting figure 3.9 we see that coupling due to tangential field components is negative; the tangential field component is that part returning to the source and hence passing through the sensing coil in the opposite direction to the radial component. Raab suggests that the general source-sensor coupling can be expressed in vector-matrix form as [Raab]

$$f_{out} = \frac{M}{r^3}\cdot\begin{bmatrix}1 & 0 & 0\\ 0 & -0.5 & 0\\ 0 & 0 & -0.5\end{bmatrix}\cdot f_{source} = \frac{M}{r^3}\cdot S\cdot f_{source}$$

(19)

where f_{source} is a matrix that takes one of the following forms:

$$f_{source} = \begin{bmatrix} f_x \\ 0 \\ 0 \end{bmatrix} ; f_{source} = \begin{bmatrix} 0 \\ f_y \\ 0 \end{bmatrix} ; f_{source} = \begin{bmatrix} 0 \\ 0 \\ f_z \end{bmatrix} \qquad (20)$$

for an x,y or z aligned source coil respectively. With this approach we are merely rotating the source to select the appropriate factor of 1 or –0.5 to account for radial or tangential coupling, whilst the sensing coil remains static. To calculate the sensor output for *any* orientation, Raab applied a series of position and orientation vector transformations using orthogonal rotation matrices, which allow alignment of a equivalent source and sensor pair. Equation 19 can then be applied and the resulting output of the real sensor found by applying orientation transformations. The principle equation used to calculate the sensor output is:

$$f_{out}(\alpha,\beta,\psi,\theta,\phi)_i = \frac{M}{r^3} \underbrace{T_\phi T_\theta T_\psi \underbrace{T_{-\alpha} T_{-\beta} S \underbrace{T_\alpha T_\beta f_{input}}_{\text{Source aligned to equivalent sensor}}}_{\text{Output from equivalent sensor}}}_{\text{Output from actual sensor}} \qquad (21)$$

where T_α, T_β, T_ψ, T_θ and T_ϕ, are the orthogonal rotation matrices given in figure 3.10. See [Goldstein] for a description of rotation matrices. The input vector f_{source} may take any combination of x,y, and z source coils and f_{out} has three corresponding components ($i = 0..2$) that represent the independent outputs from three orthogonal sensing coils. The calculation method is described in detail in appendix C. Equation 21 was computed in a Mathcad[3] worksheet, the results of which were post-processed in Matlab[4]. A unit sphere was constructed graphically by converting the spherical coordinates $(r,\theta,\phi,)$ to their Cartesian equivalents (x,y,z) and plotting them using the built-in *surf(x,y,z)* command. The f_{out} data was then scaled and processed to create a new colour map

---

[3] See www.mathsoft.com

[4] see www.mathworks.co.uk

which was applied to the surface of the sphere, thus giving a visual picture of the sensor output for all positions around the source coil(s). This method allows rapid identification of field nulls and their pattern around the unit sphere.

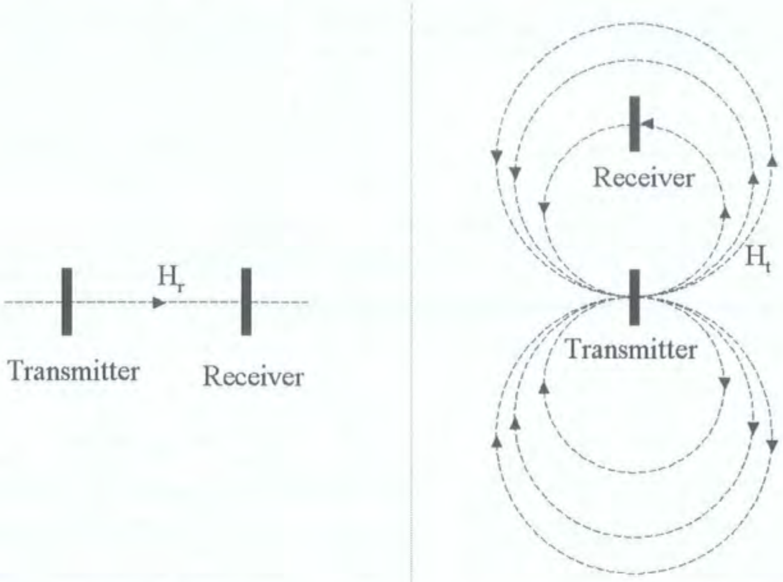

Radial Coupling Tangential Coupling

Figure 3.9 Showing radial and tangential coupling modes

$$T_{\alpha}(\alpha) := \begin{pmatrix} \cos(\alpha) & \sin(\alpha) & 0 \\ -\sin(\alpha) & \cos(\alpha) & 0 \\ 0 & 0 & 1 \end{pmatrix} \qquad T_{\psi}(\psi) := \begin{pmatrix} \cos(\psi) & \sin(\psi) & 0 \\ -\sin(\psi) & \cos(\psi) & 0 \\ 0 & 0 & 1 \end{pmatrix}$$

$$T_{\beta}(\beta) := \begin{pmatrix} \cos(\beta) & 0 & -\sin(\beta) \\ 0 & 1 & 0 \\ \sin(\beta) & 0 & \cos(\beta) \end{pmatrix} \qquad T_{\theta}(\theta) := \begin{pmatrix} \cos(\theta) & 0 & -\sin(\theta) \\ 0 & 1 & 0 \\ \sin(\theta) & 0 & \cos(\theta) \end{pmatrix}$$

$$T_{\phi}(\phi) := \begin{pmatrix} 1 & 0 & 0 \\ 0 & \cos(\phi) & \sin(\phi) \\ 0 & -\sin(\phi) & \cos(\phi) \end{pmatrix}$$

Figure 3.10 Orthogonal rotational matrices

3.4.1 Physical Approximations to Ideal Sensors

It should be noted that the term *sensor output* in this context refers to the H-field intercepting the infinitely small magnetic loop produced by similarly small source loops with current I flowing through them. The sources f_x, f_y and f_z in equation 14 are therefore the currents flowing through the source coils, which in this case were assumed to be equal to unity. The most accurate physical equivalent to the ideal sensor is a small coil whose open-circuit voltage is measured to indicate the field strength in that region.

$$V_{oc} = j\omega A\mu H_i N\cos\theta \qquad (21)$$

where A is the coil area, H_i the field strength of the of the incident magnetic field, N the number of turns, μ the permeability and θ the angle between the coil axis and the magnetic field vector.

3.4.2 Single Source and Sensor Coils

A single source coil was defined along the x-axis while single x,y or z sensing coils were moved around the unit sphere in the simulation, as shown in figure 3.11. The resulting field nulls can clearly be seen in figure 3.12, where the modulus of the output sensor (i.e. absolute output values) is shown. Modulus values form a valid assumption given that RFID transponders are not affected by the sense of the induced EMF. The darkest regions indicate field nulls (no mutual coupling) which causes total failure in the inductive RFID system; the lightest regions are where the coupling is strongest. The z-sensor produces an identical pattern to the y-sensor, but with the pattern rotated 90 degrees in elevation. The plots have been normalised to the strongest region of all three plots to show that the y and z sensors produce a maximum around 70% of the maximum using an x-sensor.

These results are easily confirmed by measurement. A large coil of 10 cm diameter was excited by a 50 ohm RF source at 125 kHz to produce the source field, while a smaller coil of around 1 cm diameter was connected to an oscilloscope and moved around the source at approximately constant radius.

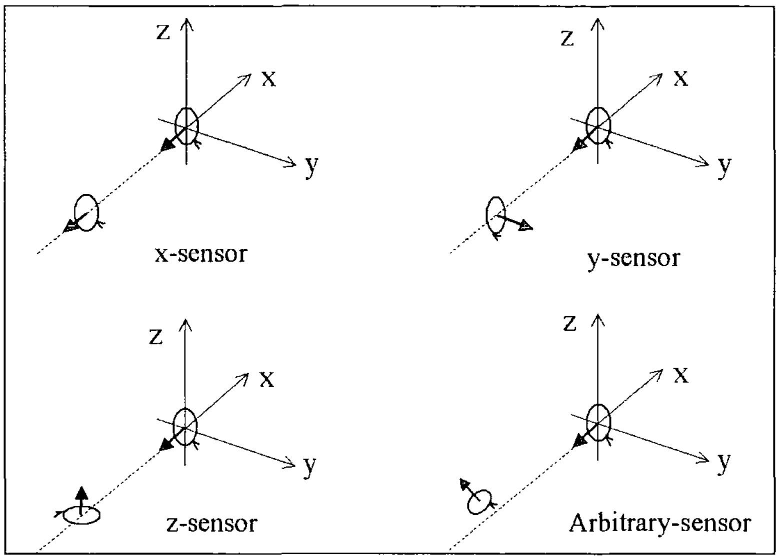

Figure 3.11 Single source and sensor orientation, showing x, y, z and arbitrarily-orientated sensors

3.4.3 Discussion

Regions of system failure are clearly identified by the black regions. These are dependent on the transponder sensor orientation. Any sensor orientation may be evaluated using this method with the same conclusion: field nulls are always present (see appendix C for an example of general sensor orientation). System flexibility is thus compromised and arrangements must be made to ensure that, for a given application, null-inducing orientations are avoided. This may be impossible for some applications such as air baggage tagging where RFID labels are fixed to the luggage at random orientations.

Since the x,y and z coils are orthogonally arranged, their respective fields do not interact. This permits simultaneous excitation which is investigated in the following section.

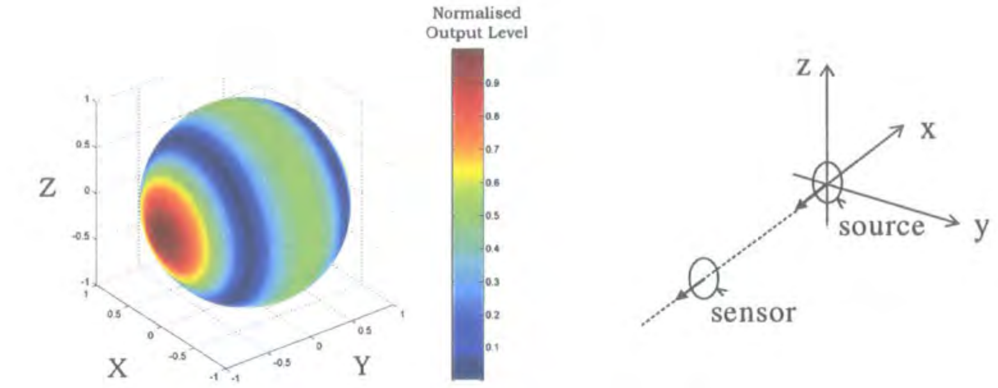

(a) Sensor and source coils aligned along x-axis.

Layout

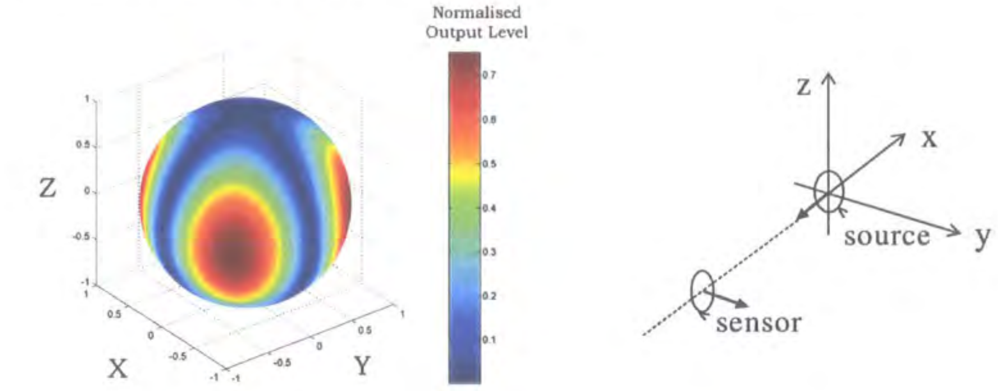

(b) Source aligned along x-axis; sensor aligned along y-axis.

Layout

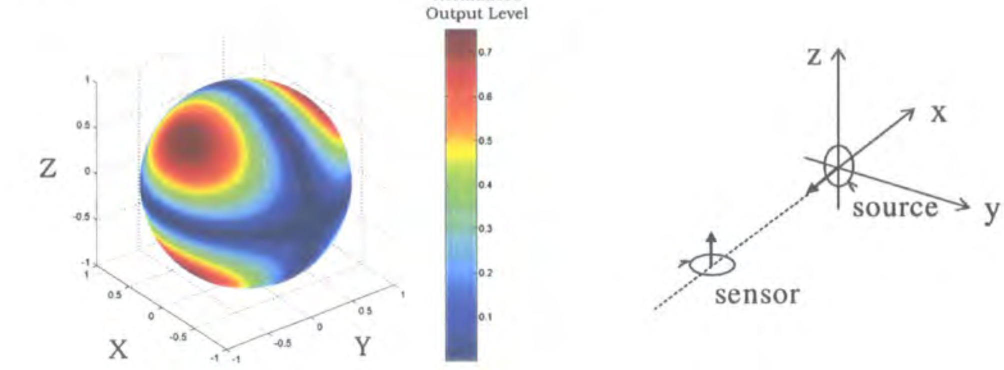

(c) Source aligned along x-axis; sensor aligned along z-axis.

Layout

Figure 3.12 Output of sensor positioned around x-orientated source coil. Sensor orientations as indicated.

3.5 Elimination of Orientation-dependent Nulls

The use of two or more transmission or receiving coils in positioning system has been documented. An early example is described by Kalmus [Kalmus62] in which a pair of receiving coils was used to track the distance and orientation between two military vehicles. This method was later improved by using two source coils excited in phase quadrature [Kalmus64]. In another example, wire loops were used in an emergency location system for underground mines [Murphy]. This system used radiating *(far-field)* coils buried under the ground plane as modelled in [Olsen]. More recently, the concept of using either three orthogonal transmission coils [Palmero02] or three sensing coils [Palmero99] has been investigated with the aim of increasing the performance of inductive coupled networking devices. In a typical application, an inductive ASK communication channel between a wireless headset and a mobile phone is established. The inductive physical layer has an advantage over radiating communication systems such as Bluetooth and 802.11b in that the communication "bubble" is inherently small due to the $1/r^6$ power-range property of inductive coupling. This brings increased security and a reduction in interference from noise sources such as other nearby personal networks.

3.5.1 Orthogonally Disposed Sensor Coils

In this section we consider a transponder that uses three orthogonally arranged coils with the aim of eliminating field nulls. In figure 3.13(a) the result of straightforward recombination is seen, in which the x,y, and z-orientated coils are connected such that the induced emf's are summed directly. It is assumed that each coil is buffered such that its impedance cannot affect the other coils. Positive and negative signals from each coil combine to produce new regions of zero coupling and strong coupling. The location of these regions is dependent on the relative phase of the driving currents in each transmitter coil, i.e., 0 or 180 degrees.

Using a more sophisticated approach, the absolute magnitudes of each induced EMF can be summed resulting in the profile of figure 3.13 (b). This method operation requires ideal signal (lossless) rectification to remove the effects of summing positive and negative combinations. The result is a coupling space lacking any nulls, although strong and weak regions remain. In a variation of this method, the sum of the square of each output is formed, then the square root calculated. The resulting profile is shown in figure 3.13(c).

Another method involves selecting the coil which produces the strongest signal. This method required that rectification takes place, otherwise zero output results when all sensor outputs are zero or negative. The resulting sensor output is shown in figure 3.13(d). This process requires additional processing, since selection of the most appropriate sensor must be updated dynamically as the transponder's orientation and position change.

The above methods may be compared by plotting the sensor output as it travels around the vicinity of the source. In figure 3.14 the output is given as a path around the azmuthal plane is traced at an elevation angle of 0 degrees. The rectifying and sensor selection methods both produce positive output for all azimuthal angles, but the strongest output is produced by the rectifying method. Note that the root-sum-squares method produces an output that intersects the points common to the other methods.

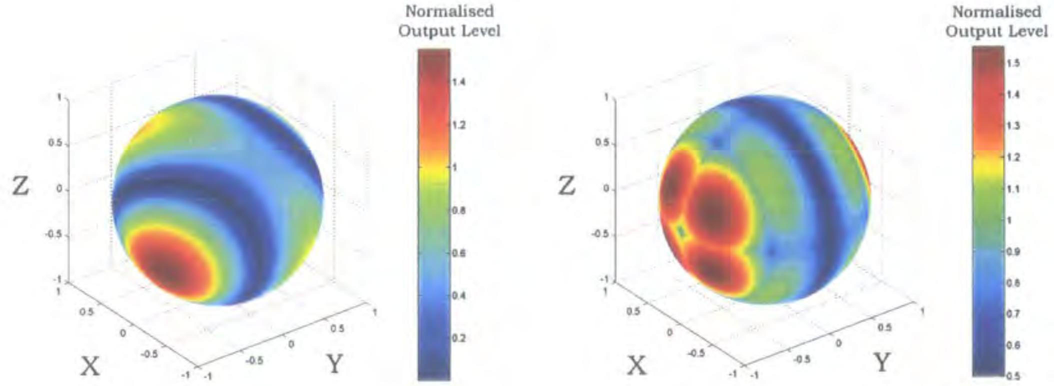

(a) Output of three axis sensor using direct summation when placed near single source coil.

(b) Output of three axis sensor using summation of rectified coil outputs.

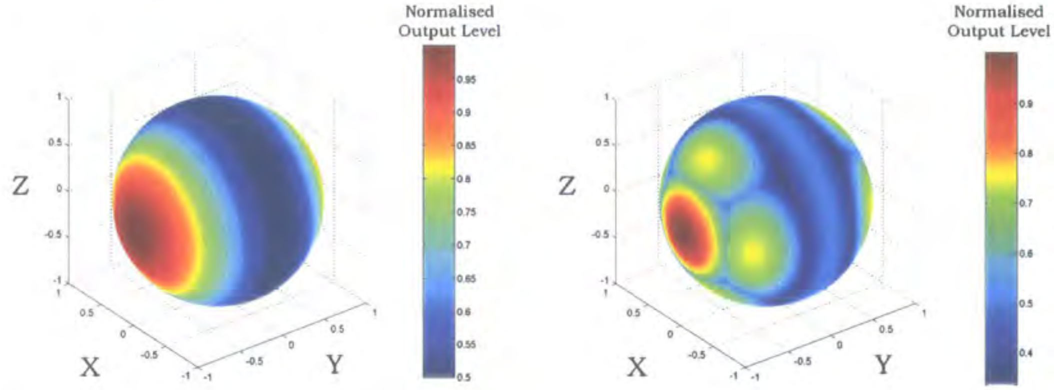

(c) Output of three axis sensor using root-sum-square of rectified coil outputs.

(d) Output of three axis sensor using best coil selection.

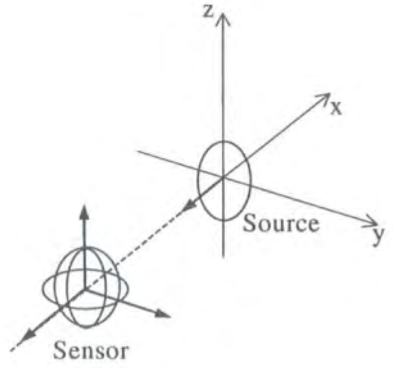

Layout

Figure 3.13 Orthogonal sensor output using single source coil orientated along x-axis.

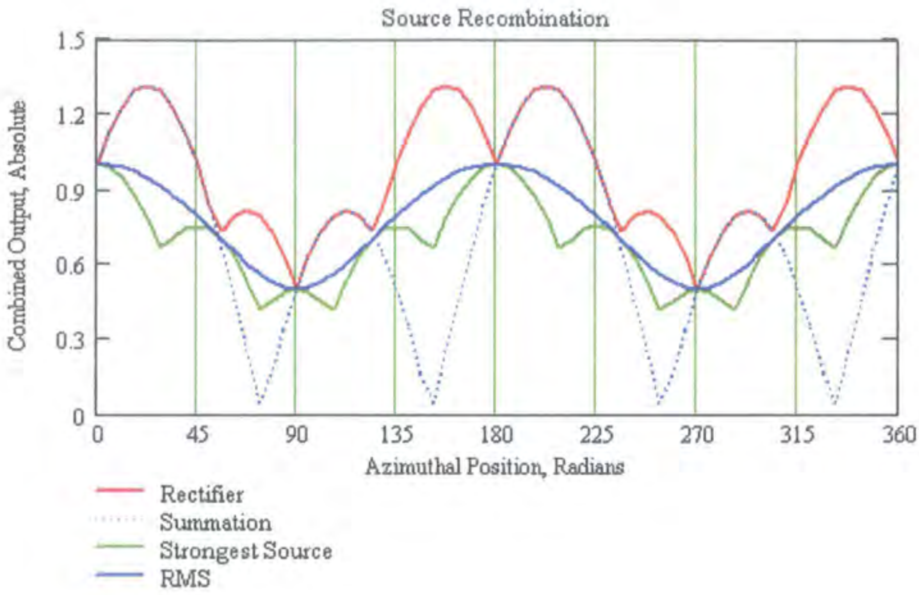

Figure 3.14 Comparison of source recombination methods.

3.5.2 Discussion

In RFID applications, transponder complexity must be minimised; an increase in the number of transponder coils and associated circuitry would not be advantageous from the perspective of cost. Examples of the circuitry required for three-coil sensors can be found in [Palmero99] and [Giunta]. Generally, recombination of the signals from orthogonal sensor coils must be carried out using at least a summing amplifier. In addition, an impedance buffer must be used between each coil and the summing amplifier to avoid impedance shunting effects due the combined parallel impedance of each coil. This requires power to activate the amplifiers, which cannot be extracted until the signals have been appropriately recombined. This requires the use of passive rectifying circuits that produce DC supply currents for the active circuits.

Another requirement of an orthogonal transponder coil arrangement is a load modulator capable of loading all three transponder coils to achieve optimal direct load modulation performance. Provided that the modulator ON impedance is considerably smaller than the combined parallel impedance of all three coil circuits, this does not present difficulty, and due to parallel resonance, the effective coil impedance is increased near resonance. (see Chapter 5 for more information on this effect.)

A further effect of using multiple transponders would be the coupled impedance that appears in the interrogator circuit due to the presence of the transponder. This was not considered in the above model. Three coupled impedances would appear in the interrogator circuit representing each of the three transponder coils. Careful coil-matching would be required to minimise the reactive element of the resulting coupled impedance, which could otherwise affect interrogator tuning.

Passive RFID requires a different approach that does not require additional transponder circuitry. This can be achieved by using orthogonal source coils in such a way that existing transponders do not require alteration. This is considered in the next section.

3.5.3 Orthogonally Displaced Source Coils

We replace the single source coil with three orthogonal coils and revert to a single transponder coil. The fundamental difference between this arrangement and that of section 3.5.1 is that we must control the *distribution* of signals, not their recombination. To this end we may control the following source parameters: relative phase, time slots and relative magnitude. We consider here only relative phase and time slotting.

Considering first of all relative phase, the output of an x-orientated sensor obtained by driving all source coils simultaneously and in phase is shown in figure 3.15(a).

Regions of null coupling result close to strong positive coupling areas. This also occurs when using y and z orientated sensors. By changing the phase of one or more source coils, the region of strongest coupling moves for a given sensor orientation, but null regions always remain. In figure 3.15(b) the effect of phase inversion of the z-orientated source coil using an x-orientated sensor is clearly seen by alteration of the region of strongest coupling.

In order to remove nulls in mutual coupling a method of selecting the best source coil is required such that it transmits independently. Such systems have been described [Palmero02] for use in inductive networking devices, but they require that both nodes have active transmitters to determine which source coil should be used. In passive RFID applications a transponder will not reply unless sufficient mutual coupling exists (i.e. the best source coil is being used), therefore received signal strength cannot solely be used to select the best source coil. Instead, each source coil could be activated in rapid succession to determine which instigates a response. If more than one source coil provides a response, the demodulated signal amplitude could be used to determine which gives the strongest mutual coupling. If this method were implemented in an ideal fashion then the sensor output would appear as illustrated in figure 3.15(c), where the output from an x-orientated sensor evaluated for each source coil separately (x,y,z) and the strongest output chosen. Note that the absolute (or magnitude) of the sensor output was compared and therefore figure 3.15(c) represents the (ideal) rectified sensor output; it does not distinguish between phase reversal between the sensor terminals. This is valid as the transponder does not itself distinguish between 0 and 180 degrees voltage phase. We see from figure 3.15(c) that coupling nulls are eliminated and that the weakest coupling is around 35% of the maximum level, which causes a reduction in range in these regions for passive RFID.

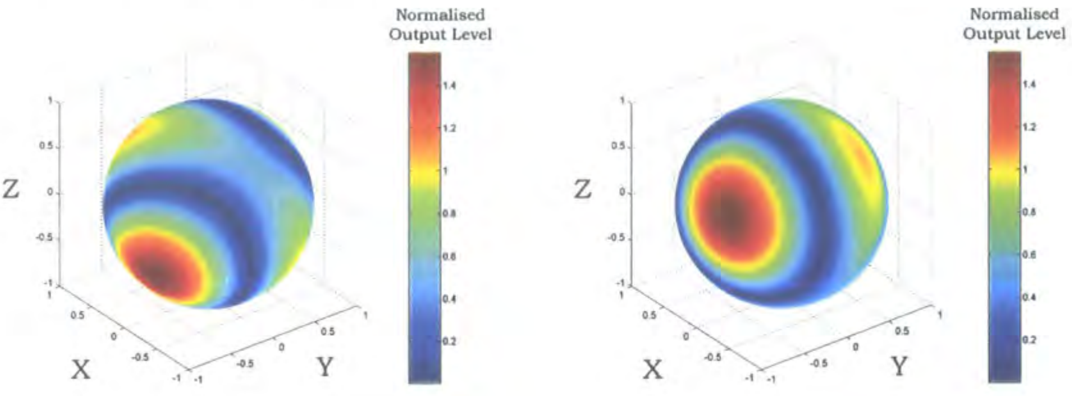

(a) Output from single x-orientated sensor placed near three simultaneously active source coils.

(b) Output from single x-orientated sensor placed near three simultaneously active source coils having phase inverted z-source.

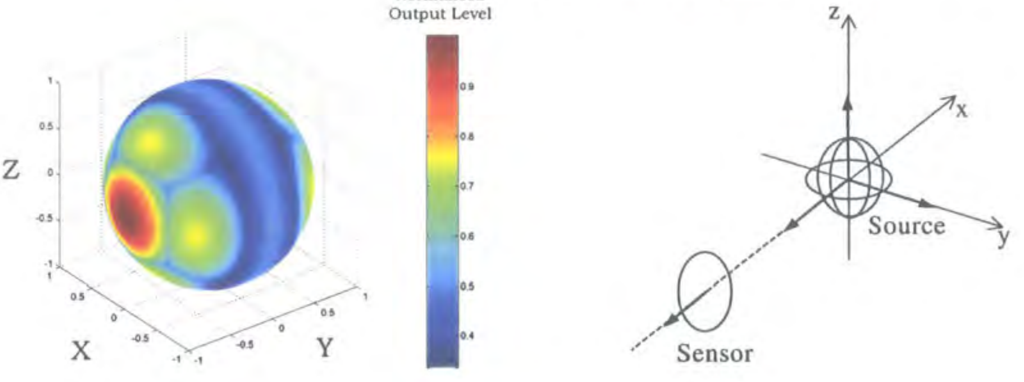

(c) Output from single x-orientated sensor placed near three time-multiplexed source coils (best source coil selected).

Layout

Figure 3.15 Output from single x-orientated sensor placed near three orthogonal source coils

3.5.4 Discussion

The use of multiple interrogator coils is more attractive than multiple transponder coils since the complexity is contained within the interrogator enabling the use of existing low-cost transponders. This is in contrast to inductive personal communication devices, which have both active transmitter and receiver, and so can afford to employ more complex methods for removing coupling nulls.

In order for the multiple interrogator coil method to work effectively, the correct source coil must be activated for each transponder orientation and position. This decision would be based on a number of criteria:

(a) Whether a successful reply was received,

(b) The strength of the demodulated signal

(c) Interrogator current dampening caused by the mutual coupling between interrogator circuit and transponder.

Methods (b) and (c) could be used to refine the selection process when two or more coils satisfy (a).

3.6 Summary

General limitations to the inductive coupling mechanism have been investigated in the context of passive proximity RFID. Maximisation of the quasi-magnetostatic near-field produced by a solitary circular coil was found which may be used to determine the most appropriate coil radius for a given maximum range. It was also observed that a large coil produces a relatively weak magnetic field near its centre. Equations for mutual inductance between two coplanar, coaxial coils were given, then used to find the conditions imposed on coil size for maximum mutual inductance. Conditions for maximum mutual inductance or uniform mutual inductance across a specified separation distance were found and may be used to determine the most appropriate interrogator coil radius given the transponder coil radius.

The coupling problem was extended to three dimensions and general source-sensor orientations by assuming magnetic point sources, which is valid when the radius of separation is larger than the coil radii. This approach used was based on a method described by [Raab] and demonstrated the occurrence of coupling nulls that hinders simple RFID systems.

Orthogonal multiple-coil arrangements were considered in an effort to eliminate coupling nulls and therefore enhance the flexibility of passive RFID systems. By employing an orthogonal arrangement within the sensor (transponder) field nulls can be eliminated. This was most effective when using the rectify-add method. The use of orthogonal source coils also enabled elimination of coupling nulls, and was favoured due to the fact that no transponder modifications are necessary. In order to eliminate nulls by this method, each source (or interrogator) coil must be activated separately within its own time slot otherwise nulls occur due to interaction between the fields. Suggestions for determining which coil should be active for a given transponder orientation were given.

3.6.1 Further Work

An interesting extension to the work on orthogonal coils would be to consider the effect of ferrous coil cores on the field patterns. The presence of ferrous material would distort the magnetic flux lines, tending to draw the surrounding field through the coil.

This may aid in the elimination of coupling nulls and help to reduce coupling dips observed when using orthogonal air coils.

Another variation would be the use of non-identical orthogonal coils. As an example, this would reduce volume requirements by making the y and z-plane coils thin and rectangular so that the required space was similar to that of the x-plane coil alone. Obviously a reduction in null elimination performance would be expected, but limitations on feasible coil size reduction could be investigated.

4 *Shield Effects on RFID Systems*

4.1 Introduction

In the previous chapter it was shown that inductive RFID technology imposes severe design requirements upon coil separation distance and orientation. In long-range applications the coils will ideally have large cross section area, inductance and quality factor. Within cost and size restrictions transponder coil inductance should therefore be maximised. The interrogator coil should produce a strong alternating magnetic field and should be highly sensitive to impedance modulation. In this chapter we focus on the extent to which these attributes are compromised when the interrogator or transponder is placed close to conducting sheets, generally referred to here as *shields*.

The effect of placing an inductive coil near a shield is to alter its apparent impedance. This causes the field supplied to the transponder coil to weaken due to the combined effects of detuning of the resonant circuit and an increase in the apparent resistance presented to the reader circuit. Sensitivity to load modulation is also reduced by these effects. Methods of compensation such as adaptive tuning and adaptive sampling may be required to minimise the impact of shields on performance. These methods aim to maximise the receiver signal-to-noise ratio, and are discussed further in chapters 5 and 7, but require characterisation of the extent to which inductance and resistance is altered by shields.

It is therefore necessary to characterise the extent to which coil impedance is altered by the presence of shields, particularly with respect to coils designed for RFID interrogators, which must be able to detect passive transponders fixed to metal surfaces.

4.2 Review

We define a shield to be a planar surface whose cross-sectional area is appreciably larger than its thickness. The effect of such shields on inductive coils has been studied in the past within the context of shield effectiveness, which describes the degree to which coupling is reduced between two coils by insertion of a thin shield between the coils. Levy derived an equation for the electric field attenuation imposed when a conducting shield is placed between two coaxial coils [Levy]. This was achieved by considering the effect of eddy currents induced in the shield and both source and receiving coils by using image coils. The analysis was confined to the near-field region such that the coupled impedance appearing at the transmitting coil due to the shield could be found by finding an expression for the induced EMF caused by eddy currents. By this method, Levy was able to deduce formulas for the change of self inductance and equivalent resistance of a coil placed near a conducting shield. The analysis included the influence of frequency and shield conductivity, but did not consider the effect of shield permeability, limiting its usefulness to non-ferrous shielding materials. The change of inductance and resistance in the presence of a conducting shield is given by the following equations [Levy]:

$$\Delta L = -\frac{21.6An^2 10^{-9} e^{-3.6\left(D/r\right)}}{1+\left(\dfrac{78.8}{rT\gamma f}\right)^2} \qquad \text{(H)} \tag{1}$$

$$\Delta R = \left(\frac{1}{\gamma T}\right)\frac{1.42n^2 10^{-5} e^{-3.6\left(D/r\right)}}{1+\left(\dfrac{78.8}{rT\gamma f}\right)^2} \qquad (\Omega) \tag{2}$$

Where ΔL is the change in inductance; ΔR is the change in resistance; T is the shield thickness in cm; r is the coil radius in cm, from axis to centre of winding; γ is the percent conductivity of the shield, (for annealed copper, $\gamma = 1$); D is the distance from coil to the centre of the shield in cm; n is the number of turns; and f is the frequency in Hertz.

Levy's work focused primarily on magnetic shield effectiveness, which is most relevant to EMC applications. Further analytic investigations have been conducted [Ball], to describe this effect. Three major methods were summarised in a paper by Moser [Moser], who categorised the analysis methods into there types: Levy's eddy current approach (described above), direct solution of the electromagnetic equations and a transmission line method. In general these methods report that the shield effectiveness depends on coil separation and shield thickness, while it is independent of the exact position of the shield between the coils (provided it remains perpendicular). In addition, at frequencies below a few tens of kilohertz the magnetic fields can be considered to be quasi-static.

An alternative model was described by Terman [Terman], who suggested that the effect of a conducting shield might be described as a coupled impedance. This results in a simple transformer equivalent circuit in which the coil is modelled as the primary inductance and resistance. The shield is then modelled as resistance and inductance in the transformer secondary, the effect of which is to reduce the inductance and increase the resistance of the primary. However the degree of coupling between the shield and coil must be described by a coupling coefficient, which leads to leakage inductance terms in the primary and secondary circuit. These terms represent flux produced by the coil that does not couple with the shield. The calculation of coupling coefficient would require field calculation and so was not regarded as a convenient method of calculation.

In [Olsen] and [Hasselgren] the basic shielding mechanism is described, where it is classified by material type and geometry. Perfect conducting shields, referred to as Perfect Electric Conductors (PEC) produce eddy currents when alternating magnetic flux attempts to pass through them. The eddy current oppose flux by deflection so that flux lines tend to travel parallel to the surface rather than through the shield. In contrast, a perfect magnetic shield possessing high permeability draws magnetic flux into the shield normal to the surface and is called a Perfect Magnetic Conductor (PMC). These characteristics may be exploited when using numerical simulation; a boundary of zero normal flux may be used for perfect conductors, and a boundary of zero tangential flux used for perfect magnetic shields. It is important to realise that perfect conducting shields are ineffective at D.C., since eddy currents will not be induced. The contrast between PMC and PEC boundary conditions is illustrated in figure 4.1, where simulated magnetic flux patterns created by a coil suspended above PMC and PEC sheets are illustrated. The simulation was computed using Maxwell 2D software[5] as an eddy current problem in the x-y plane.

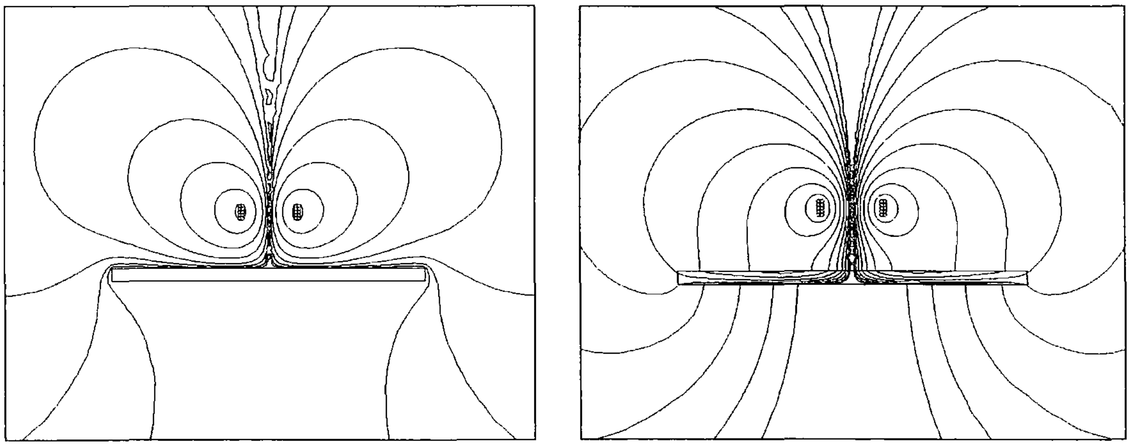

Figure 4.1 Comparison between PMC and PEC Shield.
Left picture shows PEC, right picture PMC. Simulation frequency is 125 kHz.

---

[5] Ansoft Corporation

Shields may also be classified according to geometry; open shields do not isolate the shielded region in all directions whereas closed shields are designed to produce complete isolation. In this chapter, we consider open planar shields as they are most commonly encountered in RFID applications, in which transponders are often fixed to metallic host objects. The subject of closed shields in RFID has been considered for special applications in RFID [Calderbank], in which magnetic flux produced by the reader must penetrate a closed shield in order to read a transponder buried in the metallic structure. It was found that a small air gap around the surface allowed sufficient flux to link with the transponder coil (figure 4.2). This approach requires high inductance coils for both reader and transponder with ferrite cores so that flux is attracted through the coils. The impact of open shields on read-range was quantified by measurements taken from an RFID prototype system.

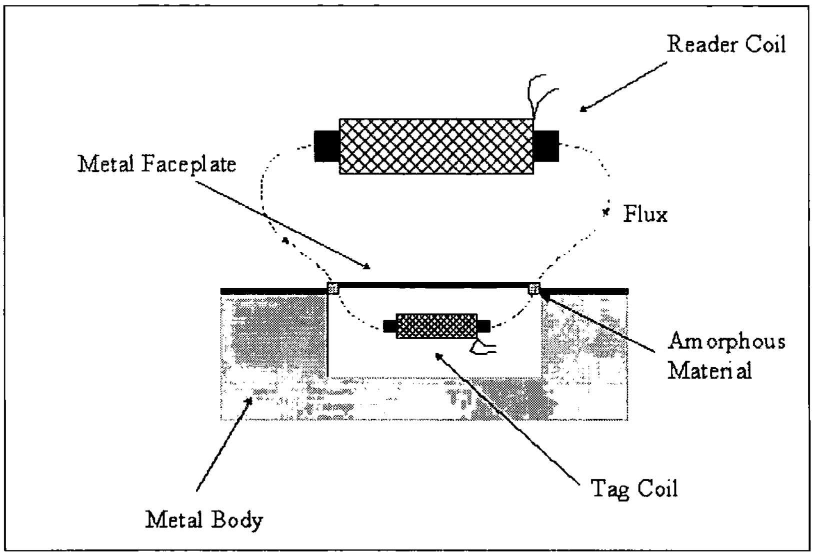

Figure 4.2 Reader – Transponder coil arrangement for closed-shield application showing path of magnetic flux linking reader and transponder (see [Calderbank]).

4.3 Description of Method

The arrangement under consideration here is illustrated in cross-sectional form in Figure 4.3, where a circular coil is suspended above a sheet of conductive material at a separation distance of *D* mm. The coil plane is perpendicular to the sheet plane. An Agilent 4294A impedance analyser was used to evaluate coil impedance (i.e. inductance and equivalent series resistance). The coil-source separation, *D*, was taken to be the distance from the shield surface to the centre of the coil.

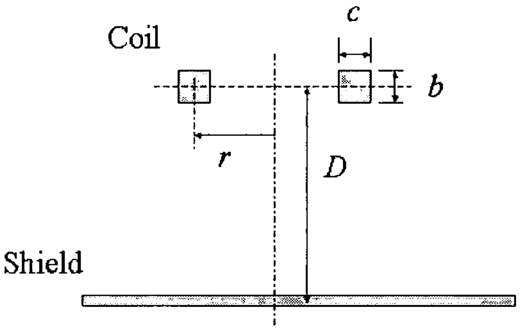

Figure 4.3 Arrangement of coil and shield as a cross sectional view showing key dimensions.

4.3.1 Shield Parameters

Planar shields may be considered as either having an infinite surface area or as being sufficiently large compared to the coil under consideration that it may be considered to be infinite. Field leakage will occur around finite shields, which may be regarded as leakage flux, and is therefore assumed to be frequency independent.

Infinite shields are often used to investigate the fundamental shielding mechanism, while finite shields are used to observe edge effects. We consider finite shields that are sufficiently large to behave approximately as the infinite shield would, but would also permit observation of edge effects if required.

The key shielding parameters are thickness (*T*), conductivity (σ) and relative permeability (μ_r). A PEC shield has relative permeability of 1 and infinite conductivity. It is physically approximated by high-grade electrical copper. PMC shields have infinite permeability and zero conductivity and are simulated as non-conductive, high permeability materials.

A variety of shield materials were used, including ferrous and non-ferrous. They are summarised in table 4.1, which gives the thickness of each sample. Levy mentions that the minimum shield area should be greater than $8r^2$, which is largest for coil A, at 180.5 cm^2. Shield samples were cut to 15 cm square, with an area of 225 cm^2, except for the iron sheet, which measured 16 * 10 cm.

Shield Type	Thickness (cm)
1/16 Copper	**0.16**
1/200 Copper	0.0127
Galvanised Steel	0.127
1/8 Aluminium	.318
1/16 Aluminium	.163
Iron	0.05
Zinc-Plated Steel	.111
Stainless Steel	0.025

Table 4.1 Summary of conducting shields used for measurement

4.3.2 Restrictions

For a given shield area, restrictions on coil-shield separation and shield thickness apply when using Levy's equations for resistance and inductance. These constraints are necessary to maintain a claimed accuracy of ±10%, and are summarised by the following inequalities[6]

$$0.15r < d < 0.9r \quad (3)$$

$$T < 0.2r \quad (4)$$

The corresponding coil-shield separation limits are between 0.71cm and 4.28 cm for coil A, between 0.12 cm and 0.72 cm for coils B and C and between 0.17 cm and 1.03 cm for coil D. Shield thickness must be less than 0.95 cm for coil A; 0.16 cm for coils B and C; and 0.23 cm for coil D. Shields of up to 1/16 inch (~0.16 cm) are therefore most suitable, though thicker shields may be used with coil A. Shields of up to 1/8 inch (around 3.2 mm) were used which is slightly out with the above constraints when using coils B, C and D.

4.3.3 Test Coils

Various coils were studied, four of which are described in table 4.2. The test set consists of one commercially wound coil (D), two interrogator coils (B and C) designed for Seaward Electronic interrogators and a large reference coil (A), whose relatively large surface area provides comparison.

---

[6] there are other restrictions on coil geometry given by Levy but all are satisfied by the coils described herein

Description	**Coil Radius, *r* (cm)**	***b* (cm)**	***c* (cm)**	**Number of Turns *n***	**Wire Gauge (SWG)**	**Nominal Inductance (μH) @125 kHz**	**Nominal ESR (Ω) @125kHz[*]**	**SRF**
A (Large Coil)	4.75	0.5	0.2	70	32	1080	12.7	678 kHz
B (Small Coil, Coreless)	0.8	0.6	0.2	231	36	770	13.9	1.786 MHz
C (Small Coil, Ferrite Core)	0.8	0.6	0.2	190	36	769	9.1	1.76 MHz
D Thin Coil	1.145	0.15	0.21	460	46/47[†]	7340	210	863 kHz

* Includes resistance of fixture wires † Estimated by direct measurement

Table 4.2 Summary of coil properties used for shielding measurements

Coil C was designed to work in an RFID interrogator designed by Seaward Electronic. A ferrite slug is screwed into the coil former along the coil's axis which permits simple adjustment of the coil inductance, as shown in figure 4.4(a). This was necessary because coil winding had to be performed by hand which can result in considerable variability of the inductance. When the required inductance is achieved, the slug position is then fixed permanently. In figure 4.4(b) the inductance variation versus slug position is illustrated. It was important to determine whether the ferrite slug impaired performance in the vicinity of metallic surfaces compared to the air-cored equivalent. Coil B was therefore used as a comparison, which has no ferrite core but whose inductance matches that of coil C. Coil D is a commercially wound transponder coil with an inductance of 7.3 mH, which is designed to resonate with the 210 pF on-chip capacitance of a Philips HT1 RFID transponder [Hitagic]. The resonant frequency was 128.2 kHz, close to the 125 kHz HT1 operational frequency. Note the relatively high resistance of this coil, a consequence of using many turns of fine wire.

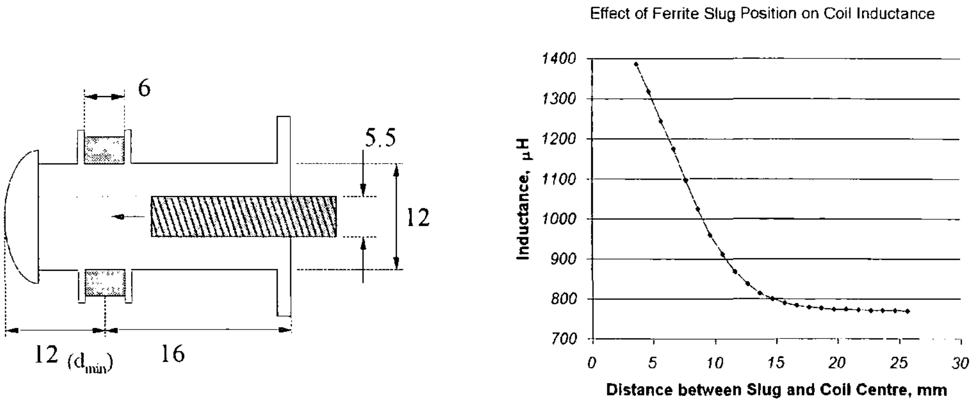

(a) (b)

Figure 4.4 (a) Coil B and C assembly (Seaward interrogator coil) showing location of coil and ferrite tuning slug; (b) variation of coil inductance versus sistance between slug and coil

4.4 Effect of Copper Shielding

If we assume high quality annealed copper, for which $\gamma = 1$ and $\mu_1 = 1$, an approximation to the perfect conducting shield can be made. Coils A and D were positioned at various distances from copper sheets as depicted in figure 4.3.

4.4.1 Results: Coil A

The change of inductance and resistance was recorded at 1 kHz, 10 kHz and 125 kHz for various separation distances[7]. The minimum separation distance is determined by equation 3. Note that the separation distance includes one half of the coil thickness (0.25 cm for coil A). The results for coil A and 1/16 and 1/200 copper sheets are summarised in figures 4.4 – 4.7.

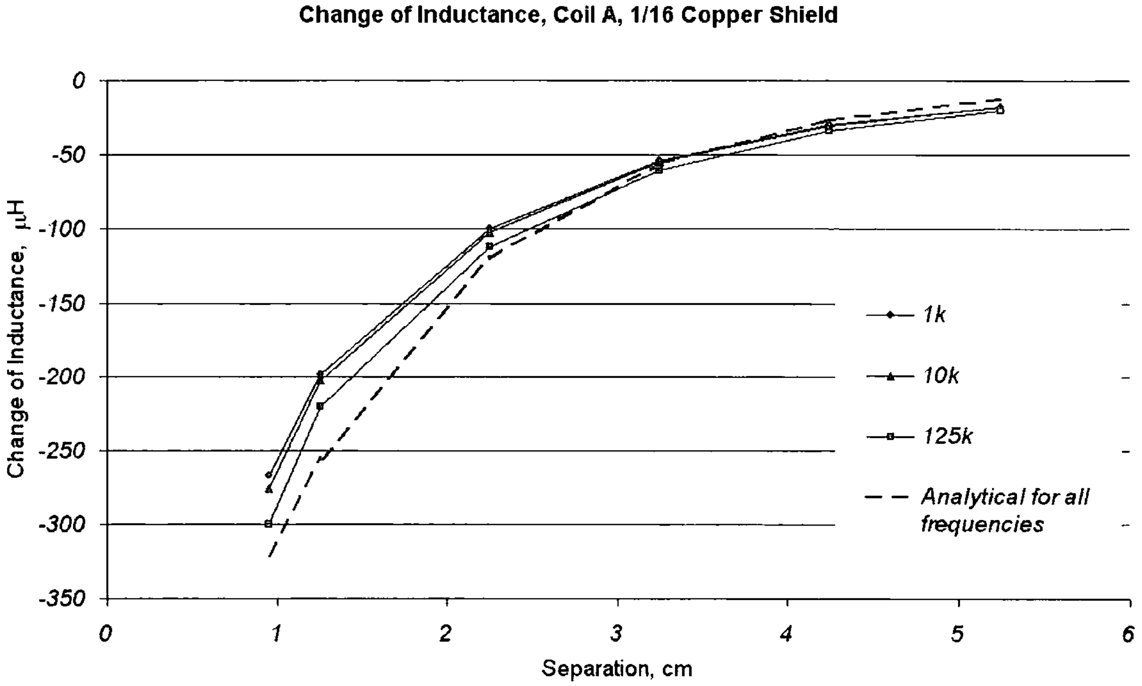

Figure 4.5 Effect of 1/16 copper sheet on coil A inductance versus separation distance.

---

[7] Analyser settings were: voltage source mode (500 mV); bandwidth setting of 2; no averaging, frequency span of 1kHz – 1 MHz; open/short calibration ON.

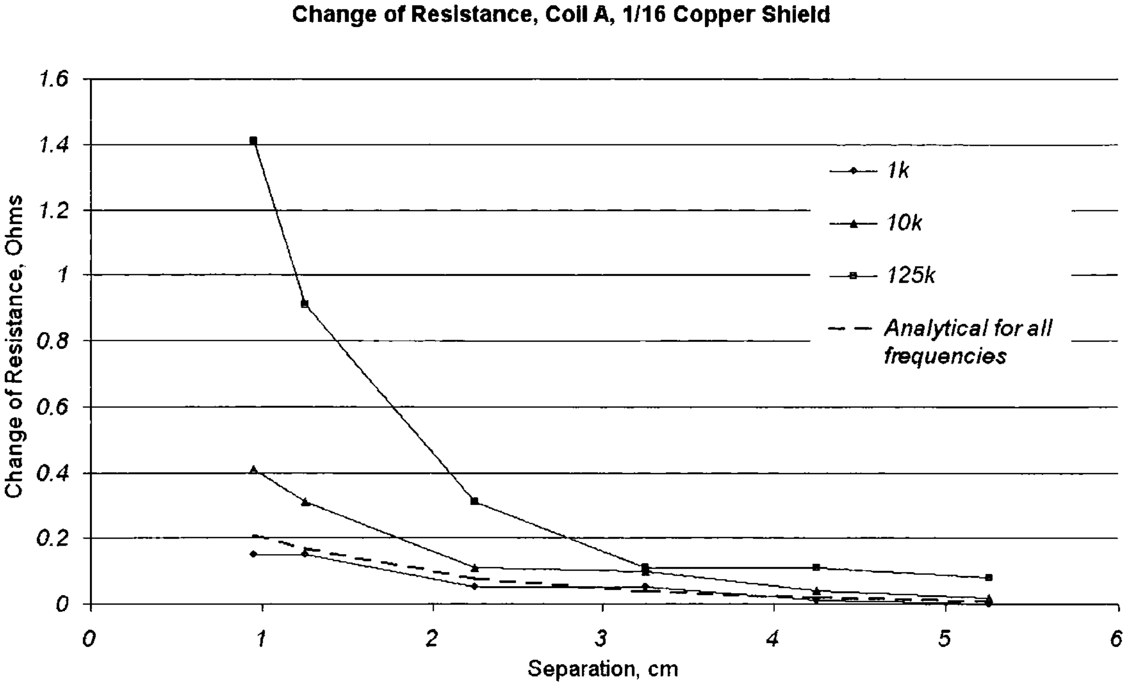

Figure 4.6 Effect of 1/16 copper sheet on coil A resistance versus separation distance.

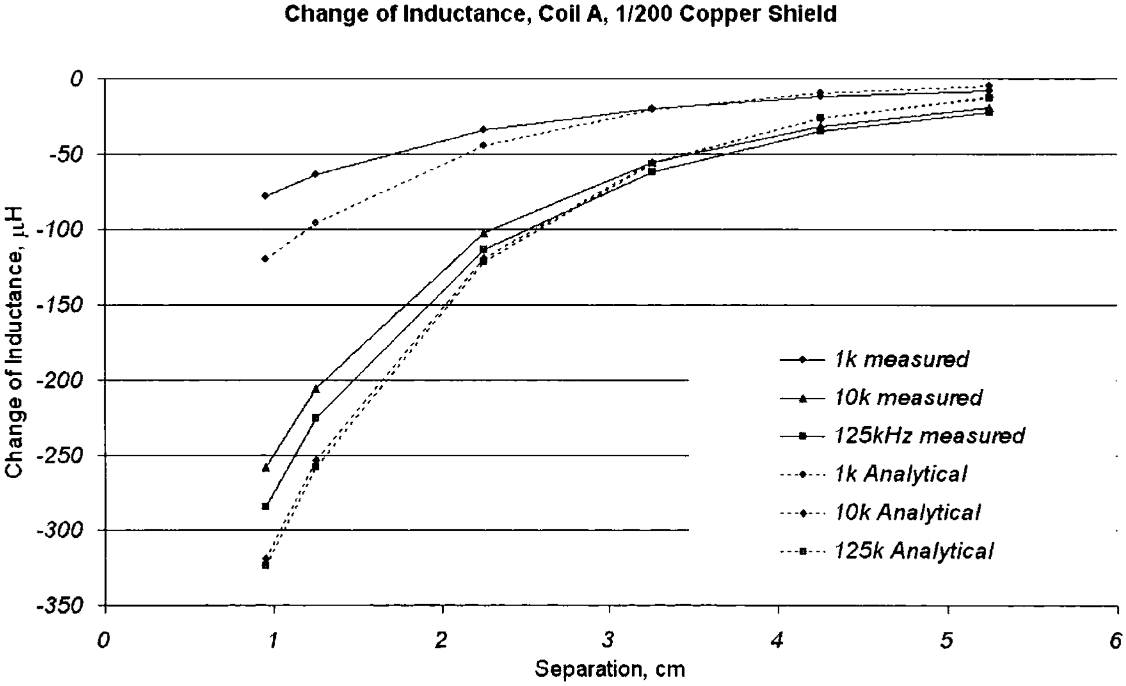

Figure 4.7 Effect of 1/200 copper sheet on coil A inductance versus separation distance.

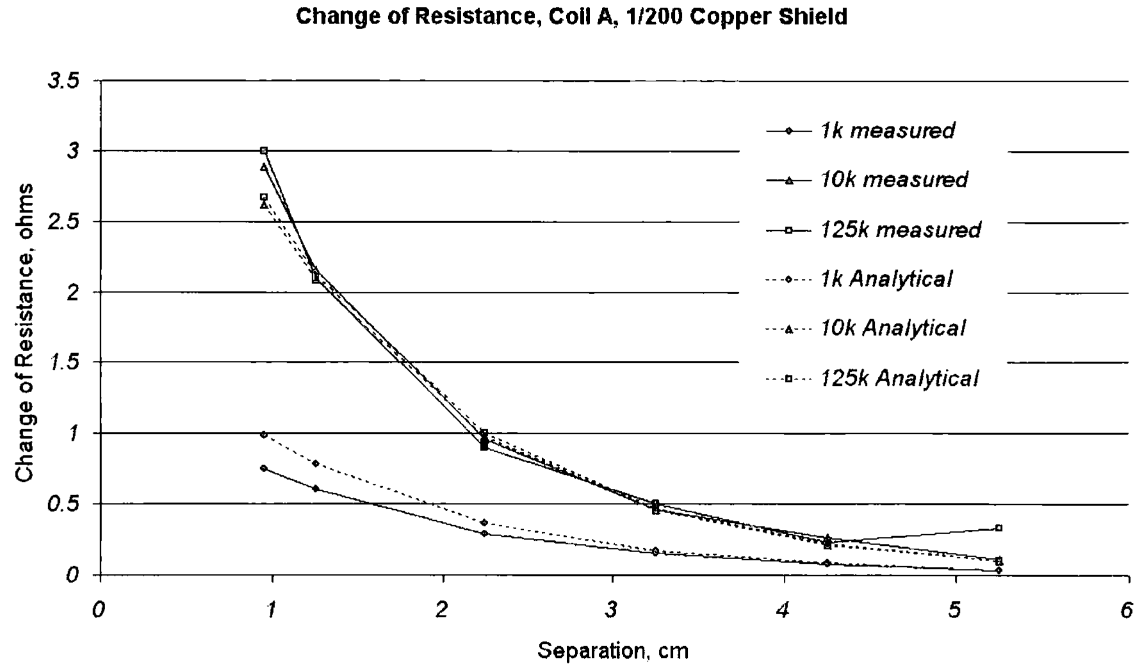

Figure 4.8 Effect of 1/200 copper sheet on coil A resistance versus separation distance.

With the 1/16 copper sheet, inductance change is reasonably consistient across the frequencies under consideration (figure 4.5). Results from using equation 1 predict a similar behaviour, as indicated by the dotted line. Change of resistance is strongly frequency-dependent (figure 4.6), with a sharp rise at 125 kHz. The model however predicts that the shield effect is not dependent on the frequency range 1 kHz – 125 kHz as shown by the dotted line. This line agrees with the measured effect at 1 kHz, but diverges at higher frequencies.

The procedure was repeated using 1/200 copper sheet. The resulting graph of inductance (figure 4.7) shows strong dependency on frequency, with change of inductance increasing at closer proximity and higher frequency. The analytical results are in good agreement with the measurements, although the curves diverge at close proximity. (This trend was observed for all measurements, due to exceeding the lower limit imposed on distance D.) Measurement and analysis are also well matched for change of resistance, with good agreement in frequency dependence (figure 4.8).

4.4.2 Results: Coil D

The experiment was repeated using coil D, which is much smaller than coil A. The lower limit on separation distance was reduced in accordance with equation 3. The results are shown in figures 4.9 – 4.12.

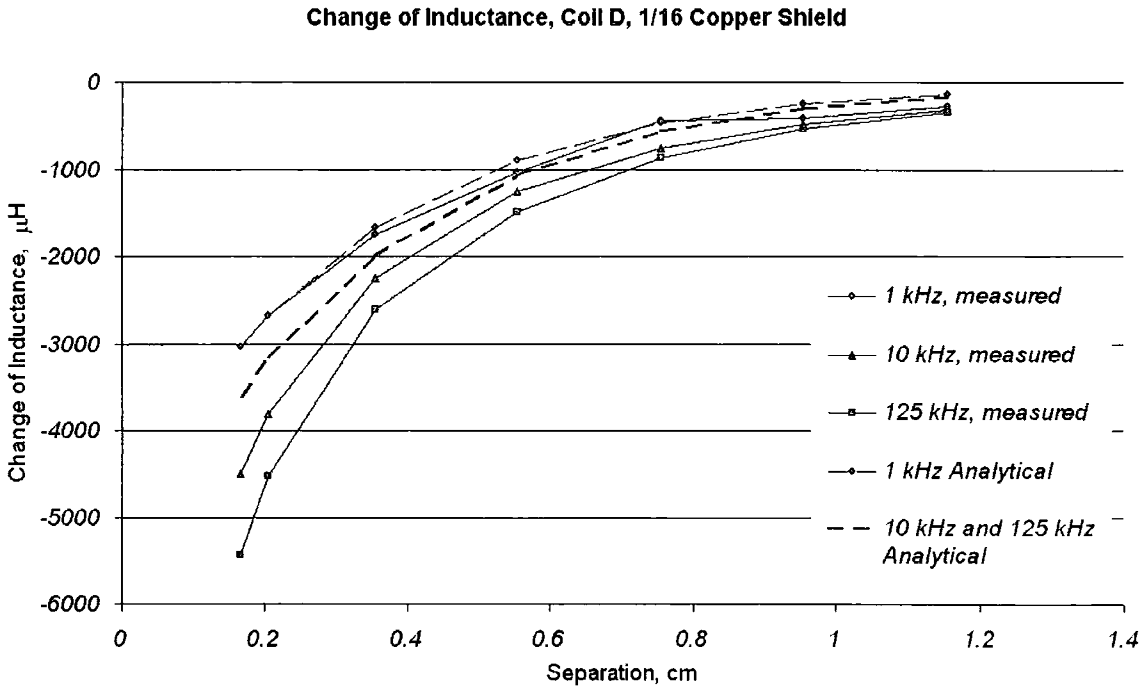

Figure 4.9 Effect of 1/16 Copper sheet on coil D inductance versus separation distance.

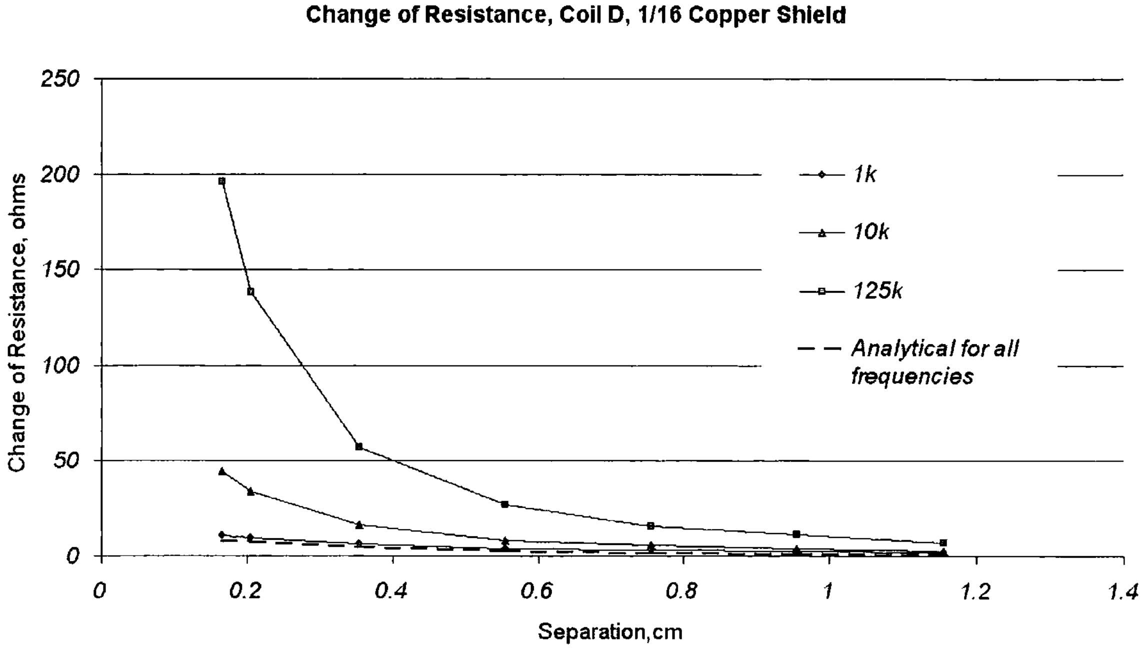

Figure 4.10 Effect of 1/16 copper sheet on coil D resistance versus separation distance.

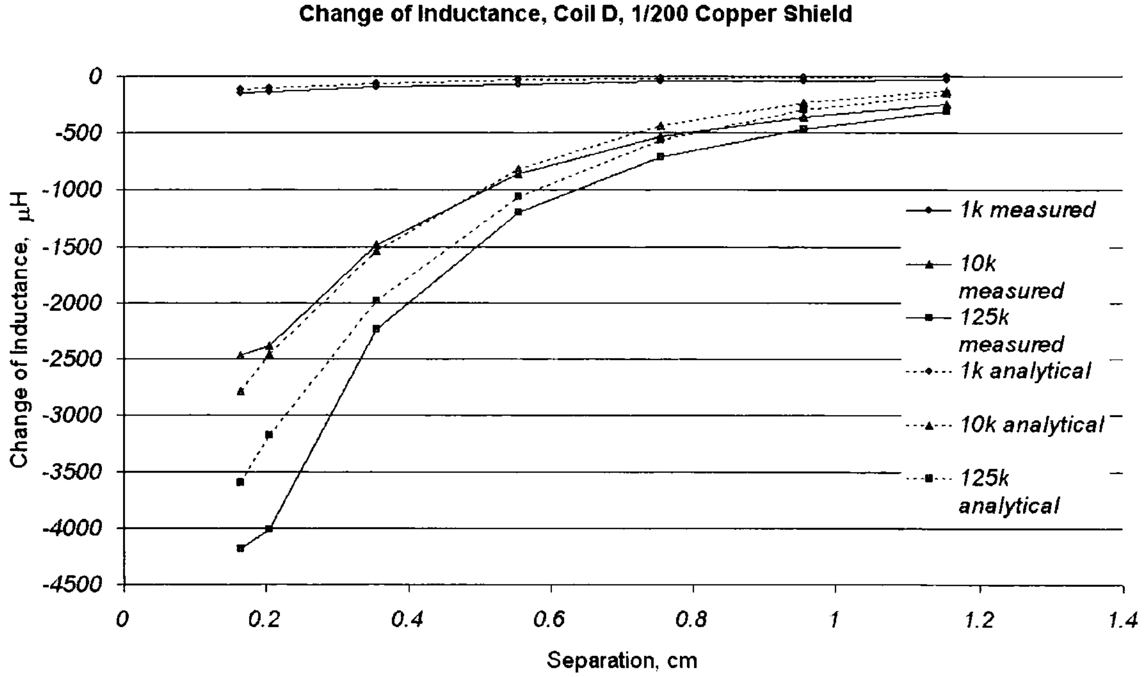

Figure 4.11 Effect of 1/200 copper sheet on coil D inductance versus separation distance.

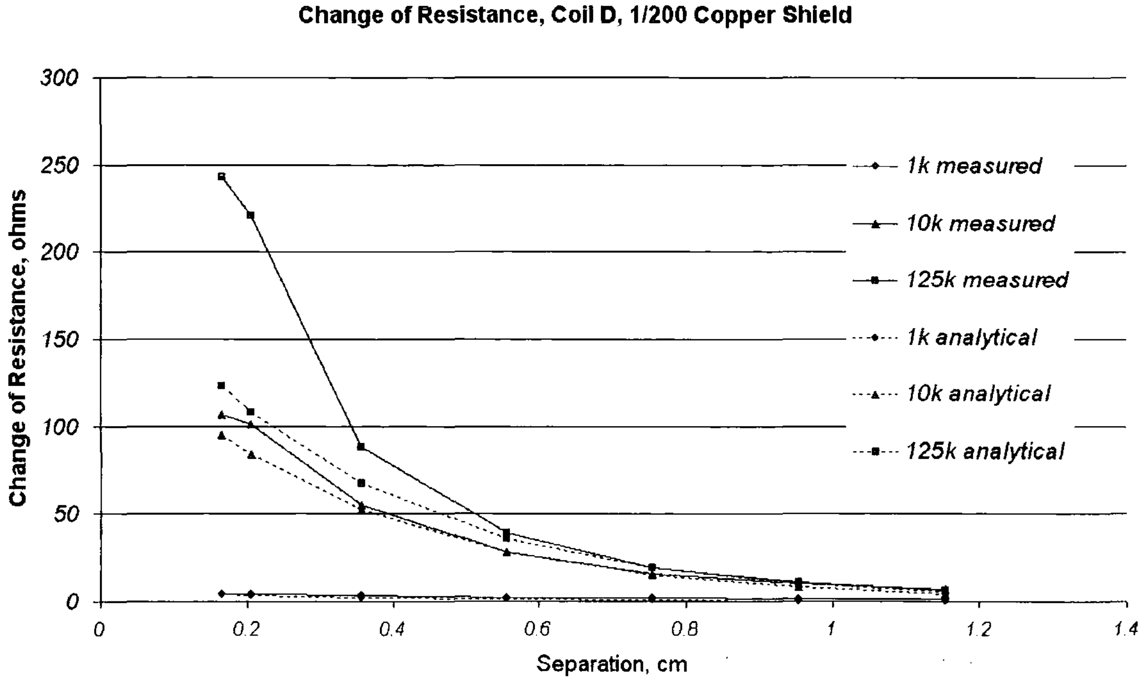

Figure 4.12 Effect of 1/200 copper sheet on coil D resistance versus separation distance.

The change of inductance using 1/16 copper shows dependency on frequency, with some distinction between 1 kHz and 10/125 kHz being reflected in the analytical results (figure 4.9). The analytical result for change of resistance again showed little variation with frequency (figure 4.10), giving good agreement with the results at 1 kHz, but not at 10 kHz and 125 kHz, where the change of resistance increases more rapidly. The characteristic is similar to that seen in figure 4.6.

With 1/200 copper the model predicts similar inductance curves as the measurements (figure 4.11) although the 125 kHz curves diverge at close proximity. With regard to coil resistance (figure 4.12), the model predicts a degree of sensitivity to frequency, however a large difference is seen between measurement and calculation at 125 kHz when the separation falls below 0.6 cm.

4.4.3 Discussion

From the above results, the model is seen to give a useful approximation to the effect of copper shielding on coils. This would apply for other shield metals for which $\mu_r \cong 1$. Model accuracy improves as the distance increases for change in both inductance and resistance, which is consistent with Levy's remarks.

Investigation of the model showed that sensitivity to frequency is determined by the squared terms in the denominator of equation 1, which includes coil radius, shield thickness and conductivity. In the case of shield thickness, sensitivity to frequency reduces as the shield thickness becomes less than the skin depth. For the case of resistance, the effect of shield thickness and conductivity is higher due to the extra $1/\gamma T$ term in equation 2.

Differences between measurement and model may be attributed partly to the shield thickness relative to skin depth. Skin depth is calculated using:

$$\Delta = \sqrt{\frac{\rho}{\pi\mu_o\mu_r f}} \tag{5}$$

This gives a minimum skin depth in copper of 0.0185 cm at 125 kHz. Comparing this to the shield thickness given in table 4.1, we see that 1/16 copper is considerably thicker than the skin depth, whereas 1/200 copper is thinner than the skin depth. Moser comments that in during the formulation of the general shielding equation, Levy assumed that the induced potential on both sides of the shield would be identical, and hence that the eddy currents would be evenly distributed through the shield from one side to the other. He further commented that this would restrict the validity of the solution to shields of thickness less than the skin depth. This leads to the assumption that the distribution of current in shields much thicker than the skin depth is uniform, which is not the case. This has the greatest effect on change of resistance curves, as seen by comparing figure 4.6 and figure 4.8, where the model accuracy is greatly improved when using 1/200 copper compared to 1/16 copper. Further evidence of this is seen in figure 4.9, where the measured and calculated inductance curves using 1/16 copper diverge at the highest frequency. Moser further comments that the accuracy of Levy's shielding equation seems to get better as the frequency is lowered, which is consistent with the results presented here.

Despite this assumption, differences between measurement and calculation remain at higher frequencies, particularly with respect to change in resistance. One possible explanation is the onset on self-resonance. This effect can be explained by considering the variation of resistance during the onset of parallel resonance. At resonance, the coil impedance is real and equal to the *dynamic impedance*, given by L/RC, where L is the coil inductance, C the parasitic capacitance and R the coil losses[8]. At frequencies higher or lower than the resonant frequency, the real part of coil impedance gradually decreases as shown in figure 4.12(a). The width of the curve depends on the quality factor of the coil, which is given by $R/\omega L$. Since the presence of a shield causes the inductance to fall and resistance to rise, the quality factor lowers, causing the curve of resistance to widen as shown in figure 4.12(b). If the frequency is sufficiently high to coincide with the slope of the resonance curve, then the measured resistance is composed of combination of eddy current losses, copper losses and the additional apparent resistance due to the onset of resonance. The resonance curve for coil D and 1/200 copper is shown in figure 4.12 including the widening of the curve in the

---

[8] This is considered at greater detail in chapter 5

presence of the shield, which produces a larger increase in the resistance measured at 125 kHz. Since dynamic impedance is often greater than 1 MΩ, this effect can add significantly to measured resistance at lower frequencies.

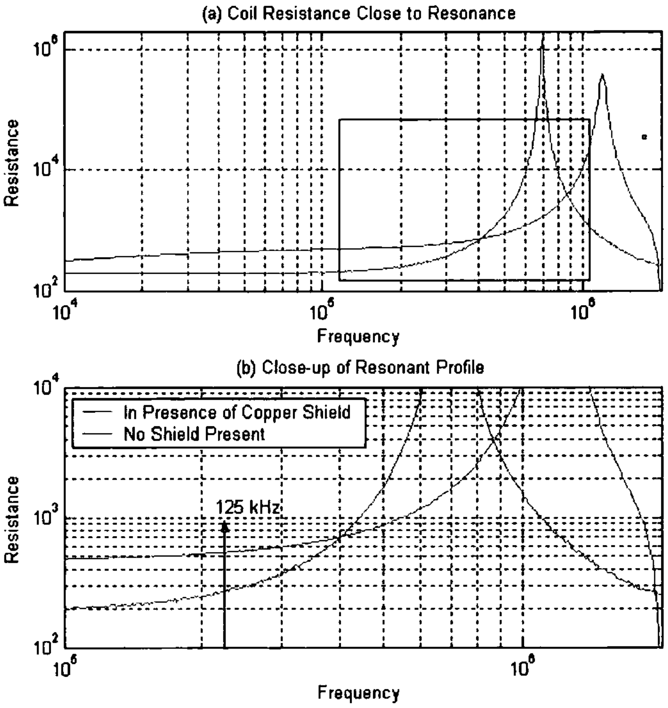

Figure 4.12 Effect of shield on resonant response and change in resistance
(a) complete curve, (b) close up of boxed section

4.5 Effect of other Metals

For ferromagnetic materials, whose permeability is greater than unity, measured and calculated results can differ considerably using the above model. Moser observed this when investigating the problem of shield effectiveness. In this case, the use of steel shielding material gave far higher attenuation in measurement than predicted by the model.

To better understand the effect of ferrous materials on coil impedance, coils A and D were placed directly on various sheets in a *mount on metal* configuration, while coils B and C were placed as close to the metal sheets as permitted by the coil formers dimensions (which is 12mm as indicated in figure 4.4(a)). Mount on metal configurations are commonly encountered in RFID applications. An example of this is when the transponder has to be mounted on the case of a desktop computer which is normally constructed of thin steel.

Common ferrous materials such as steel and iron generally have sufficiently high conductivity to give rise to eddy currents, and sufficient permeability which tends to increase inductance by lowering the reluctance of the path taken by flux linking the coil. At low frequencies the coil inductance is increased by the presence of such materials and at high frequencies it is reduced by the presence of eddy currents. Therefore there should exist a frequency at which one effect balances the other, producing no net change of coil inductance. Unfortunately this cannot be exploited in RFID because the frequency at which this occurs is dependent on coil and shield parameters, and in particular shield thickness. It is however useful to observe and compare the impedance changing characteristics of various ferrous and non-ferrous metals as a function of frequency, and so quantify the expected change of inductance and resistance to be encountered in coils designed for RFID.

The minimum SRF encountered between coils A-D is 1.79 MHz. Therefore an upper frequency limit of 1MHz was specified to minimise the influence of self-resonance.

4.5.1 Results

The results observed by applying each shield in table 4.1 to coils A-D are summarised in figures 4.13 – 4.16. In these graphs, a clear distinction between ferrous metals (iron, steel) and non-ferrous metals (copper, aluminium, stainless steel) can be seen in the percentage change of inductance graphs. The percentage change in inductance was calculated using

$$\%L = \frac{L_{shield} - L_{nom}}{L_{nom}} \cdot 100 \qquad (6)$$

where L_{shield} is the inductance in the presence of shield material, and L_{nom} is the nominal inductance. A similar expression was used to calculate the percentage change in resistance. Each group of metals is circled corresponding to ferrous materials, thick non-ferrous materials and thin non-ferrous materials. At low frequencies ferrous materials cause an increase of the coil inductance, while non-ferrous materials have little influence. An exception is Coil A, which experiences a 10-20 % reduction of inductance at the lowest frequency of 100 Hz using thick copper and aluminium sheets.

Depending on the excitation frequency, ferrous materials may cause coil inductance to increase or decrease, and may be characterised by the frequency at which no change of inductance occurs. For example the inductance of coil D retains its nominal value when placed 12 mm from 0.127 cm galvanised steel. By inspection, it is apparent such points occur across a wide range of frequencies, and are sensitive to metal composition and sheet thickness. At frequencies approaching 1 MHz inductance falls rapidly due to self-resonance, resulting in the loss of individual sheet characteristics.

The results for coils B and C are show similar characteristics. These graphs differ by less than one percent with copper and aluminium sheets, confirming that the ferrite slug does not significantly alter the coil characteristics. Coincidentally, the inductance of coils B and C is unaffected in the presence of the iron sheet at the RFID frequency of 125 kHz, therefore an RFID interrogator that uses coil B or C would not be affected when placed close to this shield.

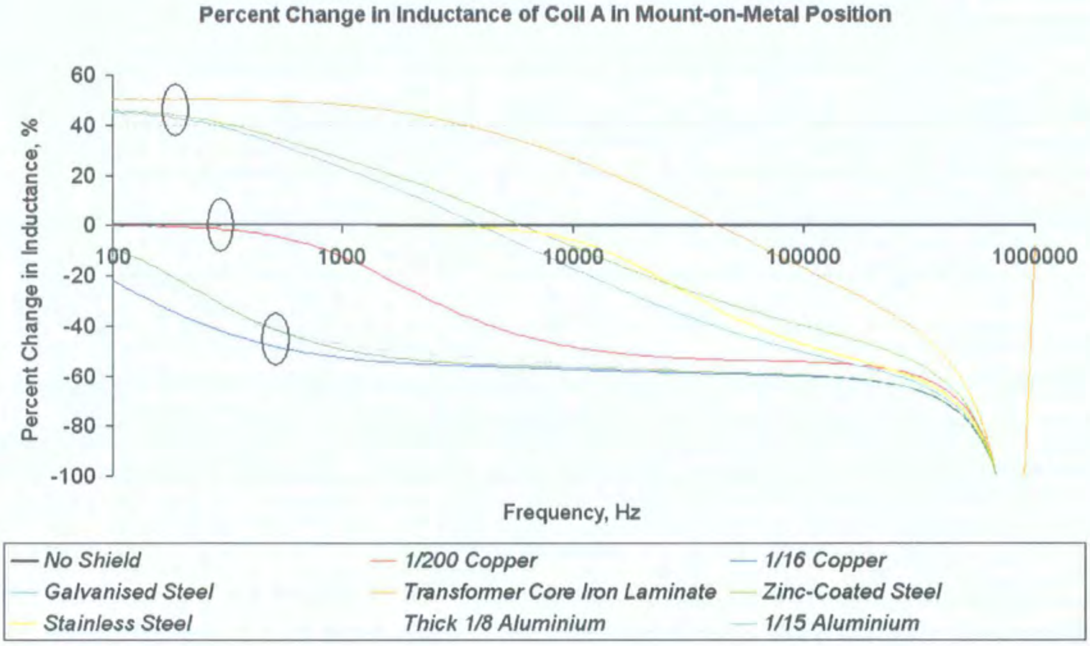

Figure 4.13 Effect of ferrous and non-ferrous shields on coil A

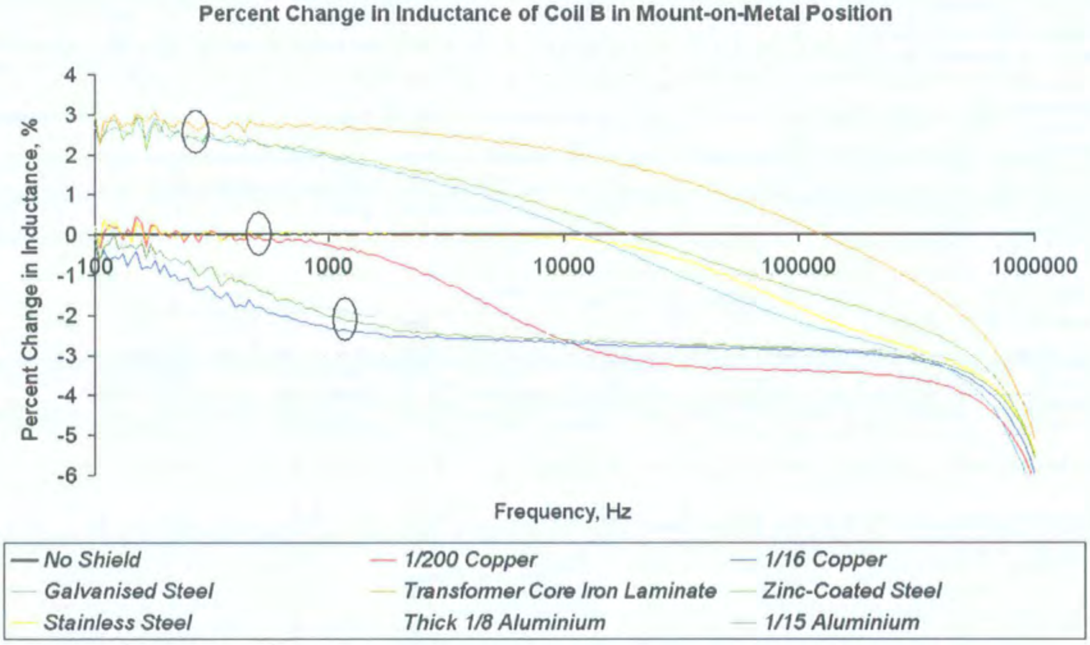

Figure 4.14 Effect of ferrous and non-ferrous shields on coil B

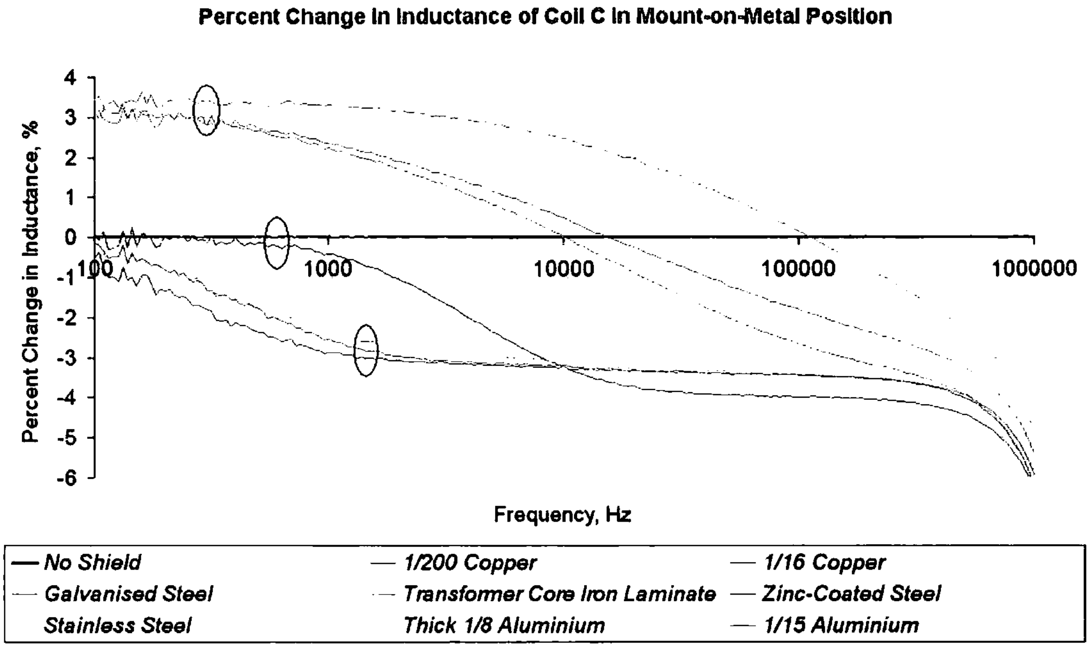

Figure 4.15 Effect of ferrous and non-ferrous shields on coil C

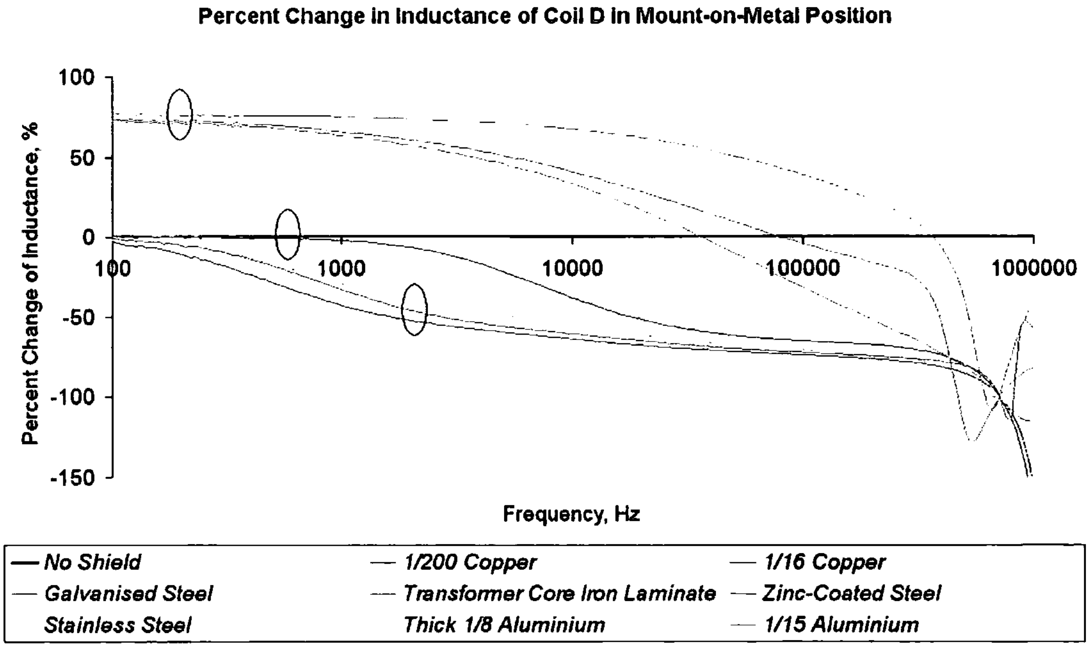

Figure 4.16 Effect of ferrous and non-ferrous shields on coil D

4.6.1 Analysis and Discussion

An important observation is that coils B and C are less affected by the presence of shield material than coils A and D. This is due to the combination of small coil area and minimum separation distance. The minimum separation distance was 12 mm (imposed by the coil former). The maximum change of inductance below 1 MHz was around ±4 %, compared to ±50 % and ±75 % for coils A and D respectively. Coils B and C are therefore suited for use in RFID interrogators because they produce a stable impedance to the tuned coupled circuit comprising interrogator and transponder. Note that coil D is for use in transponder assemblies but produces the greatest change of inductance. As described in section 4.6, this can severely reduce system sensitivity and would dominate the interrogator read range if coil B or C were used.

4.5.1.1 Relationship between Skin Depth and Shield Thickness

In general, thin copper and stainless steel sheets do not influence coil inductance until the frequency increases beyond a transition frequency, which was around 1 kHz for 1/200 copper shield, and 10 kHz for the stainless steel shield. By rearranging equation 5, the frequency at which skin depth equals shield thickness can be found:

$$f = \frac{\rho}{\pi \mu \Delta^2} \qquad (\Delta = T) \qquad (7)$$

In table 4.3 the resulting frequencies for several sheets are shown. With reference to figure 4.13, the transition points for stainless steel and 1/200 copper occur near the calculated frequencies.

Shield Type	Transition Frequency, for which $(\Delta = T)$
1/8 Aluminium	6.6 Hz
1/16 Copper	17 Hz
1/16 Aluminium	25 Hz
1/200 Copper	2.7 kHz
Stainless Steel	36.5 kHz

Table 4.3 Transition frequencies

Fall-off characteristics beyond the transition frequency were compared with the model by computing the change of inductance versus frequency for 1.200 copper and stainless steel using equation 1. The results for 1/200 copper (figure 4.17) show that the frequency at which significant inductance change occurs is similar between measurement and model, but the analytical curves predict a larger change of inductance than the measured amount. The model suggests that for frequencies above that given by equation 7, there is no further change of inductance with frequency and the curve becomes flat. This is explained by the fact that eddy currents induced in the shield now flow in a narrow region near the surface and so the shield thickness plays no further part in their distribution. Note that the error between calculation and measurement increases at zero separation distance. When using real coils, particularly high inductance coils required in passive RFID applications, that have significant winding capacitance[9], self-resonance influences this profile causing the change of inductance to increase. This effect is more obvious for stainless steel (figure 4.18) because the transition frequency is far higher that of copper and therefore at high frequencies the flat region is completely eliminated by self-resonance effects. There is good agreement between the model and measured response at the transition point for stainless steel.

---

[9] This occurs due to capacitance between each layer of the winding. In RFID, coils must be as small as possible and produce large inductance, requiring many layers of fine wire. The resulting capacitance is often several hundred picofarads.

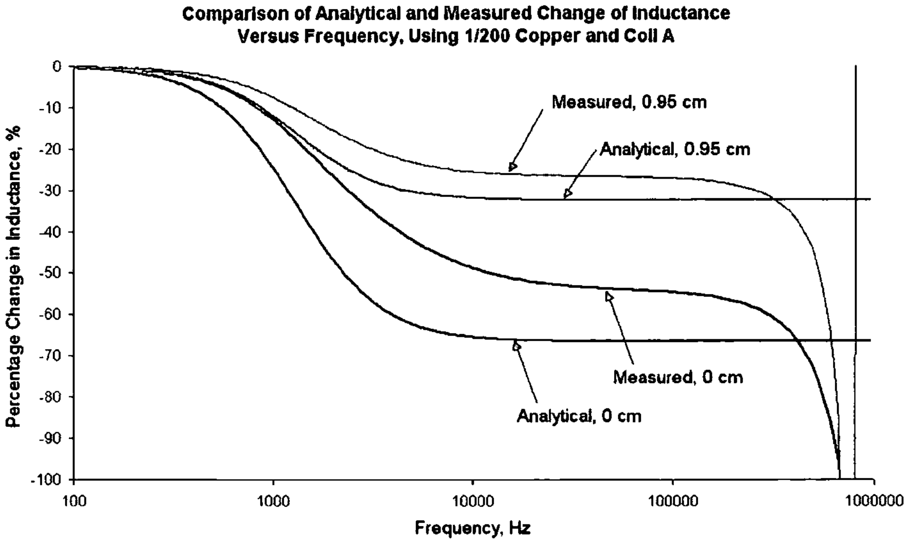

Figure 4.17 Effect of eddy currents in 1/200 copper shield

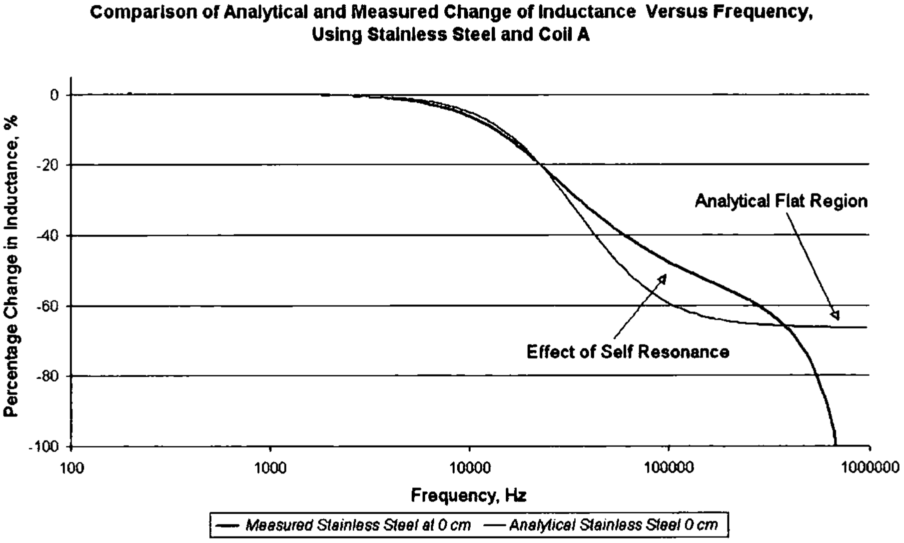

Figure 4.18 Effect of eddy currents in stainless steel shield

4.1.1.1 Properties of Ferrous Shields

From the measurements taken, the effect of ferrous materials can be generalised to some extent. It takes the form of enhanced inductance at very low frequencies, steadily decreasing inductance as the frequency rises, until at some frequency related to permeability, conductivity and separation distance is reached, the inductance is equal to its nominal value. Beyond this frequency inductance decreases in a similar manner caused by non-ferrous shields. To illustrate the interaction between permeability and conductivity, an eddy current (AC) field simulation was carried out using Maxwell 2D software. The problem was created in the x-y plane and represents a winding comprising 10 turns suspended above a thick shield composed of 1010 steel. At low frequency (100 Hz) magnetic flux easily penetrates into the shield (figure 4.19(a)), effectively reducing the magnetic path reluctance and increasing inductance. In addition the flux lines enter the shield perpendicular to the surface in a similar fashion to the PMC shield shown in figure 4.19(b). As the frequency increases to 125 kHz, flux still enters the shield but is now confined to a thin layer, and no longer enters perpendicular to the surface. This behaviour lies between PMC and PEC shield characteristics. The simulated distribution of current density is also shown at 100 Hz and 125 kHz in figure 4.20, where at 125 kHz the confinement of eddy currents to near the shield surface is clearly seen. At 100 Hz eddy current distribution in the shield is reasonably uniform.

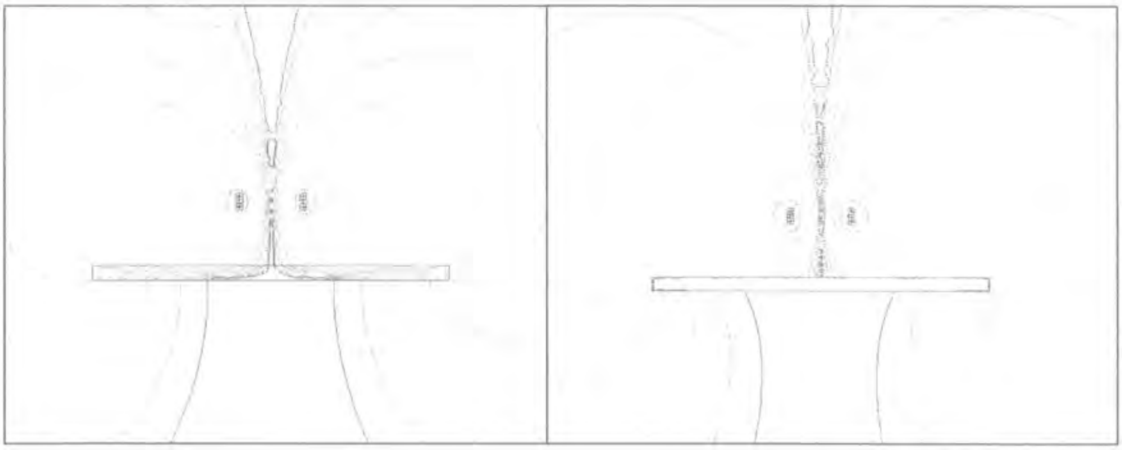

(a) (b)

Figure 4.19 Simulated magnetic flux density for coil above steel shield at 100 Hz (a) and 125 kHz (b).

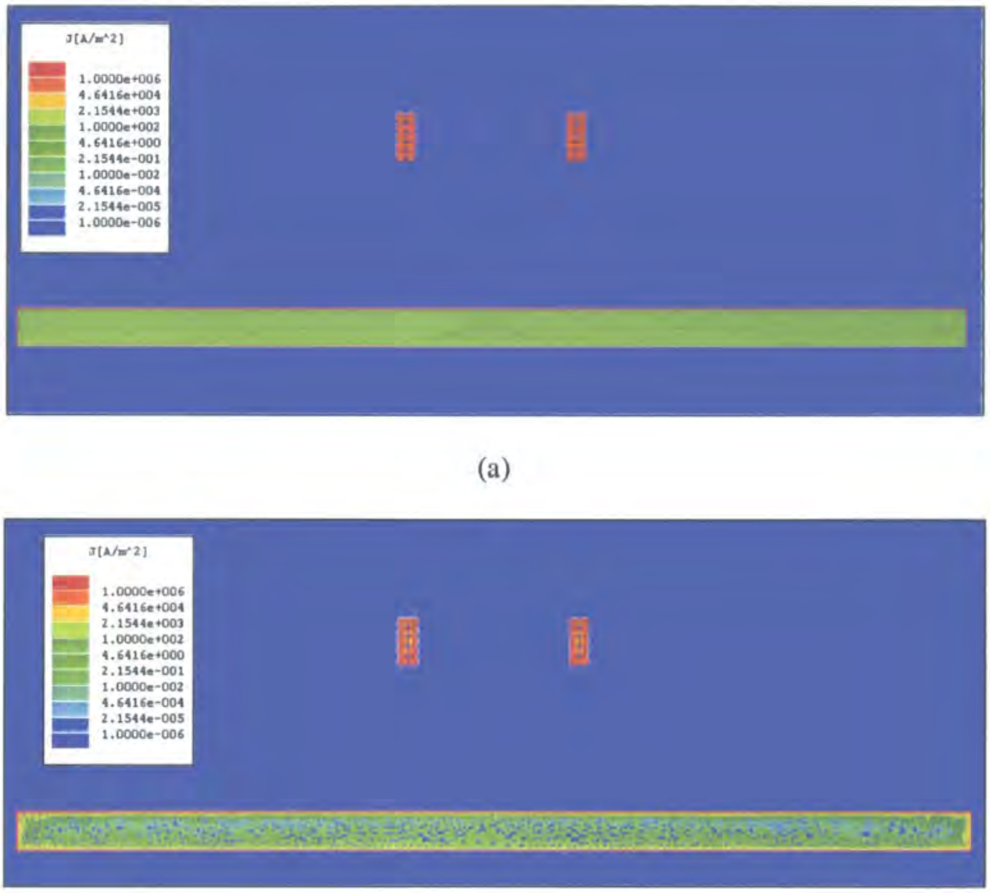

(a)

(b)

Figure 4.20 Simulated distribution of current density for coil above steel shield at 100 Hz (a) and 125 kHz (b).

Derivation of an exact relationship between effects of eddy currents and permeability was not attempted due to the complexity of analysis. However a possible method for approaching this problem is suggested in section 4.7.

It is possible to characterise the effect of increasing shield permeability on coil inductance by calculating the impedance matrix for conductors in the Maxwell software. The impedance matrix is calculated by stimulating each conductor in turn, the other conductors being electrically open circuit, and takes the following form:

$$Z = \begin{bmatrix} R_{11} + j\omega L_{11} & R_{12} + j\omega L_{12} & .. & R_{1n} + j\omega L_{1n} \\ R_{21} + j\omega L_{21} & R_{22} + j\omega L_{22} & .. & .. \\ .. & .. & .. & .. \\ R_{n1} + j\omega L_{n1} & .. & .. & R_{nn} + j\omega L_{nn} \end{bmatrix}$$

where $R_{nn} + j\omega L_{nn}$ is the self-impedance of circuit *n*, and $R_{12} + j\omega L_{12}$ is the mutual impedance coupling between circuit 1 and 2. Note that $L_{12} = L_{21} = M_{12}$ and that:

$$k_{12} = \frac{L_{12}}{\sqrt{L_{11} L_{22}}}$$

The element of interest here is $R_{11} + j\omega L_{11}$, which is the self-impedance of the coil suspended above a shield. Two loops were simulated, the first with a radius of 4.75 cm representative of coil A, the second with a radius of 1 cm. Ten turns of SWG 32 copper were bunched about the radius to simulate the each winding. The shield thickness was 0.0127 (1/200 inch). The impedance matrix approach requires an axi-symmetric model to represent the complete circular loop of each winding turn. Impedance matrices were calculated at 100 Hz for various coil-shield separations and shield material properties. The results are summarised in table 4.4 and an example of the magnetic flux pattern around a coil positioned above an iron shield shown in figure 4.21. The resistance values were virtually unaffected by the presence of the shield at this frequency and so were not included. Inspecting the results in table 4.4, it is clear that, for the separation distances considered here, all ferromagnetic shields have a similar influence on coil inductance at low frequencies to any great extent, and therefore steel and iron can be approximated as perfect magnetic conductors. The copper shield has little effect on coil inductance at this frequency. By progressively incrementing the simulation frequency, it would be possible to find the frequency at which a particular ferromagnetic shield caused no change of inductance.

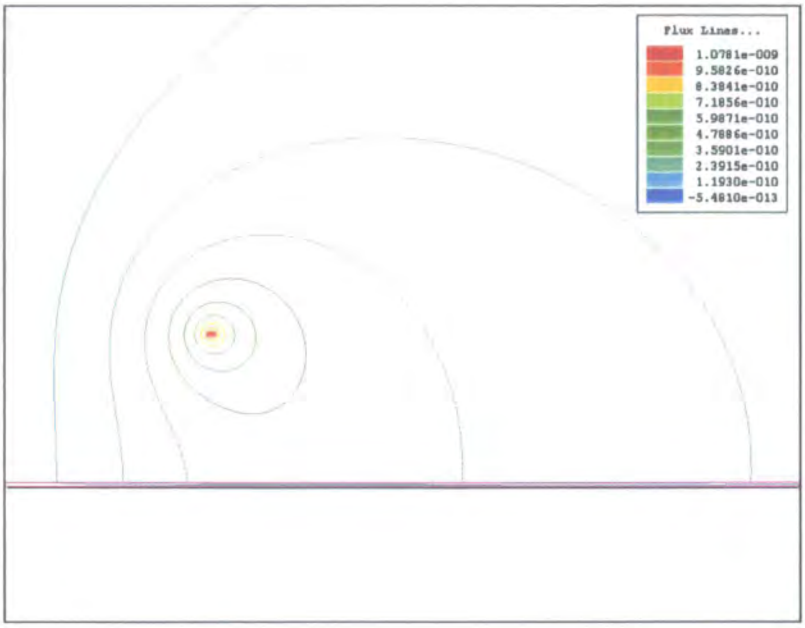

Figure 4.21 Magnetic flux pattern around a 1 cm radius coil, above 0.0127 cm (1/200 inch) iron shield. Frequency = 100 Hz.

Shield Material	Coil Radius = 4.75 cm; separation distance = 1 cm		Coil Radius = 4.75 cm; separation distance = 0.3 cm		Coil Radius = 1 cm; separation distance = 0.5 cm	
	Coil Inductance (nH)	Percent Change of Inductance (L_{11})	Coil Inductance (nH)	Percent Change of Inductance (L_{11})	Coil Inductance (nH)	Change of Inductance (L_{11})
No Shield	376.71	0 %	376.71	0	59.958	0
Copper	376.53	-0.05 %	376.4	-0.08 %	59.956	-0.003 %
1008 Steel	415.63	+10.33 %	472.41	+25.4 %	64.51	+7.59 %
Iron	422.39	+12.13 %	486.25	+29.08 %	64.851	+8.16 %
PMC (μ_r = 100,000)	425.99	+13.08 %	493.52	+31.01 %	65.012	+8.43 %

Table 4.4 Simulated shielding effects on coil by impedance matrix approach.
Frequency = 100 Hz.

4.6 Impact on RFID System Performance

The previous sections have focused on the effect of placing conducting shields near inductive coils. In this section, we briefly inspect the impact this has on interrogator and transponder performance.

Interrogators typically employ series resonant circuits, in which the coil is made to resonate in series with a capacitor, which maximises current passing through the coil at resonance and therefore also the magnetic field strength. In contrast, a parallel resonant circuit is used in transponders to maximise voltage developed across the transponder chip. Alteration of coil inductance due to the presence of conducting shields has two effects. Firstly, the resonant frequency is altered by the change of inductance. Secondly, the resonant response is dampened by the increase of resistance. If the change of resistance and inductance is known, then a modified response may be calculated and assessed to determine the reduction in performance.

4.6.1 Series Resonance Mode

The effect of shields on the series resonant circuit may be described by the following expression:

$$|Z_{series}| = \sqrt{(R + R_{adj})^2 + \left(\omega(L + L_{adj}) - \frac{1}{\omega C}\right)^2} \qquad (8)$$

where C is the series capacitance, R the total series loss, R_{adj} the change of resistance and L_{adj} the change of inductance caused by shields. At resonance, and in the absence of shields, equation 8 reduces to simply R. The change of inductance and resistance due to 1/200 copper shielding placed 12 mm from coil B was measured at 125 kHz, which is below self-resonance. A predicted response was then calculated by using equation 8. Coil B was then connected in series with 2 nF capacitance, resulting in a resonant frequency close to 125 kHz and the total series impedance measured using a network analyser. The calculated and measured results are shown in figure 4.22, where good agreement can be seen. A slight frequency offset exists between measurement and calculation caused by assuming that the capacitor has exactly 2 nF capacitance in the model, when in reality tolerances cause the capacitance to deviate slightly. Note that the resonant frequency increases by around 2.5 kHz as the inductance reduces in the presence of the copper shield. Note also that the resistance at the new resonant frequency has risen by around 1 Ω in the presence of shielding. However, the impedance presented to a fixed-frequency generator would be higher: around 9 Ω in this case, as indicated by the dotted line which would cause the current passing through the coil to reduce significantly.

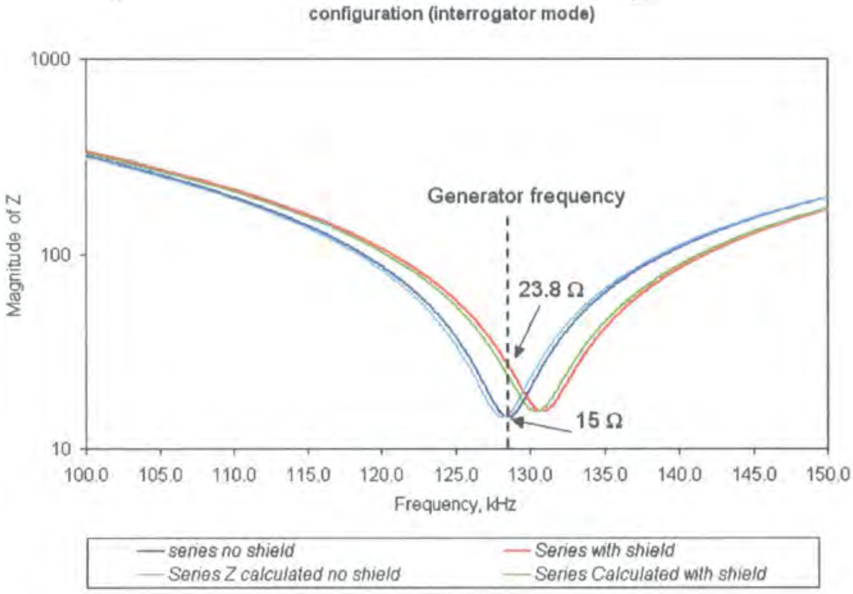

Figure 4.22 Effect of 1/200 copper placed 12 mm from coil B in series resonant mode. Indicated values are the resistances seen by fixed-frequency generator with and without shield.

4.6.2 Parallel Resonance Mode

The response of a parallel resonant circuit may be also characterised by the total impedance. However, here we inspect the real part of impedance as seen by the transponder chip at resonance. This may be calculated from:

$$Z = \mathrm{Re}\left\{\frac{j\omega\left(L + L_{adj}\right) + \left(R + R_{adj}\right)}{1 + j\omega C\left[j\omega\left(L + L_{adj}\right) + \left(R + R_{adj}\right)\right]}\right\} \tag{9}$$

where the variables are as before, but connected in parallel. As discussed in chapter 5, for reasonably high quality factors ($Q > 10$) the impedance of the circuit at resonance is given by the dynamic impedance

$$R_{dyn} = \frac{\left(L + L_{adj}\right)}{C\left(R + R_{adj}\right)} \tag{10}$$

A comparison between measured and calculated resonance is shown in figure 4.23 which was measured under the same conditions as the series circuit. There is a similar difference in the resonant frequencies as with the series result, but the magnitudes of the peaks also differ. This is due to losses in the capacitor, which lowers the dynamic impedance slightly at resonance. The dynamic impedance calculated by equation 10 is 27.5 kΩ (without shield) and 25.5 kΩ (with shield), which compares well with the measured values of 26.5 kΩ (without shield) and 24.3 kΩ (with shield). For a fixed system frequency the presence of copper shielding causes the dynamic impedance presented to the transponder chip drop by 69 % (from 26.5 kΩ to 8.2 kΩ).

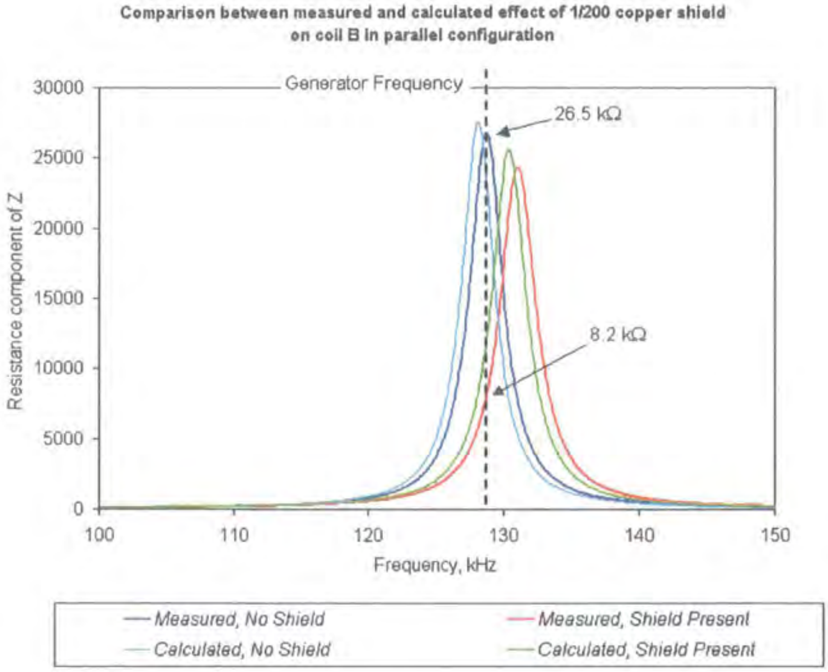

Figure 4.23 Effect of 1/200 copper placed 12 mm from coil B in parallel resonant mode. Indicated values are the dynamic resistance values seen the transponder chip with and without shield.

4.6.3 Discussion

From the perspective of an RFID transponder, a drop in dynamic impedance reduces power delivery and deteriorates load modulation performance. From the interrogator's perspective, detection sensitivity to load modulation is reduced due to the increase of apparent resistance in the series resonant circuit. Due to the close proximity of interrogator and transponder, these effects generally occur simultaneously when conducting surfaces are present; usually the effect is dominant in either transponder or interrogator depending on which is closest to the conducting sheet.

Potential compensation methods may include adaptive tuning mechanisms and adaptive sampling techniques. Varactors or tuneable inductance circuits may be used to facilitate tuning compensation in the interrogator, but this would not compensate for increasing resistance. Adaptive sampling is considered further in chapter 7. In general, field strength regulations on Short Range Devices (SRD) limit the maximum field strength that may be generated by the interrogator [ETSI300]. Therefore, since the presence of conducting shields increases resistance, a reduction in range and detection sensitivity will occur.

4.7 Further Work

This work has focused on the problem of shield and coil arranged in the same plane (figure 4.3). Shields have been approximated as being infinite in size in comparison to the coil dimensions. An extension of this work would be to investigate the dependency of coil impedance when placed at the edge of conducting sheets. Some basic measurements were made at the edges of shields, where the inductance was found to increase. The maximum increase was often found when the coil surface area was bisected between air and shield. A further extension might be to investigate the effect of mounting a coil behind an aperture cut into the shield. Some investigation was undertaken with this arrangement during the design of a commercial security entrance system, in which the RFID interrogator coil was mounted behind a square aperture cut into a steel faceplate. It was found that if the coil radius is smaller than the aperture radius, then sufficient flux travelled through the aperture to energise a small key-fob type RFID transponder placed nearby. Effects of aperture size and shape were however were not fully characterised.

The effect of ferrous shields was observed and relationships were identified, such as the combined effect of shield conductivity and permeability on coil impedance. However, Levy's equations could not be applied in this situation; a more complete solution is required. One possible method is to adapt existing methods cited in the literature currently used to derive expressions for the shield effectiveness, which quantifies the attenuation of voltage induced in a receiving coil due to the presence of a transmitting coil when a thin shield is inserted between the coils. Moser outlines a direct-vector field solution to this problem. It requires expressions for the magnetic potential at the transmitting coil in the presence of a shield. Other expressions derived for the potential at the shield and at the receiving coil would not be required here. Using the magnetic potential equation, equations for the magnetic and electric field at the coil could be found and their ratio used to find the coil impedance in the near-field region. This would provide an approximation to the coil impedance, provided that the radiation resistance was low, which is generally true for electrically small coils. However, numerical solutions are required to solve the magnetic potential equation, since an integration involving Bessel function products is required. Furthermore, the impedance would only be valid at the point at which the electric to magnetic field ratio was computed (for example at the centre of the coil). The solution would however include the effect of permeability.

4.8 Summary

The impedance influencing property of conducting shields placed in close proximity to RFID coils was investigated. This situation arises often in RFID applications for both interrogator and transponder because they are members of the same coupled circuit. Equations originally derived by Levy [Levy] to model shield effectiveness were found to agree with measurements, particularly for the case of coil inductance. Greatest accuracy was found when the shield thickness was less than the skin depth, which is in agreement with Moser [Moser].

The effect of ferrous shields was characterised by measurement, since Levy's impedance equations do not include variation of material permeability. In the presence of ferrous shields, coil inductance was found to increase at low frequencies, and decrease at higher frequencies. The frequency at which eddy current and material permeability effects balance, producing no change of coil inductance, depends on the following shield parameters: permeability, conductivity, shield thickness and proximity.

Results from the above measurements were applied to the problem of proximity RFID by analysing interrogator and transponder circuits to determine their behaviour in the presence of conducting shields. The resonance frequency changes according to the change in inductance. Most important however is the increase of equivalent series resistance, which causes reduction of both interrogator current and transponder dynamic impedance. These effects are both compounded by shifting of the resonant frequency. The resulting performance implications include the reduction of magnetic field strength, transponder load modulation and interrogator modulation sensitivity.

General RFID proximity dependencies include system sensitivity to distance and orientation, as discussed in the previous chapter, and reduction of performance in the presence of conducting shields, as discussed in this chapter. An embedded automatic identification device that utilises the appliance power cable rather than free-space coupling as a communications channel was designed to eliminate such dependencies in RFID proximity systems and is described in the next chapter.

5 Non-Contact Electrical Cable RFID

5.1 Introduction

Free-space coupled mechanisms for proximity RFID were considered in chapters 3 and 4. Fundamental limitations were identified regarding orientation and proximity to metallic surfaces which can limit the range and flexibility of proximity RFID. In this chapter a new coupler design is described called cable RFID which differs from the air coupled method in that closed magnetic paths are used. In contrast to loosely coupled coils, where the coupling factor is often below 1 % [Finkenzeller], the coupling factor achieved by the new design approaches unity. This is achieved by winding the coil around a highly permeable core through which the appliance power cable is passed (figure 5.1). A high frequency oscillating current is then sent through the power cable, energising the coil and activating a transponder IC. An integral feature of this technique is the exploitation of mains inlet filter to achieve a return path for the high-frequency line current which is discussed in the next chapter. The design was found to be comparable to a current transformer regarding the inductive coupled mechanism however possesses different characteristics particularly with respect to power transmission, load modulation and performance versus size tradeoffs.

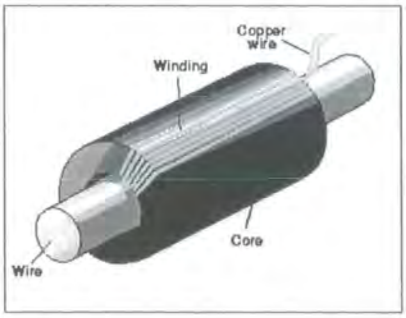

Figure 5.1 RFID cable coupler principle, showing toroidal winding placed around cylindrical core. The core material has high permeability.

5.1.1 Motivation

A new approach was pursued with the aim to extend the range of proximity RFID and to enable the embedding of transponders within the power cable of mains-powered appliances. The development of embeddable transponders was required specifically according to the needs of Seaward Electronic Ltd. Performing electrical safety tests requires access to each appliance's identification code prior to testing If it were possible to energise an embedded transponder and read its contents immediately upon plugging the appliance into the test port, the tester would automatically identify the DUT and the select most appropriate test routine. In addition, test data gathered from previous testing (and unique to the particular D.U.T.) could be read from either the transponder or a central database, thus allowing the user to review the test history and tailor the test procedure accordingly. It was therefore proposed that the appliance power cable might be utilised as a communication channel for automatic identification prior to appliance testing.

By embedding the transponder coupler device within the power cable structure, it becomes possible to identify any electrical device attached to the cable by passing current through the cable which energises the transponder. Other cabling applications could benefit from this technique, for example, situations in which cables are located behind walls, routed through conduits, or installed in large bundles, and require rapid identification during installation or servicing.

5.1.2 Principle

The principle of cable RFID is illustrated in figure 5.2. Rather than coupling coils at close range (the method of proximity RFID), the RF modulated carrier travels through power cabling attached to the DUT and interrogation takes place while the PAT and appliance are connected together. This channel is fully compatible with the signalling method used by the majority of inductive RFID transponder systems. Since the power cable must be used during safety tests the method utilises an already present channel and allows automated identification prior to testing. The method also creates the potential for extending the range of automatic identification methods that are based on passive RFID.

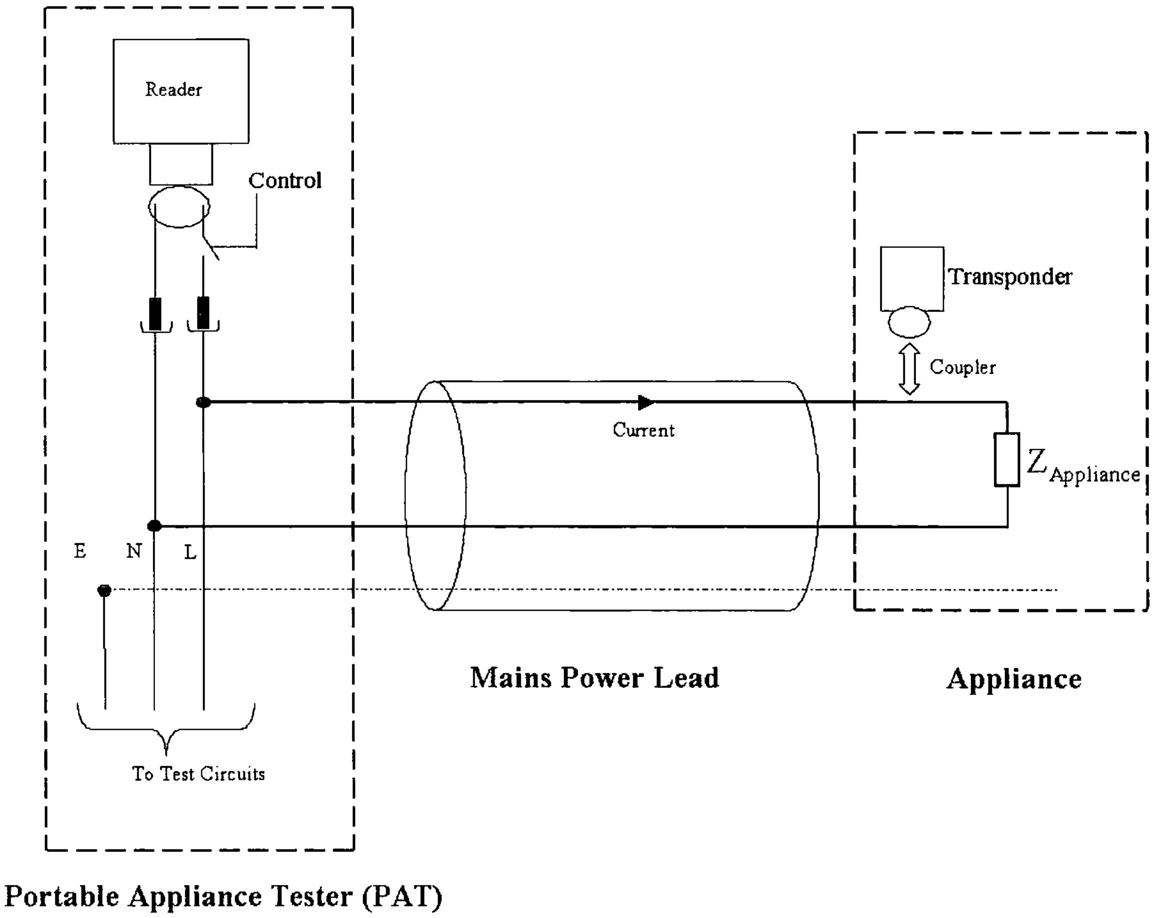

Figure 5.2. Illustration of cable RFID system, showing location of interrogator within PAT and utilisation of power cable to instigate communication with transponder.

If commercial RFID transponder ASIC's are to be adopted (hence avoiding the need for a new mixed-signal ASIC design), cable RFID must be compatible with the direct-load modulation signalling method. The inductive coupler described in this chapter has similar properties to proximity RFID systems and is compatible with direct-load modulation signalling provided modifications are made to the interrogator circuit. In fact, it is shown that the same equivalent circuit may be used to describe proximity and cable RFID.

5.1.3 Assumptions

The operational frequency is 125 kHz at all times which is compatible with commercial low frequency RFID transponder ASIC's. Higher RFID channels such as the 13.56 MHz ISM band were not directly considered but most of the following analysis would be applicable at higher frequencies. The cable RFID systems considered here were limited to frequencies ranging a few hundred kilohertz due mainly self-resonant effects in the couplers. This is not a fundamental limitation in itself, however performance would be reduced in long-cable applications (discussed in chapter 6) as would tolerance to any variation of primary circuit loads. Furthermore, signalling is currently permitted at 125 kHz on low-voltage electrical installations according to European Normative 50065. Power-line signalling is discussed further in chapter 9.

5.2 RFID Transponder IC Characteristics

The purpose of the coupler is two-fold: to develop sufficient voltage to activate the transponder IC, and to allow direct load modulation to take place. In order to activate power-on reset, a typical CMOS RFID transponder requires between 2 and 5 Volts (peak) across its terminals. Chip power requirements have been reported as low as 5 μW [Friedman], [Kaiser], and minimum power consumption is generally less than 100 μW.

5.2.1 Chip Impedance

It is important to determine the transponder ASIC impedance variation when direct-load modulation is taking place. As an example, the Philip's Hitag 1 transponder chip impedance was measured by load substitution. This simple method involves replacing the transponder with an equivalent impedance consisting of a capacitor and resistor connected in parallel such that the voltage recorded using the chip is equal to that using the substituted impedance. Since the nominal chip capacitance is known from manufacturer specifications (210 pF) the equivalent chip resistance may be estimated by finding the correct resistance which when placed in parallel with this capacitance produces the correct voltage. Effects of the on-chip voltage limiter are minimised by using the minimum chip voltage at which valid operations occurred (chip impedance reduces as the voltage becomes active). Chip resistance was estimated for both modulator ON and OFF conditions during an ID number request operation using the prototype interrogator described in chapter 7. The results are summarised in table 5.1. For the purposes of simulation in later sections modulator resistance values were chosen to be 100 kΩ (OFF) and 1 kΩ (ON).

	Chip Voltage (peak)	Equivalent Substitute Resistance	Power
Modulator OFF	3.19 V	80 kΩ	63.1 μW
Modulator ON	1.5 V	2.5 kΩ	450 μW

Table 5.1 Measured chip resistance for minimum operational voltage

5.3 Alternative Coupling Mechanisms

In this section the coupler is described from initial concept to prototype. In particular, design decisions involving physical coupling are highlighted. In order to improve understanding of the inductive coupling arrangement early experiments were conducted using inductive coils and straight current-carrying conductors.

5.3.1 Coil Positioned Close to Cable

An early concept was developed by placing an inductive loop close to a current carrying conductor to establish mutual inductance. The loop and wire were orientated as shown in Figure 5.3. Circular magnetic flux lines surround the current-carrying wire which couple with the wire loop placed nearby. The degree of coupling is a function of geometry including loop radius (described by *x*), number of loop turns and proximity (described by *r*) and may be estimated mathematically by finding the mutual inductance between the wire and loop.

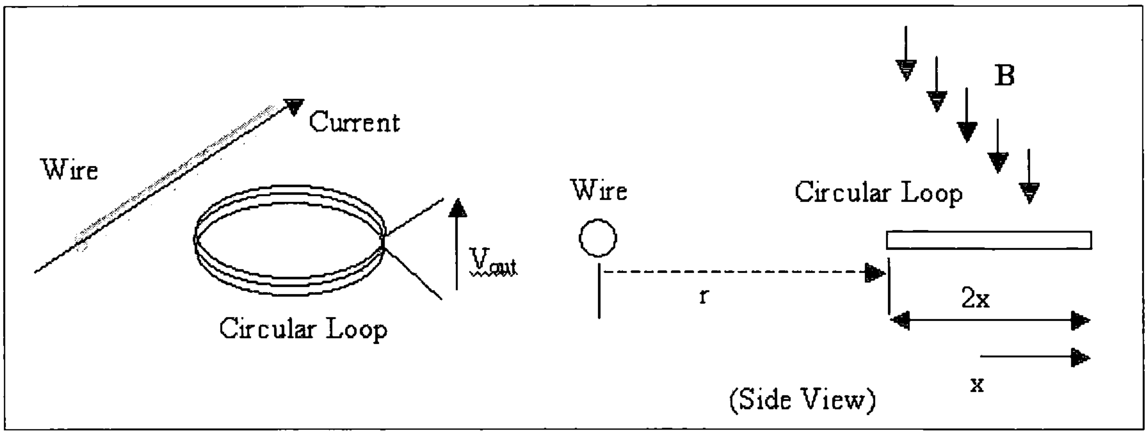

Figure 5.3: Wire and loop arrangement

5.3.2 Deriving Mutual Inductance Expressions

In this section two procedures for calculating the mutual inductance are described. The first method assumes a uniform distribution of magnetic flux across the loop area; the second method takes into account variation of field strength as a function of separation, *r*.

5.3.2.1 Method 1

Referring to Figure 5.3, *x* is the coil radius and *r* the separation distance.

$$V = -N_{coil}\frac{d\phi}{dt} \qquad \phi = \int B.ds \quad \text{or} \quad \phi = BA$$

If *r* is considerably larger than the cable radius then the magnetic field density, *B*, may be considered as composed of uniform vertical lines. We could further assume that at separation distance, *r*, *B* is constant from *r* to *r+2x*. For a straight conductor, the magnetic field may be expressed by:

$$B = \frac{\mu_0 I}{2\pi r} \qquad [\mathrm{Wb/m^2}]$$

Flux though the coil is then:

$$\phi = BA = \frac{\mu_0 I \pi x^2}{2\pi r'} \qquad [\mathrm{Wb}]$$

where r' is the average distance between coil and cable, equal to $r+x$:

$$\phi = \frac{\mu_0 I x^2}{2(r+x)}$$

Applying Faraday's law:

$$V = -N_{coil}\frac{d}{dt}\left(\frac{\mu_0 I x^2}{2(r+x)}\right) = -\frac{N_{coil}\mu_0 x^2}{2(r+x)}\frac{dI}{dt}$$

Thus the mutual inductance is defined as:

$$M = \frac{\mu_0 N_{coil} x^2}{2(r+x)} \quad [\mathrm{H}] \tag{1}$$

5.3.2.2 Method 2

Now assuming that the *B* field varies across the area of the coil (in the direction of *r*) and referring to Figure 5.4:

$$\phi = \int_{s_2} B.ds_2 \quad [\mathrm{Wb}]$$

Where s_2 is the area of the coil. Note that ***B*** varies in the direction of *r*. A square coil of side dimension *2x* is assumed which simplifies the derivation.

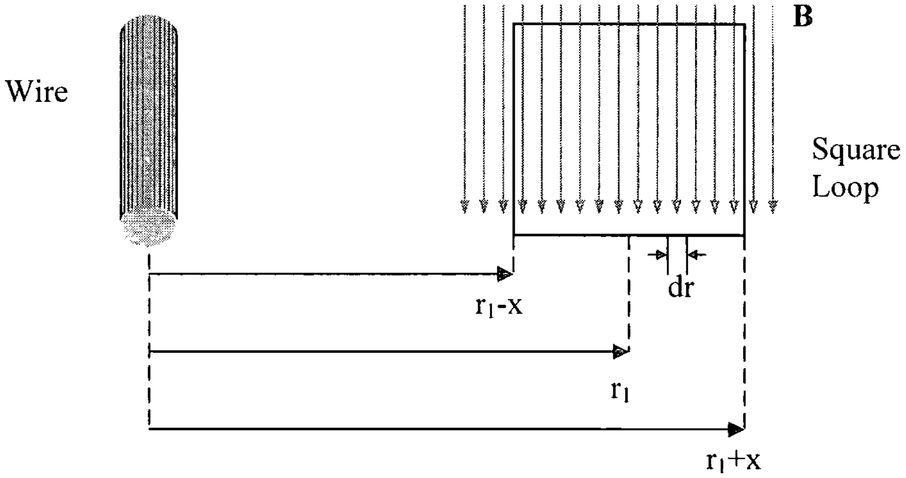

Figure 5.4: More accurate model of wire and loop

A strip of the loop surface has area *2xdr*, and therefore flux linkage may be expressed as:

$$\phi = \int_{r=r_1-x}^{r=r_1+x} B2xdr = \frac{2\mu_0 Ix}{2\pi}\int_{r_1-x}^{r_1+x}\frac{1}{r}dr = \frac{2\mu_0 Ix}{2\pi}\left[\ln(r)\right]_{r_1-x}^{r_1+x} = \frac{2\mu_0 Ix}{2\pi}\left(\ln(r_1+x)-\ln(r_1-x)\right)$$

$$= \frac{\mu_0 Ix}{\pi}\ln\left(\frac{r_1+x}{r_1-x}\right) \quad [\mathrm{Wb}]$$

mutual inductance is therefore given by:

$$V = -N_{coil}\frac{d\Phi}{dt} = \frac{-N_{coil}\mu_0 x}{\pi}\ln\left(\frac{r_1+x}{r_1-x}\right)\frac{dI}{dt}$$

$$\Rightarrow M = -\frac{V}{dI/dt} = \frac{N_{coil}\mu_0 x}{\pi}\ln\left(\frac{r_1+x}{r_1-x}\right) \quad [\mathrm{H}] \qquad (2)$$

It is then useful to recalculate method 1 for a square coil (again of side length x):

$$\Phi = BA = \frac{\mu_0 I}{2\pi r}A$$

where A is given by $A = (2x)^2 = 4x^2$. Mutual inductance may then be derived:

$$\Phi = \frac{4\mu_0 I x^2}{2\pi r'} = \frac{2\mu_0 I x^2}{\pi r'} \Rightarrow V = -\frac{2N_{coil}\mu_0 x^2}{\pi r'}\frac{dI}{dt} \Rightarrow M = \frac{2N_{coil}\mu_0 x^2}{\pi r'} \quad (\mathrm{H}) \qquad (3)$$

Note that r' is used which extends to the mid-point along the coil width.

5.3.2.3 Comparison

Equations (2) and (3) were evaluated for various r, as shown in figure 5.5 where the loop radius was 3.4cm. The resulting plots agree, except when r is small, when (2) gave slightly higher inductance. This is due to the fact that the field is strongest near the wire surface. Since mutual inductance is directly proportional to induced voltage, the voltage across an experimental coil placed near a current-carrying conductor was measured to confirm the profile of mutual inductance. An active buffer was used to remove any loading effects of the probe. The resulting curve included in figure 5.5. has the same characteristic as the theoretical curves, particularly in the far-range. The measured voltage falling more rapidly in the near-range.

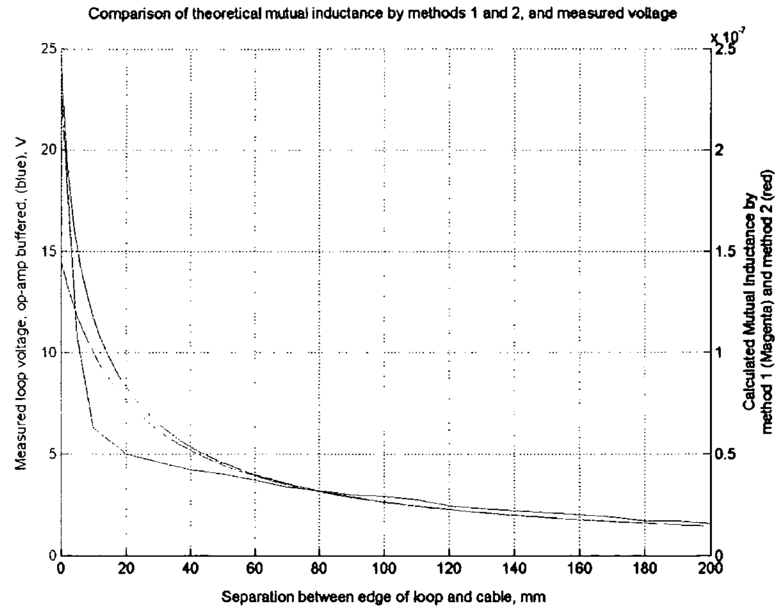

Figure 5.5: Theoretical mutual inductance compared with measured voltage versus separation.

5.3.2.4 Further experimental Observations

It was found that as the wire is moved along the side of the loop (figure 5.6) a null point (i.e. zero mutual inductance) exists at the mid-point. This is caused by the symmetry of the field produced by the wire.

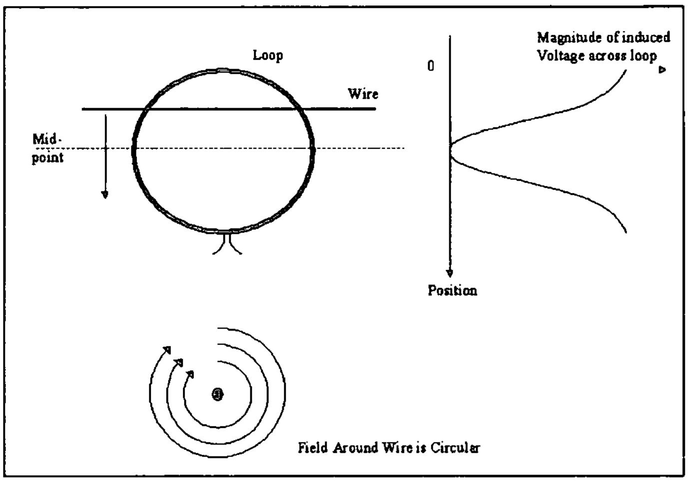

Figure 5.6. Illustrating null point in the mutual inductance at the centre axis of the loop

5.3.3 Discussion

The achievable mutual inductance by this method is extremely low as seen in figure 5.5 and is considerably less than achieved by conventional proximity RFID (cf. figure 3.5 in chapter 3). A more direct means of coupling to flux produced around the wire was required.

5.3.4 Optimal Arrangement

To increase coupling between the wire and coil a Toroidal winding was used (figure 5.1). This arrangement ensures that the same flux passes every loop (though there is variation of flux density from the inner wall of the core to the outer). Increased coupling is achieved by the fact that flux passes perpendicular to the plane of each winding loop, and that the loop area is positioned as close to the wire as possible.

5.4 Characterisation of Inductive Coupler

In order to compare the coupler design to an ideal transformer several couplers were constructed with windings of between 5 and 40 turns of 36 SWG enamelled copper wire. Each winding was disposed such that its width was less than 5mm and the number of layers accumulated naturally. Figure 5.7. shows the general arrangement. Bunched windings were used such that the winding copper is concentrated in a defined region and disposition of the winding did not influence the resulting inductance and capacitance. This leads to repeatable winding inductance and a simpler manufacturing process.

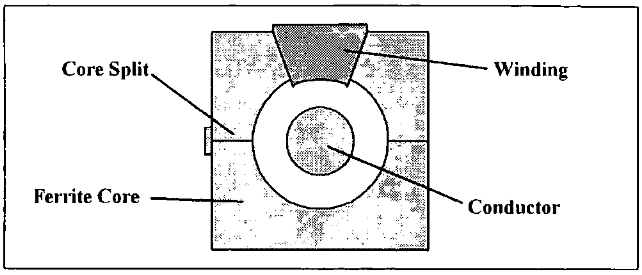

Figure 5.7. Arrangement of winding around core.

5.4.1 Toroidal Arrangement

Ring ferrite cores were used to increase inductance and as a former on which to wind the coil. Split-core ferrites were used as they can be easily attached and removed from wires and are less susceptible to saturation from high line current. The core used was a broadband noise suppression type manufactured by Steward EMC with part reference number 28A2025-0A0. The inner radius accommodates 3-core mains cable rated at 3 A. The essential core dimensions are summarised in figure 5.8.

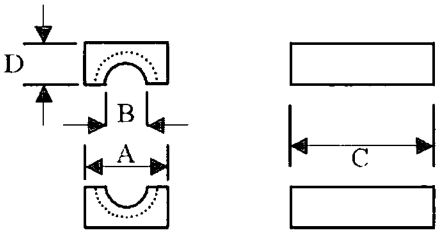

Drawing of Split Core

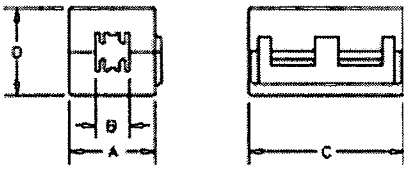

Drawing of Core Housing

Dimension	Size, in mm
Core A	14.99
Core B	3.30
Core C	29.16
Core D	7.44
Housing A	17.9
Housing B	7.00
Housing C	32.5
Housing D	18.4

Figure 5.8 Ferrite core and housing dimensions

Core type 28 ferrite material was chosen which has a permeability of around 850 (DC - 1 MHz,), bulk resistivity of 10^5 ohms and saturation flux density of 325 mT. At frequencies above 1 MHz core permeability reduces as shown figure 5.9 while losses increases until the core becomes predominantly resistive, at which point the core attenuates the signal by dissipating heat. However, below 1 MHz the core exhibits high permeability and low loss.

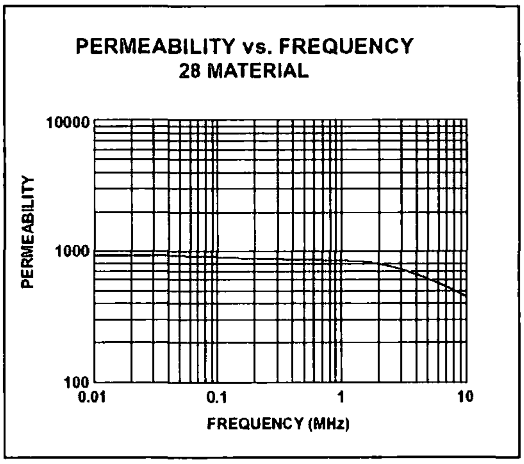

Figure 5.9 Frequency response of core permeability, type 28 Steward ferrite material[10]

5.4.2 Inductance and Self-Resonance

The inductance of each coupler was measured using an Agilent 4294A impedance analyser in the frequency range 10 kHz–10 MHz[11]. As an illustration of the results obtained, the inductance and equivalent resistance of the 10 turn coupler is shown in figure 5.10. and 5.11. respectively, where self-resonance is clearly seen at around 6.6 MHz. This occurs due to a combination of capacitance between each turn of the winding and capacitance between the core and winding. Note that inductance reduces

---

[10] Source: Steward EMC, www.steward.com

[11] Analyser settings: 5 mA current source.

by around 30% between 10 kHz and 100 MHz due to the variation of core permeability with frequency. Self-resonance occurs as a peak in the equivalent resistance along with zero reactance. Above the self-resonant frequency the core is predominantly capacitive since the winding capacitance shunts the inductance and resistance terms. This can be seen more clearly by inspecting the equivalent model for the coupler in figure 5.18, which is discussed in section 5.6.1.

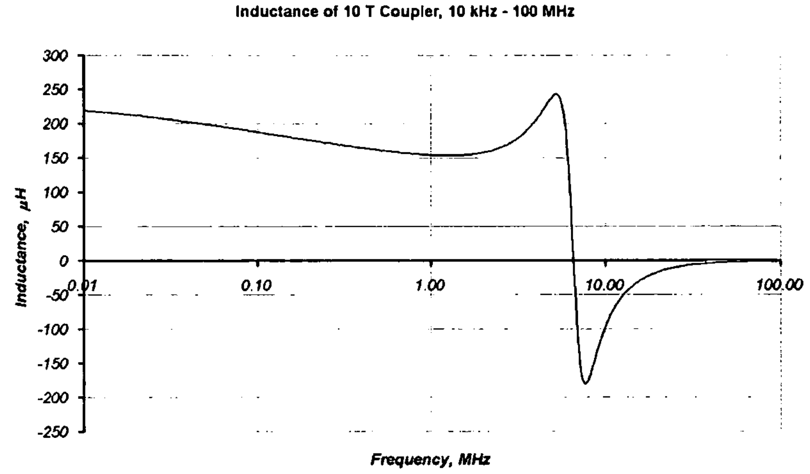

Figure 5.10. Inductance of 10 turn coupler from 10 kHz to 100 MHz

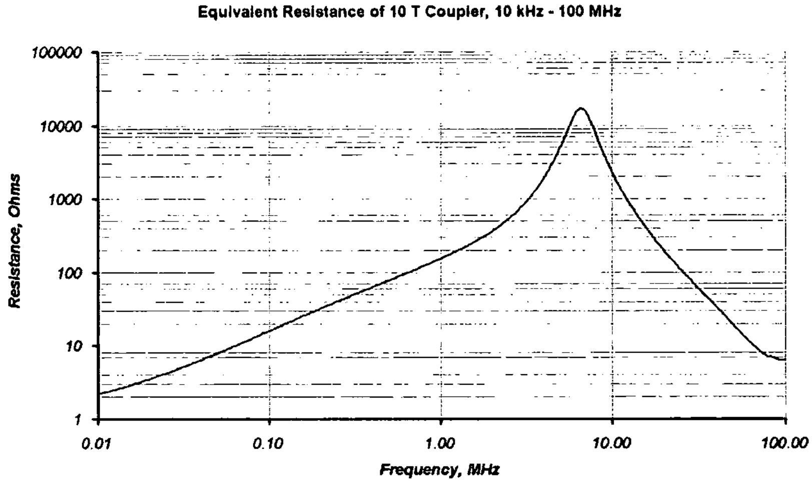

Figure 5.11 Equivalent resistance of 10 turn coupler

The inductance at 125 kHz and at self-resonant frequencies for all couplers were collated and are presented in figures 5.12. and 5.13. In figure 5.12 inductance can be seen to increase with the number of turns in accordance with the inductance equation; inductance, L, varies as the square of the number of turns, N, according to the following equation:

$$L = \frac{\mu\mu_0 N^2}{C_1} \text{ (H)} \qquad \text{where } C_1 = \frac{A_e}{l_e} = \int\frac{dA}{l} \text{ (cm}^{-1}\text{)} \tag{4}$$

Where A_e is the average area through which the flux passes and l_e is the effective magnetic path length equal to the average circumference of the core [Snelling]. By assuming that flux is evenly distributed between the core inner radius and outer radius, these parameters may be expressed by the core dimensions:

$$A_e = \frac{A_{core} - B_{core}}{2C_{core}} \qquad l_e = \pi\left(\frac{A_{core}}{2} + \frac{B_{core}}{2}\right) \tag{5}$$

By further assuming that core permeability remains constant for all couplers, for a constant frequency of 125 kHz a constant of proportionality $\mu\mu_0/C_l$ between L and N can be computed for the 10 turn coupler. This was used to plot the black line in figure 5.12 which shows the same relationship as the measured data. Note that the 30 turn coupler falls below this trend line, indicating a degree of inductance variability caused by the combined effect of deviation of material permeability from one sample to the next, and by the use of bunched windings.

In figure 5.13 the SRF is seen to decrease as more turns are used. This is consistent with the assumption of increasing capacitance as more turns are added.

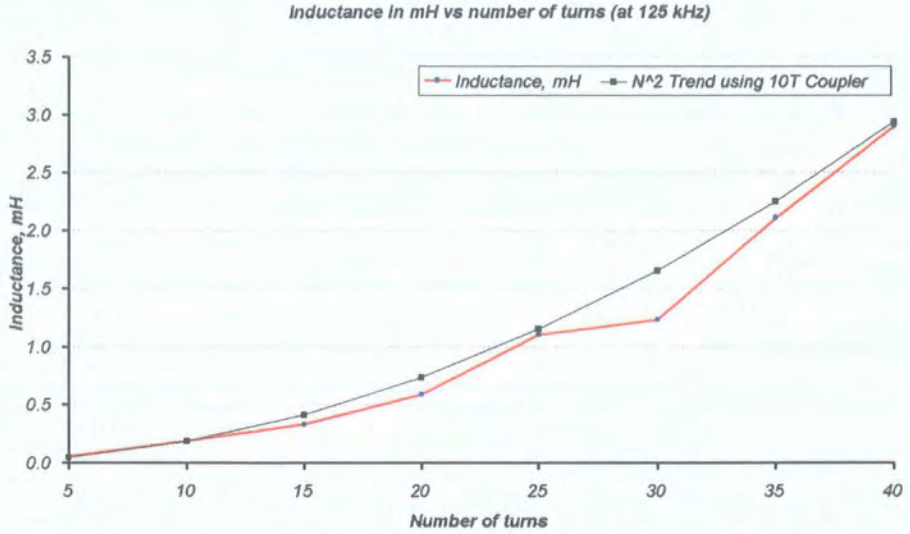

Figure 5.12. Coupler inductance versus number of winding turns

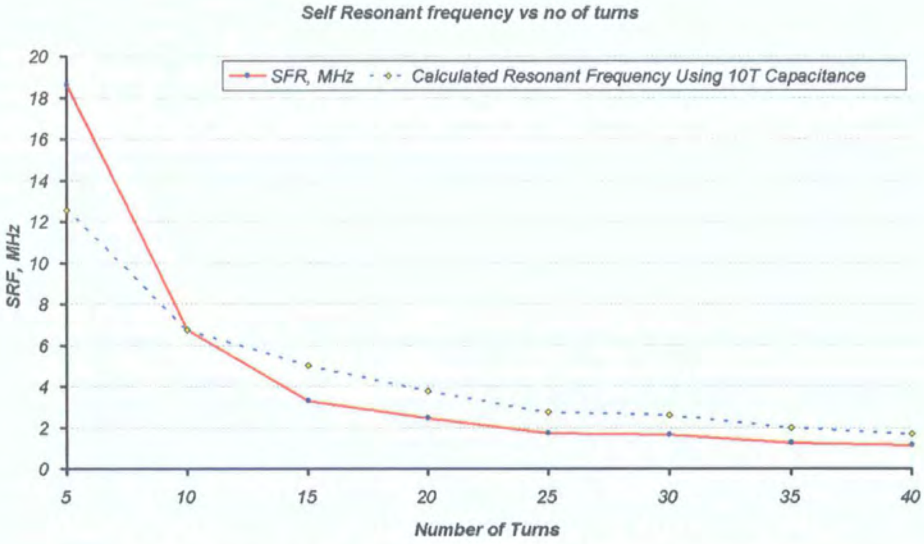

Figure 5.13. Self Resonance frequency of coupler versus number of turns

5.4.3 Coupling Coefficient

Leakage flux generated by the coupler may be quantified by measuring the coupling coefficient. It indicates the effectiveness with which a particular coupler is able to harness flux generated by the wire within its core; any flux not passing through the winding does not contribute to the mutual inductance. A convenient procedure for measuring leakage inductance is well known and may be found in [MacFayden]. It is calculated by the following equation:

$$k = \sqrt{1 - \frac{l_p}{L_p}} \tag{6}$$

L_p is the inductance measured while the secondary terminals are open and l_p the inductance measured while the secondary is short-circuited. Hence k is equal to unity when $l_p << L_p$ and is equal to zero when $l_p = L_p$ (no coupling). This procedure is reciprocal in that the secondary and primary may be swapped to give the same result.

Leakage inductance was measured for each coupler using the above method. The results shown in figure 5.14. indicate that the coupling coefficient remains reasonably constant for all couplers, taking values between 0.85 and 0.9. This result is useful because it indicates that the number of turns does not significantly alter the coupling coefficient and hence mutual inductance remains predictable.

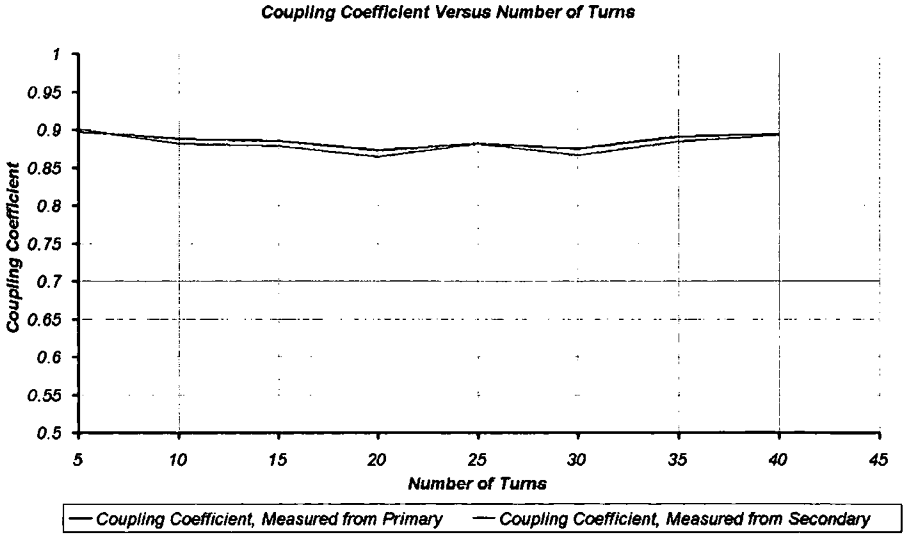

Figure 5.14 Coupling coefficient versus number of turns

5.5 Proof of Concept

The concept of a self-powered circuit that is able to communicate by direct-load modulation was investigated using an early prototype that simulates a functional RFID transponder. A coupler with 40 secondary turns was attached to a circuit comprising voltage rectifier, pulse generator, low-power comparator and direct-load modulator. The schematic is shown in figure 5.15. A voltage doubling rectifier was employed to produce a D.C. supply for the comparator and binary counter. This approach is similar to that used by Friedman *et al* [Friedman]. Diode D_3 is used to half-wave rectify the carrier, producing a trigger signal that is compared to a reference voltage derived from the D.C. rail. The resulting output is fed into a 7 bit counter that produces a sub-carrier signal which controls a MOSFET switch. Resistor R_4 causes the coupler voltage to fluctuate by intermittently loading coil coupler secondary impedance. The carrier frequency was set to 125 kHz, giving a sub-carrier frequency of 1 kHz. A series resonant circuit was placed in the primary circuit that resonates at the carrier frequency and amplifies the voltage between capacitor C_5 and inductor L_1 by the quality factor (Q). The secondary impedance is coupled into the primary circuit, modifying the primary Q. During load modulation, primary Q varies periodically which manifests as weak amplitude modulation of the tap-point voltage. These oscillations were sensed by a simple envelope detector, D_5, whose time constant $\left(1/R_5C_6\right)$ was set to the sub-carrier frequency. The resulting signals are illustrated in figure 5.15.

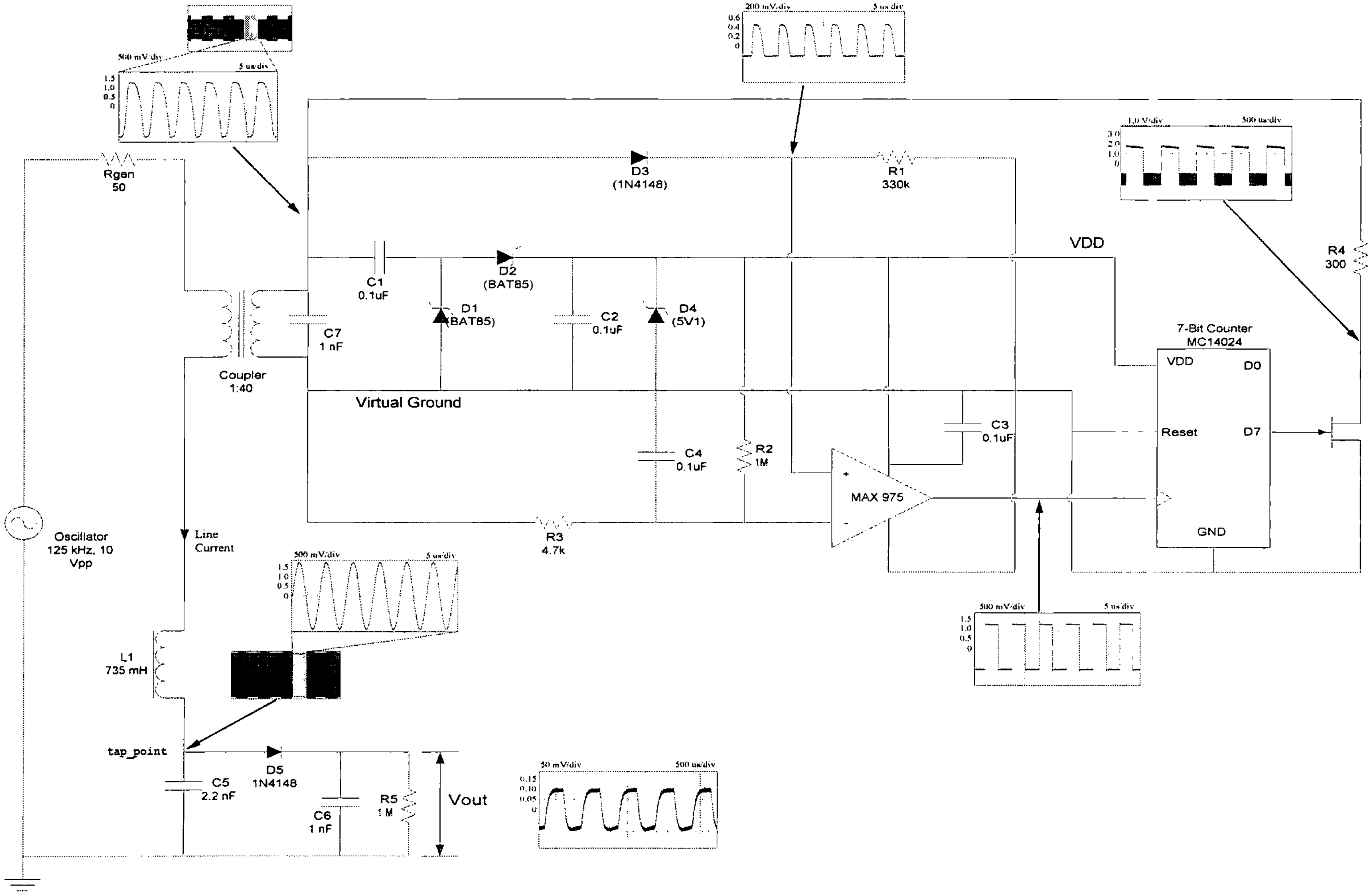

Figure 5.15. Circuit diagram of cable-RFID concept circuit, showing cable and transponder circuits. Important waveforms are also shown

For correct operation upper and lower limits must be placed on the value of resistor R_4. The lower limit is determined by the power requirement of the circuit, since the average power is reduced by amplitude modulation of the carrier. If the value of R_4 is increased such that is greater than the unloaded secondary impedance load modulation is severely attenuated. It was however observed that detection was possible for $R_4 \leq 4k\Omega$. A graph of signal-to-noise ratio at the detector output, SNR_o, versus R_4 is shown in figure 5.16. Noise content was assumed constant and measured by averaging the detector output in the absence of any load modulation. Sources of noise include carrier leakage from the primary circuit, which was included in the averaging, and is assumed band-limited since out of band signals are attenuated by the series resonant circuit. The measured amplitude of time-averaged noise was independent of the number of samples used, which ranged from 2 – 4096, and averaged 25.5 mV. Deformation of the modulating signal occurs for $R_4 \leq 500\Omega$, causing the SNR to decrease slightly. The mechanism of load modulation was shown to be feasible.

Commercial RFID transponder chips employ more advanced circuit design that used here, but the principle is the same: a self powered circuit that is capable of direct-load modulation. Of course meaningful data can only be conveyed by the transponder when some form of memory is used to store unique information, such as an identification number. Furthermore, low power consumption is a priority in wireless proximity RFID applications since available power may be the order of micro-watts [Kaiser].

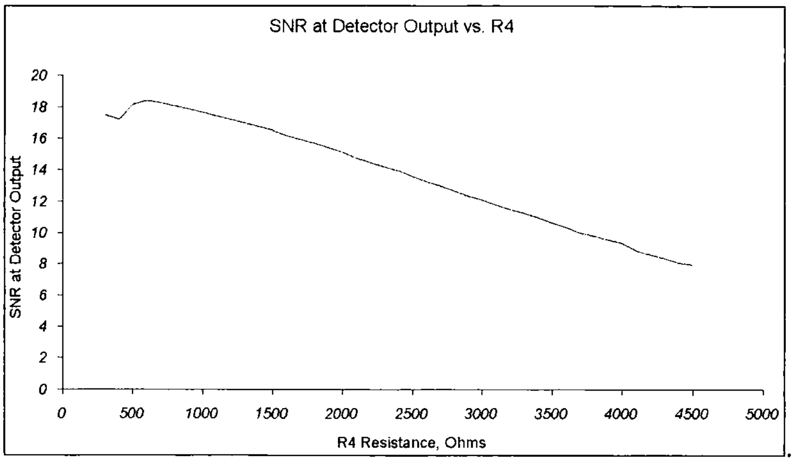

Figure 5.16 SNR at Detector output versus load modulator resistance, R_4.

5.5.1 Power Requirements

Power transmission is improved in wire-based RFID applications due to higher coupling efficiency and is considered in section 5.7. The comparator, counter, modulator and rectifier all require minimum power for operation. To find the minimum operational power the line current was reduced to the minimum working value. By decreasing the value of R_4 to the minimum possible value, the minimum fully operational power was found. The resulting minimum power consumption was 39.8 μW at the DC power rail, which required line current of 1.8 mA RMS. Under these conditions V_{DD} was 2 V. In order to avoid shunting the coil voltage too severely, R_4 was increased to 2 kΩ (lower values resulted in insufficient power for the circuit) which gave a detector output voltage of 29 mV and SNR of 10.7 dB. The primary resonant circuit Q was around 9, calculated either by measuring the ratio of tap point voltage to generator voltage, or by calculating the ratio of reactance to circuit losses.

Lower values of R_4 were permitted by increasing the primary current. In table 5.2. circuit parameters are compared for line currents of 1.8 mA and 5.1 mA. In the latter case the detector output SNR is doubled at 20 dB.

In this design efficiency is dominated by the 50 Ω resistor residing in the primary circuit, which is the internal impedance of the waveform generator. Total primary power loss, including the coupled transponder impedance, amounts to 1766 μW (high current) and 219 μW (low current). Ignoring I^2R losses due to the generator resistance, the remaining total primary losses, *including* the coupled transponder resistance, were 465 μW and 57 μW. Comparing these figures to the transponder DC power consumption, we may conclude that additional power is consumed by:

- Losses in inductor L_1, due to copper and core loss,
- Coupler losses in the form of hysteresis loss,
- Losses in the voltage rectifier circuit.

Although power losses increase considerably as the line current is increased beyond the minimum operational requirement, the SNR is approximately doubled at the detector output.

Generator Voltage, peak-peak	Line Current, RMS	R_4	I_{DD} (DC Rail)	V_{DD}	Power drawn from DC rail	Detector voltage peak-peak	SNR at detector output
0.97 V	5.1 mA	300 Ω	37.6 μA	3.9 V	146 μW	250 mV	20
0.338 V	1.8 mA	2 kΩ	19.9 μA	2 V	39.8 μW	29 mV	10.7

Table 5.2. Key circuit parameters under high and low line current conditions

5.6 Circuit Model

In this section equivalent models are developed to describe the transponder and interrogator circuits and their interaction. This model is applicable to both cable RFID and conventional proximity RFID tagging systems; the principle difference between them lies in the degree of coupling between interrogator and transponder. A basic interrogator-transponder model takes the form of two coupled circuits, as illustrated in figure 5.17. The primary circuit (on the left) represents the interrogator circuit including the power cable and appliance filter. The secondary circuit (on the right) represents the transponder which is inductively coupled to the interrogator circuit by the cable coupler.

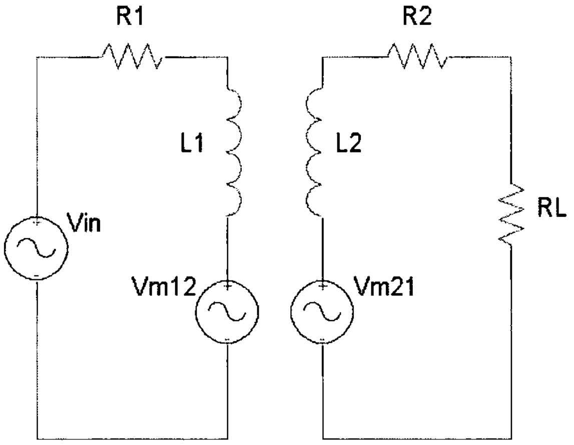

R_1	Primary resistance
R_2	Secondary resistance
L_1	Primary inductance, formed by placing wire through core
L_2	Secondary inductance, formed by secondary winding of N turns
R_L	Resistance attached to terminals of secondary winding
V_{m12}	Induced primary voltage due to secondary current
V_{m21}	Induced secondary EMF due to primary current
V_{in}	Primary exciting voltage; system energy source
I_1	Primary current
I_2	Secondary current

Figure 5.17. Equivalent circuit used to model inductive coupler, including symbol definitions

5.6.1 Transponder

The cable RFID transponder may be modelled in isolation by the circuit shown in figure 5.18. Coil L_2 with equivalent series resistance R_2 is connected to a capacitor C_2 which creates parallel resonance at the resonant frequency and thus raises the terminal voltage by a factor Q. If ideal resonance were possible then $R_2 \rightarrow 0$ and the coupler reactance would become infinite, eliminating the effect of finite winding inductance. In reality, winding loss ensures that the effect of finite winding inductance is not eliminated and the tuned circuit presents a finite impedance to any load R_L connected across the terminals. The transponder chip is represented as a parallel combination of resistance and capacitance, the latter accounting for chip capacitance. Chip capacitance is often maximised for RFID transponder ASICs to eliminate the requirement of an external resonance capacitor. For example, the Philips Semiconductor Hitag 1 transponder chip has 210 pF on-chip capacitance. This would resonate directly at 125 kHz if a coil having inductance 7.7 mH were connected.

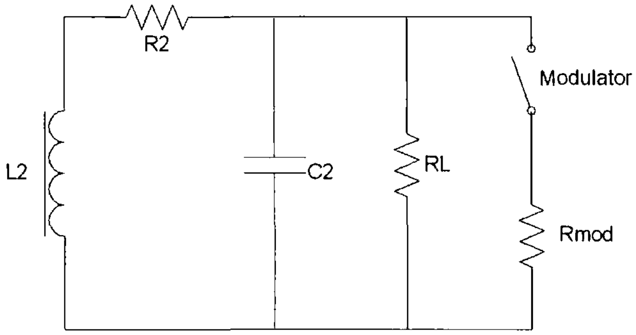

Figure 5.18 Transponder equivalent circuit

Direct-load modulation is represented by an additional resistance introduced across the chip resistance when the modulator is switched ON as shown. Note that capacitive modulation is also possible where the resonant circuit is detuned by switching an additional capacitor across C_2 [Roesner].

The amount by which resonance raises the coupler circuit impedance may be calculated by inspecting the equivalent series resonant circuit. The series equivalent of C_2 and R_L, may be calculated using [Boys]:

$$R_{series} = \frac{R_L}{1+(\omega C_2 R_L)^2} = \frac{R_L}{1+Q^2} \tag{7}$$

$$C_{series} = \frac{1+(\omega C_2 R_L)^2}{C_2(\omega R_L)^2} = \frac{C_2(1+Q^2)}{Q^2} \tag{8}$$

assuming that the modulator is OFF, and $Q = \omega C_2 R_L$ is the quality factor. Note that for $Q^2 >> 1$ equations 7 and 8 simplify to become:

$$R_{series} \cong \frac{R_L}{Q^2}, C_{series} \cong C_2$$

Circuit Q is reduced when switching the modulator ON, and a small shift in the resonant frequency occurs due to the change in C_{series} as given by equation 8. The total transponder impedance at resonance including chip impedance may be written as (noting that $\omega L_2 = 1/\omega C_{series}$):

$$Z_{resonance} = \frac{\omega L_2 (j\omega L_2 + R_{series} + R_2)}{j(R_{series} + R_2)} \tag{9}$$

When the total quality factor $Q = \omega L_2 / (R_{series} + R_2)$ is moderately high (> 10) then we further note that $\omega L_2 >> (R_{series} + R_2)$ which allows simplification of equation 9 to:

$$R_{dynamic} = \frac{\omega L_2}{\omega C_{series}(R_{series} + R_2)} = \frac{L_2}{C_{series}(R_{series} + R_2)} \tag{10}$$

where $R_{dynamic}$ is the transponder impedance at resonance. Equation 10 shows that the impedance of the coupler secondary circuit becomes resistive at resonance.

5.6.2 Interrogator Equivalent Circuit

The purpose of the primary circuit is to provide energising current to the coupler and a means for detecting direct-load modulation. Within the scope of this work, the primary circuit comprises: power cabling, plugs and EMC mains inlet filter.

As will be discussed in section 5.8, basic sensitivity to direct-load modulation is poor due to the small variation of coupled impedance given by equation 7 when the load is modulated. This is further exasperated by the limitations on the variation of transponder chip impedance, particularly with regard to the lower limit (see section 5.2.1.). Capacitive and inductive elements were therefore placed in the primary circuit to increase load modulation sensitivity inducing series resonance as shown in figure 5.19. The impedance of a series resonant circuit is given by:

$$Z_{series} = R_g + Z_{coupled} + j\left(\omega L_1 - \frac{1}{\omega C_1}\right) \tag{11}$$

where $Z_{coupled}$ represents the impedance of the transponder circuit coupled to the interrogator circuit. At resonance, $\omega = \omega_0$, and equation 11 reduces to $R_g + Z_{coupled}$.

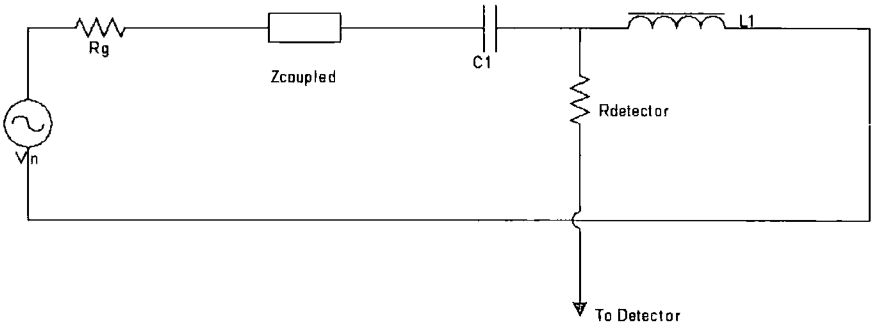

Figure 5.19 Interrogator equivalent circuit

If $Z_{coupled}$ is real, the primary circuit Q becomes:

$$Q_{series} = \frac{1}{\left(R_g + Z_{coupled}\right)}\sqrt{\frac{L_1}{C_1}} \qquad (12)$$

Therefore the interrogator circuit Q is modified by the presence of the coupled transponder.

5.6.3 Primary Referred Equivalent Circuit

In this section the interaction between transponder and primary circuit is described. From the theory of inductively coupled circuits, $Z_{coupled}$ may be expressed as:

$$Z_{coupled} = \frac{(\omega M)^2}{Z_{secondary}} \qquad (13)$$

where M is the mutual inductance and $Z_{secondary}$ the total transponder impedance. Note that $M = k\sqrt{L_1 L_2}$ and that the inclusion of parameter k shows dependency on the degree of coupling between the transponder and the cable. The coupled impedance appears as an additional impedance in the primary circuit and therefore equation 11 becomes:

$$Z_{series} = R_g + j\left(\omega L_1 - \frac{1}{\omega C_1}\right) + \frac{(\omega M)^2}{Z_{secondary}} \qquad (14)$$

Referring to figure 5.17, equation 13 may be derived by considering the induced EMF, V_{m21}, that appears in the secondary due to the current, I_1, passing through the primary, which may be expressed using the fundamental equation of inductive coupling:

$$V_{21} = j\omega I_1 M \qquad (15)$$

V_{m21} behaves as a voltage source whose internal impedance is dictated by inductor copper loss and which causes current, I_2, to flow in the secondary circuit when a load is attached to the terminals. Due to the reciprocal property of mutual inductance, a similar EMF appears in the primary circuit (V_{12}) due to the presence of the secondary current circuit. Summing the voltages around the transponder (secondary) circuit:

$$\begin{aligned}&Vm_{2,1} - I_2(j\omega L_2 + R_2) - V_{RL} = 0\\&\Rightarrow V_{RL} = j\omega M I_1 - I_2(j\omega L_2 + R_2)\end{aligned} \tag{16}$$

A similar expression may be found for the primary circuit:

$$\begin{aligned}&V_{in} - (I_1 R_1 + j\omega L_1) + Vm_{1,2} = 0\\&\Rightarrow V_{in} = I_1(R_1 + j\omega L_1) - j\omega M I_2\end{aligned} \tag{17}$$

Noting that Lenz's law dictates that the voltage across inductor L_1 must oppose $Vm_{1,2}$, we can may express the secondary current, I_2, as:

$$I_2 = \frac{Vm_{2,1}}{(R_2 + R_L) + j\omega L_2} = \frac{j\omega M I_1}{(R_2 + R_L) + j\omega L_2}$$

Substituting this into equation 17 allows the primary impedance to be expressed as:

$$\frac{V_{in}}{I_1} = (R_1 + j\omega L_1) - j\omega M \frac{j\omega M}{(R_2 + R_L) + j\omega L_2}$$

$$\Rightarrow Z_{primary} = (R_1 + j\omega L_1) + \frac{\omega^2 M^2}{(R_2 + R_L) + j\omega L_2} \tag{18}$$

The first term of equation 18 is simply the primary impedance while the second term is the coupled impedance given by equation 13. Equation 16 confirms that the loaded secondary voltage results from the induced EMF minus the voltage drop across R_2 and R_L. Equation 18 shows that the primary-referred equivalent model of a transponder consists of the series combination of primary coupler inductance and the coupled transponder impedance $Z_{coupled}$ (see figure 5.19).

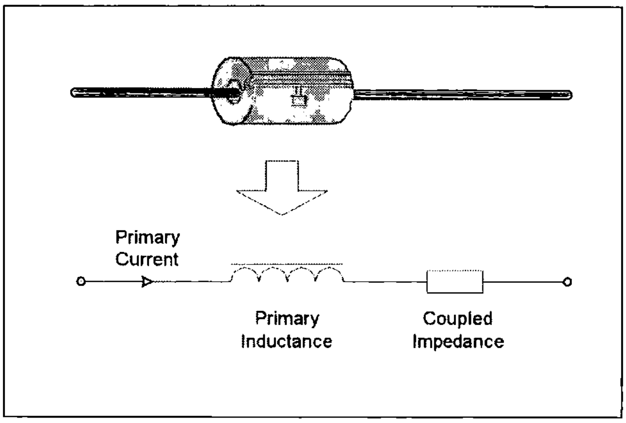

Figure 5.19. Equivalent model of a coupled transponder as seen from the primary circuit.

5.6.4 Secondary Referred Equivalent Circuit

When analysing the circuit from the perspective of the transponder, it is convenient to refer all circuit parameters to the secondary circuit. The secondary referred circuit parameters may be derived in a similar fashion to the previous section and are summarised in Figure 5.20. These equations can be found in relevant literature, for example Terman [Terman]. There are several notable features of this equivalent circuit. Firstly, the Thevenin voltage source V_{eq} is frequency dependent since it depends on the primary current which in turn results from the primary coupled impedance. Secondly, negative inductance appears in the transponder circuit which has the effect of increasing the secondary resonant frequency, ω_0. Thirdly, the coupled resistance is frequency dependent and adds to the existing transponder losses. This equivalent circuit was used for analysing conditions of optimal power transfer in section 5.7.

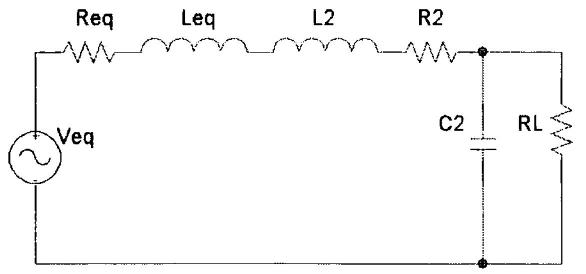

(Entire Circuit Transferred to Transponder Equivalent Circuit)

$$R_{eq} = \frac{(\omega M)^2 R_1}{R_1^{\,2} + (\omega L_1)^2} \tag{19}$$

$$L_{eq} = \frac{-(\omega M)^2 L_1}{R_1^{\,2} + (\omega L_1)^2} \tag{20}$$

$$V_{eq} = V_1 \frac{\omega M}{R_1 + j\omega L_1} \tag{21}$$

Figure 5.20. Equivalent circuit referred to secondary

5.6.5 Effect of Finite Winding Inductance

Since neither coupler primary nor secondary have infinite reactance a shunting effect occurs when R$_L$ is greater than the reactance of the winding. This causes a drop in the expected output voltage as the parallel impedance of R_L (referred to the primary) and the primary reactance ($j\omega L_1$) is less than the primary reactance alone. The effect is illustrated by re-arranging equation 18 and assuming ideal windings so that R_1 and R_2 become zero:

$$Z_{primary} = j\omega L_1 + \frac{\omega^2 L_1 L_2}{R_L + j\omega L_2} = \frac{j\omega L_1 (R_L + j\omega L_2) + \omega^2 L_1 L_2}{R_L + j\omega L_2} = \frac{L_1}{L_2}\left(\frac{j\omega L_2 R_L}{j\omega L_2 + R_L}\right) \tag{22}$$

The term in parenthesis represents the parallel impedance of R_L and $j\omega L_2$ which is multiplied by the *inductance ratio*, L_1/L_2, to give the primary impedance. By inspecting equation 13 we see that, provided $\omega L_2 >> R_L$, the primary impedance is simply the product of the load and the inductance ratio, thus:

$$Z_{primary} = \frac{L_1}{L_2} R_L = \left(\frac{N_1}{N_2}\right)^2 R_L \qquad (R_L << \omega L_2) \tag{23}$$

If however the secondary reactance is comparable to or less than the load then the primary impedance is reduced by the parallel effect and equation 23 is no longer valid.

In practice placing a capacitor across the winding significantly increases its impedance as discussed in section 4.6.1.

5.7 Power Transfer and Chip Voltage Characteristics

In this system power must be sourced from the carrier component of the EMF induced across the coupler winding in order to energise the passive transponder. Field gap signalling (or On/Off Keying) creates spectral sidebands but these do not contribute significantly to the available power. We therefore consider the *unmodulated* carrier when analysing the power transferred between primary and secondary circuit.

Maximising the power available at the transponder by impedance matching is not itself a priority in this design. However, to ensure transponder activation, it is most important to develop sufficient voltage across the transponder chip. The minimum transponder power requirement is defined by the chip impedance for the minimum operational voltage as excess power is dissipated as heat within the voltage limiter. Analysis of the power transfer curves is still useful however, since this reveals the chip voltage profile as a function of R_L (the transponder chip resistance) and establishes a relationship between primary circuit impedance and transponder dynamic resistance in the context of power transfer. Study of the latter effect is important in understanding factors that affect direct load modulation, which is the subject of section 5.8.

Power transfer between V_{in} and R_L was measured by connecting various couplers to a primary circuit comprising a generator and resistance, then recording the voltage appearing across a variable resistance connected across the winding terminals. Each coupler was made to resonate by placing a capacitor across the winding terminals (in parallel with the resistance) causing resonance at a frequency of 125 kHz. The couplers differed only by the number of secondary turns wound around the core. The resulting power curves are shown in figure 5.21, for which the generator settings were V_{in} = 0.5 Volts (peak) and R_G = 50 Ω. The corresponding chip voltage is shown in figure 5.22. Peak power occurs when R_L is equal to the impedance of the secondary-referred coupler circuit, which includes the coupled effect of the primary circuit. The matched power is reasonably constant at around 95 μW for each coupler considered.

The power and voltage curves may be calculated using the equations described in section 5.6.4. The power appearing across R_L was calculated using:

$$P_{RL} = \frac{|V_{RL}|^2}{R_L}$$

where, with reference to figure 5.20., the chip voltage, V_{RL}, may be calculated using equation 21 to give an equivalent Thevenin voltage source appearing within the secondary circuit:

$$V_{RL} = V_{eq} \frac{Z_{parallel}}{Z_{parallel} + R_{eq} + R_2 + j\omega(L_{eq} + L_2)} \tag{24}$$

where $Z_{parallel}$ is the parallel impedance of C_2 and R_L. The required coupler impedance parameters were measured as described section 5.4.2. and used to evaluate equations 23 and 24. The resulting theoretical power and voltage curves are shown in figures 5.23 and 5.24. Good agreement is seen between the measured and analytical curves, particularly with respect to the impedance required for optimum power matching and maximum chip voltage.

An expression for the point of maximum power transfer may be derived by modifying equation 10, which describes coupler's dynamic impedance, to account for the primary-coupled impedance described by equations 19 and 20:

$$R_{dynamic} = \frac{L_2 + L_{eq}}{C_2\left(R_2 + R_{eq}\right)} \tag{25}$$

Note that R_L is not included in equation 24 since we are considering the power matching between R_L and the rest of the circuit. Equation 25 was used to calculate the theoretical load-matched condition for each coupler. The results are summarised in table 5.3 which agree with the respective peaks of each power curve in figure 5.21. These optimum resistance values are important in understanding the impedance of the resonant coupler looking into the winding terminals. At resonance this impedance becomes real and equal to the resistance given by equation 25. Each optimum resistance value shown in table 5.3 is equal to the maximum attainable resistance that each tuned coupler is able to present to the transponder chip in the presence a coupled primary circuit.

	Number of Turns on Coupler Secondary Winding				
	5	10	15	20	30
Optimum Value of R_L for power matching	207.6 Ω	798.1 Ω	1665 Ω	3359 Ω	7843 Ω
Change in Transponder Inductance Due to Coupled Primary Circuit	0.1 %	0.071 %	0.055 %	0.045 %	0.044 %

Table 5.3 Some important transponder calculations including calculated optimum R_L values for power matching and change of transponder inductance.

It is important to note that equation 25 is only valid when the transponder resonant frequency is not significantly affected by coupled inductance L_{eq}. If this is not the case the dynamic resistance calculated using equation 25 is no longer valid at 125 kHz, but at the new resonant frequency. The change of transponder inductance due to the coupled primary circuit was calculated and showed less than 0.1 % variation for all couplers (table 5.3). Inspection of equation 20, which gives the primary-coupled inductance, shows that when $R_1 = 50\Omega$, as used during measurement, the denominator is dominated by R_1^2 since $(\omega L_1)^2 << R_1^2$, and therefore the approximate relationship $L_{eq} \propto L_1^2$ is true (assuming constant secondary inductance). Since primary inductance is created using only a single turn[12] the coupled inductance is greatly reduced compared with a similar system in which several primary turns were used. Equation 25 is therefore sufficiently accurate in calculating the dynamic resistance (and condition for power matching) since the resonant frequency is not appreciably altered by the primary circuit.

The method used here for calculating transponder power and voltage for various R_L could be used to assess the effect of primary circuit elements on transponder operation by including them in the secondary referred coupled impedances. The problem is then reduced to a simple Thevenin equivalent circuit that contains all circuit properties.

---

[12] In fact, it could be argued that $N_{primary} < 1$, since the return wire (typically the neutral wire) may lie some distance from the coupler.

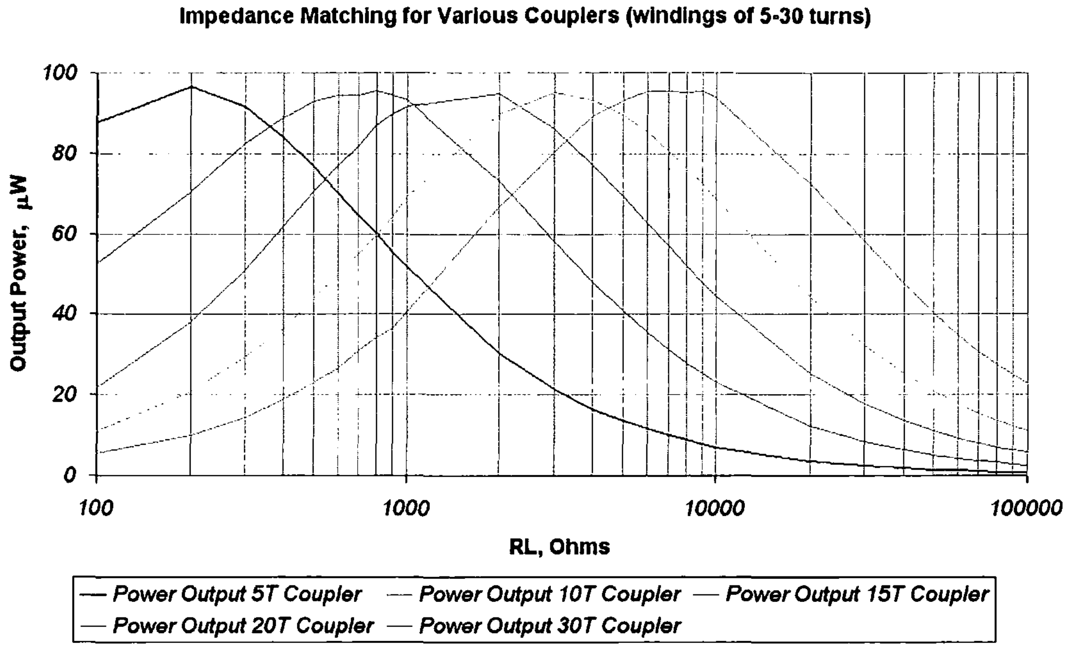

Figure 5.21. Graphs of measured transponder power versus chip load, R_L

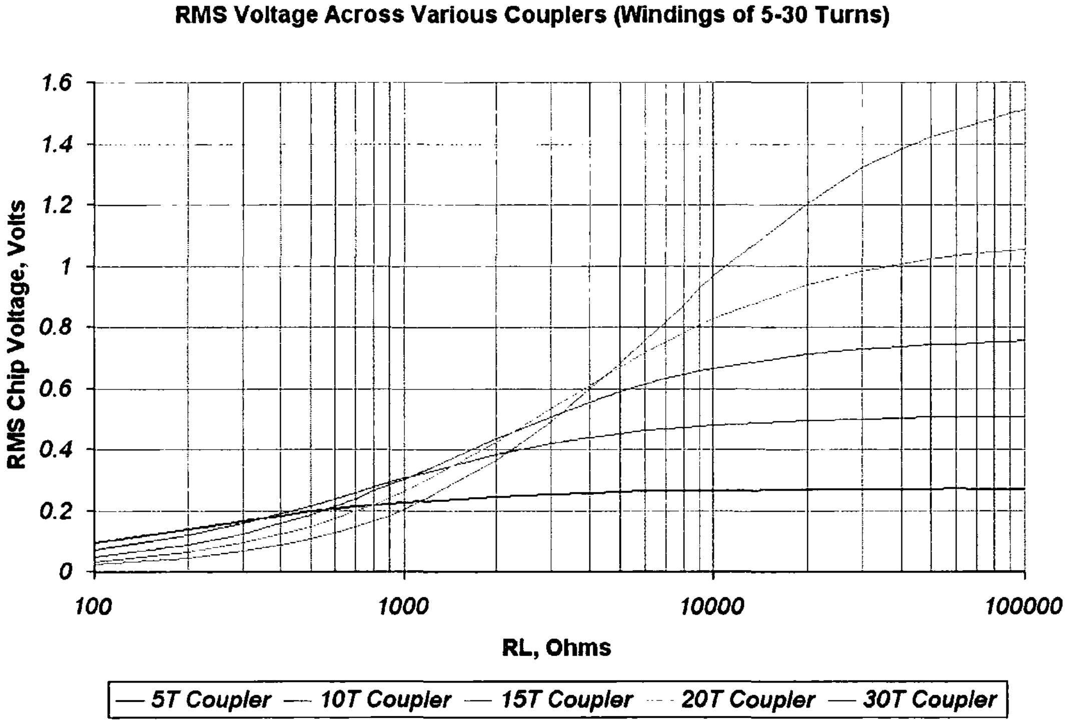

Figure 5.22. Graphs of measured chip voltage versus R_L

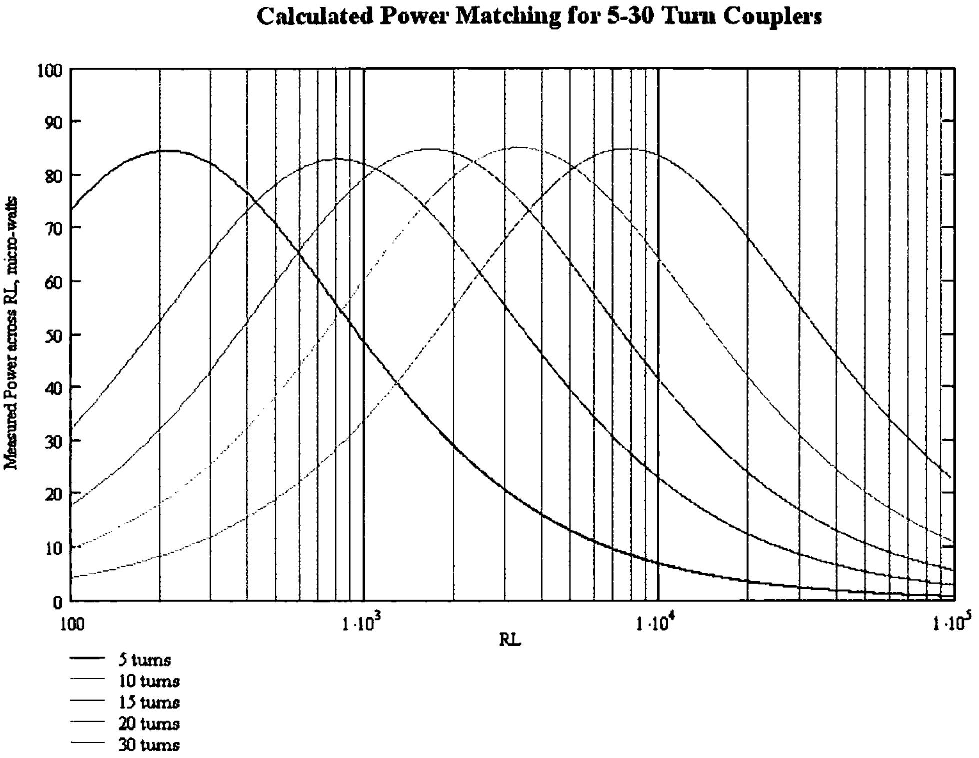

Figure 5.23. Theoretical power transfer characteristics

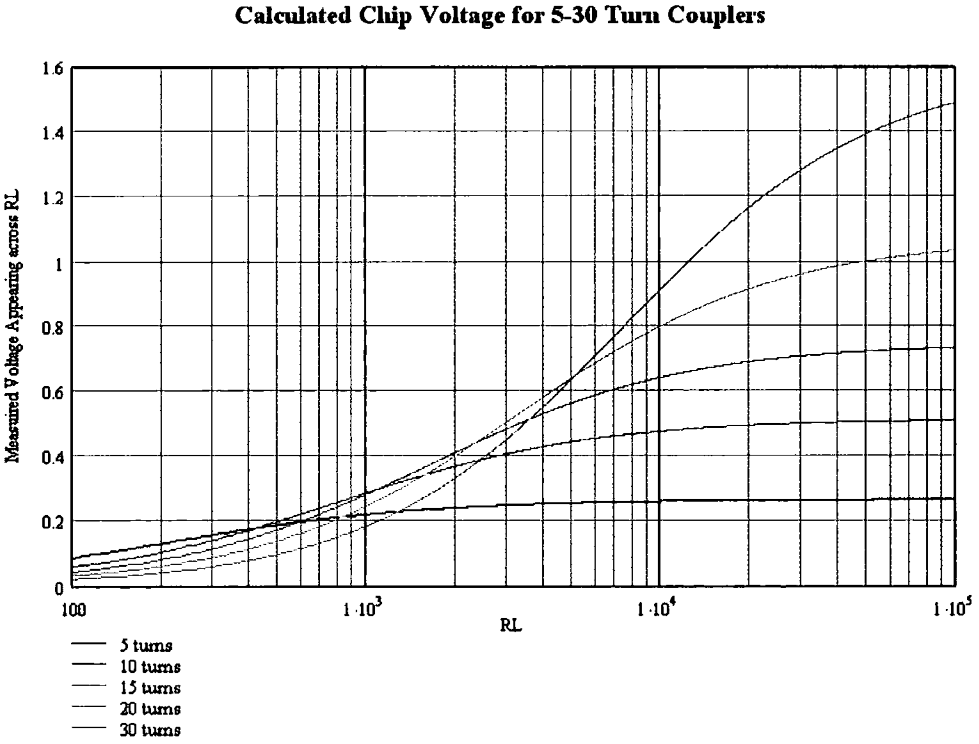

Figure 5.24. Theoretical chip voltage characteristics

5.8 Optimal Conditions for Direct-Load Modulation

We have already seen that transponder dynamic resistance is influenced by the coupler circuit parameters in a fashion described by equation 10. When the transponder wishes to convey information to the interrogator, it does so by altering R_L (the chip resistance) causing variation in its own dynamic resistance. This occurs virtually instantaneously since the interrogator and transponder are inductively coupled; the transponder effectively forms an extension to the interrogator circuit. These perturbations must be sensed by the interrogator in order to retrieve the sent information.

In contrast to the secondary-referred circuit used in the previous section a *primary-referred* equivalent circuit is used to investigate direct-load modulation sensitivity. This method is useful for calculating the small variations of primary circuit impedance caused by modulation of the coupled transponder impedance, which was described by equation 13. The coupled transponder impedance appears as an additional series impedance in the interrogator circuit, although an equivalent parallel coupled impedance could also be used. The parallel equivalent impedance would appear across the primary inductance, L_1, and would be calculated using equation 22.

5.8.1 Non-Resonant Primary

We consider the circuit shown in figure 5.25(a) in which the coupler is simply attached to the cable and a resistor is connected across the secondary winding terminals. Adopting the series coupled impedance given by equation 13 we may calculate the total primary impedance using the following expression:

$$Z_{primary} = R_g + j\omega L_1 + \frac{\left(\omega k\sqrt{L_1 L_2}\right)^2}{R_2 + j\omega L_2 + \dfrac{R_L}{1 + j\omega C_2 R_L}} \qquad (26)$$

which is similar to equation 14 except for the omission of primary capacitance. Note that the primary cable is assumed to be sufficiently short that distributed inductance, capacitance and resistance are ignored. Direct-load modulation occurs by variation of R_L in equation 26. Several couplers were used in the primary circuit of figure 5.25(a) and the primary impedance measured by an impedance analyser[13]. Modulation was simulated by choosing two values for R_L similar to those generated by the Philips Hitag 1 transponder (see section 4.2.1.). The chosen values were 100 kΩ and 1 kΩ. Impedance data gathered earlier (see section 4.4.2) was used to evaluate equation 26 to produce analytical figures for comparison with the measurements. The resulting primary impedance characteristics are shown in figure 5.26., which shows the magnitude of primary impedance for each coupler connected to the simulated modulator loads. The reactive component of the primary impedance was very small in comparison to the real component of impedance. The analytical and measured curves show good agreement. The primary resistance retains a reasonably constant value of 9 - 10 ohms when the modulator is OFF (R_L = 100 kΩ), and steadily reduces according to the number of winding turns when the modulator is ON (R_L = 1 kΩ). This graph shows the fundamental load modulation mechanism in which the coupled impedance is used to directly alter the primary impedance.

An alternative analytical approach may be used to explain the difference in the curves shown in figure 5.26: we can calculate the coupled impedance using the alternative parallel form given by equation 22. The dynamic resistance of the coupler is estimated in the form of that given by equation 10 which is the equivalent impedance appearing

---

[13] Agilent 4294A Impedance analyser. Instrument settings were: 100-200 kHz range, 50 mV Voltage Source, Bandwidth Level of 4.

across the secondary winding inductance at resonance. This is then transformed by the coupler turns ratio to an equivalent primary impedance using equation 23.

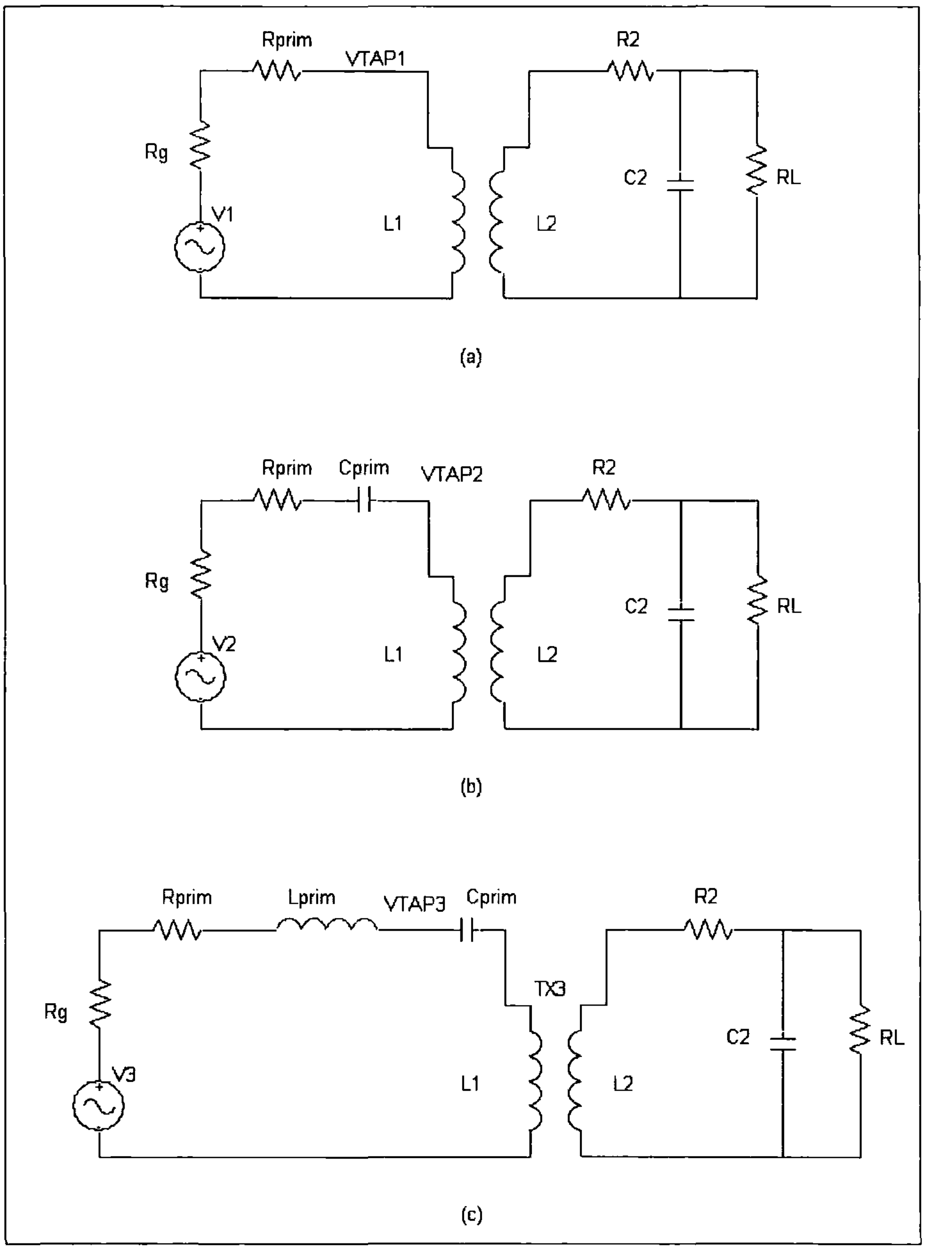

Figure 5.25. Three embodiments of cable RFID circuit. (a) non-resonant primary, (b) typical proximity RFID circuit and (c) high sensitivity circuit.

The effect of imperfect coupling could be included, but in this case the idealised relationship between turns ratio and inductance ratio is no longer valid. However the following approximate relationship derived by MacFadyen can be used [MacFayden]:

$$Z_{coupled} \cong \left(k\frac{N_1}{N_2}\right)^2 R_{dynamic} = \left(\frac{k}{N_2}\right)^2 R_{dynamic} \quad (N_1 = 1) \qquad (27)$$

This relationship is accurate for transformers with superimposed windings, in which case leakage flux lies between primary and secondary windings. Evaluating equations 10 and 27 resulted in the approximate theoretical curves shown in figure 5.26 , which are compared with measured impedance. This result confirms that the primary coupled impedance may be approximated by transformation of the secondary dynamic resistance according to the turns ratio as given by equation 27.

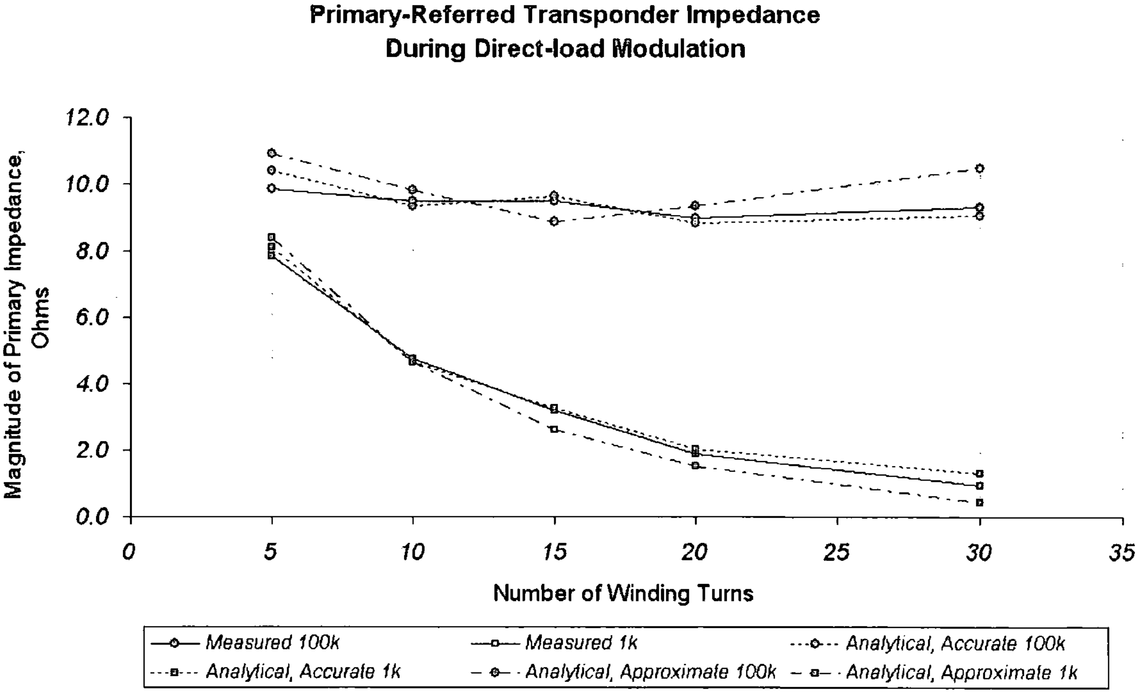

Figure 5.26. Analytical and measured direct-load modulation characteristics using non-resonant primary, showing effect of number of winding turns and modulator resistance.

5.8.2 Sensitivity Enhancement by Non-Coupled Resonant Primary

Inspection of figure 5.26 shows that when using the non-resonant primary load-modulation impedance varies by only a few ohms. Considering that transponder ASICs are likely to posses smaller variations of R_L during load modulation, this does not constitute a highly sensitive modulation mechanism. Furthermore, it is difficult to sense such impedance variations directly, particularly when the generator source impedance is likely to exceed the maximum variations of coupled impedance.

The circuit was modified by placing a non-coupled series resonant circuit in the primary circuit as shown in figure 5.25(c). This has three important benefits. The first is the creation of a resonant voltage that is highly sensitive to variations of coupled impedance. Note however that since this resonant circuit is not directly coupled to the transponder, that is, flux does not link between the primary inductor and the coupler, critical coupling issues are avoided. Critical coupling effects occur when two resonant circuits both possessing high quality factors are coupled together, with the result that transponder current is severely dampened by mutual interaction of the circuits. The occurrence of critical coupling depends on the individual circuit quality factors and the coupling coefficient, and is discussed further in chapter 7. The second benefit brought by using a primary resonant circuit is that primary current is maximised at the operational frequency, thus increasing the induced transponder voltage as given by equation 15. The third benefit is a degree of noise suppression brought to the system by the band pass filter characteristic of the resonant circuit.

A fundamental disadvantage of using a resonant primary is that sensitivity to direct-load modulation becomes dependent on losses in both primary and secondary circuits. This occurs because the resonant voltage VTAP3, shown in figure 5.25(c), is used to sense perturbations in the primary circuit impedance and is equal to the generator voltage multiplied by the circuit Q. Therefore losses in the circuit cause a reduction in the magnitude of VTAP3 and, most importantly, inhibit the *change* of VTAP3 in response to transponder load modulation.

To test this proposition a test circuit was assembled that allowed variation of the primary and secondary Q by resistive pots (see figure 5.27). Primary resonance was created using a variable inductor (L_{prim}) set to an inductance of 577 μH and a 2.8 nF capacitor (C_{prim}). Maximum secondary Q occurs when coupler winding resistance is minimised (this was measured to be 55.8 Ω using a 20-turn coupler) and when $R_L \to \infty$. Secondary circuit Q was determined by inserting additional resistance between L_2 and C_2. Line current was provided by a digital line driver as used in the prototype interrogator described in chapter 7. As described in chapter 7 the line driver must be protected against over-current by placing a resistor in the primary circuit. The maximum primary Q was therefore determined by combination of limiting resistor (20 Ω), driver resistance (3.5 Ω), coupler loss (145 mΩ) and primary inductor loss (6.7 Ω), giving 30.3 Ω total primary loss at 125 kHz. Variation of the magnitude of VTAP3 was then measured for modulation resistor values of 100 kΩ and 1 kΩ as the primary and secondary losses were increased. The resulting sensitivity plot is shown in figure 5.28 which shows that the maximum VTAP3 modulation level (11.8 V) occurs when the primary and secondary losses are minimised. This plot also shows that, for the circuit considered, deviations in primary resistance close to the minimum value produces a greater change in sensitivity than deviations in secondary resistance. Of course this outcome is dependent on the resistances used in the modulator but since the values used are indicative of real transponder modulators, this is an important observation.

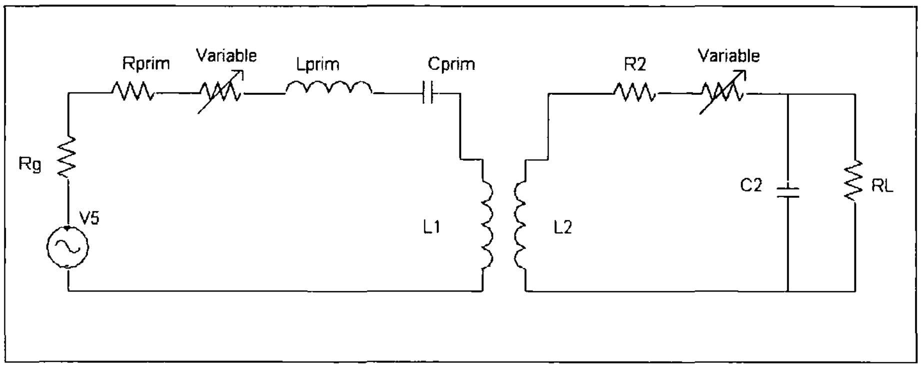

Figure 5.27. Placement of variable resistors for direct-load modulation sensitivity investigation

To generalise the problem of sensitivity to direct-load modulation, a primary-referred model was derived using equation 18 and noting that VTAP3 may be calculated using the following equation:

$$VTAP3 = I_{line}\left(Z_{coupled} + j\left(\omega L_1 - \frac{1}{\omega C_{prim}}\right)\right) \tag{28}$$

where I_{line} is given by:

$$I_{line} = \frac{V_{in}}{R_{prim} + j\left(\omega\left(L_1 + L_{prim}\right) - \frac{1}{\omega C_{prim}}\right) + Z_{coupled}} \tag{29}$$

$Z_{coupled}$ is given by equation 13. Equation 28 was then used to calculate voltage modulation using from:

$$\Delta V = \left|VTAP3\left(MOD\_ON, R_{primary}, R_{secondary}\right) - VTAP3\left(MOD\_OFF, R_{primary}, R_{secondary}\right)\right| \tag{30}$$

were *MOD_ON*, *MOD_OFF* represent the state of R_L. Note that the coupling coefficient was set as 0.9. The resulting plot is shown in figure 5.29, showing good agreement with the measured result. Equation 30 can therefore be used to calculate the expected modulation sensitivity and may be altered to accommodate alternate choices of coupler or transponder.

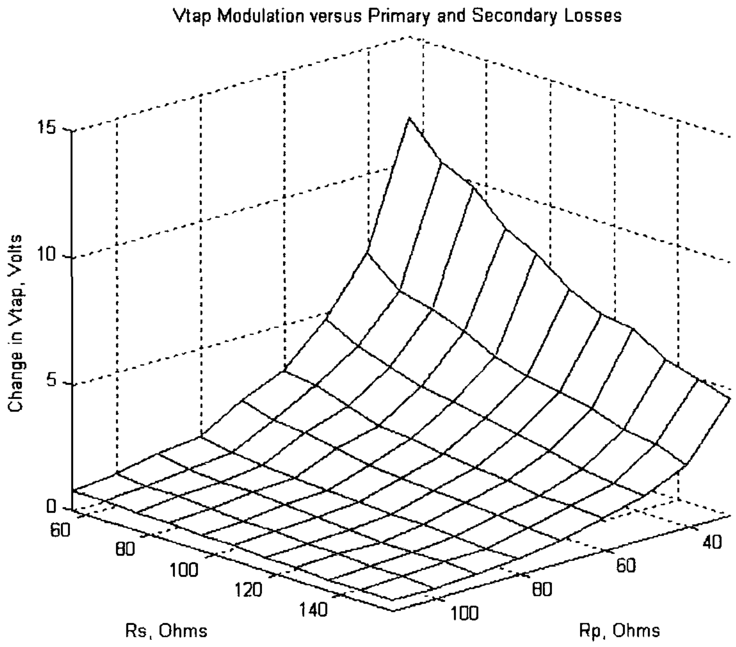

Figure 5.28. Measured direct-load modulation sensitivity to primary and secondary circuit losses

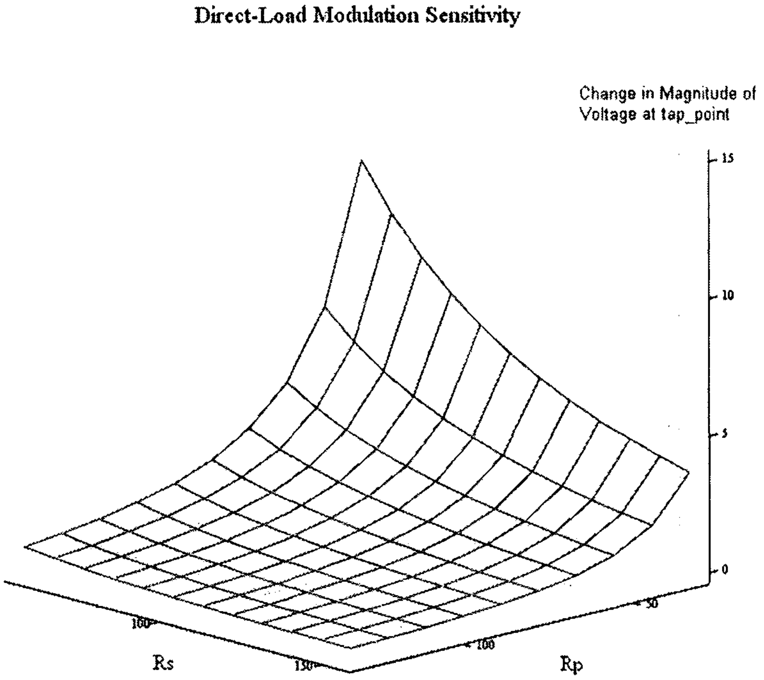

Figure 5.29. Theoretical direct-load modulation sensitivity to primary and secondary circuit losses

5.8.3 Comparison

The advantage gained by using a resonant primary can be seen by comparing the extent of VTAP modulation for each of the circuits shown in figure 5.25. In Figure 5.25(b) a capacitor has been included in the primary circuit which resonates with the coupler primary inductance. This circuit is analogous to the standard proximity RFID method, in which the primary and secondary resonant circuit are inductively coupled. However since the primary inductance is composed of a single turn in cable RFID the primary inductance is considerably smaller than that found in proximity interrogators. The resulting primary Q is extremely low; around 1.3 in the circuit analysed here, and little advantage is had over the non-resonant approach. For the circuit in figure 5.25(b) the required primary capacitance was 0.96 μF.

Each circuit was simulated to evaluate the modulation of VTAP in response to load modulation. The ratio of modulator ON to modulator OFF resistance is described by a factor, η, which is given by:

$$\eta = \frac{R_L(Modulator\_ON)}{R_L(Modulator\_OFF)} 100\% \qquad (31)$$

For example the nominal modulator values of 1 kΩ (ON) and 100 kΩ (OFF) yield $\eta = 1\%$. The secondary impedance, $Z_{secondary}$, in equation 13 then becomes:

$$Z_{secondary} = R_2 + j\omega L_2 + \frac{\frac{\eta}{100} R_L}{1 + j\omega C_2 R_L \frac{\eta}{100}} \qquad (32)$$

The results are shown in figure 5.30 in which the factor η varies between 1 % and 100 %, and the primary resistance is either minimised or given the value 100 Ω. Secondary loss is unaltered. Clearly sensitivity reduces as η decreases for every circuit as would be expected since this is the source of load modulation. It is apparent that, due to low circuit *Q*, circuits (a) and (b) are virtually identical; there is no benefit in resonating directly with the coupler inductance. We see also that the performance of circuit (c) is strongly dependent on the primary losses, as found in the previous section, and that gains in sensitivity compared with circuits (a) and (b) diminish as these losses increase.

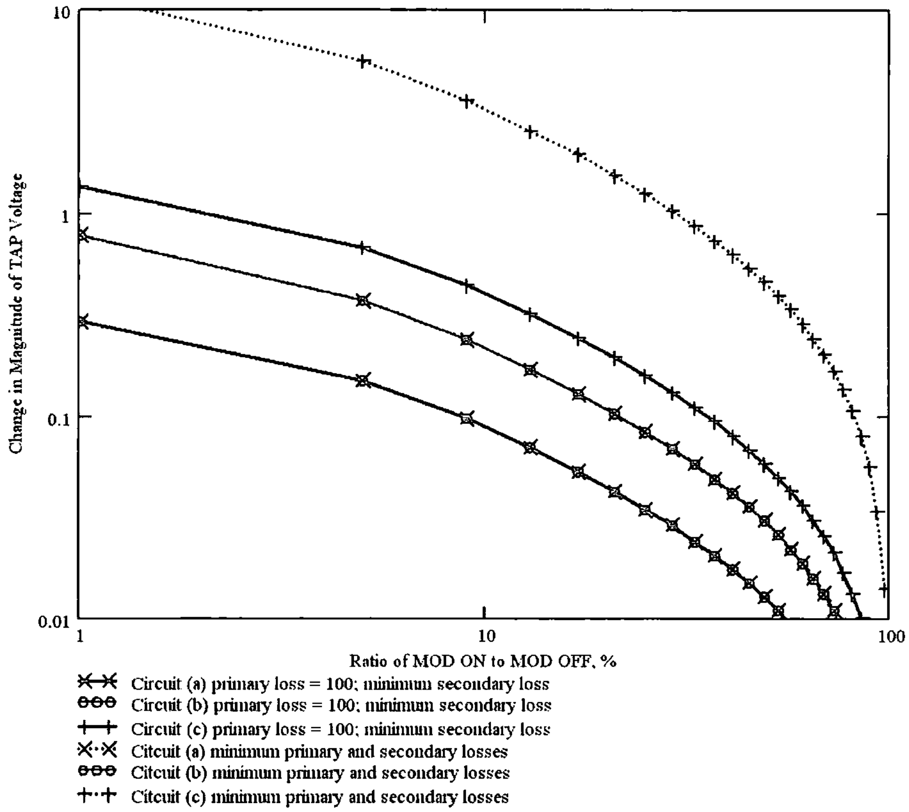

Figure 5.30. Sensitivity of primary circuit to load modulation at transponder for various primary circuit configurations.

5.8.4 Discussion

Clearly circuit (c) in figure 5.25 offers the highest sensitivity to load modulation and is therefore the optimal method of those considered here. This method is however sensitive to the primary and secondary *Q*. Another advantage of circuit (c) is that sufficiently high VTAP voltages may be generated such that amplification of the signal before detection is not required. In fact, as described in chapter 7, it is necessary to *reduce* the magnitude of VTAP3 before feeding to the detector as the measured voltage reached was around 90 volts (peak).

5.9 Existence of Null points in Load Modulation

A common problem encountered in proximity RFID is loss of the load modulation signal at the detector due to interaction between the primary (interrogator) and secondary (transponder) resonant circuits which, when offsets in circuit tuning exist, can introduce phase modulation of the carrier rather than the intended amplitude modulation. Tuning offsets commonly occur as a result of tolerance limits on winding inductance but may also manifest as variation of capacitance. A static ASK detector would not be able to detect phase modulation and complete failure would occur. In most cases a combination of amplitude and phase modulation occurs due to tuning offsets which must be compensated for by adjusting the detector characteristic such that it is optimally configured to detect the same degree of amplitude and phase modulation. Fundamental similarities between proximity and cable RFID coupling means that the same effect is seen in cable RFID, and similar measures must be taken to optimise performance. In this section modulation of the primary tap point voltage is calculated in the presence of primary and secondary tuning offsets. Implementation of an adaptive detector is described in section 7.7, chapter 7.

Variation of the primary tap point voltage which forms the detector input (see figure 5.19) is calculated using the circuit equations developed in section 5.6. Tuning offsets may be caused by errors in either resonant capacitor or inductor (or both) and was measured by variation of capacitance since capacitor losses are more stable. In contrast, variation of inductance would require adjustable ferrite cores which tends to produce high variability of equivalent ESR of the inductor depending on the ferrite position [Snelling]. Transponder impedance is found by expanding the denominator of equation 13:

$$Z_{\mathrm{secondary}}(C_2) = \frac{\dfrac{R_m R_L}{j\omega C_2}}{R_m R_L + \dfrac{1}{j\omega C_2}(R_m + R_L)} \tag{33}$$

Referring to figure 5.18, $R_L = 100k\Omega$ represents the transponder chip resistance with the modulator OFF and R_m the chip resistance with modulator ON. The function variable is the transponder capacitance, C_2. We may then calculate the line current and tap point voltage by assuming that capacitor C_{prim} is grounded (see figure 5.25 (c)):

$$I_{line}(C_2, C_{prim}) = V_{in}\left(R_{prim} + j\left(\omega(L_{prim} + L_1) - \frac{1}{\omega C_{prim}}\right) + \frac{\left(\omega k\sqrt{L_1 L_2}\right)^2}{Z_{\mathrm{secondary}}(C_2)}\right)^{-1}$$

$$V_{tap\_point}(C_2, C_{prim}) = \frac{I_{line}(C_2, C_{prim})}{j\omega C_{prim}} \tag{34}$$

Finally, the change in tap point voltage is calculated by varying R_m between infinity (open-circuit) and the modulator value, assumed to be 1 kΩ, giving a modulator OFF / ON resistance ratio of 100/1:

$$V_{\mathrm{modulation}}(C_2, C_{prim}) = V_{tap\_point}(C_2, C_{prim})\Big|_{Rm=1k\Omega} - V_{tap\_point}(C_2, C_{prim})\Big|_{Rm=\infty} \tag{34}$$

The resulting behaviour is illustrated in figure 5.31, where the magnitude of tap voltage modulation is seen to reach a maximum when primary and secondary capacitance values are equal to their ideal resonant values (i.e. when the relationship $\omega = 1/\sqrt{LC}$ holds). If the capacitance is varied about the ideal values then modulation sensitivity reduces, becoming negative in some cases. A region of zero amplitude modulation exists on either side of the peak in figure 5.31 which marks points of communication failure. The corresponding phase variation of tap voltage is shown in figure 5.32, where positive and negative peaks are seen on either side of the peak of amplitude modulation. These approximately correspond with the region of zero amplitude modulation as illustrated in figure 5.33 where the transponder is assumed to be perfectly tuned and the interrogator tuned state varies. Phase modulation is close to zero degrees at maximum amplitude modulation, while amplitude modulation is small at peaks of phase modulation. The characteristic was confirmed by measuring the amplitude of the analogue detector output voltage in an operational cable RFID system (see chapter 7 for a description of the interrogator). It was assumed that the detector output amplitude is linearly dependent on the amplitude modulation of tap voltage, which is the input to the detector. These measurements were recorded during interrogator-transponder communication using the Philips Hitag 1 transponder. An ID number request was repeatedly issued by the interrogator and the transponder replied by direct-load modulation (figure 5.34). The allowable range of primary and secondary capacitance is limited by the necessity to maintain sufficient transponder voltage for operation. The approximate range is indicated by a white rectangle in figure 5.31. It is clear that similar behaviour is observed by the system and that adaptive demodulation is required at the detector. Simulation and measurement Z values (amplitude in volts) are different because measurements were taken at the detector output whereas simulation values relate to the detector input signal. As described in section 7.7, chapter 7, an adaptive amplitude-phase detector can be matched to the angle of load modulation (i.e., the relative amount of amplitude and phase modulation) to produce a strong base band signal, even when amplitude modulation vanishes.

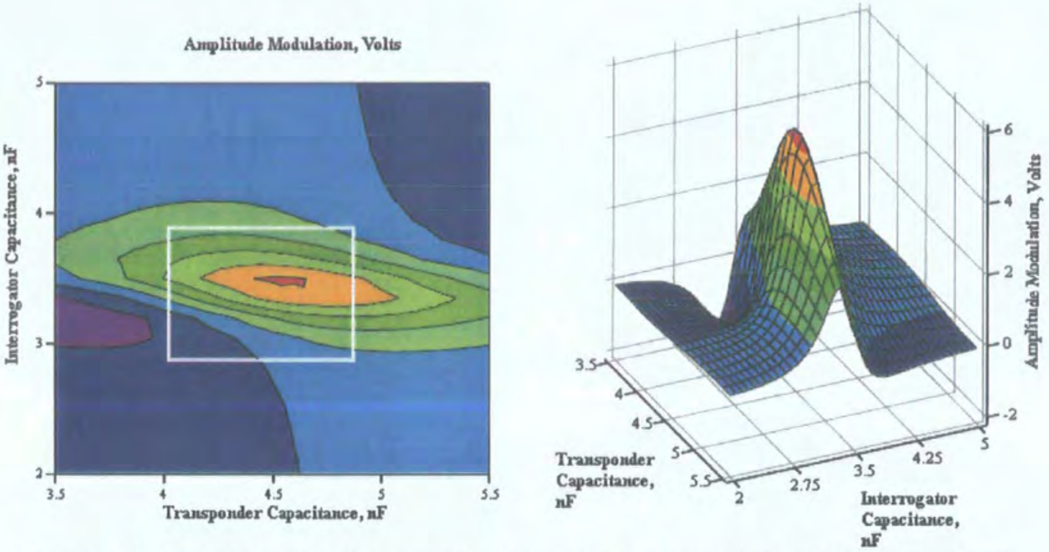

Figure 5.31 Simulated amplitude modulation of detector voltage due to direct-load modulation at transponder, showing peak modulation sensitivity when primary and secondary capacitances are optimally tuned to respective inductances. White rectangle indicates measured range (see figure 5.34).

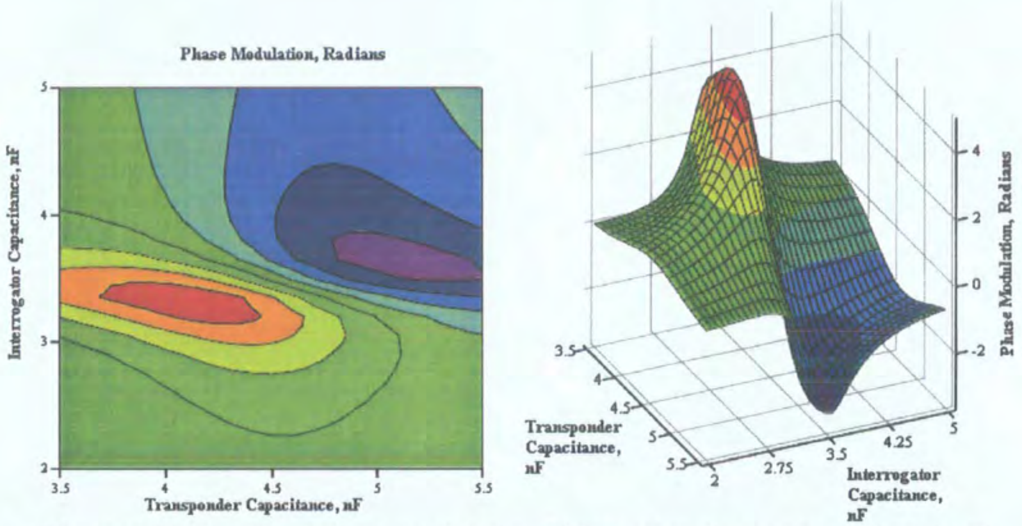

Figure 5.32 Simulated phase modulation of detector voltage due to direct-load modulation, showing two peaks of opposite sense.

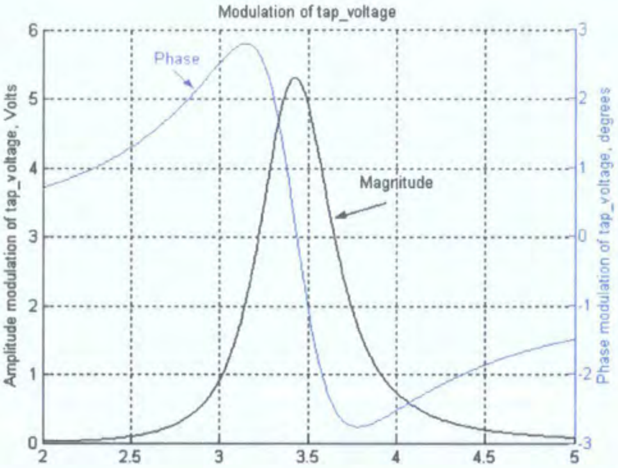

Figure 5.33 Amplitude and phase modulation of detector voltage as a function of interrogator capacitance due to direct-load modulation. Transponder is ideally tuned (transponder capacitance is 4.7 nF).

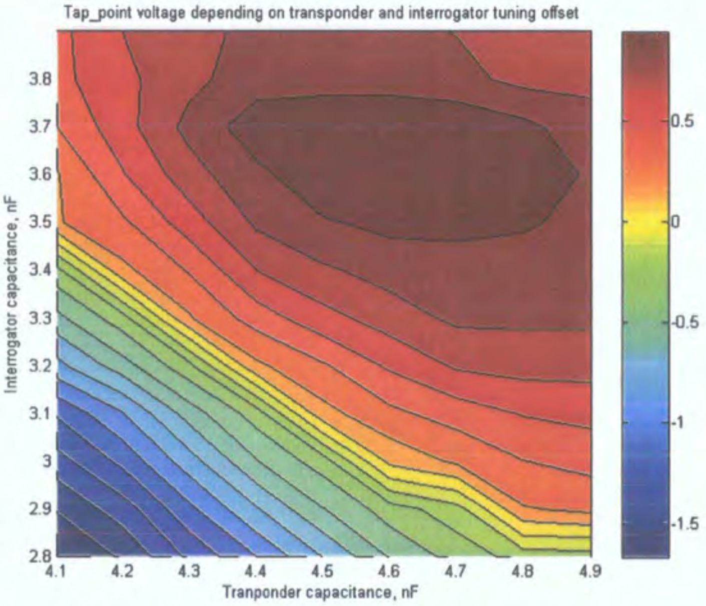

Figure 5.34 Measured amplitude modulation of detector output voltage in operational cable RFID system, showing region of maximum sensitivity and region of zero amplitude modulation.

5.10 Implementation

An experimental coupler has been used during this work comprising a simple split ferrite core design with plastic case. Although appropriate for the purposes of characterising the electrical properties of the inductive communication system, applications suitable for this coupler are limited to those in which fitment is possible at manufacturing time. This has potential benefits for high volume electrical goods because the transponder may be fitted to the electrical power circuit without requiring galvanic connection to the power circuitry. Galvanic connection would most likely require redesign of the power circuits to accommodate the device, followed by compliance testing. The inductive coupler would instead be fixed to the live or neutral wire inside the casing. This would maintain the status of the device as a separate component that could, in principle, be owned by the electrical test company and not the manufacturing company. As a result, the control of IP and specific data stored in the transponder could be maintained by the test company to ensure data security and compatibility with test equipment.

An alternative form of the inductive coupler was conceived in which the transponder is miniaturised to the extent that it may be placed within the standard electrical fuse (figure 5.35). The electrical fuse is the only removable part of a consumer appliance that provides direct access to the live wire (and hence common-mode current) and is therefore the optimal point at which to place the inductive transponder. It is believed that such an arrangement would provide a facility for retro-fitment of transponders in older host appliances. The concept of a transponder-enabled fuse has been developed using a small ferrite bead manufactured by MMG-Neosid[14]. This has an initial permeability of around 1000, and was found to be suitable for establishing a tuned coupler for use with the Hitag 1 RFID transponder. When considering core-miniaturisation it should be remembered that capacitance must be applied across the winding terminals to achieve a tuned circuit and that the resulting capacitor element(s)

---

[14] Type 35-002-38

may constitute an appreciable proportion of the total available volume. The secondary copper winding and transponder chip die also consume space.

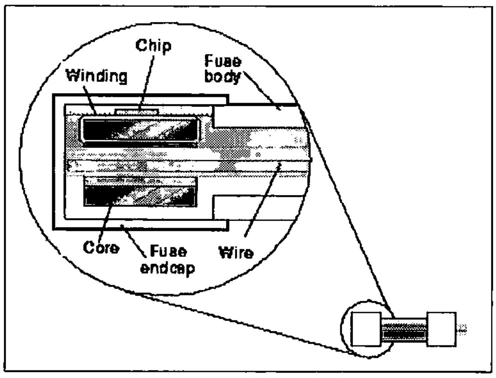

Figure 5.35 Placement of transponder in standard electrical fuse.

5.11 Summary

In this chapter an inductive coupling mechanism was devised that permits passive direct-load modulation to occur across an appliance power cable. An alternative direct coupling mechanism was investigated but produced insufficient mutual inductance. Circuit analysis was used to derive primary and secondary referred equivalent circuits, which were then used to find power transfer and load modulation characteristics supported by the coupler design. A simple, low-cost design was desirable and the coupler comprises a minimum of components (ferrite core, winding, external capacitor and transponder IC). Furthermore, it is designed to operate with commercial load-modulation ICs that are exclusively used in the low-power RFID applications considered in chapters 3 and 4. This ensures compatibility with RFID interrogators following providing some modifications of the interrogator transmit circuit are carried out. Sensitivity to direct-load modulation was enhanced by the use of a resonant circuit that is not coupled to the transponder secondary. This arrangement is sensitive to interrogator and transponder Q and nulls can appear in the load modulation pattern when tuning errors occur. Nulls may be eliminated by the use of an adaptive phase detector, as described in chapter 7. It is also shown in chapter 7 that decoupling of the primary resonant circuit and transponder inductance prevents the onset of critical coupling, which can occur when primary and secondary circuit losses become small. Due to the expected variation of primary cable impedance in the intended applications (see chapter 6 and 9), elimination of critical coupling is of benefit to cable RFID.

In the next chapter it is shown that the appliance inlet filter may be utilised as a return path for the interrogator carrier current, permitting appliance identification via the power lead and thus creating an automated identification system for electrical safety testing procedures.

6 *Analysis of Complete Cable RFID System*

6.1 Introduction

In this chapter we consider the complete cable RFID system comprising RFID cable coupler, appliance power lead and appliance inlet filter. As stated in the previous chapter a return path must exist between live and neutral wires for the RFID current. An integral path is provided for by the inlet filter attached to mains devices. Such filters have X-class capacitors fitted directly between live and neutral wires that provide attenuation of differential mode noise between the power line and appliance. The role assumed by the filter is illustrated in figure 6.1, where a transponder is placed around the power line conductor at an arbitrary position along the power cable.

To study the effects of power cable and filter on cable RFID performance a methodical analysis of the system is carried out, starting with characterisation of the primary-referred impedance characteristic of the RFID coupler in the frequency domain[15]. Typical EMC inlet filters are then characterised by measurement and modelling concluding with generalisations of filter characteristics relevant to the cable RFID approach. Finally the problem of long power cables is considered, where effects of resonance (standing waves) are analysed by adopting a transmission line model of the power cable. This model is solved by two approaches: a discrete transmission line model based on a technique described by Christopoulos [Christopoulos], and a frequency based transmission matrix approach. Conditions for minimum transmission line effects were found using this model.

---

[15] In the previous chapter, the primary-referred impedance was considered at fixed frequency.

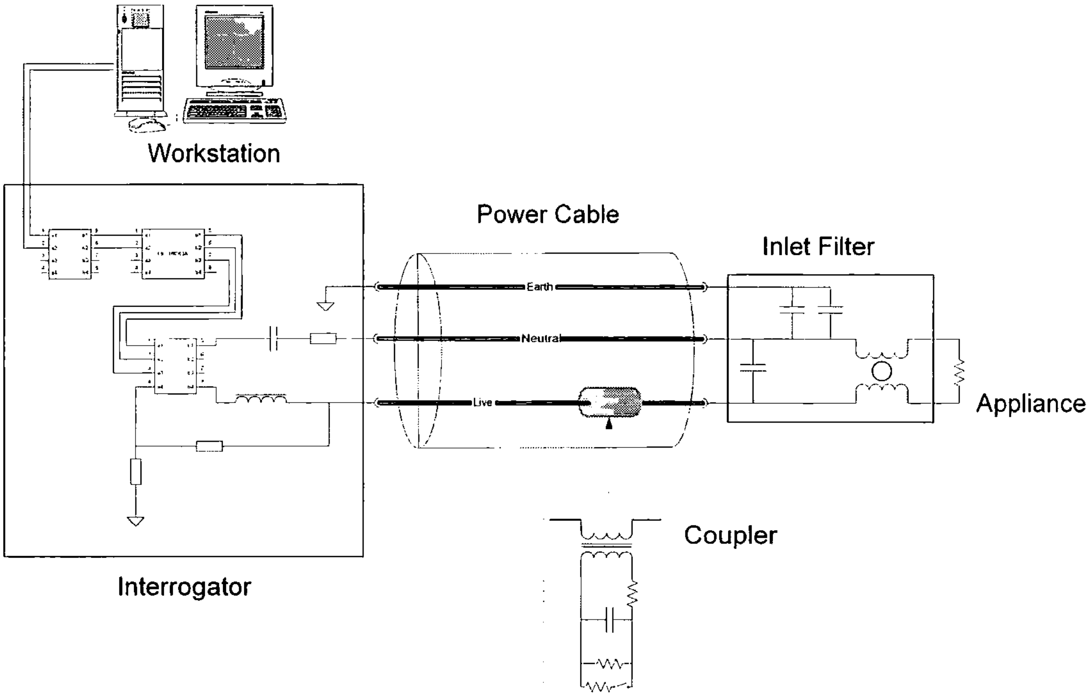

Figure 6.1 Illustration of complete cable RFID system showing location of RFID interrogator, DUT power cable, RFID transponder and mains inlet filter.

6.2 Primary-Referred Impedance in the Frequency Domain

In chapter 5 direct-load modulation performance was evaluated by analysing the primary referred impedance which included the coupled transponder impedance. In this section we study this impedance as a function of frequency with the aim of understanding the interaction between the coupled transponder and the mains inlet filter. We model the primary impedance by equation 26 of chapter 5 and include the high frequency cable resistance:

$$Z_{primary} = R_{total} + j\omega L_1 + Z_{coupled} \tag{1}$$

where $Z_{coupled}$ is given by equation 13 in chapter 5 and R_{total} is the sum of DC and AC losses. AC losses become important when the ratio of conductor radius to skin depth becomes greater than 4 at which point the AC resistance may be accurately determined by the following equation [Seshardi]:

$$R_{ac} = \frac{L}{2\pi a}\sqrt{\frac{\omega\mu_o\mu_{copper}}{2\sigma_{copper}}} \tag{2}$$

where L is the wire length in metres, a the wire radius, σ_{copper} the conductivity of copper which is assumed to be 5.8×10^7 Mhos/m and μ_{copper} is the relative permeability of copper which is assumed to be 1.

To confirm calculations, a coupler with 20 secondary turns was fixed around a short length of solid copper wire and the primary impedance measured by an impedance analyser across the frequency interval 10 kHz - 10 MHz. Distributed inductance and capacitance of the wire could be ignored here due its short length. The coupler secondary was made to resonate at 125 kHz by adding 2.8 nF capacitance to the winding terminals. The wire parameters were L = 7 cm and a = 0.37 mm[16]. The result of evaluating equation 1 is shown in figure 6.2 along with the measured magnitude and phase response. As the frequency is increased from 10 kHz to 10 MHz parallel resonance occurs at 125 kHz in the measured impedance with a corresponding reduction of phase through zero degrees. This was followed by series resonance at around 460 kHz accompanied by increasing phase. A similar trend was predicted by the analytical approach, except that series resonance was less pronounced and occurred around 90 kHz higher than by measurement. To check validity of the analytical approach, a spice model was created using the same model parameters, as shown in figure 6.3. The resulting curve is included in figure 6.2 and shows the same profile as the analytical approach. The spice model also confirmed that the inductive coupler could be adequately modelled by the lossy transformer component TX1. Differences between the measured and predicted series resonant characteristics can be attributed to modelling

---

[16] The copper wire had tin-coating which was removed at each end before attaching to the impedance analyser fixture.

of the secondary winding losses. The main components of secondary losses are winding resistance, hysteresis loss in the core and capacitor resistance. These components were regarded as a lumped quantity and measured at 125 kHz (the point at which parallel resonance occurs). In this instance the lumped resistance was 50.2 Ω. As frequency increases, losses in the secondary winding increase causing the magnitude of the coupled impedance to fall. During series resonance in the primary circuit the reduced coupled impedance causes the total impedance at resonance to fall. Equivalently, this can be seen in figure 6.2 where the measured phase response rises more steeply from $-\pi/2$ (loss less capacitive) to $+\pi/2$ (ideal inductive) which is synonymous with higher circuit Q[17].

---

[17] See p. 140 in Terman [Terman] for resonance curves showing this relationship.

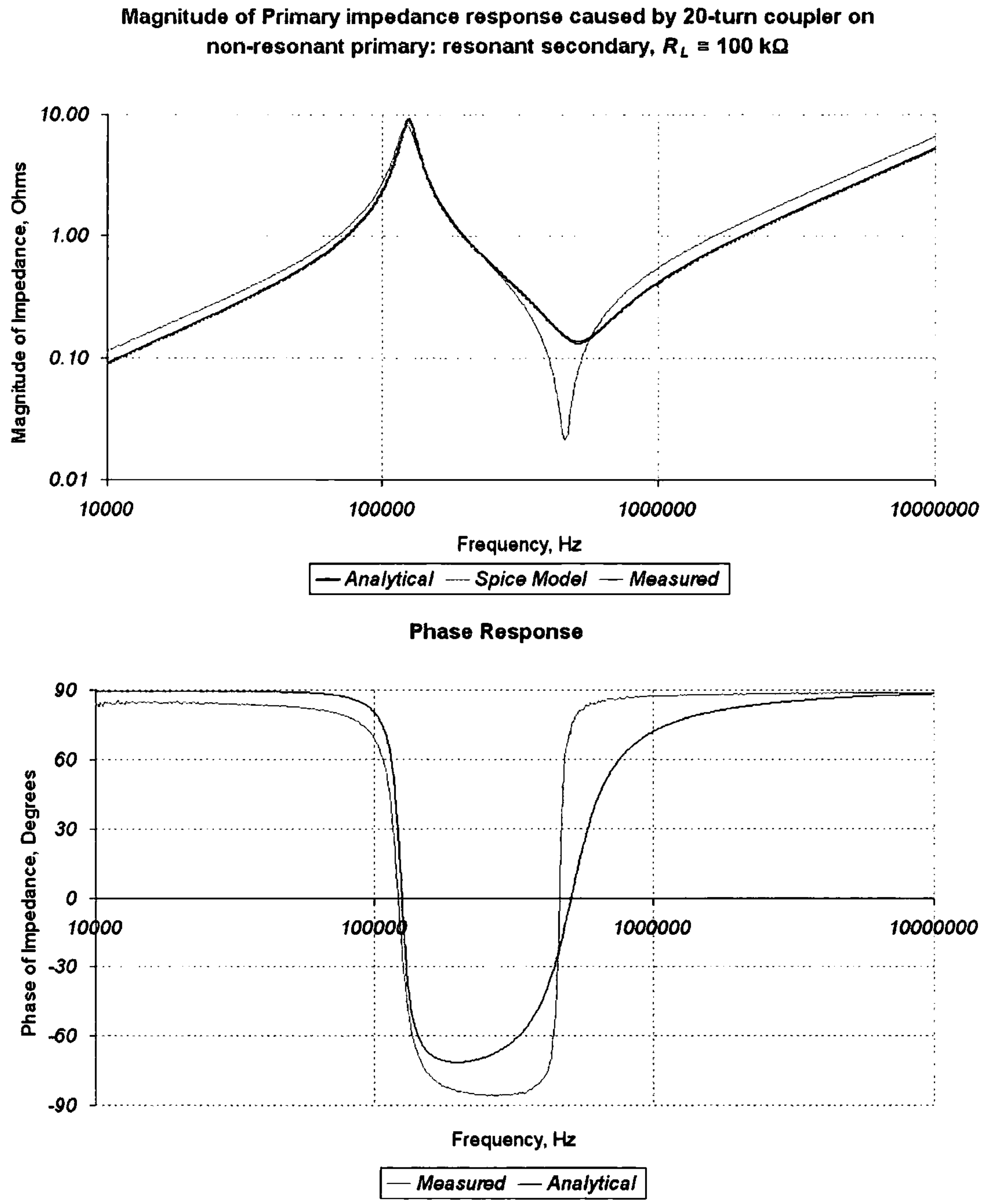

Figure 6.2 Magnitude and phase of primary-referred impedance caused by 20 turn coupler attached to short copper wire.

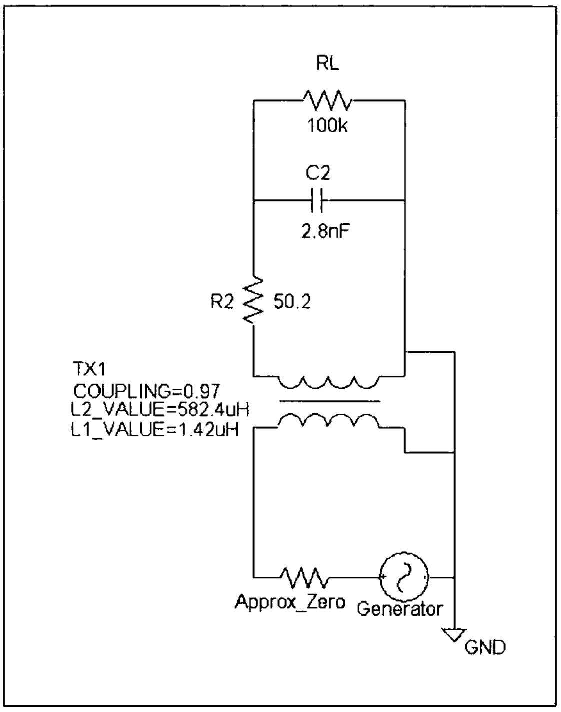

Figure 6.3 Spice model for calculation of impedance curve shown in figure 6.2.

6.2.1 Analysis of Resonant Effects

The resonant curve in figure 6.2 may be more clearly understood by inspecting properties of the coupled impedance. The coupled impedance, $Z_{coupled}$ was found in chapter 5 to be:

$$Z_{coupled} = \frac{(\omega M)^2}{Z_{secondary}} \tag{3}$$

where $M = k\sqrt{L_1 L_2}$ and $Z_{secondary}$ is the transponder circuit impedance given by:

$$Z_{secondary} = R_2 + j\omega L_2 + \frac{\dfrac{R_L}{j\omega C_2}}{R_L + \dfrac{1}{j\omega C_2}} \tag{4}$$

The impedance of a coupler having 20 secondary turns is compared with the total primary-referred impedance in figure 6.4, where it is seen that the coupled impedance dominates the total primary impedance at the dominant resonant point. If we limit our attention to frequencies close to the dominant resonant frequency (125 kHz here), the coupled impedance may be approximated as a parallel RLC circuit. By plotting the phase response of $Z_{coupled}$ (figure 6.5) the characteristic of parallel resonance is clearly seen as the phase decreases through zero degrees from $+\pi/2$ to $-\pi/2$, remaining capacitive thereafter. However we see from the magnitude response (figure 6.4) that the coupled impedance does not retain the characteristic of classical parallel resonance (which returns towards zero impedance above the resonant frequency) but rather shows increasing impedance above the resonant frequency. Departure from the parallel circuit equivalence is caused by frequency dependencies of the real and imaginary components of $Z_{coupled}$.

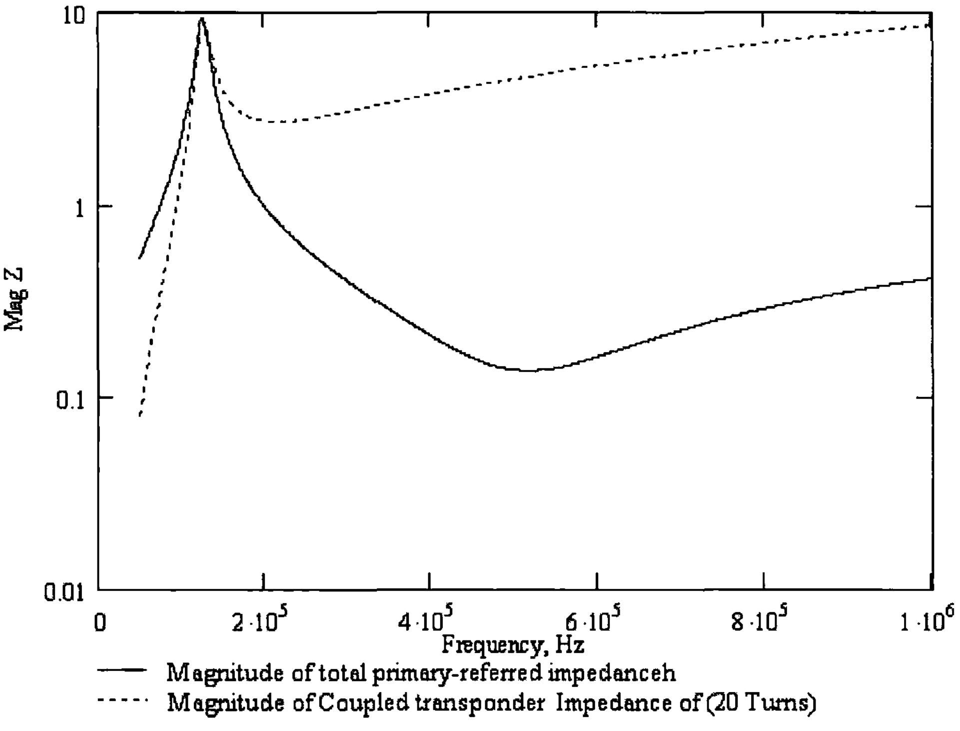

Figure 6.4 Comparison between magnitude of coupled impedance and total primary impedance (20 turn coupler)

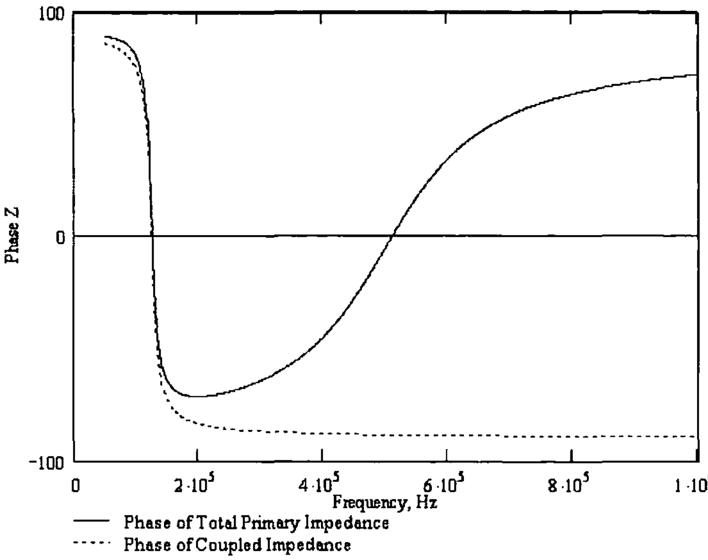

Figure 6.5 Phase response of coupled impedance (20 turn coupler)

The most important parameter of interest here is circuit reactance which may be used to explain both resonant points seen in figure 6.2. In figure 6.6 three reactance curves are compared: the total primary reactance, the coupled reactance and the inductive reactance of the coupler primary. We see that resonance occurs at two points (indicated by dotted vertical lines) where the inductive reactance is neutralized by the capacitive reactance of the coupled impedance.

As mentioned above, the lower resonant point (close to 125 kHz) is of parallel type. The coupled reactance reaches zero degrees before the total primary reactance and therefore resonance occurs when the coupled reactance becomes negative and equal to the inductive reactance of the primary inductance. To illustrate this, a magnified version of figure 6.6 is shown in figure 6.7. Although the interaction between coupled and primary impedance would appear to be in the form of series resonance, the decreasing phase of the coupled impedance dominates and creates parallel resonance.

At the second resonant point (at around 500 kHz) the coupled reactance resonates once again with the primary reactance, but since the phase of the coupled impedance is no longer decreasing rapidly series resonance occurs. This causes the phase of the total primary impedance to increase while the coupled impedance phase remains close to $-\pi/2$.

The coupler may therefore be approximated in the primary circuit by an equivalent parallel RLC circuit for frequencies near parallel resonance, which dominates the primary impedance. However this equivalent circuit does not hold for higher frequencies, where resonance occurs for a second time, this time in series form between the coupled impedance and primary inductance.

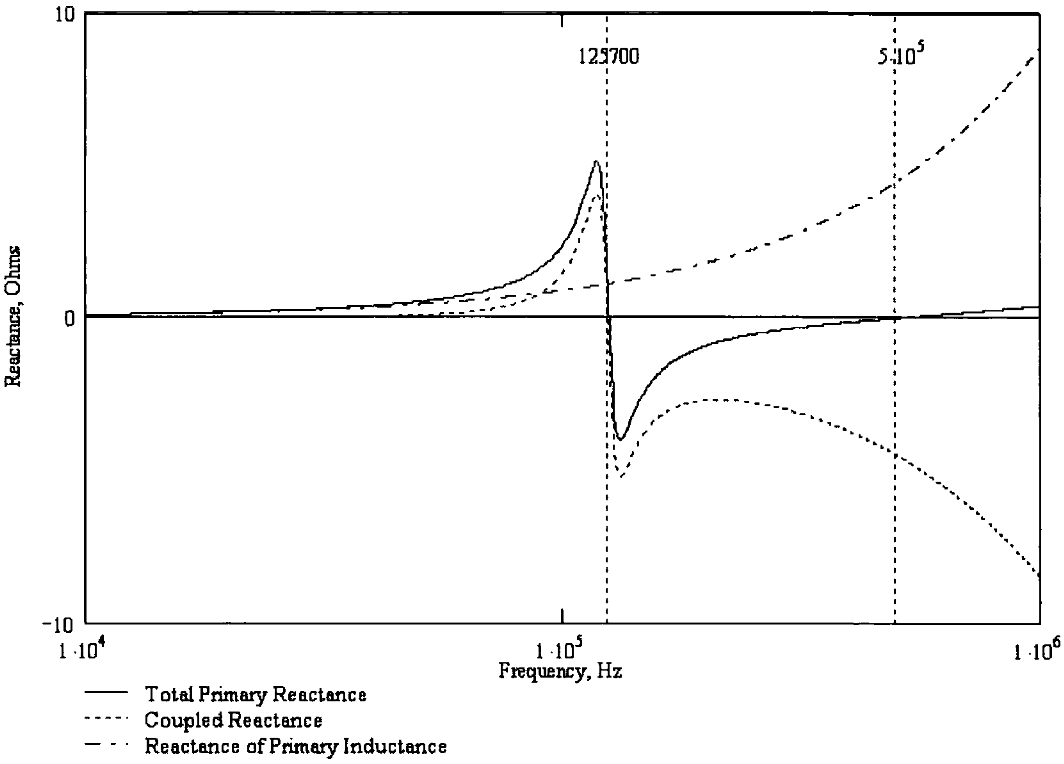

Figure 6.6 Reactance curves for total primary circuit, coupled impedance and primary inductance (20 turn coupler)

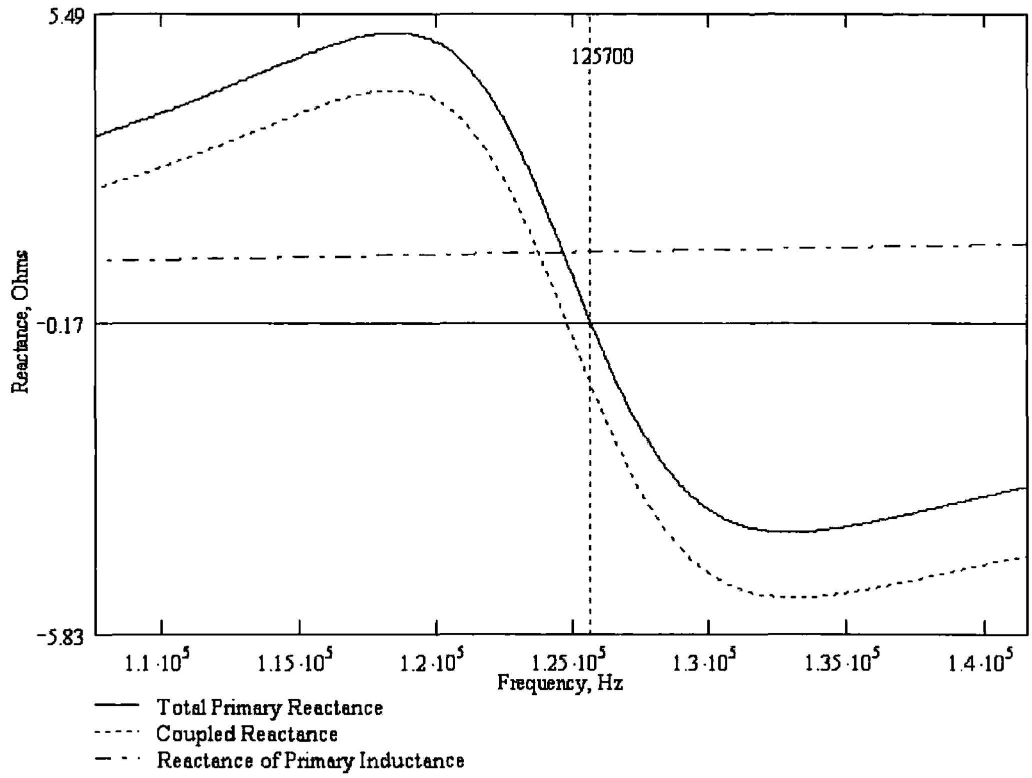

Figure 6.7 Close up of reactance curves showing resonance at 125 kHz.

6.3 Inlet Filter Characterisation

The inlet filter depicted in figure 6.1 is designed to attenuate differential and common mode noise between the power line and appliance [Williams]. Inlet filters must attenuate high frequency produced by the appliance to reduce power-line emissions. Emission limits are imposed by EMC standards such as European EMC standard EN 50081 [EN50081], which requires measurement of conducted emissions from 150 kHz to 30 MHz. The power line is simulated by connecting an artificial mains network[18] according to EN 55022 [EN55022]. A degree of immunity to mains-borne noise is also provided by the inlet filter. Generic European EMC standard EN 50082 [EN50082] requires conducted RF immunity testes between 150 kHz and 100 MHz.

---

[18] Often called a Line Impedance Stabilization Network (LISN).

A detailed circuit representing the typical inlet filter is shown in figure 6.8. Differential noise is attenuated by X-class[19] capacitors C_{x1} and C_{x2}, which have a typical capacitance of 0.1 μF. These capacitors have significant lead inductance and series resistance. Common mode noise is attenuated by a common mode choke and Y-class capacitor[20]. Capacitors C_{y1} and C_{y2} are ideally identical and divert common mode current to ground with a few thousand Pico farads. It is assumed that they do not play an role in the operation of cable RFID systems since the RFID signal is differential mode. Additional common-mode attenuation is provided for by two current compensated inductors that pose high impedance to common-mode currents and ideally zero impedance to differential currents since both windings are wound on a common core such that flux due to differential currents cancel. In reality, leakage inductance exists due to restrictions on the minimum spacing between the two inductor windings as dictated by the high voltage rating. If the core saturates it is no longer capable of common-mode attenuation. Resistor R_1 is sometimes included with a value of a few megaohms that encourages discharging of C_{x1} thus preventing hazardous voltages from remaining at the input terminals.

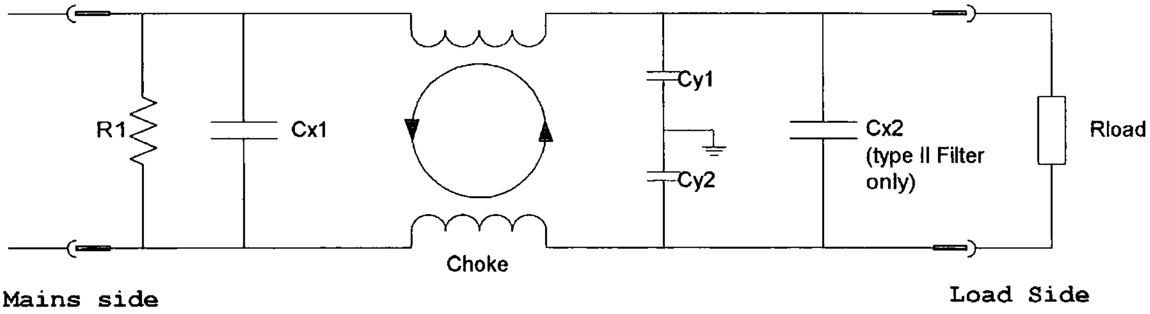

Figure 6.8 Generalised inlet filter equivalent circuit

---

[19] X-class refers to capacitors which must withstand continuous mains level voltage across their terminals. Failure of this component posses a fire hazard.

[20] Y-class capacitors carry the same burden as X-class capacitors, but with the additional risk of electrical shock on failure.

The influence of the inlet filter on cable RFID communication is characterised by finding the impedance presented to the RFID circuit by the filter under different load conditions. In many cases, capacitor C_{x2} is not used which significantly alters the filter characteristics under extreme loading conditions. The worst case operating conditions occur when R_{load} is either open-circuit or short-circuit, since filter resonance is maximised under these conditions. Short-circuit conditions should never occur in correctly-functioning appliances because they must be switched OFF while conducting electrical safety tests. However an appliance fault may have occurred since this results in a short-circuit condition across the filter load terminals. It is imperative that this does *not prevent automatic identification prior to testing.*

To investigate the ramifications of open and short circuit conditions for cable RFID, equivalent circuits were derived that describe the behaviour of two types of inlet filters. Type I filters do not posses capacitor C_{x2} and were represented by a Schaffner inlet filter, type FN 323-1/05. Type II filters do posses capacitor C_{x2} and were represented by a Delta Electronics EMI filter, type 06AK2D. A third filter was used that does not include C_{x2} or common-mode choke, as typically found in switched-mode power supplies. All filters posses an X-class capacitor fixed to the input terminals. A summary of filter component values is given in table 6.1.

Equivalent circuits that represent type I and II filters under open and short load conditions for differential signalling are shown in figure 6.9 where L_{cap} and R_{cap} represent the inductance and series resistance respectively of capacitor C_{x1}, and *choke leakage* represents the residual leakage inductance of the common-mode choke. Choke leakage inductance was measured as the series inductance across one inductor while the other was electrically shorted and is included in table 6.1. These circuits were validated by comparing spice simulations with measured data.

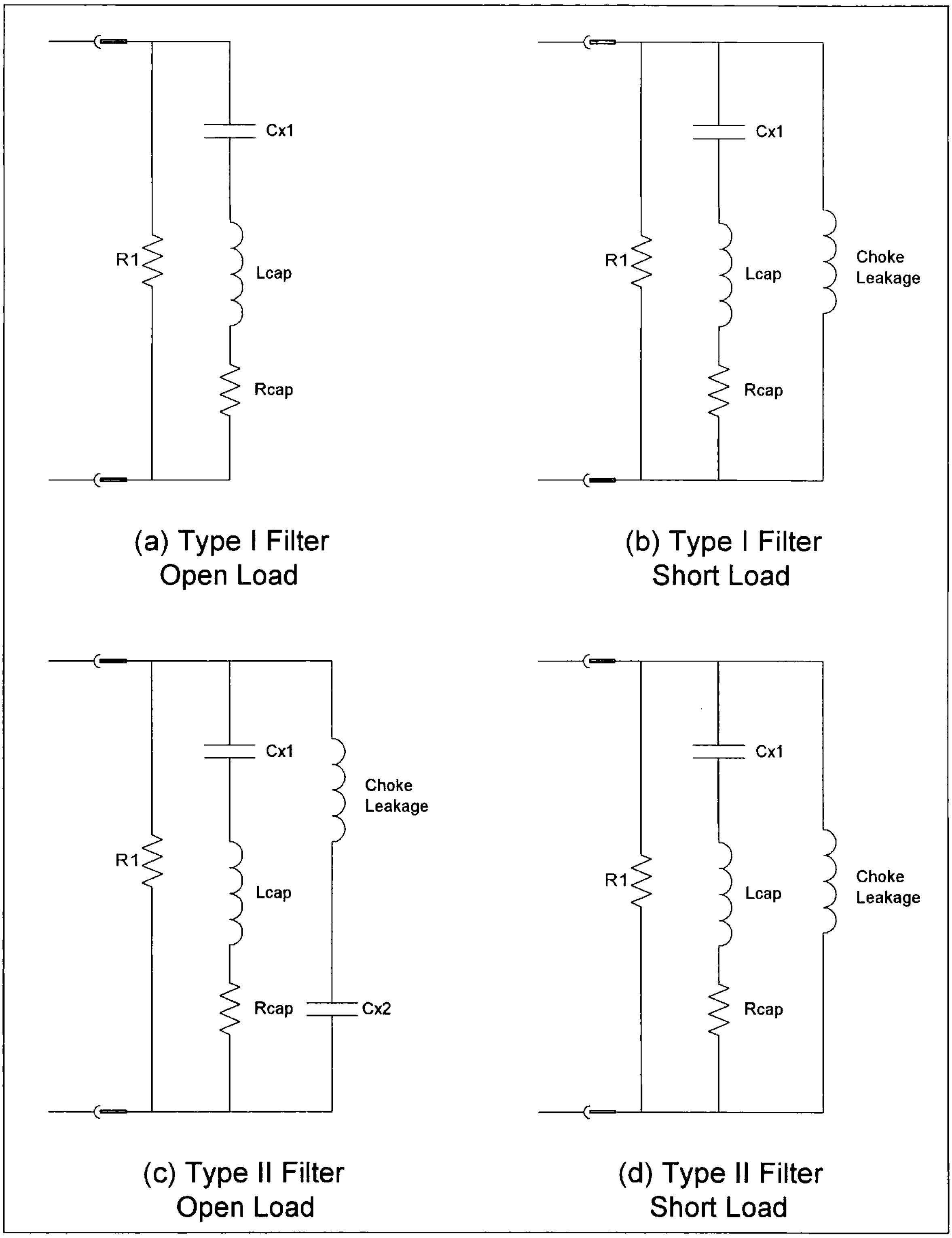

(a) Type I Filter Open Load

(b) Type I Filter Short Load

(c) Type II Filter Open Load

(d) Type II Filter Short Load

Figure 6.9 Equivalent Circuits for Type I and type II Inlet Filters (differential mode) under Open and Short Circuit Load Conditions

Parameter	Schaffner FN 323-1/05 (Type I)	Delta Electronics 06AK2D (Type II)	Switch Mode Power Supply Filter
C_{x1}	0.047 μF	0.1 μF	0.47 μF
C_{x2}	Not fitted	0.1 μF	Not fitted
R_1	Not specified	2.2 MΩ	910 kΩ
Choke Inductance	2 × 2.8 mH	2 × 1.3 mH	None fitted
Choke Leakage Inductance (by measurement)	30 μH	20 μH	-
C_{y1}	2200 pF	3300 pF	471 pF
C_{y2}	2200 pF	3300 pF	471 pF

Table 6.1 Filter parameters

Filter input impedance (as presented to the RFID circuit) was measured using an impedance analyser for various open and short-circuit conditions fixed to the load side (see figure 6.8). The attached load varied between open and short-circuit so that the maximum variation of filter impedance characteristics is observed. It is assumed that open-circuit conditions exist when the appliance is switched off as required during electrical safety testing. Short-circuit loads may occur when a fault exists in the appliance that causes a short condition between live and neutral lines. As can be seen in figures 6.10 and 6.11, filter characteristics for finite loads lie between those for open and short conditions.

Filter resonance occurs when the attached load approaches open or short conditions but is less prominent for loads near the typical nominal load impedance of 50 ohm[21] . Parallel resonance occurs close to the lower compliance range of each filter, around 150 kHz, and manifests between the differential capacitor (s) and choke leakage inductance. Series resonance occurs due to lead inductance in C_{x1} in both type I and II filters and is not dependent on the value of load connected. This is primarily due to the absence of

---

[21] The attenuation of inlet filters is normally specified using 50 ohm input and output resistances.

loading on the mains side of the filter; input impedance is measured with open input terminals. Additional series resonance occurs with the type II filter (figure 6.11) due to the lead inductance of capacitor C_{x2}. It is seen that this term is dependent on the value of load attached, appearing only when the attached load is of high resistance. The equivalent circuit for a type II filter with open load is shown in figure 6.9(c), where two series resonant circuits can be seen connected in parallel. Load R_L appears in parallel with C_{x2} (not shown) and therefore regulates series resonance between C_{x2} and the leakage inductance.

The equivalent filter circuits are useful in calculating the impact of inlet filters on cable RFID performance. They may be combined with the coupled transponder impedance described in section 6.2 to form a complete model. To validate the equivalent filter circuits spice circuit models were designed and evaluated (figure 6.12). Input impedance was calculated by the ratio of input voltage to current flowing through a small-valued resistor placed between the generator and filter. Parameters such as capacitor ESR and lead inductance were estimated by impedance measurement then refined to produce a close match to the measured impedance curves. Note that parameters of the real components are frequency dependent and therefore some deviation in the frequency domain is to be expected. The resulting simulation impedance curves are shown in figures 6.13 and 6.14 for type I and type II filters respectively. Comparing figures 6.10,6.13 and figures 6.11, 6.14, close agreement between simulation and measurement is seen after parameter refinement, confirming that filter behaviour may be modelled adequately using the equivalent circuits shown.

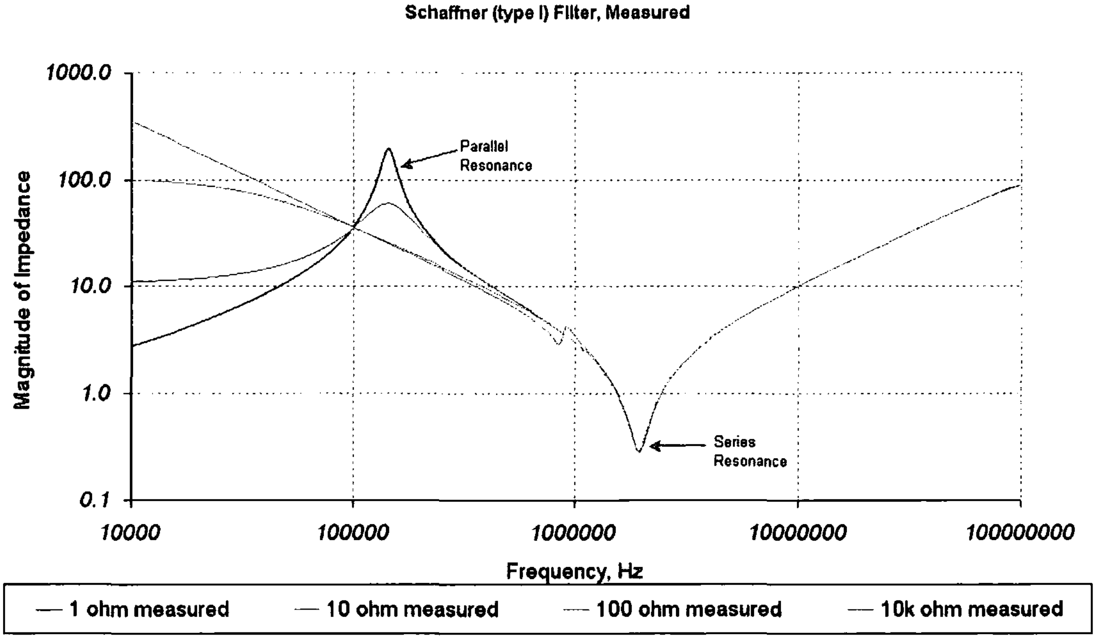

Figure 6.10 Measured input impedance response of Type I filter. Impedance measured at mains inlet side as various loads were attached to appliance side.

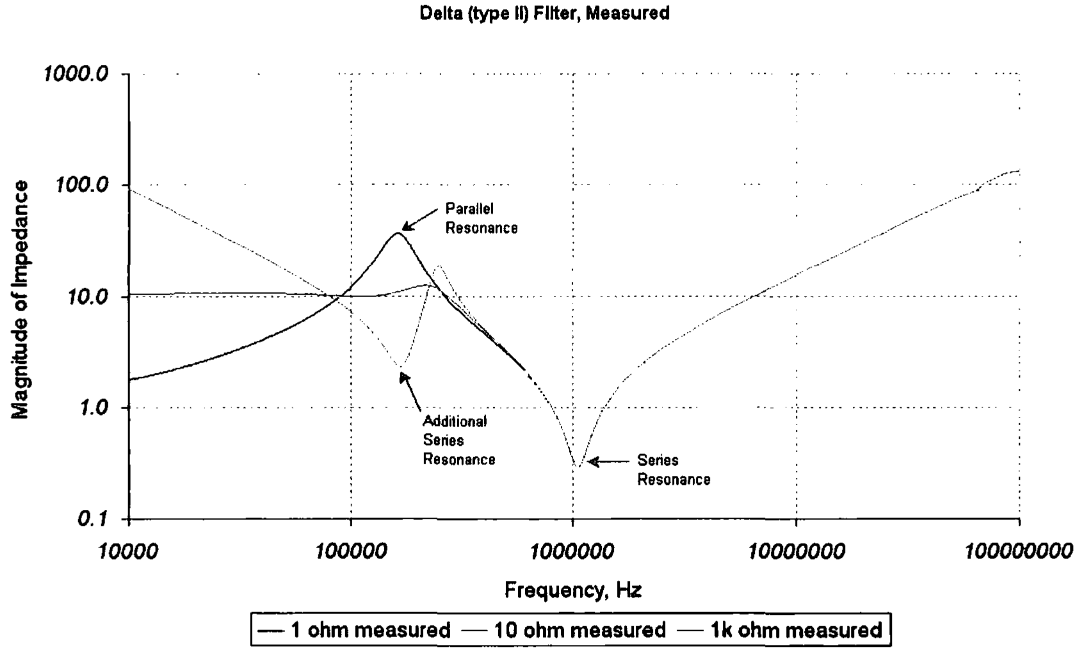

Figure 6.11 Measured input impedance response of Type II filter. Impedance measured at mains inlet side as various loads were attached to appliance side.

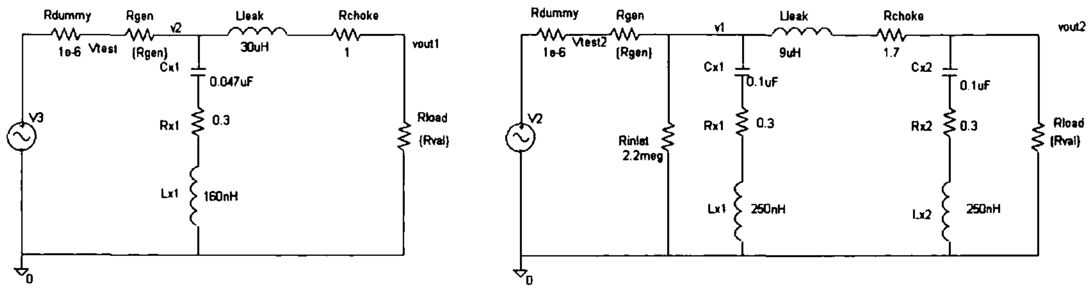

Schaffner Filter (Type I)

Delta Filter (Type II)

(a)

(b)

Figure 6.12 Spice model of Type I (a) and Type II (b) filters, showing equivalent circuit components and values

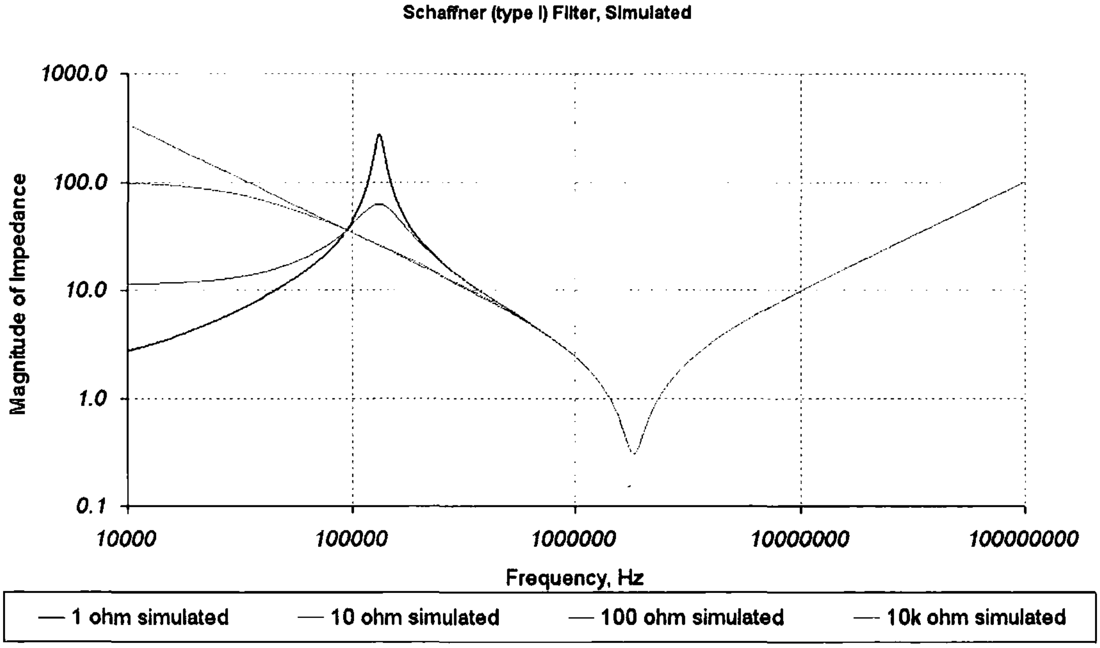

Figure 6.13 Simulated input impedance of Schaffner (type I) filter.

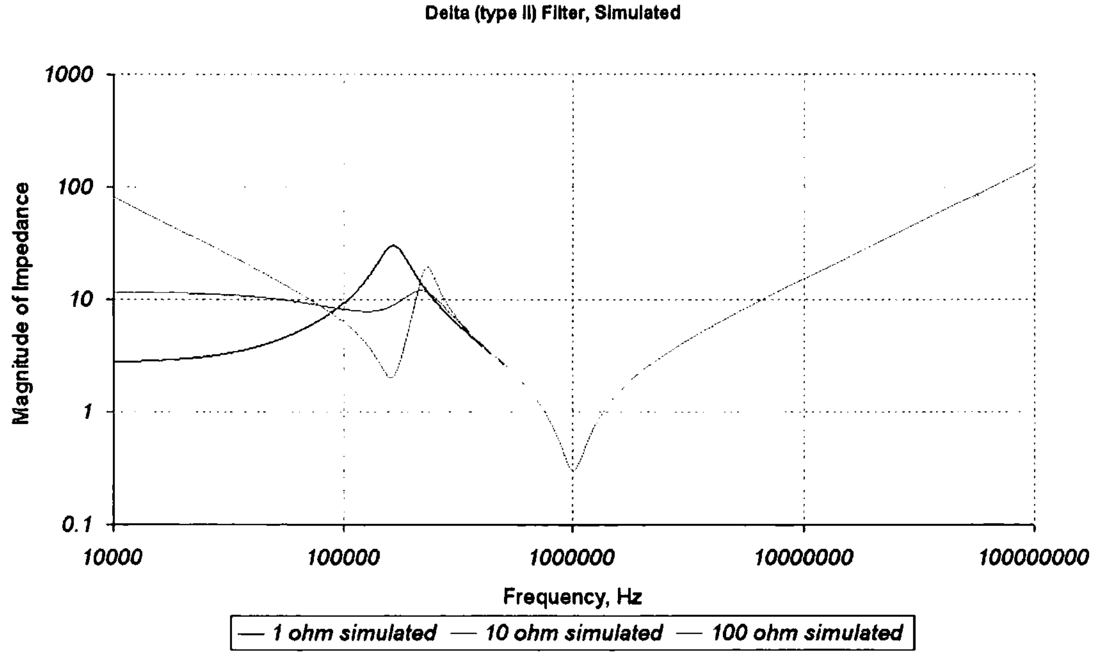

Figure 6.14 Simulated input impedance of Delta (type II) filter.

6.3.1 Other Filter Configurations

Additional elements may be present in some inlet filters. Typical components include voltage suppressors and additional differential line chokes that are intended to increase attenuation of differential or common mode interference, particularly in heavy-switching environments. Typical transient suppressors include voltage-dependent resistors, Zener diodes and gas discharge tubes. Filter input impedance would be affected by additional line chokes in that they further isolate loads connected to the load side from the input impedance, since the chokes appear after the inlet capacitor. This would not compromise the RFID cable performance and in fact the input impedance would be similar to those filters considered; only filter insertion loss would increase. Voltage suppressors would not become active for the low voltage cable RFID system, but may contribute to the total input capacitance.

6.4 Effect of Filter on RFID Circuit

In this section interaction between the coupled transponder impedance and inlet filter is analysed with the aim of establishing whether cable RFID is able to utilise the return path provided by the filter. The aim of cable RFID is to sense load modulation caused by the transponder coupled to the power cable using the circuit formed by the power cable connected to the DUT inlet filter. As discussed in chapter 5 load modulation manifests as small variations in the coupled transponder impedance and is sensed by the interrogator using a series resonant tank placed in the primary circuit. System evaluation was carried out by measuring the combined impedance of a power line attached to an inlet filter with a coupler fitted. Load modulation performance for various filter loads, primary circuit configurations and various inlet filters was then measured.

In the previous section is was observed that self-resonance of the inlet capacitor (C_{xI}) is independent of the resistance appearing at the load side of the filter. This is only valid while the input side is loaded by a generator of zero impedance. The effect of finite generator impedance is to dampen the resonant effects seen in figures 6.10 and 6.11, particularly with regard to self-resonance of the inlet capacitor (C_{xI}) as illustrated in figure 6.15. Considering the prototype interrogator described in chapter 7, generator losses include driver resistance, inductor losses and current limiter resistance, which typically combine to give between 30 Ohms and a few hundred Ohms total primary circuit loss. Relaxation of filter resonance improves sensitivity to direct-load modulation because perturbations in primary impedance are more predictable.

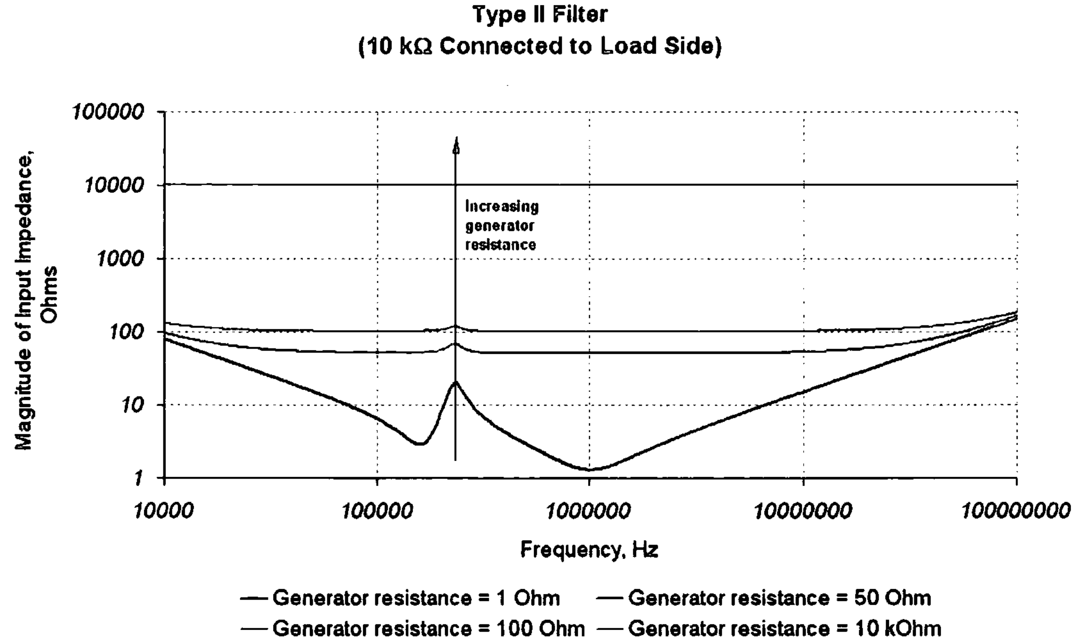

Figure 6.15 Effect of generator resistance on filter input impedance response simulated using PSpice model, showing reduction in resonant characteristics.

Direct-load modulation was measured for various filters attached to the power cable using a coupler with 20 secondary turns fixed around the live conductor. The transponder was placed approximately 10 cm from the inlet filter. In addition, a primary series resonant tank (as discussed in section 5.8, chapter 5) was included to assess its impact on load modulation. The circuit input impedance was measured using an impedance analyser connected to the cable plug. A typical graph is shown in figure 6.16, recorded using a type II filter, resonant primary circuit and open load attached to the filter load-side. The impedance response of the primary circuit is virtually identical regardless of the load attached to the coupler, except for the region close to the transponder resonant frequency. Note the onset of cable resonance above 10 MHz where the wavelength becomes comparable to the cable length. This effect is investigated later in section 6.5.4. A magnified view centred at this frequency (125 kHz) is shown in figure 6.17, where variation in the primary circuit impedance is clearly seen as the transponder load impedance varies. In this example the primary impedance varied by around 10 ohms due to load modulation, assuming a near-zero phase angle, which modifies the primary circuit Q by an amount given by equation 12, section 5.6.2, chapter 5. As discussed in section 5.8, chapter 5, actual variation of resonant tap-point voltage depends on initial primary and secondary circuit Q. In figure 6.18 primary resonance has been removed so that resonance occurs in the primary due only to the coupled impedance and filter impedance. Note that the coupled impedance now asserts resonance near 125 kHz which dominates over resonance between filter capacitor C_{x2} and the choke leakage inductance, producing a similar change of primary impedance as observed using primary resonance. This result highlights the fact that the use of primary resonance does not generally cause an increase in primary circuit modulation in response to transponder load modulation; it is designed to produce a highly sensitive resonant voltage whose variations may be easily sensed by the interrogator as described in section 5.8, chapter 5.

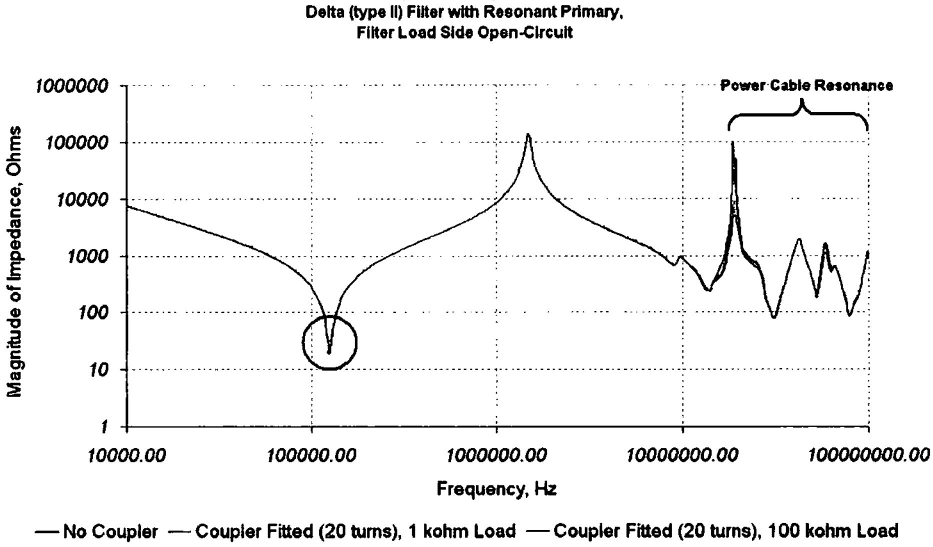

Figure 6.16 Impedance response of complete system during direct load modulation. System configuration: Type II filter with open-circuit at load side, resonant primary circuit. Circled region is magnified in figure 6.17.

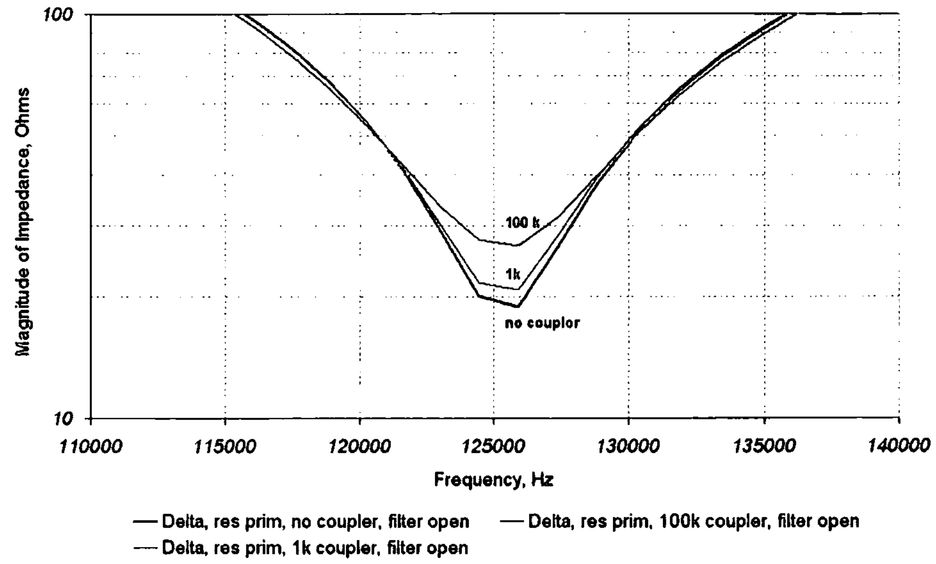

Figure 6.17 Enlarged portion of figure 6.16 at 125 kHz, showing effect of direct load modulation on primary impedance.

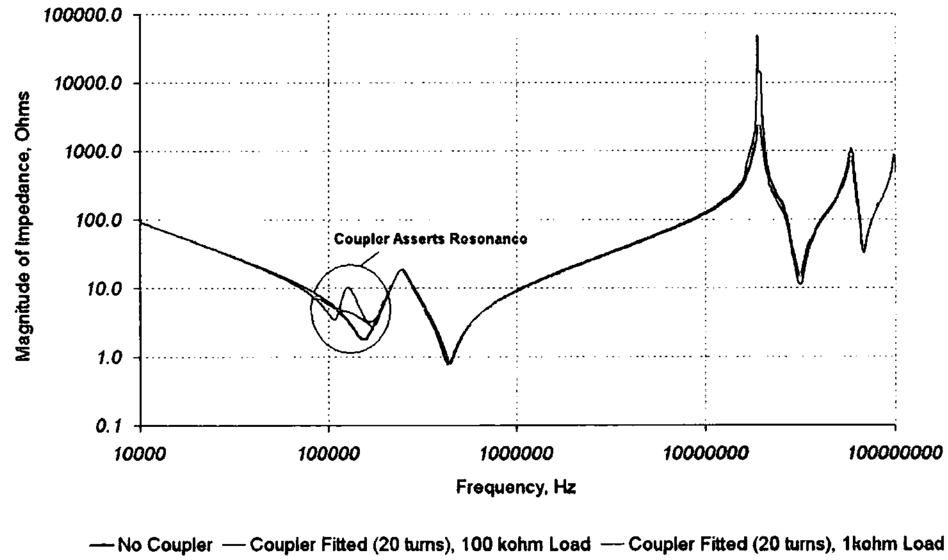

Figure 6.18 Second example of complete system response. Configuration: type II filter with open-circuit at load side, primary resonant circuit not present.

Several circuit configurations were investigated in the way described above: measuring changes in the primary impedance caused by transponder load modulation. Circuit combinations included three filter types (type I, type II and switched-mode power supply filters, the presence or absence of a primary resonant circuit and open or short-circuit conditions at the filter's load-side. The collated results are illustrated in figure 6.19, which shows variation in the magnitude of primary impedance achieved for each circuit combination and transponder loads of 100 kΩ and 1 kΩ. Load modulation was extrapolated at the transponder operating frequency of 125 kHz. For comparison, an idealised circuit is also included in which the filter is replaced by a simple electrical short, giving optimal signalling conditions. The dotted line shows percentage variation in the primary impedance caused by transponder load modulation. Interestingly, there is no specific optimal combination. For example, similar primary modulation is observed using a type II filter with open load side (point (a)) to that using no filter (point (b)), provided a primary resonant circuit is used. An important general trend is that primary impedance modulation is always greater while the filter is open-circuit (normal PAT test conditions) than short-circuit (appliance fault having occurred). Direct-load modulation is therefore more effective under open-circuit filter conditions.

Each circuit combination listed in figure 6.19 was tested under real conditions using a Philips Hitag 1 transponder chip attached to an IEC power lead. A prototype interrogator described in chapter 7 was used to perform ID read operations. It was found that communication was possible for all of the combinations considered above. In addition, excess primary resistance of up to 200 Ω could be tolerated. The addition of excess primary resistance causes a reduction in primary circuit Q, and therefore dampening of load modulation sensitivity.

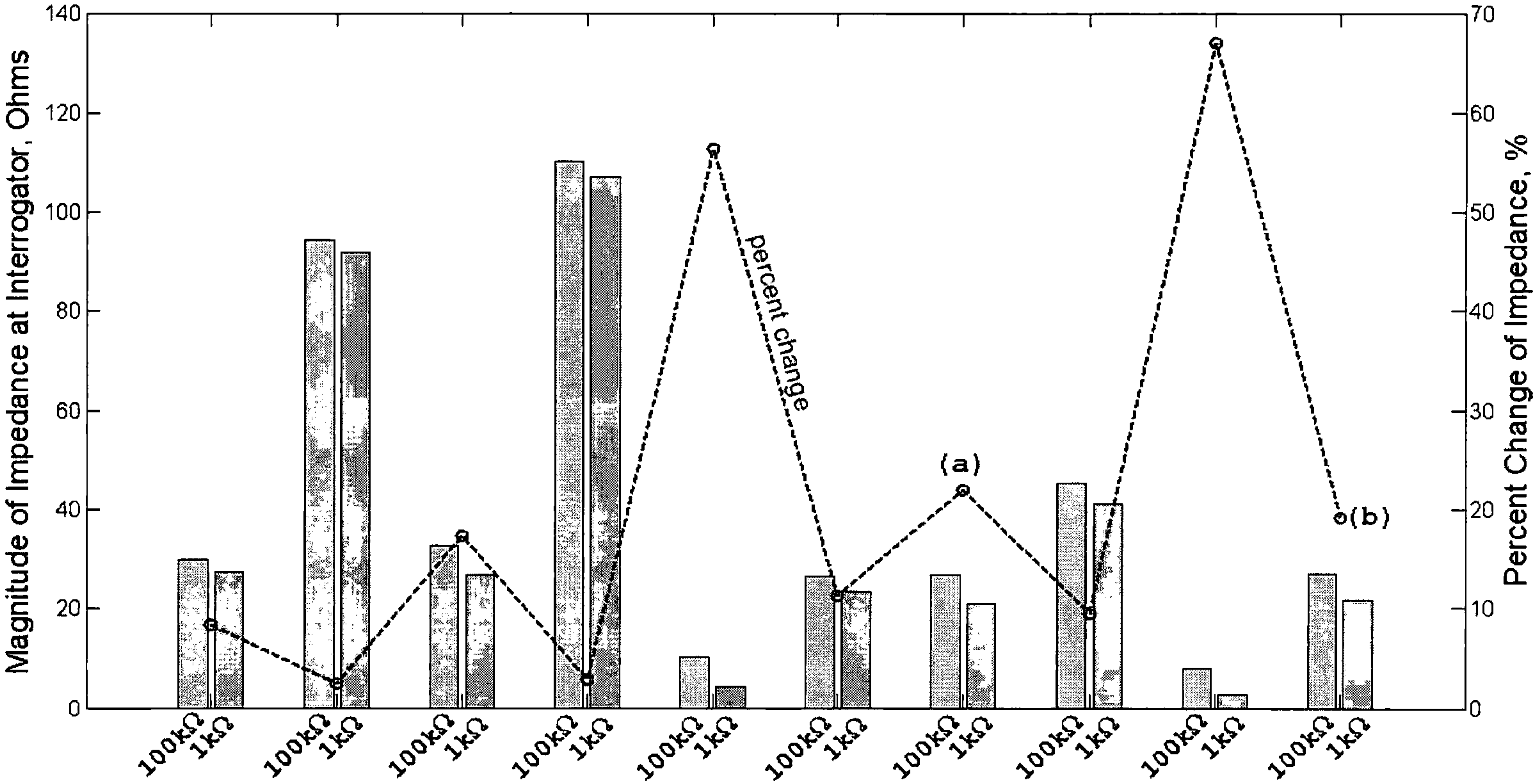

Filter Load	open	short	open	short	open	short	open	short		
Interrogator Configuration	non-resonant primary		resonant primary		non-resonant primary		resonant primary		non-resonant primary	resonant primary
Filter Type	Schaffner (type I)				Delta (type II)				Short (no load)	

Figure 6.19 Evaluation of load modulation sensitivity depending on configuration of interrogator and inlet filter.

6.5 Effect of Electrically Long Cables

Power cables have thus far been modelled as a fixed frequency-dependent resistance, which is a suitably accurate approach for short IEC power cables (0-2 metres). As the power cable length increases it becomes necessary to take into account the effect of cable capacitance and inductance. By considering the conductors as being parallel transmission lines, it is possible to model long power cables by transmission line methods. Frequency-based and time/space-based methods were evaluated for the problem. Regardless of the method, it is necessary to incorporate the transponder coupled impedance within the model. In this section the term *long cable* refers to cables whose length is comparable or greater than the signal wavelength, in which case standing waves can occur on non-terminated lines.

6.5.1 Solution by Transmission Matrix Method

The problem can be approached from a theoretical perspective by adopting impedance matrices that represent long power cables modelled as transmission lines and impedances representing the transponder and filter. This method is compared to a discretised transmission line model in section 6.6. The arrangement under consideration is shown in figure 6.20, where a transponder is separated from the interrogator by a long power cable represented as transmission line. Voltages and currents may only be solved at specific points in the system using this approach; the system must be broken into smaller blocks to reveal signals at different points along the power cable. In section 6.6 it is seen that a discrete transmission line method solves for the current and voltage at every discrete point along the power cable which provide an alternative solution not easily obtainable by the transmission matrix method.

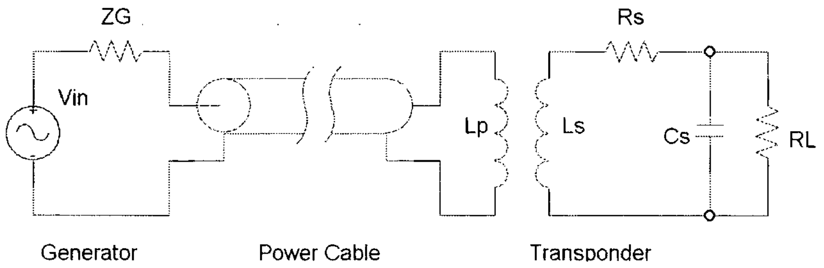

Figure 6.20 Model layout for transponder placed at end of long cable

As discussed in chapter 5, the induced transponder EMF is proportional to primary current (equation 15 chapter 5), and therefore transponder output voltage gives a direct indication of the local current magnitude. This property is exploited in some EMC tests where a current probe is moved along the a wire carrying RF current and the positions of peak induced EMF can be found that correspond with peaks in the standing waves long the wire [Williams]. Standing waves appear when the source and end termination impedances are not equal to the characteristic impedance of the cable.

Assuming an sinusoidal excitation source, the method of transmission matrices may be used to calculate voltages and currents at input and output ports of two port networks that represent the power cable, transponder and inlet filter. Two port networks are lumped models of any linear, time-invariant component that allow output signals to be calculated given input signals.

Of the various types of two-port networks, the transmission matrix [Rizzi] is particularly appropriate for the current analysis since transmission matrices may be cascaded to describe a complete electrical system as shown in figure 6.21. The transmission matrix that represents a transmission line section relates the input and output voltages and currents by:

$$\begin{bmatrix} V_1 \\ V_2 \end{bmatrix} = \begin{bmatrix} A & B \\ C & C \end{bmatrix} \begin{bmatrix} V_2 \\ I_2 \end{bmatrix} = \begin{bmatrix} \cosh(\gamma(f)d) & Z_o(f)\sinh(\gamma(f)d) \\ \frac{1}{Z_o(f)}\sinh(\gamma(f)d) & \cosh(\gamma(f)d) \end{bmatrix} \begin{bmatrix} V_2 \\ I_2 \end{bmatrix} \tag{5}$$

where elements A,B,C, D are complex quantities that describe the two-port network. For the transmission line, *d* is the cable length , Z_o the characteristic impedance and $\gamma(f)$ is the cable propagation coefficient. Standard distributed transmission line model parameters were used (see figure 6.23) comprising per metre resistance (R_d), inductance (L_d), capacitance (C_d) and shunt conductance (G_d). The characteristic impedance is given in the normal fashion by:

$$Z_o(f) = \sqrt{\frac{(R_d + j\omega L_d)}{(G_d + j\omega C_d)}} \tag{6}$$

and the propagation coefficient by:

$$\gamma(f) = \sqrt{(R_d + j\omega L_d)(G_d + j\omega C_d)} \tag{7}$$

When several two-port networks are connected in series the chain rule may be applied to find the total transmission matrix by multiplying each transmission matrix in order. For example, if n networks are connected in series then a total matrix, *T*, may be calculated by $T = \prod_i T_i$.

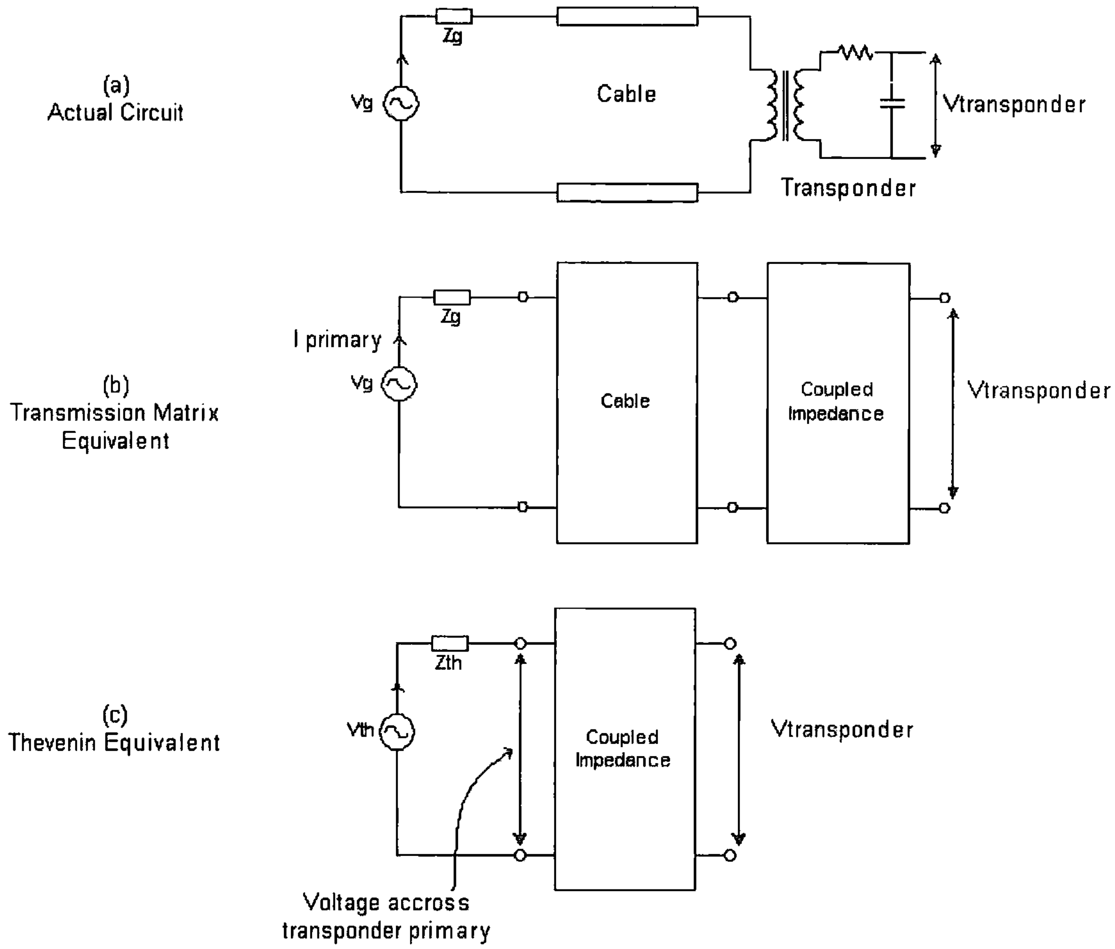

Figure 6.21 Equivalent transmission matrix model of transponder fixed at end of long power cable

6.5.2 Thevenin Equivalent

Specific transmission matrix equations have been derived by Rizzi [Rizzi] that allow reduction of a complex network to equivalent Thevenin source and impedance parameters as illustrated in figure 6.21 (c). The Thevenin voltage and impedance are calculated using:

$$V_{th} = \frac{V_G}{A_T + C_T Z_G} \tag{8}$$

$$Z_{th} = \frac{B_T + D_T Z_G}{A_T + C_T Z_G} \tag{9}$$

where V_{th}, Z_{th} are the Thevenin voltage and impedance respectively. A_T,B_T,C_T and D_T are elements of the transmission matrix, T, that represents the network to the left of the transponder. In this way all circuit components to the left of the transponder are represented by a simple Thevenin source.

6.5.3 Equivalent input Impedance

In a similar fashion, the input impedance of a complex circuit is reducible to an equivalent impedance, Z_{input}, using:

$$Z_{input} = \frac{A_T + Z_L B_T}{Z_L C_T + D_T} \tag{10}$$

where A_T,B_T,C_T and D_T are elements of the total transmission matrix representing all networks to the right of the section of interest (see figure 6.22).

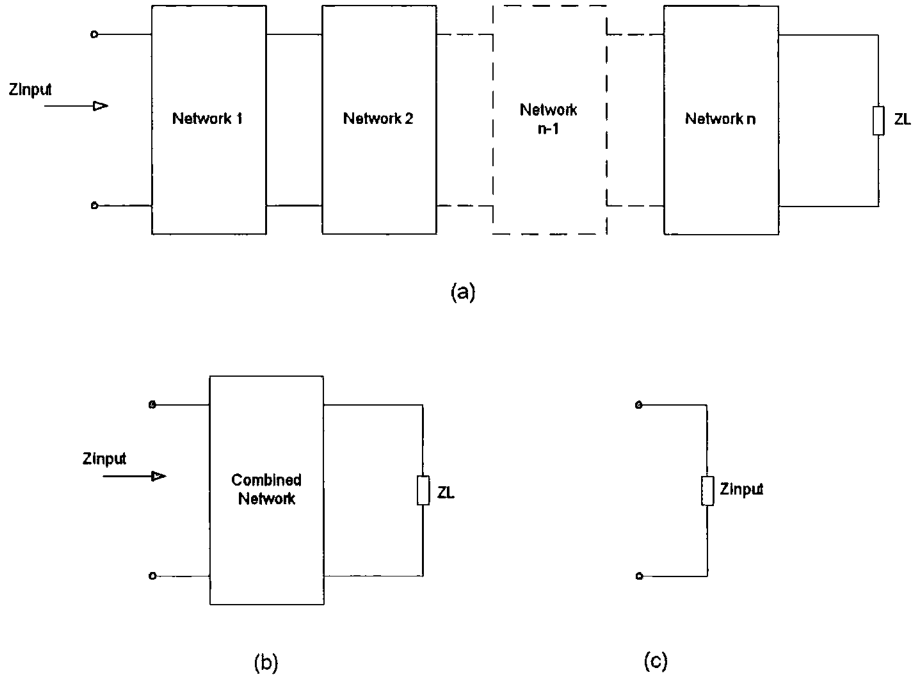

(a)

(b)

(c)

Figure 6.22 Reduction of network to equivalent input impedance. (a) original network, (b)reduced network (using chain rule), (c) equivalent input impedance calculated using equation 10.

6.5.4 Modifying the Cable Model

The power cable configuration is restricted to three core (live, neutral and earth) stranded flex cable. Regarding the power cable as a symmetrical transmission line parameters L_d, R_d and C_d can be calculated using the following relations [Seshardi]:

$$R_d = \frac{1}{a}\sqrt{\frac{\mu f}{\pi\sigma}}\ \Omega/m,\ L_d = \frac{\mu}{\pi}\cosh^{-1}\left(\frac{d}{2a}\right) H/m,\ C_d = \frac{\pi\varepsilon_{real}}{\cosh^{-1}\left(\frac{d}{2a}\right)} F/m \quad (11)$$

where a is the wire radius in metres and d is the wire separation in metres m. Distributed inductance and capacitance were measured using an impedance analyser and compared with calculated quantities. Internal inductance of the conductors was not included. Note that the stranded nature of the wire results in some approximation of the conductor parameters, particularly with respect to inductance and resistance. It is possible to apply correction factors to 11, such as those described in [Anastasiadou] that accounts for the stranded wire, but this was not included here because good agreement between analysis and measurement was found to be possible by approximating solid wire cores.

Dielectric losses in the insulation are accounted for by including a loss factor, $\Lambda(f)$, that modifies the shunt conductance (G_d) according to:

$$G_d = \omega C_d \Lambda(f) \quad (12)$$

$\Lambda(f)$ is a function of frequency that is related to the imaginary component of insulation permittivity ($\varepsilon = \varepsilon_{real} - j\varepsilon_{imaginary}$) and may also be expressed as a loss tangent, $\tan\delta$, according to [Snelling]:

$$\Lambda(f) = \tan\delta = \frac{\sigma}{\omega\varepsilon_{real}} \quad (13)$$

where σ is the dielectric conductivity. The real component of permittivity (ε_{real}) relates to dielectric capacitance and was assumed to be constant in this analysis.

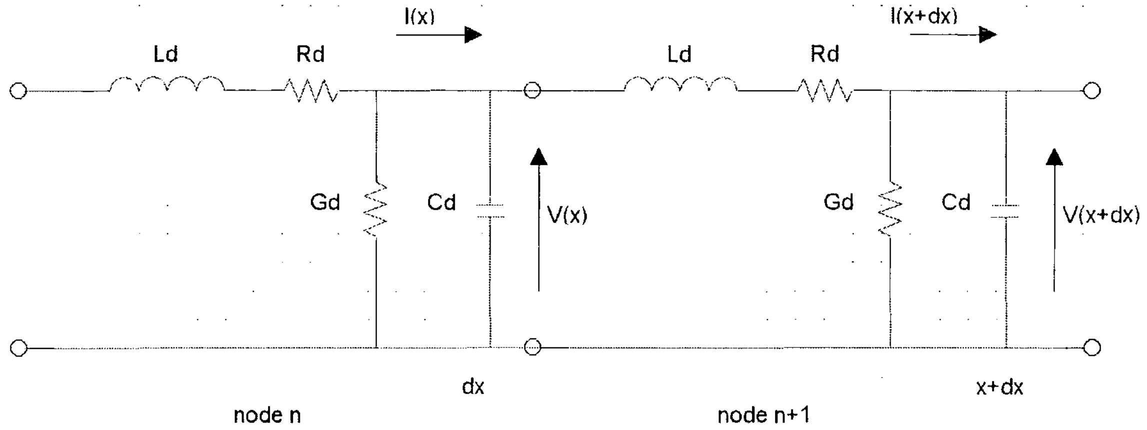

Figure 6.23 Distributed cable model

The loss tangent was estimated using a method described by Tsuzuki [Tsuzuki02], in which a linear function of frequency is used of the form $\Lambda(f) = \tan\delta = a_2 f + b_2$. Tsuzuki also considered frequency dependency of the cable capacitance in power line cabling, but the results showed little variation above 5 MHz.

To validate quantities L_d, R_d, G_d and C_d, the characteristic impedance of 6A three core power cabling was measured at a frequency of 125 kHz using open and short-circuit tests. These are combined according to the following well known expression to find the characteristic impedance:

$$|Z_o| = \sqrt{|Z_{short}||Z_{open}|} \qquad (14)$$

Tests were performed using 1m and 100m cable lengths. The effective power cable conductor radius was calculated by observing that the cable is composed of 24 wire strands, each 0.2 mm in diameter, and calculating the total cross-section area. The effective conductor radius was calculated to be $a = 4.9 \cdot 10^{-4} m$. Conductor spacing is determined by a and the insulation thickness, which was measured to be $1mm$, giving

$d \cong 2mm$. As discussed earlier, these are unadjusted stranded wire approximations. Material parameters were assigned as follows: $\mu = 1$, $\sigma = 5.8 \cdot 10^7$ mho-m^{-1} (for copper) and $\varepsilon = 3.17$ for (PVC insulation). The resulting values of characteristic impedance were found using equation 6 and are compared with those calculated using equation 14 in table 6.2. Similar values can be seen confirming that the approximations described may be applied for at low frequencies. For this simulation, the dielectric loss tangent was represented using $\tan\delta = -0.5 \cdot 10^{-9} + 0.1$ which is similar to that used by Tsuzuki.

Method	Characteristic Impedance, Z_o
Using open/short test at frequency of 125 kHz; cable length 100m	86.05 Ω
Using open/short test at frequency of 125 kHz; cable length 1m	91.00 Ω
Using calculated impedance parameters at 125 kHz	94.77 Ω
Using calculated impedance parameters and assuming ideal transmission line (R_d, G_d negligible)	94.60 Ω

Table 6.2 Comparison of characteristic impedance of 6A power cable using various methods of measurement and calculation.

To investigate the effect of approximations to power cable parameters, the input impedance of a section of three core power cable with length 100m was measured and compared with the analytical result calculated using equation 10. In figure 6.24 the termination impedance was an open-circuit condition and in figure 6.25 the termination impedance was reversed to a short-circuit condition. Measured impedance is included for comparison and shows good agreement with the calculation, particularly with regard to position of resonant peaks/troughs and the general decay of impedance towards higher frequencies.

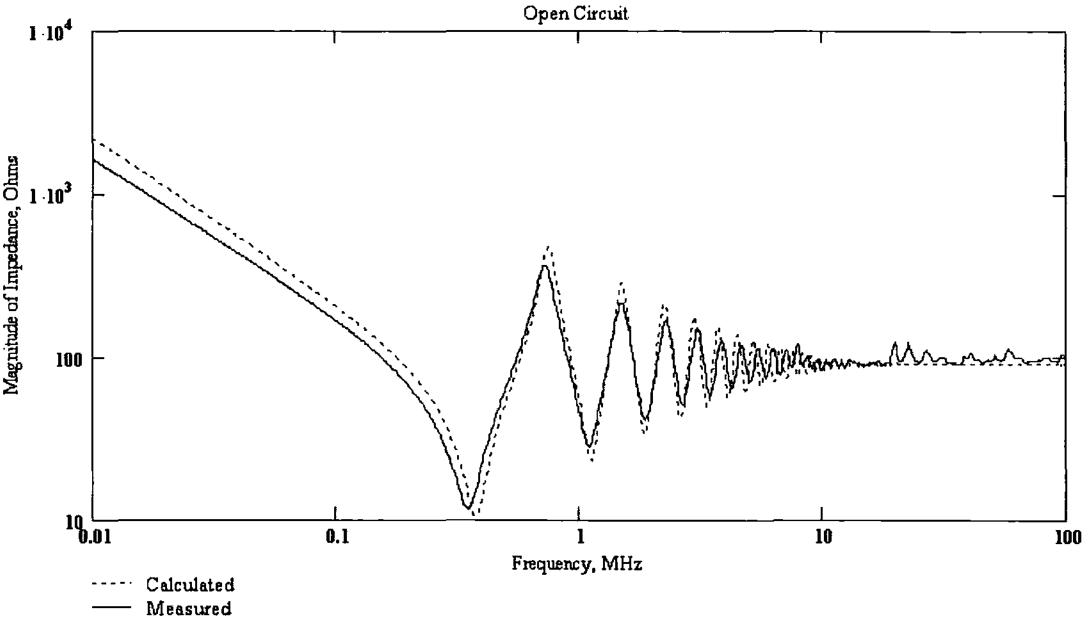

Figure 6.24 Comparison between measured and calculated input impedance of 100m 6A power cable terminated by open-circuit.

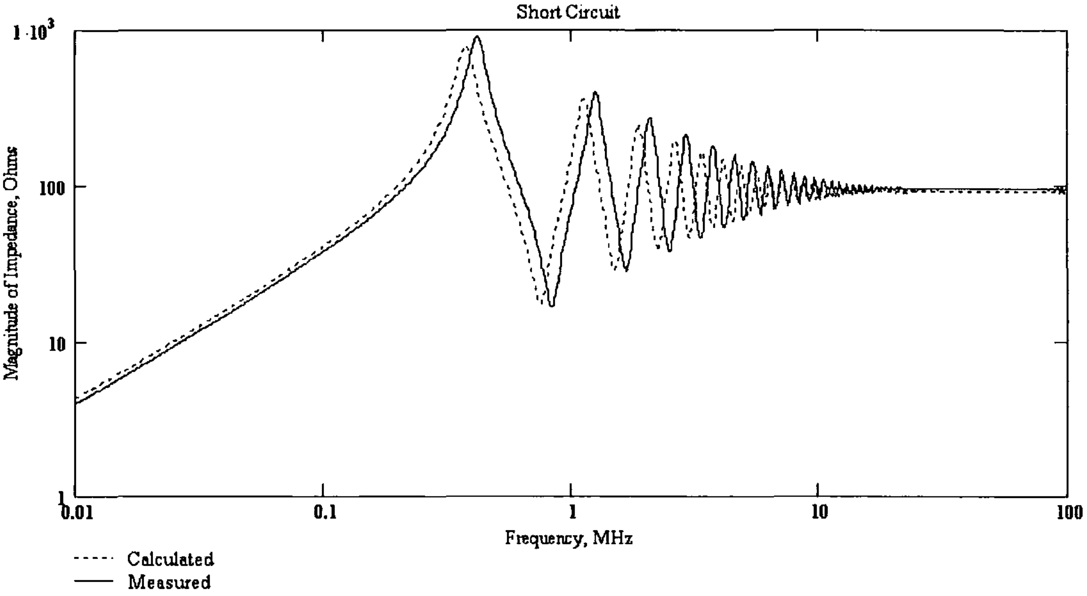

Figure 6.25 Comparison between measured and calculated input impedance of 100m 6A power cable terminated by short-circuit.

6.5.4.1 Alternative Matrix Method

It is also possible to characterise cable input impedance by the scatter parameter approach. This is an alternative matrix-based approach based on knowledge of reflection coefficients at each port input and output. Reflection characteristics may be measured using a network analyser. The general scattering matrix of an n-port network is defined as:

$$S = \begin{bmatrix} S_{11} & S_{12} & \dots & S_{1n} \\ S_{21} & S_{22} & \dots & S_{2n} \\ \dots & \dots & \dots & \dots \\ S_{n1} & S_{n2} & \dots & S_{nn} \end{bmatrix}$$

Thus n^2 scatter parameters are required for an n port network. To measure scatter parameters of cables whose characteristic impedance (typically 90 Ω) is not equal to that of the measuring cables (typically 50 Ω), it is necessary to compensate for the difference by a suitable measurement method. In [Tsuzuki01], Tsuzuki describes a method whereby the cable is inserted as a shunt load between the test cables using a simple T-piece (figure 6.26(a)). The signal flow graph for this configuration is shown in figure 6.26(b) where the T-piece is represented by a three-port network. The shunt load that represents the power cable may be reduced to a two-port network composed of a shunt admittance, Y, equal to the input impedance of the cable residing between two transmission lines of characteristic impedance Z_o (figure 6.26(c)). Assuming the network is reciprocal[22], scatter parameters may then be calculated according to [Rizzi]:

$$S_{11} = S_{22} = \frac{-YZ_0}{YZ_0 + 2},\ S_{21} = S_{12} = \frac{2}{YZ_0 + 2} \qquad (15)$$

---

[22] The condition for reciprocity in a two port network is $S_{21} = S_{12}$.

Measured[23] and calculated scatter parameters are compared in figure 6.27 for 6A power cable of length 1m, where the input impedance was calculated using transmission matrix approach described earlier. Transmission line resonant effects clearly visible in the transmission and reflection paths are caused primarily by transmission line effects, but are also determined to a lesser extent by characteristics of the connectors used which have a non-ideal frequency response.

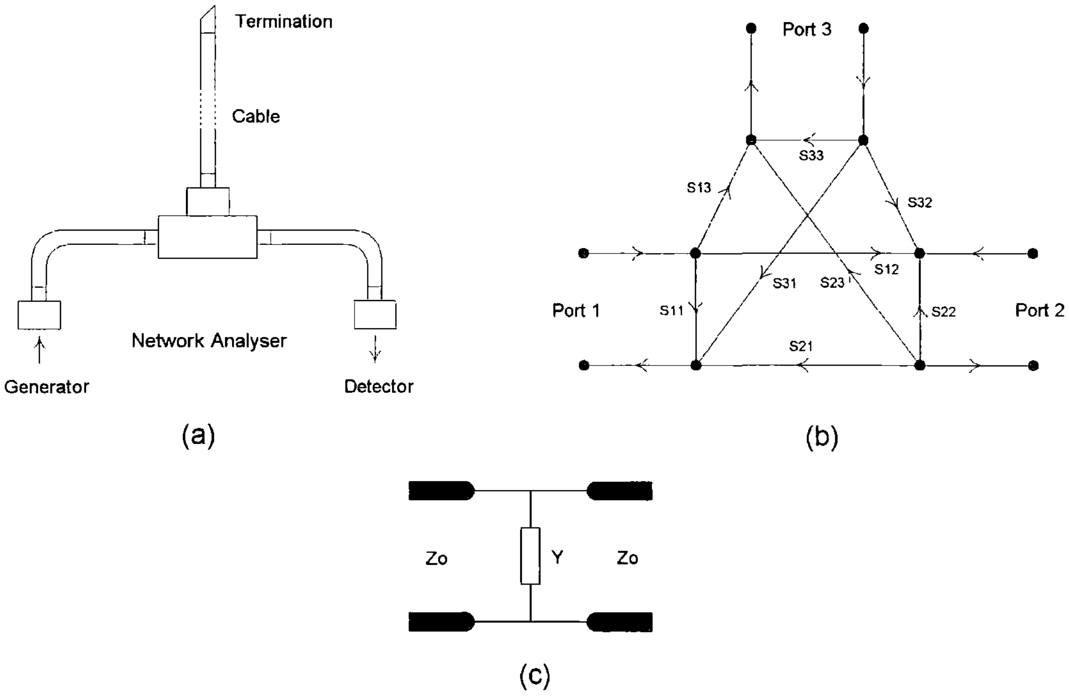

Figure 6.26 Alternative method of cable characterisation using scatter parameters. (a) Connection of cable to Network analyser using T-piece, (b) signal flow graph showing three-port description of T-piece, (c) equivalent two-port circuit used for analysis.

---

[23] Measurements were made using a network analyser: type Rohde & Schwarz ZVCE with 50 Ω test set.

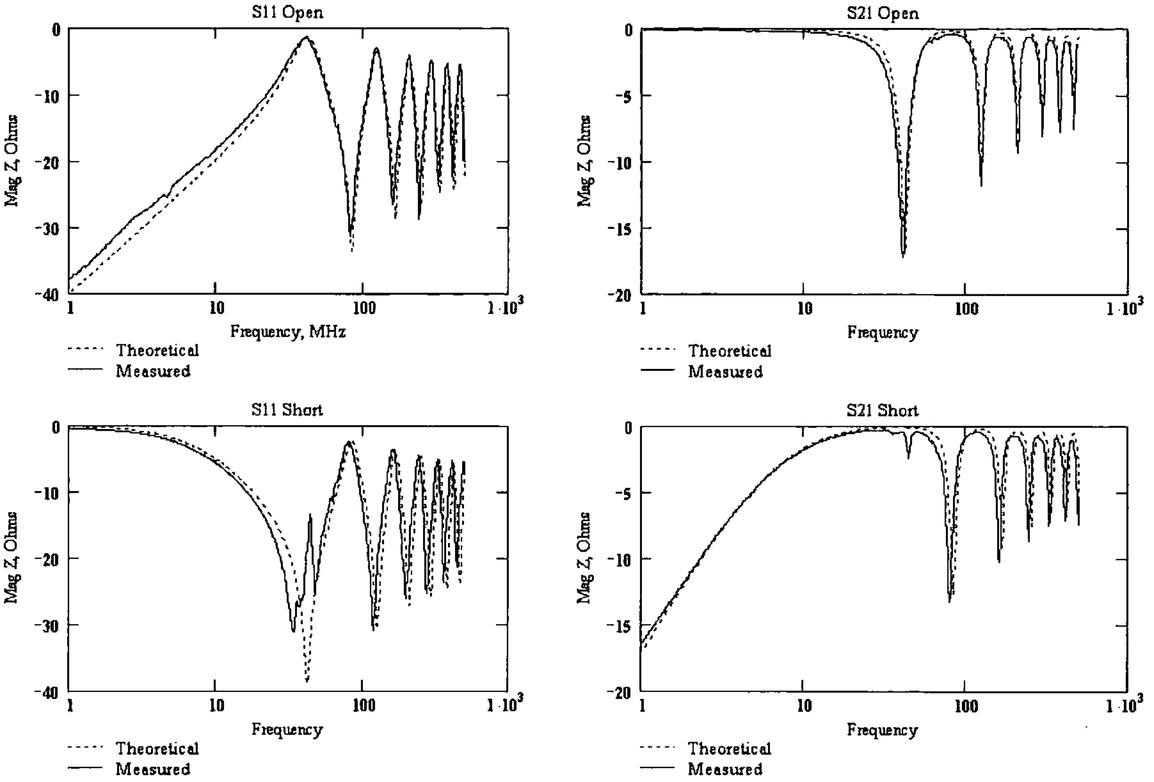

Figure 6.27 Measured and calculated scatter parameters compared for 1m 6A power cable under open and short termination conditions.

The method of scatter parameters would be useful in modelling the effect of discontinuities caused by fixing transponders to the power cable in terms of signal reflections. However useful information such as transponder voltage, line current and standing wave effects are directly calculable using ABCD transmission matrices; the scatter parameters are designed to provide information regarding reflection of energy at discontinuities. In this context, transmission matrices are more appropriate for calculation of the above parameters, particularly when changes of characteristic impedance occur frequently.

6.5.5 Transponder Fixed to End of Long Power Cable

When standing waves occur on long power cables the transponder voltage is directly affected. In chapter 5 it was stated that the open-circuit coupler voltage is proportional to line current (equation 15, chapter 5) in the fashion of a current transformer. It was therefore expected that the presence of standing patterns in line current should result in variation of the transponder voltage as its position is altered along the power cable. In this section it is shown that the coupled impedance representing the transponder can be combined with the matrix approach described above to model the effect of standing waves on long power cables.

The system comprises a transponder fixed to the end of a long power cable as depicted in figure 6.20. The transponder is modelled as described in section 5.6, chapter 5 including secondary losses and capacitance between the winding terminals. Viewed from the primary, a transponder manifests as a coupled impedance in series with the primary reactance (see figure 5.19, chapter 5). Equations 7 and 8 were used to calculate the equivalent Thevenin source representing all circuit components to the left of the transponder (including generator and power cable) as illustrated in figure 6.21. Line current was then calculated by the following circuit equation:

$$I_{line} = \frac{V_{th}}{Z_{th} + Z_{coupled} + j\omega L_1} = \frac{\dfrac{V_g}{A + CZ_g}}{\dfrac{B + DZ_g}{A + CZ_g} + \dfrac{(\omega M)^2}{Z_{secondary}} + j\omega L_1} \qquad (16)$$

where A,B,C,D are transmission matrix parameters representing the power cable, V_g and Z_g are generator parameters and $Z_{secondary}$ is the total series secondary impedance. It is then possible to calculate the open-circuit transponder secondary voltage using equation 16 of chapter 5:

$$V_{2(open)} = j\omega M I_{line} = j\omega k\sqrt{L_1 L_2}\, I_{line}$$

Finally, the closed-circuit transponder voltage may be calculated by regarding the induced open circuit voltage as a voltage source in figure 5.19:

$$V_{2(closed)} = V_{2(open)} \frac{R_{load} \parallel \frac{1}{j\omega C_2}}{Z_{secondary}} \tag{17}$$

where R_{load} is the resistance attached to the coupler terminals. We are then able to calculate transponder output voltage in the presence of long power cables.

To verify the model a transponder was attached to one end of 100 m three-core power cable rated at 6 A that was terminated by a short-circuit. Standing waves appear along the cable above 10 MHz. Interaction between coupled impedance and cable resonant effects were observed by varying the generator frequency across the range 10 kHz – 100 MHz and measuring the transponder secondary voltage on open circuit. The transponder secondary possessed 5 turns with a corresponding nominal inductance of 40 μH, secondary losses totalling 7.8 Ω and self-resonant frequency of 18.6 MHz[24]. A probe was attached to the secondary terminals, causing reduction of self-resonant frequency to 5 MHz. A capacitor was not added across the secondary terminals as with normal operation so that the useful frequency of operation extended to several MHz, allowing observation of the interaction between cable resonance and transponder resonance. Secondary voltage was measured between 10 kHz and 10 MHz using a precision voltage source maintained at 0.5 V (peak-peak) with 50 Ω internal resistance. The measured response for $R_{load} = 10\,\text{M}\Omega$ is shown in figure 6.28 along with the calculated response. A general peak is seen due to self-resonance of the coupler, accompanied by smaller oscillations due to power line resonant effects. Line resonance is caused by mismatch between generator impedance (50 Ω) and power cable characteristic impedance (around 90 Ω) and directly influences transponder voltage. This dependency is illustrated by repeating the above procedure but using a generator

---

[24] See section 5.4, chapter 5 for a discussion of coupler properties.

resistance of 97 Ω, close to the characteristic impedance of the cable, which results in elimination of perturbations in the transponder voltage (figure 6.29). Returning to the 50 Ω generator and reducing R_{load} to 1 kΩ to imitate the process of load modulation, we see a reduction in the maximum transponder voltage and resonant frequency due to activation of load modulation (figure 6.30).

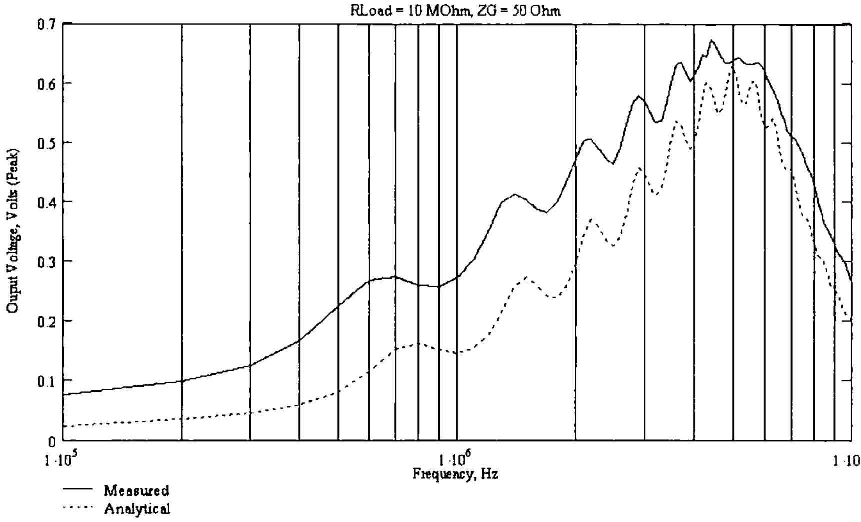

Figure 6.28 Voltage measured across coupler secondary fixed to power cable with load of 10 MΩ and generator resistance of 50 Ω, showing occurrence of transponder and power cable resonance. Cable length was 100m.

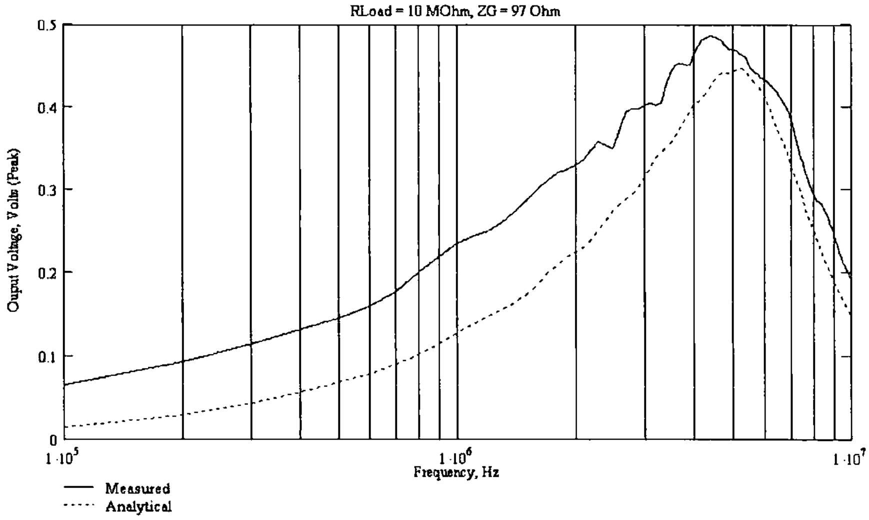

Figure 6.29 Voltage measured across coupler secondary fixed to power cable with load of 10 MΩ, generator resistance of 97 Ω and cable length 100m, showing elimination of cable resonance due to matched generator.

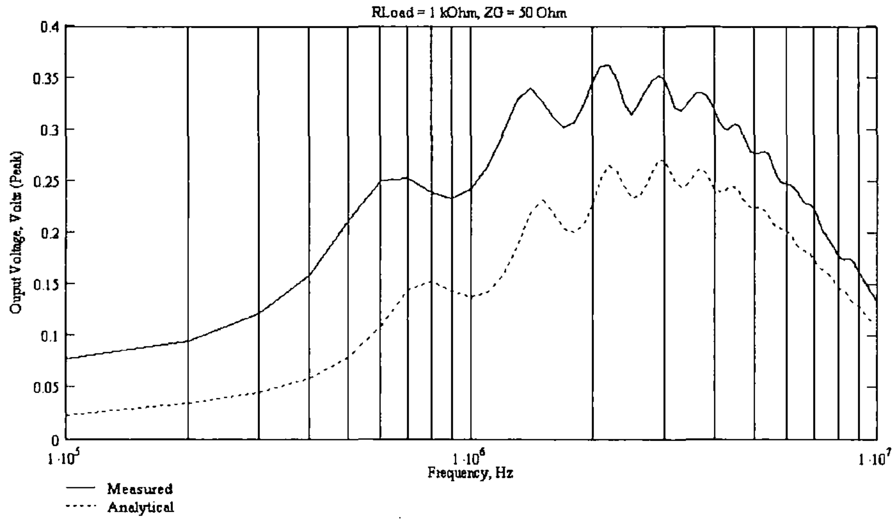

Figure 6.30 Voltage measured across coupler secondary fixed to power cable with load of 1 kΩ, generator resistance of 50 Ω and cable length 100m, showing change in characteristic due to switching load modulator ON.

Differences between measured and calculated results are most likely caused by approximations to core permeability, which in its complex form, determines both core losses and winding inductance. Variation of core permeability was investigated in section 5.4.2, chapter 5 by measuring the dependency of inductance on frequency (see figure 5.10). At frequencies below self-resonance it was observed that inductance reduces as the frequency increases and therefore the assumption of constant inductance will introduce error. In addition, secondary winding resistance was assumed to be constant in the above model causing additional error at higher frequencies.

6.5.6 Including Effect of Inlet Filter

The above approach is easily extended to include the effect of attaching a mains inlet filter at the end of the power cable by adding a term to Z_L (the termination impedance) that accounts for the filter input impedance. We continue to assume that the transponder is mounted at the end of the power cable, i.e. close to the inlet filter in which case Z_L becomes $Z_L = \left(Z_{coupled} + j\omega L_1\right) + Z_{filter}$, the term in brackets representing transponder impedance. As discussed in section 6.4, input impedance reveals transponder/filter interaction and effects of load modulation as seen by the interrogator circuit. We now use the transmission matrix approach to calculate the input impedance for a type II filter with open load-side, transponder resonant at 125 kHz and 2 m long IEC power cable for comparison with the measured impedance illustrated in figure 6.18.

In figure 6.12(b) an equivalent circuit was shown for the type II inlet filter, from which its impedance is easily obtained:

$$Z_{b1} = R_{choke} + R_{x2} + j\left[\omega\left(L_{leak} + L_{x2}\right) - \frac{1}{\omega C_{x2}}\right] \qquad \text{(load side branch)}$$

$$Z_{b2} = R_{x1} + j\left(\omega L_{x1} - \frac{1}{\omega C_{x1}}\right) \qquad \text{(mains side branch)}$$

$$Z_{filter} = \frac{Z_{b1} Z_{b2}}{Z_{b1} + Z_{b2}} \qquad (18)$$

where R_{inlet} has been ignored. The Type II filter parameters and values used are also shown in figure 6.12(b). The total termination impedance is then given by:

$$Z_L = Z_{filter} + \frac{(\omega M)^2}{Z_{secondary}} + j\omega L_1 \qquad (19)$$

Equation 19 is then used to find the input impedance as follows:

$$Z_{input} = \frac{AZ_L + B}{CZ_L + D}$$

Transmission line parameters were adjusted for the increased 13A power cable rating, including $a = 0.8mm$, $L_d = 0.8\mu H$, $C_d = 55pF$, $\Lambda(f) = -0.1 \cdot 10^{-9} + 0.04$ (cf. 6A parameters defined in section 6.5.4.). Resulting graphs of input impedance for transponder loads of 100 kΩ and 1 kΩ are shown in figures 6.31 and 6.32 respectively.

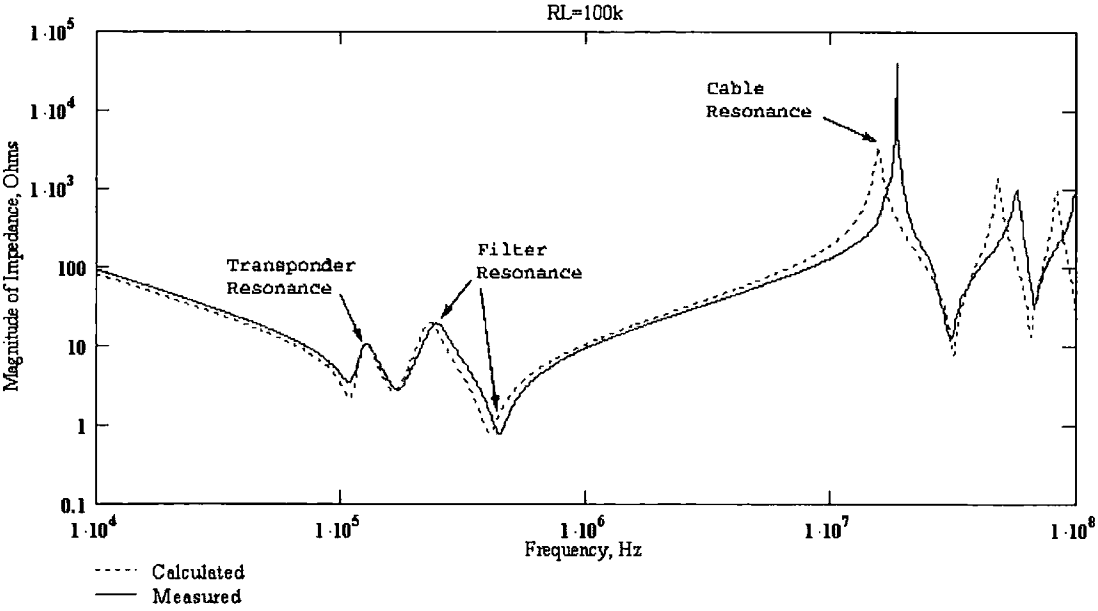

Figure 6.31 Measured and calculated input impedance of cable RFID system comprising: transponder fixed to power line, type II inlet filter and 2 m long IEC power cable, showing transponder/filter interaction and predicted cable resonance. Transponder load was 100 kΩ.

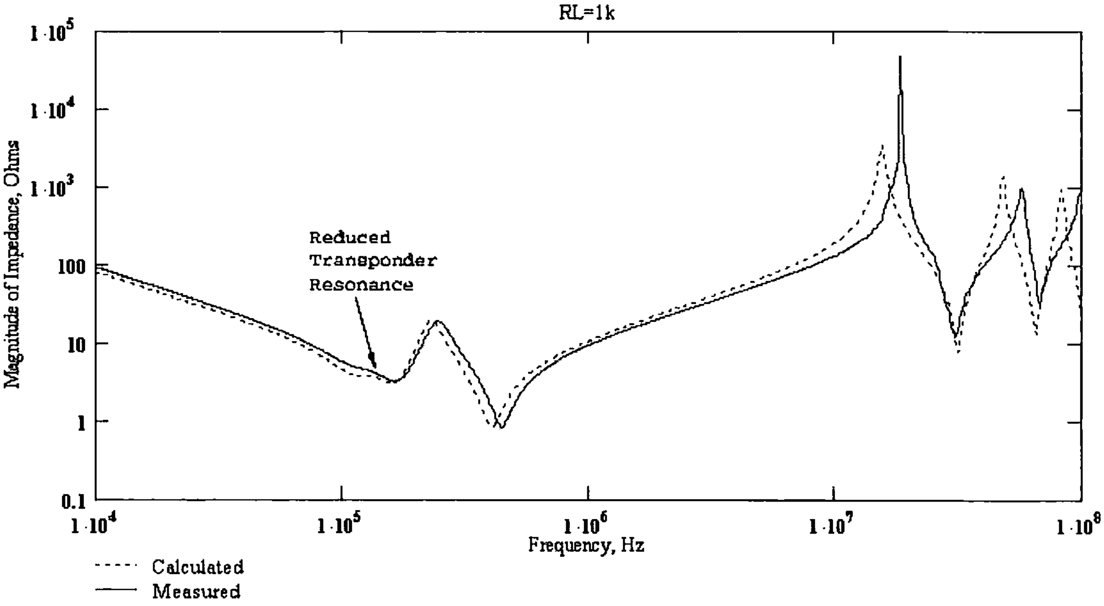

Figure 6.32 Measured and calculated input impedance cable RFID system with transponder load of 1 kΩ

These graphs compare well with figure 6.18 in section 6.4, particularly with regard to filter/transponder interaction. The transmission matrix approach is thus validated. It is important to note that since transponder resonance occurs at a frequency well below cable resonance, the solution applies for any transponder position along the cable, as will be discussed in section 6.7. It is interesting to note that similar characteristics where found by Tsuzuki [Tsuzuki01], who commented on the effect of appliance power cables on the perceived appliance impedance above 10 MHz. This can affect broadband power-line communication systems.

6.6 Solution by Discrete Transmission Line Model

In this section a discrete time/space model is briefly described as an alternative to the frequency-based transmission matrix. A discretised approach offers the benefit of solving basic quantities such as current and voltage at every discrete point along the power cable and for each time step. This provides the possibility of visualising the standing wave patterns that appear due to load mismatch, and was found to be useful for analysing the effect of fixing a transponder to long cables. The approach is based on a method developed by Christopoulos [Christopoulos], in which the electrical equations describing current and voltage along a transmission line are discretised by approximating derivative terms in the fundamental circuit equations. Finite difference equations result which may then be solved numerically to reveal voltage and current profiles along the cable. For post-processing, the results were displayed graphically using a Matlab script. The technique is described fully in appendix D, but a brief introduction is given here before presenting results.

The distributed cable is split into n subsections each with capacitance $C = dxC_d$ and inductance $L = dxL_d$, where $dx = total\_length/n$ is the width of each finite section (see figure 6.23). A constant time step is then calculated that determines the rate at which time is incremented for each iteration of the solution:

$$\Delta t = \frac{dx}{propagation\_speed} = dx\sqrt{\frac{LC}{(dx)^2}} = \sqrt{LC}$$

where Δt is the time step. Minimum time resolution is therefore dependent on element size, which in turn is a function of the number of sections required. Simulation time is therefore dependent on spatial resolution. Note that subsection spacing must be considerably smaller than the electrical wavelength: $dx << 1/f\sqrt{LC}$.

It is assumed in this simulation that the characteristic impedance is constant along the entire cable length in which case stability is maintained. For situations where the characteristic impedance is not constant, but varies along the cable, Christopoulos describes a method for maintaining stability [Christopoulos].

Calculations were implemented using a Matlab script that accepts system parameters, including source, line, termination and transponder impedances, cable length and generator frequency. During each time iteration incident and reflected waves are propagated along the cable according to the properties of each node. Voltage and current waveforms are then plotted on a graph such that each new waveform is superimposed with the previous waveform. Over several time iterations a standing wave pattern appears that allows regions of constructive and destructive interference to be identified. In practice it was found that by plotting the last 5 percent of total time steps solved, sufficiently accurate standing wave patterns[25] could be produced.

---

[25] The simulation period must be sufficiently long to allow steady state conditions to be reached at which point the solution becomes analogous to frequency based methods such as the transmission matrix approach used earlier.

6.6.1 Simulation Results

We use the discrete method to find the voltage impressed upon a transponder placed mid-point along a long power cable by inspecting the resulting standing wave patterns. Two effects cause transponder voltage to drop: cable loss and standing wave patterns. In this section we investigate the influence of standing wave patterns on lossless cabling. In section 6.7 the results are corroborated using a transmission-matrix solution. Figure 6.33 illustrates the arrangement of transponder, power cable, generator and termination impedance. It was shown in section 6.2 that a resonant coupler may be approximated by a real impedance placed in the primary circuit provided the frequency is close to the secondary resonant frequency (see figure 6.2). The transponder was therefore represented by a 10 Ω resistive load (assuming a coupler with 20 secondary turns and 100 kΩ load).

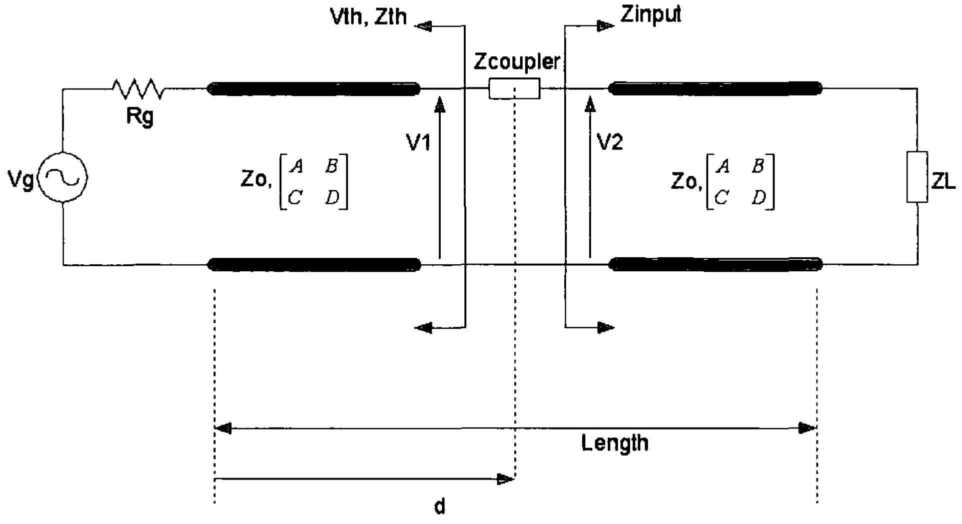

Figure 6.33 Diagram showing transponder fixed at mid-point along a cable. The cable is terminated by impedance Z_L and the transponder is represented by the equivalent primary impedance at resonance.

We regard the power cable to be lossless and of length 100 m. To induce standing waves, the system frequency is chosen to be 1 MHz or 10 MHz[26], and a source of internal resistance R_g and voltage V_g is connected to the cable. Source voltage was chosen to be $5/\sqrt{2}$ V (RMS) which is similar to that produced by the prototype interrogator. The chosen line parameters were $L_d = 0.6$ μH and $C_d = 73$ pF, resulting in a characteristic impedance of 90 Ω. During simulation, voltage and current waveforms are calculated along the cable for each discrete time step. These are then superimposed on a single plot, creating an accumulation of waveforms that shows in silhouette form standing waves which result from a given circuit configuration.

At 1 MHz and with matched source and termination impedances, the effect of placing a resonant transponder on the cable is shown in figure 6.34. This causes a voltage drop across the transponder in agreement with Ohm's Law. The white lines indicate the voltage and current profile along the cable during the final time step. The transponder can be treated as a discontinuity in the transmission line, causing mismatch and therefore standing waves, the evidence of which can be seen in figure 6.34 to the left of the transponder. To the right of the transponder no standing waves can be seen since the matched termination impedance absorbs reflections. If we increase the frequency to 10 MHz and reduce the generator impedance to 50 Ω (figure 6.35) then standing wave patterns can clearly be seen between source and transponder. In this instance, the transponder position coincides with the peak of a standing wave, rendering its effect on the cable clearly visible. In figure 6.36 the termination impedance has been set to 50 Ω and the source impedance is now matched to the characteristic impedance. We see that standing waves are present along the whole cable; the matched generator impedance

---

[26] Note that for the purposes of simulation, it is assumed the transponder has been made to resonate at the chosen system frequency.

does not eliminate resonance effects. This is caused by the discontinuity imposed by the transponder. By magnifying the region close to the transponder position (figure 6.37) a voltage drop is seen to exist between two standing wave patterns. Therefore, under some conditions, the transponder may be operated in the presence of standing waves created by impedance mismatch. A final example is given in figure 6.38 in which the operating frequency is 1 MHz. The generator impedance is 50 Ω and the termination impedance 0 Ω (short-circuit). The cable length is 150 m so that destructive interference occurs in the voltage profile close to the transponder position coinciding with maximum current. This situation causes the maximum transponder voltage to appear, as will be shown in the next section using ABCD matrices.

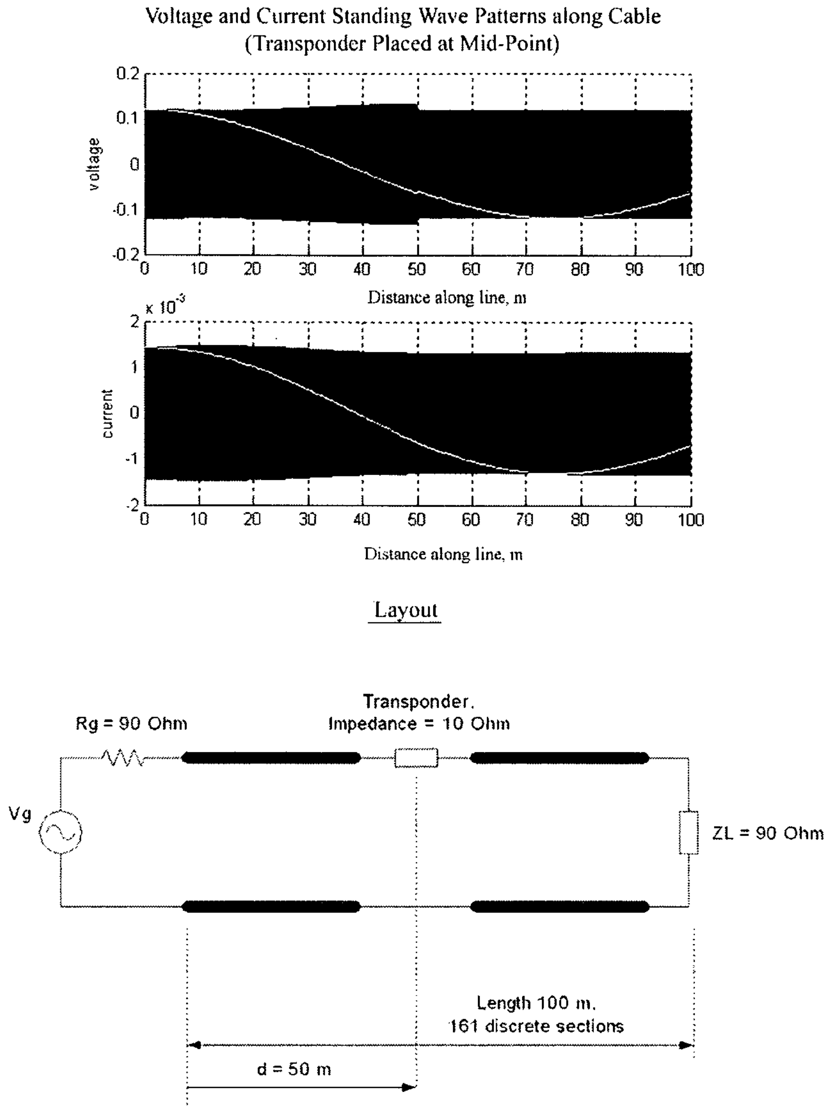

Figure 6.34 Voltage and current standing waveforms produced by transponder placed at mid-point along cable. Simulation parameters: cable length 100 m, 161 discrete transmission line sections, simulation frequency 1 MHz, generator impedance 90 Ω, termination impedance 90 Ω, transponder impedance 10 Ω.

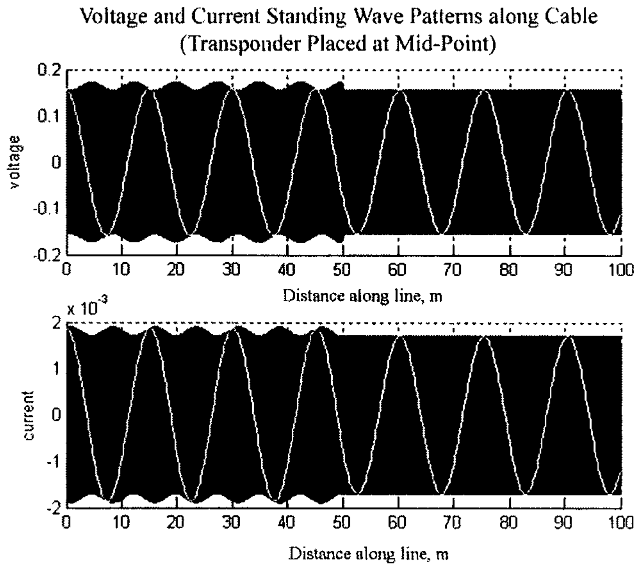

Layout

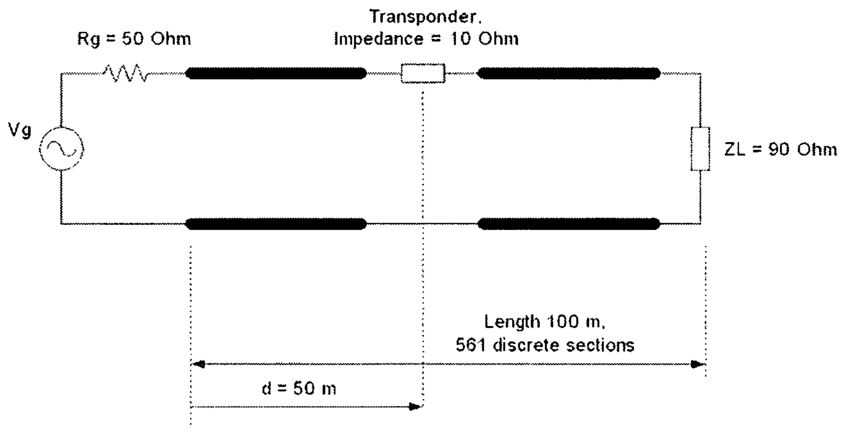

Figure 6.35 Voltage and current standing waveforms produced by transponder placed at mid-point along cable with generator impedance mismatch. Simulation parameters: cable length 100 m, 561 discrete transmission line sections, simulation frequency 10 MHz, generator impedance 50 Ω, termination impedance 90 Ω, transponder impedance 10 Ω.

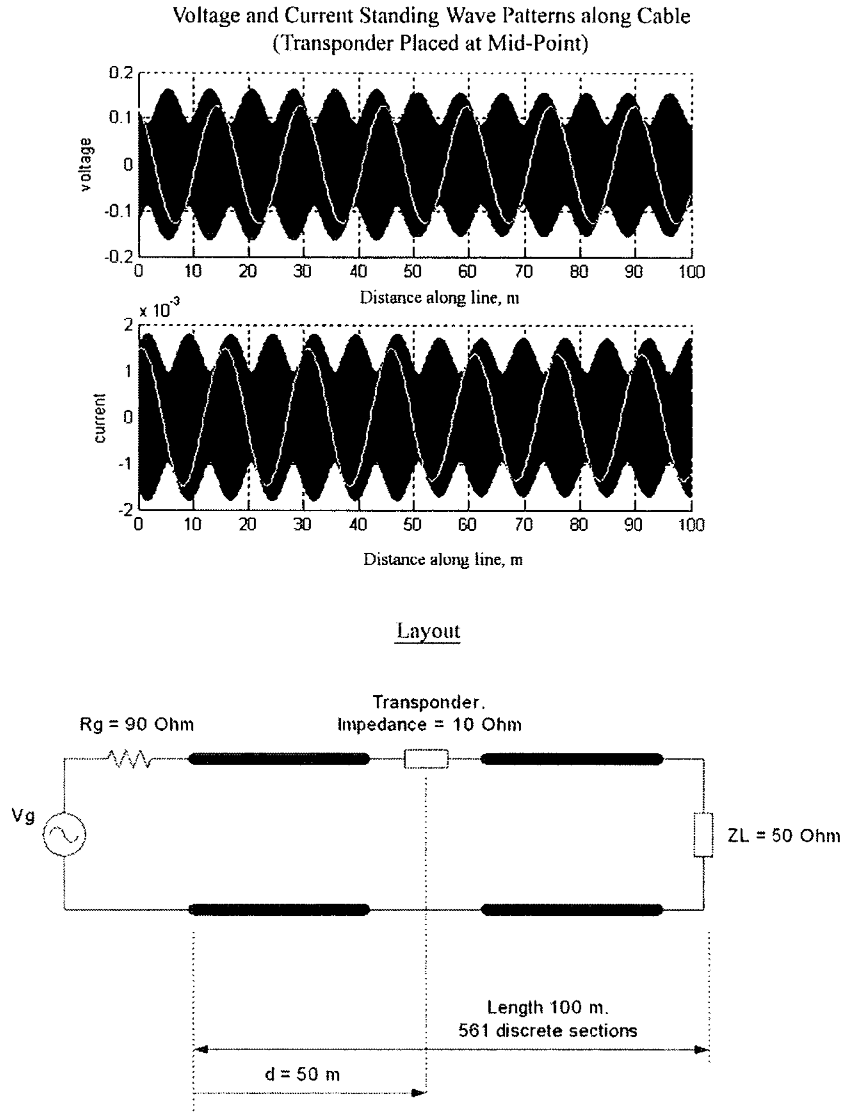

Figure 6.36 Voltage and current standing waveforms produced by transponder placed at mid-point along cable with termination impedance mismatch. Simulation parameters: cable length 100 m, 561 transmission line sections, simulation frequency 10 MHz, generator impedance 90 Ω, termination impedance 50 Ω, transponder impedance 10 Ω.

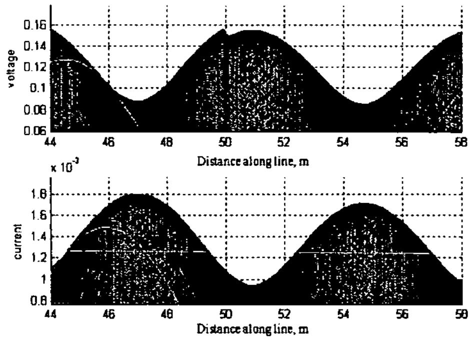

Figure 6.37 Close-up of figure 6.36, showing transponder voltage drop between two standing wave patterns at mid-point along the cable.

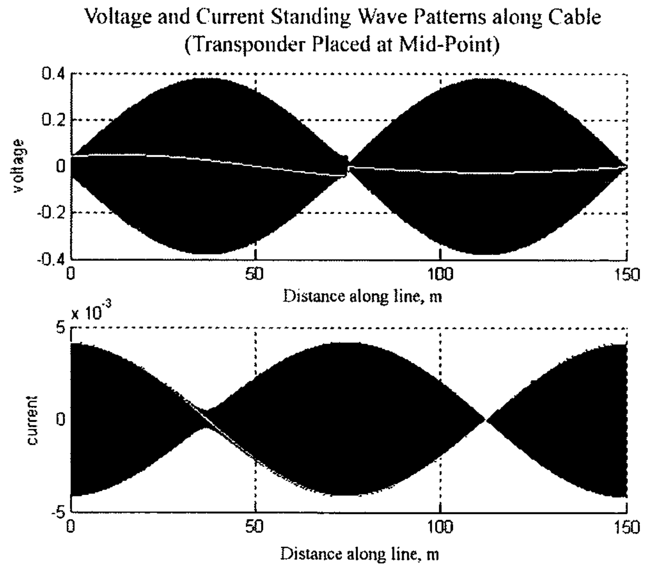
Voltage and Current Standing Wave Patterns along Cable
(Transponder Placed at Mid-Point)

Layout

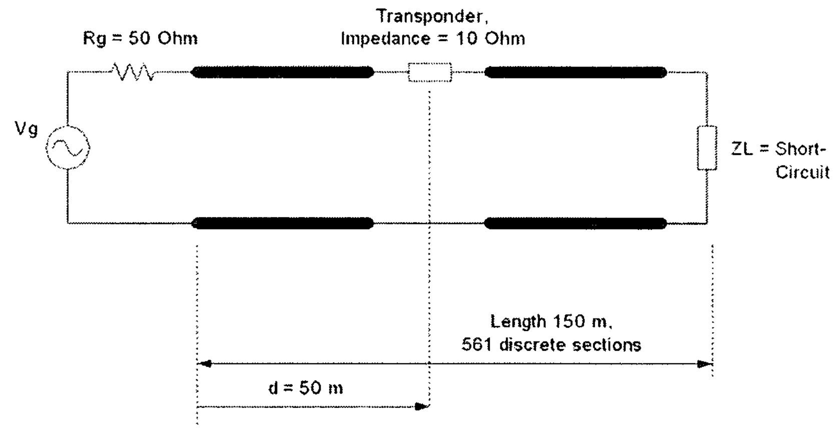

Figure 6.38 Voltage and current standing waveforms produced by transponder placed at mid-point along cable having short-circuit termination. Simulation parameters: cable length 150 m, 561 discrete transmission line sections, simulation frequency 1 MHz, generator impedance 50 Ω, termination impedance 0 Ω, transponder impedance 10 Ω.

6.7 Arbitrary Transponder Position

In this section we generalise the transponder location to any point along the line and include the effect of coupled impedance and inlet filter impedance. This is achieved by using ABCD matrices and the equivalent Thevenin and input impedance expressions described in section 6.5.

Referring to figure 6.33, the cable length is called *length* and the transponder position *d*. At the transponder position, the cable is broken into two distinct two-port networks. The equivalent Thevenin source is calculated using equations 8 and 9 to represent the generator and left cable section. The termination impedance and right cable section are reduced to the equivalent input impedance using equation 10. A simple equivalent circuit is then formed consisting of the coupled impedance placed between a Thevenin source and impedance (figure 6.39). It is then possible to generalise the transponder position by defining two sets of ABCD parameters representing the left and right cable sections that are functions of *d* and *length*. The ABCD parameters representing the left cable section are:

$$\begin{bmatrix} A & B \\ C & C \end{bmatrix}_{left} = \begin{bmatrix} \cosh(\gamma(f)d) & Z_o(f)\sinh(\gamma(f)d) \\ \frac{1}{Z_o(f)}\sinh(\gamma(f)d) & \cosh(\gamma(f)d) \end{bmatrix} \tag{20}$$

and those representing the right cable section:

$$\begin{bmatrix} A & B \\ C & C \end{bmatrix}_{rightt} = \begin{bmatrix} \cosh(\gamma(f)(length-d)) & Z_o(f)\sinh(\gamma(f)(length-d)) \\ \frac{1}{Z_o(f)}\sinh(\gamma(f)(length-d)) & \cosh(\gamma(f)(length-d)) \end{bmatrix} \tag{21}$$

Transmission line parameters were discussed in section 6.5.4. Note that the total cable length is always maintained; the relative length of each cable section varies depending on the transponder position. By solving the equivalent circuit the transponder voltage may be found as a function of position and frequency.

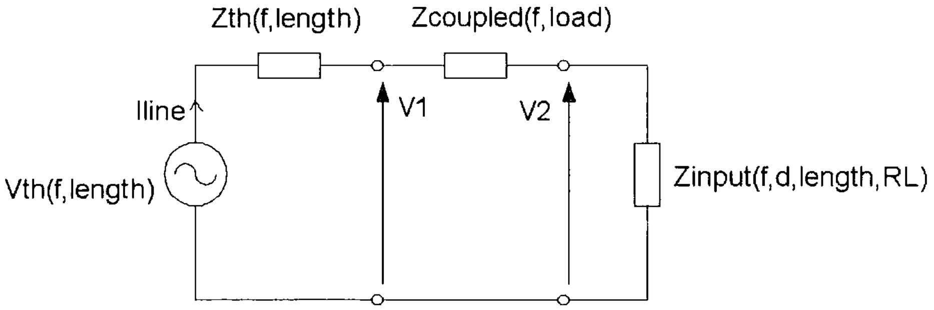

Figure 6.39 Equivalent circuit showing reduced Thevenin source and input impedance on either side of transponder coupled impedance.

6.7.1 Ideal Transponder on Resonant Cable

We return to the example given in the previous section in which the cable length is 150 m, the generator impedance is 50 Ω and the termination impedance is 0 Ω (see figure 3.38). Other parameters are as described earlier. An idealised transponder is again assumed whose impedance is equal to 10 Ω at its resonant frequency. The matrix method is applied to find the transponder primary voltage ($V_1 - V_2$ in figure 6.39) as a function of position. The resulting transponder voltage versus position profile is shown in figure 6.40, where a peak voltage of around 0.04 V can be seen when the transponder is positioned at mid-point (75 m). An equivalent graph of line current is shown in figure 6.41 where the maximum transponder current of 4.16 mA at mid-position (d = 75 m) can be identified. For d = 75 m, the resulting voltage and current values agree with those found by the discrete method. Standing wave effects at d = 37.5 m and d = 112.5 cause reduction of the line current to the values 0.17 mA and 0.057 mA respectively, with a corresponding reduction in transponder voltage.. The transponder impedance (10 Ω) prevents the line current reaching zero at these positions.

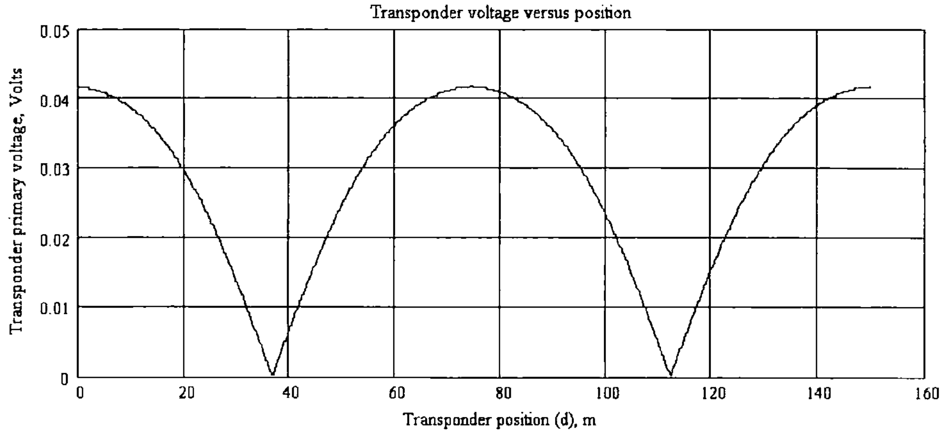

Figure 6.40 Transponder primary voltage versus position, *d*, showing maximum at mid-position.

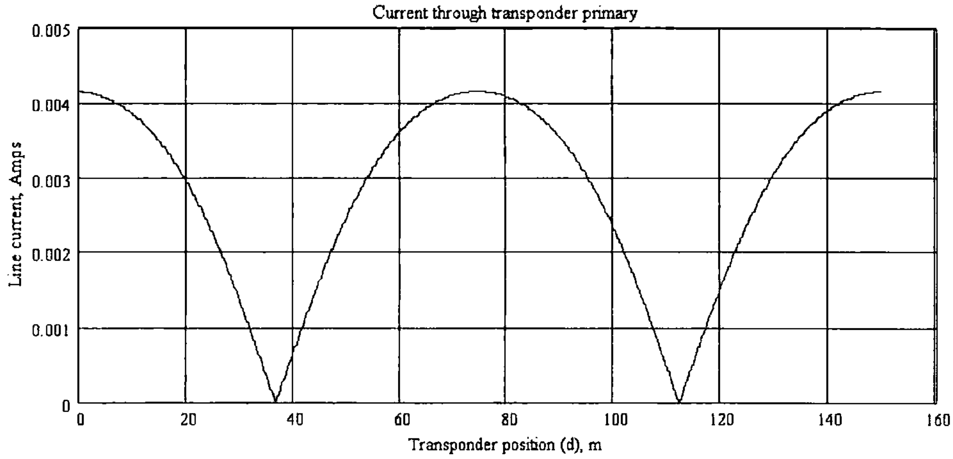

Figure 6.41 Line current versus transponder position, *d*, showing locations of maximum and minimum current.

6.7.2 Including Coupled Impedance, Filter

We now expand the basic method described above to include the complete transponder impedance and choose the default frequency of 125 kHz. The termination impedance Z_L is replaced by the impedance of a type II mains inlet filter as described in sections 6.3 and 6.5.6. The filter load-side is open-circuit (see figure 6.8). Due to the low impedance of the inlet filter under these conditions, the termination impedance behaves in a similar fashion to a short-circuit.

Since long cable lengths are required to induce standing waves at this frequency, we consider the effects of cable loss R_d and dielectric loss G_d by including them in equations 20-21. For the following simulations the cable length was 1000 m. This causes standing waves to appear at around 600 kHz and above[27]. Presented in the next three sub-sections are the voltage and current appearing at the transponder primary and secondary in response to variation of frequency or position (*d*).

6.7.2.1 Primary Transponder voltage and current

Graphs of primary transponder voltage and current versus frequency are shown in figure 6.42 and 6.43 when the transponder is positioned half way along the cable (d = 500m). Transponder voltage peaks at the designed resonant frequency, attenuating out of band variations. In contrast, line current exhibits resonance features caused by the combined effect of long cables lengths and the unmatched termination impedance. Current decays at higher frequencies due to cable losses.

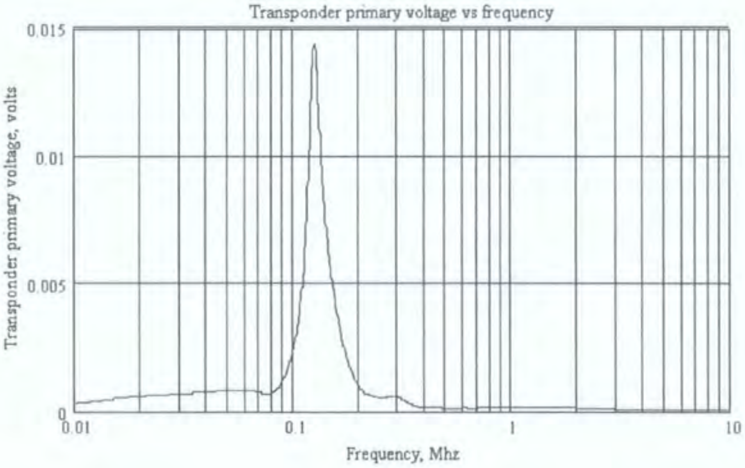

Figure 6.42 Magnitude of transponder primary voltage versus frequency at mid-point.

---

[27] Standing wave effects become prominent as the cable length approaches ¼ of the electrical wavelength, which for this system is around 250 m. The corresponding frequency is around 600 kHz (the propagation velocity is around 1.5×10^8 m/s).

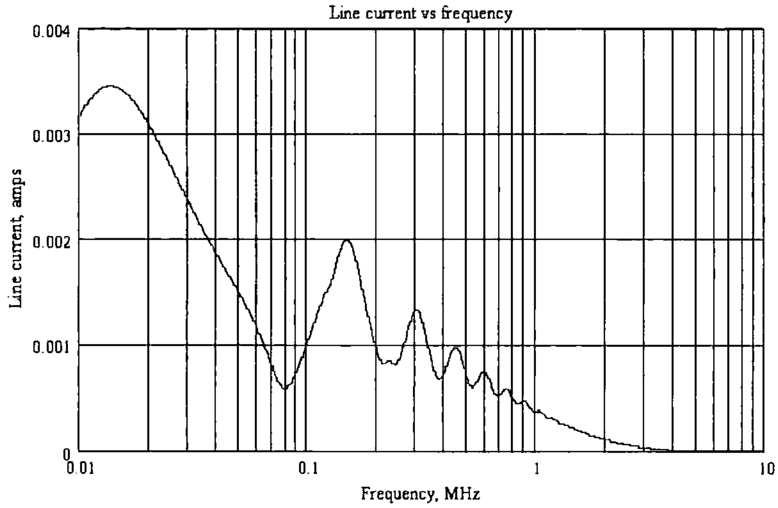

Figure 6.43 Line current versus frequency at mid-point.

We can also calculate the variation of transponder primary voltage and current versus position at the nominal operational frequency of 125 kHz (figures 6.44, 6.45). The voltage/current profiles are similar in shape with a scale factor of around 10. Since the coupled impedance is virtually a real load of around 10 ohms at the resonant frequency, Ohm's Law is satisfied. The maximum voltage of 17 mV is found by locating the transponder 477 m from the generator. The corresponding line current is 1.7 mA which may be used to find the maximum secondary output voltage (see next section). A minimum voltage of 3.3 mV occurs when the transponder is placed 700 m from the generator. The two positions represent 15 dB variation in transponder primary voltage. In addition, the profile is generally decaying as *d* increases due to cable loss between the generator and transponder (cable loss between the transponder and filter influence the equivalent impedance seen to the right of the transponder).

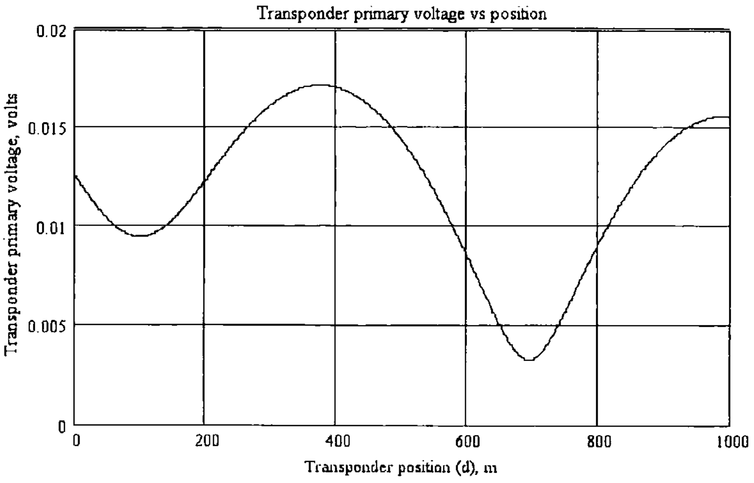

Figure 6.44 Variation of transponder primary voltage with transponder position

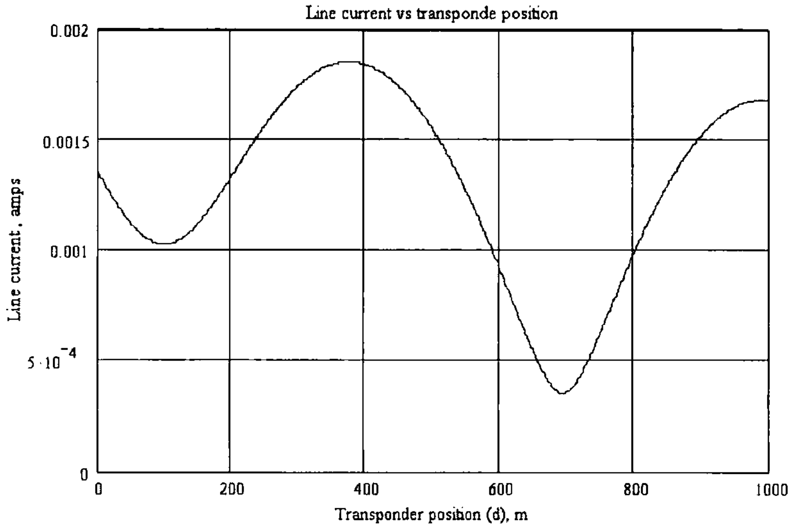

Figure 6.45 Variation of line current with transponder position.

6.7.2.2 Open-circuit and Loaded-circuit secondary Voltage

We may calculate the transponder open-circuit voltage in a similar manner to that described in section 6.5.5, where the line current was used to find the coupled secondary voltage. The closed circuit voltage is then calculated using equation 17. It was assumed that the coupler has 20 secondary turns with the same parameters described earlier in this chapter.

In figure 6.46 the open-circuit secondary transponder voltage is shown versus frequency at mid-point. The graph bears a resemblance to figure 6.28 in section 6.5.5, where the open-circuit voltage of a self-resonant coupler was calculated and measured, but differs because secondary capacitance is absent when calculating the open-circuit voltage. In this situation the decaying voltage at high frequency occurs due to cable losses rather than self-resonance of the transponder. The influence of cable resonance is also clearly visible in the open-circuit voltage profile.

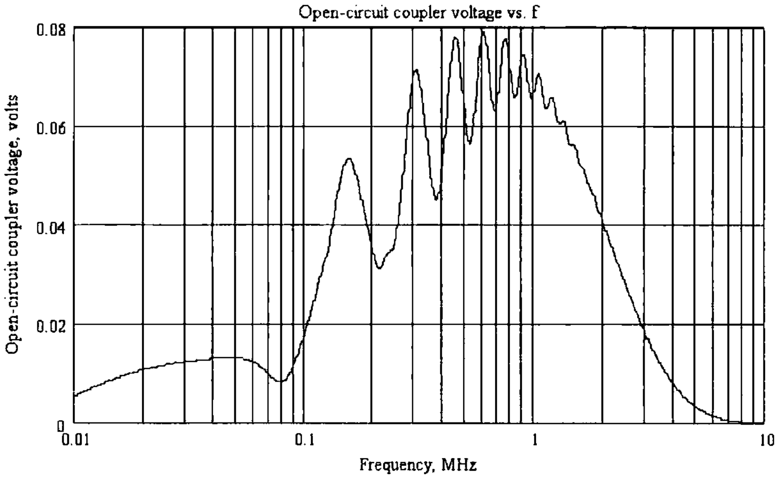

Figure 6.46 Open-circuit secondary voltage versus frequency for transponder positioned at mid-point along cable.

Graphing the transponder open-circuit voltage versus position (frequency = 125 kHz) (figure 6.47), the same profile is seen to that of the primary voltage i.e., coupler secondary voltage follows primary voltage. Closing the circuit with secondary capacitance and typical transponder chip impedance produces the same profile but magnified by the secondary *Q*, which in this example is around 10 during the modulator OFF condition. The resulting maximum and minimum chip voltages are 350 mV and 68 mV respectively, with the same 15 dB range as the primary voltage. Clearly the long cable length has resulted in significant attenuation of transponder voltage, however due to the influence of inlet filter and cable resonance, decay does not occur steadily with increasing separation from the generator, but shows varying amplitude.

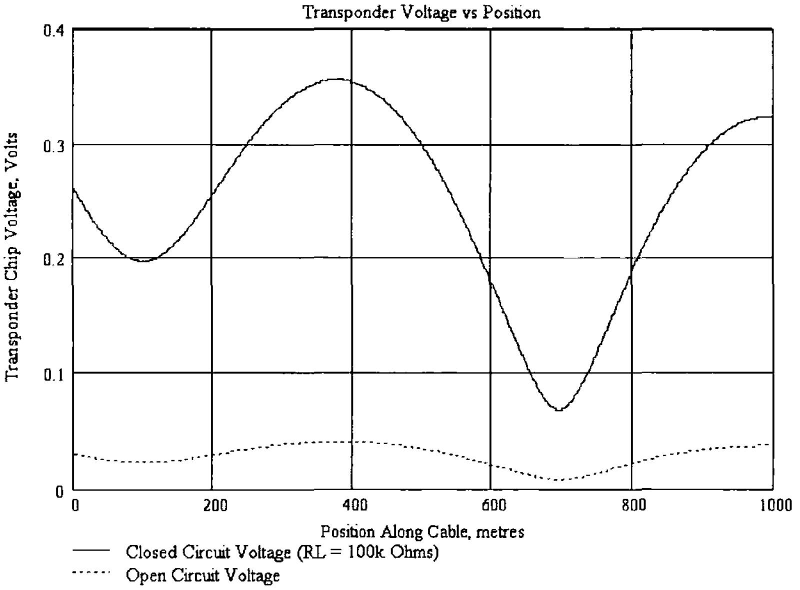

Figure 6.47 Open-circuit and closed-circuit voltage at transponder secondary versus position, *d*. Frequency = 125 kHz.

It was found that variations of transponder voltage were influenced mainly by inlet filter impedance, as demonstrated in figure 6.48 where the filter impedance was replaced by a matched load of 90 Ω to eliminate standing wave patterns between the transponder and termination impedance. The generator impedance is still 50 Ω and so reflections must take place between the generator and transponder but are negligible due to the low value of coupled impedance and do not cause significant variation of the transponder voltage. Using a matched termination the transponder voltage gradually decays as it is moved further away from the generator.

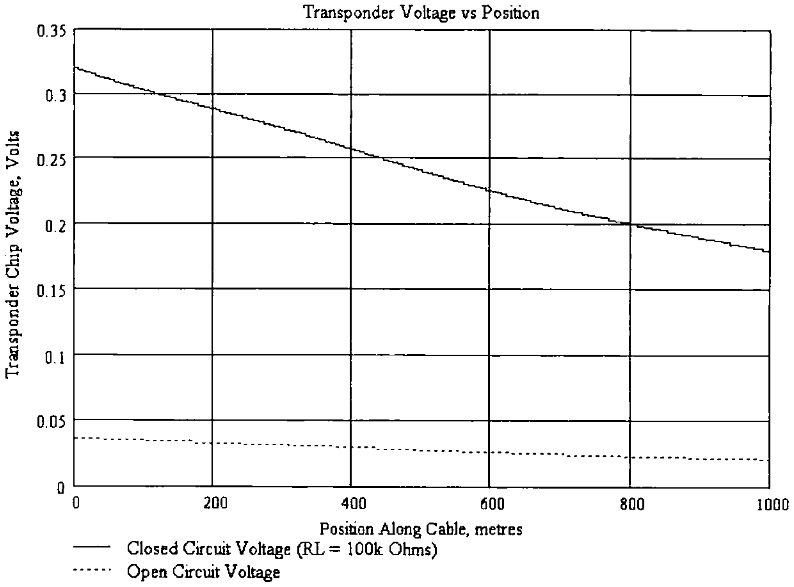

Figure 6.48 Closed circuit voltage versus transponder position for a matched termination impedance.

Finally, the variation of secondary voltage with frequency is shown in figure 6.49 for modulation ON / OFF conditions, where the secondary resonance has clearly attenuated out of band variations. For this figure transponder position is mid-point.

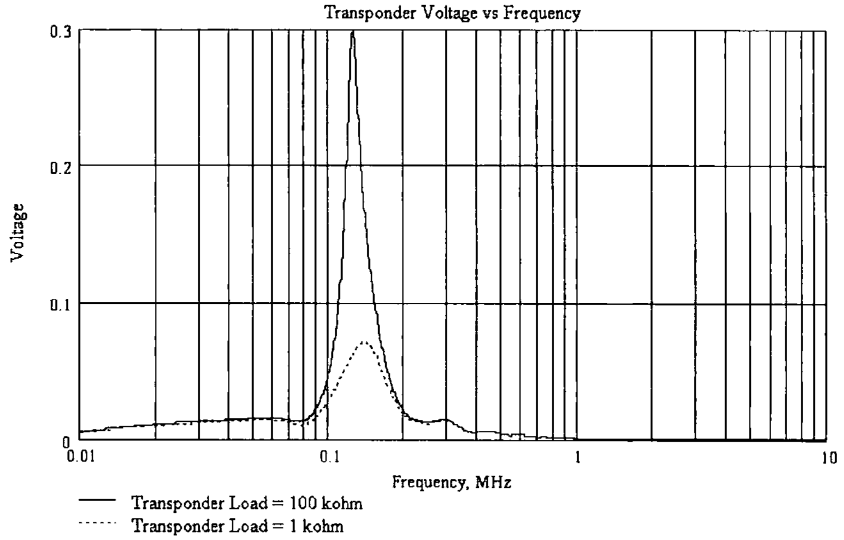

Figure 6.49 Variation of secondary voltage with frequency for modulator ON/ OFF conditions. *d* = 500m.

6.8 Summary

In this chapter the complete cable RFID system has been investigated. The main embodiment of a cable RFID system includes a appliance mains inlet filter, power cable and transponder to which the interrogator is attached. The primary-referred transponder impedance was shown to comprise a coupled impedance that interacts with the primary reactance when secondary resonance is employed. This gives rise to an additional resonant mode. An important result is that the coupled impedance cannot be modelled by static LCR components, but requires frequency dependent parameters. The coupled impedance is accounted for by a single equation that includes all effects of the coupled secondary circuit.

A study of filter impedance was undertaken to determine typical input impedance characteristics by deriving the equivalent circuits of two common filter topologies. Analysis included leakage inductance in the current-compensated choke. Worst case input impedance (open-circuit and short-circuit load-side) was modelled to ensure that load modulation occurs in the presence of such filters.

Two approaches were taken to model the effect of increasing cable length, one based on discrete space-time, the other on steady state conditions. Consistent results were obtained using these methods. These simulations were used to determine the effect of transponder position and inlet filter impedance on the standing wave patterns that occur due to impedance mismatch. The most important result was evidence that the resonant transponder is influenced by its position along the cable when standing waves are permitted to occur. The inclusion of a mains inlet filter causes strong cable resonance in the circuit due imposition of a near-short condition at the termination end. Furthermore, these resonance effects can influence transponder voltage even when the frequency is much less than a quarter wavelength.

The simulation could be used to evaluate the sensitivity of transponder voltage to transponder position in long-cable applications, and to appraise the influence of inlet filters if they are to be used as a means of return path for the carrier current. Clearly, given the freedom to choose any value of termination impedance, the value should be matched to the cable characteristic impedance in order to minimise standing wave patterns along the cable. In this case transponder voltage steadily decays as it is moved further away from the generator. The simulations could be extended to investigate how the interrogator impedance is modulated by a transponder whose position varies along the cable. Results from the simulation suggest that impedance variation will always occur in response to transponder load modulation until cable attenuation is dominant, and that the angle of modulation (i.e. relative degree of amplitude and phase change in the interrogator impedance) will vary with transponder position. This is because the equivalent magnitude and phase of input impedance comprising transponder, cable and inlet filter as seen by the interrogator will change with transponder position.

7 *Design and Evaluation of an Embedded RFID Interrogator*

7.1 Introduction

This chapter describes the development of a transponder interrogator device that was designed for three purposes. First of all, it was intended that the design be used for embedded applications within Seaward Electronic automatic identification products. Secondly, the device would be used in RFID cable applications, where it would provide measurement data consistent with the theory. Finally, the device would be used to investigate signalling over long cables and across the power line. The hardware and software design is described briefly, followed by performance analysis.

7.2 Background

A new RFID interrogator module was required for electronic appliance tagging applications at Seaward Electronic Ltd. Two application examples are the integration of cable RFID interrogators within Seaward PAT products, and the design of a new proximity RFID reader to be sold either as an accessory to existing products, or as part of a complete automatic identification package.

An early RFID proximity interrogator was designed that utilised a third-party read-write module along with the adjustable inductive coil assembly described in chapter 4. The finished product, shown in figure 2.4 chapter 2, is available in two forms: a barcode emulation unit that reads RFID transponders as if they are barcodes, producing barcode reader-compatible data, and a read-write RFID interrogator that supports the full capabilities of the Philips Hitag transponder chip, including data storage. Following conclusion of the initial design, it was decided that an in-house interrogator design would be preferred for future products since this would bring several benefits: it would remove the need to out-source modules, costs would be reduced and the ability to modify the design would provide greater flexibility for embedded applications. These benefits were offset slightly by the initial development time required. An approach was devised that permitted development of a read-write module that could also be used to research new methods such as cable RFID and power line signalling described in this thesis.

7.3 Hardware Design

The design is based around a low-cost Microchip 16C63A PIC microcontroller [PIC63] and Philips HTRC110 RF transceiver chip [hitagre], both of which are 5 V CMOS devices. Major functions are controlled across an asynchronous serial interface, including: field pulsing, received signal sampling and client-host communications. The transceiver chip incorporates antenna drivers, a synchronous detector with adaptive phase control, digital filters and a digitiser. The module is completed by various passive components required for the analogue front-end, crystal and an appropriate communications driver (such as RS-232 line transceiver). The schematic is shown in figure 7.1. A PIC emulator was used for rapid code modification and execution.

An inductive loop antenna L1 (not shown) is attached to terminals AN1 and AN2, and is made to resonate with capacitor C3. Pins TX1 and TX2 produce differential 0-5V transitions, which are filtered by C3 and L1 to produce an approximately sinusoidal voltage, V_{tap_point}, at the junction labelled tap point in figure 7.3. The fundamental of V_{tap_point} is equal to the first term in the Fourier series representation of the square voltages:

$$V_{tap\_point} = \frac{4}{\pi}V_{in}\sin(\omega t) + \frac{4}{3\pi}V_{in}\sin(3\omega t) + \frac{4}{5\pi}V_{in}\sin(4\omega t) + \ldots$$

$$\Rightarrow V_{tap\_point} = \frac{4}{\pi}V_{in}\sin(\omega t) \qquad (1)$$

Higher harmonics are naturally attenuated by the resonant circuit, but care is required to ensure that higher resonant modes (such as standing waves on long cables) do not coincide with odd multiples of the fundamental, since this could induce additional noise components.

7.3.1 Signalling

Since the transponders under consideration are of a passive nature, the transmitter must produce a continuous energising field throughout the communication process. This is achieved by using DSB-LC[28] signalling whereupon the carrier component is maximised to excite a resonant circuit located in each transponder. Messages are sent to transponders by field-gap signalling, which can be modelled as OOK[29]. Following the successful activation of a transponder, a reply in the form of direct load modulation is made, the mechanism of which was described in chapter 5. The reply may be modelled as a form of ASK[30] with very low modulation index (m) and FSK[31] subcarrier. This communication system is defined by the fact transmitter and receiver are *simultaneously active*, which places strict demands on receiver-transmitter isolation and generally places practical limits on the achievable performance in terms of receiver SNR. This aspect is explored further in section 7.5.

---

[28] Double SideBand- Strong Carrier

[29] On-Off Keying

[30] Amplitude-Shift Keying

[31] Frequency-Shift Keying

Detection of transponder messages is achieved by the simple voltage divider comprising R1 and an internal resistor connected between pin RX and analogue ground. Voltage division is required to protect pin RX since the resonant voltage at tap point can reach 100 V or more when the primary circuit Q is sufficiently high. A reduced copy of the resonant voltage is thus produced at pin RX that contains load modulation information. Direct down-conversion is carried out by a synchronous detector that samples the incoming signal at the carrier frequency. This process differs from analogue synchronous detection in that the analogue local oscillator is replaced by a sample and hold circuit, which holds the current signal level for precisely one carrier period, therefore effectively multiplying the signal by the carrier frequency. Synchronous detection is usually reserved for suppressed-carrier modulation because envelope detection is not possible. Synchronous detection in large-carrier modulation brings little benefit over envelope detection (a considerably cheaper process), except when the S/N ratio is low. In this case the nonlinearly of envelope detection causes degradation of the output S/N radio [Stremler]. The interrogator considered here exhibits low receiver input S/N due to low modulation index and the simultaneous presence of transmit and receive signals, and thus benefits considerably from the use of synchronous detection. The operation is modelled by conventional synchronous detection, which recovers the original FSK subcarrier message, *m(t)*. The complete modulated signal, *$\phi(t)$*, sent by the transponder is represented by:

$$\phi(t) = (m(t) + A)\cos(\omega_c t) \tag{2}$$

where A is the carrier amplitude and ω_c is the carrier frequency. Multiplying (2) by a local copy of the carrier signal, $\cos(\omega_c t + \theta)$, where θ accounts for local oscillator phase offset, results in the base band signal, *e(t)*:

$$\phi(t) = (m(t) + A)\cos(\omega_c t) \tag{3}$$

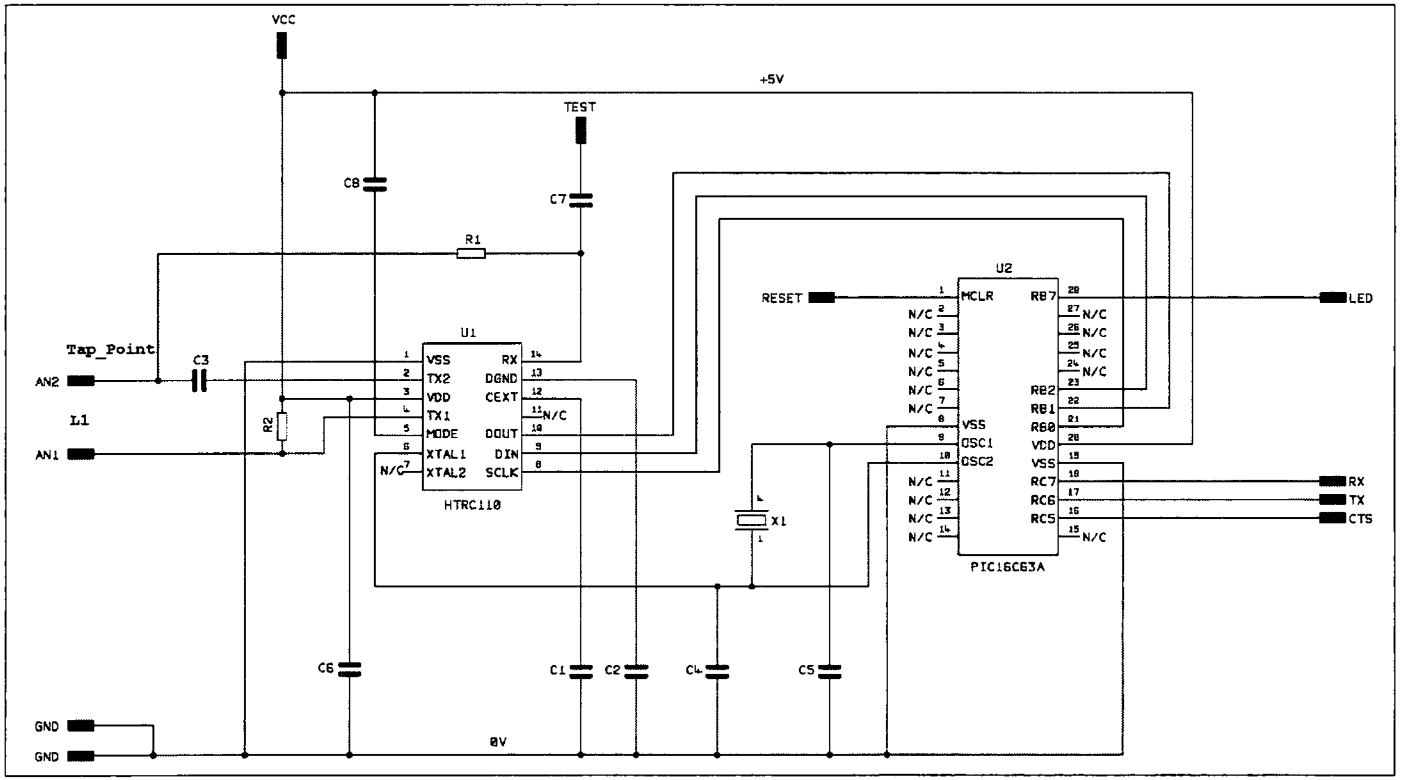

Figure 7.1 Schematic of prototype RFID interrogator showing location of tap point

where A is the carrier amplitude and ω_c is the carrier frequency. Multiplying (2) by a local copy of the carrier signal, $\cos(\omega_c t+\theta)$, where θ accounts for local oscillator phase offset, results in the base band signal, *e(t)*:

$$e(t)=\phi(t)\sin(\omega_c t)$$

$$e(t)=\frac{(m(t)+A)}{2}\left[\cos(\theta)+\cos(2\omega_c t+\theta)\right]$$

$$e(t)=\frac{(m(t)+A)}{2}\cos(\theta) \qquad (4)$$

assuming low pass filtering is implemented to remove higher frequencies. A precise local oscillator phase, θ, is easily achieved in this design because the received signal is intimately linked to the transceiver transmitter and therefore offers the additional benefit of S/N optimisation by adjustment of the detector phase offset.

Following down-conversion, the signal is digitally filtered to remove frequency products and then digitised by a dynamic-average threshold circuit. The resulting FSK digital signal is then decoded by the PIC, which samples the data stream at a rate sufficiently high to distinguish between two frequency bins representing logic levels 1 and 0. Further decoding and processing is performed by the PIC.

7.3.2 Microcontroller – Host Communications

Messages are exchanged between the microcontroller and host, which for development purposes was a standard PC via RS-232 link. An example of a real host in embedded applications would be the processor running inside a PAT unit. Another example would be the processor running inside a PDA[32] adapted to function as a portable RFID

---

[32] Personal Data Assistant

interrogator. In each case a common protocol would be required that allows exchanging of transponder data.

7.3.3 Cable RFID Interrogator

The interrogator design is easily adapted to accommodate cable RFID applications with the addition of a primary resonant tank as described in section 5.8.2, chapter 5. The driver outputs are attached directly to the cable to which the transponder is attached. For the case of Seaward PAT equipment the interrogator circuitry was placed inside the PAT housing and the interrogator drivers switched onto the power cable using relays controlled by the PAT embedded controller. This was performed prior to test phase in order to identify the DUT.

7.4 Software Design

As described above the demodulated, digitised data is sampled and decoded by a microcontroller. In addition, messages are sent to the transponder by field pulsing, which is controlled directly by software routines running in the microcontroller. Software was written in C which provides an element of portability and maintainability, if not the maximum execution speed. This became important when designing the sample and decode routines described below.

7.4.1 Structure

The program structure is shown in figure 7.2, which describes a diagnostic program that searches for transponders placed in the proximity of the reader using a "*set_cc()*" message. This message instigates a response from transponders in the vicinity which reply by sending their unique identification numbers. The recovered identification number is then compared with a locally stored copy to determine whether the recovered code is valid. Running totals of correct and erroneous results are then sent to the host computer for display. Alternative variants of this program include a full read/write program that is capable of reading data from memory and writing new data. We limit our attention here to the *set_cc()* program as an example of the software design.

After initialisation, the program checks for any commands sent from the host computer, an example of which might be a request to alter the demodulator phase setting, and then calls *set_cc()*. This function initiates the relevant field pulsing pattern for transponder identification number request and then waits for a defined period before commencing sampling and decoding. Referring to the state diagram (figure 7.2) several operations are carried out during the wait period, including rapid filter settling routines that accelerates settling of the HTRC110 digital filters. Recall that the receiver is connected directly to the transmit circuit by a voltage divider and therefore field pulsing has the effect of disturbing the digital filters.

The digitised baseband signal is then sampled by a *while* loop that incorporates a variable sample delay:

```
while(DIN != data_sense){
                        DelayUs(1);  //approx sample period is 1us
                        n++;
                        GOT_SAMPLES = HIGH;
                        GOT_SAMPLES = LOW;
                        }
```

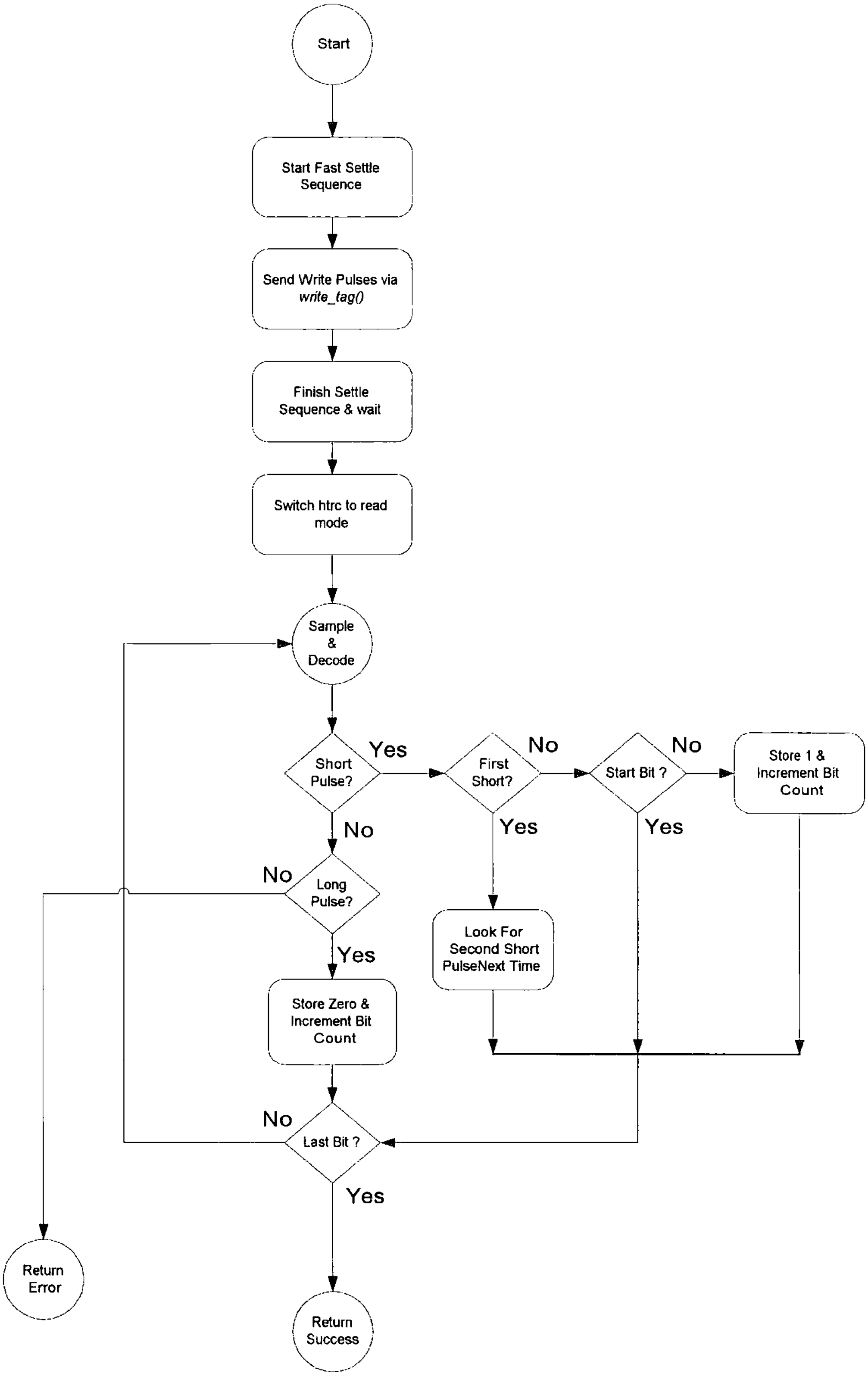

Figure 7.2 Program flow for *set_cc()* operation
(transponder identification requires and receive routine)

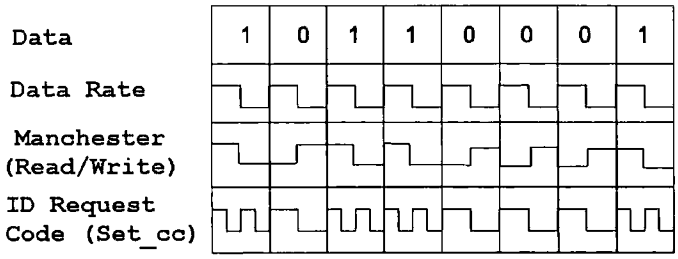

Figure 7.3 Illustration of two codes used in transponder reply messages: Manchester coding for memory read/write operations, and ID request code for identification number request operation

In this code extract, the label *DIN* is equal to the digitiser output from the HTRC110 chip, *data_sense* is a flag that indicates whether the baseband data stream was inverted (see figure 7.4), *DelayUs()* is a function that causes the microcontroller to idle for one microsecond, *n* is the sample count and *GOT_SAMPLES* is linked to an output pin that can be monitored to display the sampling on an oscilloscope. Therefore, if the data stream is not inverted (*data_sense = 0*), sampling occurs whenever the input data signal *DIN* is high. Similarly, the data signal is sampled low if it is inverted (*data_sense = 1*). Sampling stops when *DIN* changes sense once again, at which point decoding takes place. Decoding was implemented as a series of *if* statements that test the number of samples recorded and the previous data history to determine the current logic bit. Note that logic '1' is decoded as two short pluses, while logic '0' is decoded as a single long pulse. This code scheme, illustrated in figure 7.3, is only adopted during transponder identification phase. A different code is used for transponder read and write operations, in the form of Manchester coding, which requires a different decode routine. Note that in order for decoding to proceed in *real-time*, the sample/decode routine must complete within one half of a bit period; sampling occurs over half of each bit period. The shortest available period of 128 μs occurs between each short pulse. An extract of the decoding routine is:

```
...else if( (n >= 12) && (n < 18) ){
```

```
                // we should have found a zero
                data_cpy &= 0xFE;                // write a '0' to the data buffer
                if(data_cnt < 7){
                        data_cpy = data_cpy << 1;
                }
                n = 0;
                data_cnt++;
                BIT_FOUND = HIGH;
                BIT_FOUND = LOW;
                continue;
        }
```

Where the sample bin for long pulses has been set between 12 and 17. A logic zero is recorded in the buffer *data_cpy[]* and a shift operation is performed to accommodate the next bit. Flag *BIT_FOUND* is linked to another output pin for debugging.

Within this *if-else* structure, we may also test for invalid features, such as very short pulses that may have been caused by noise:

```
        ...if( ( n >= 1 ) && ( n < 4 ) ){
                //abort the operation if very short waveforms are detected
                DATA_IND = HIGH;
                DATA_IND = LOW;
                CLK = HIGH;
                return(0);
        }
```

Here, *DATA_IND* indicates that false data has taken place, at which the program responds by pulling *CLK* high to immediately terminate read mode and sending an error message. A screenshot of the actual process during program execution is shown in figure 7.4(a), in which a Hitag transponder identification number is being sampled and the *GOT_SAMPLES* and *BIT_FOUND* flags updated after decoding. Decoding is carried out between sampling operations. In figure 7.4(b) the data stream has been inverted by adjusting the synchronous demodulator phase. Sampling now occurs on low parts of the digital stream since variable *data_sense* has inverted and the same identification number is recovered.

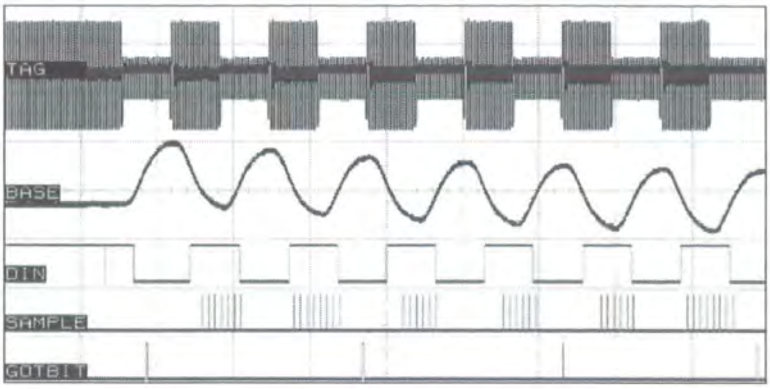

(a)

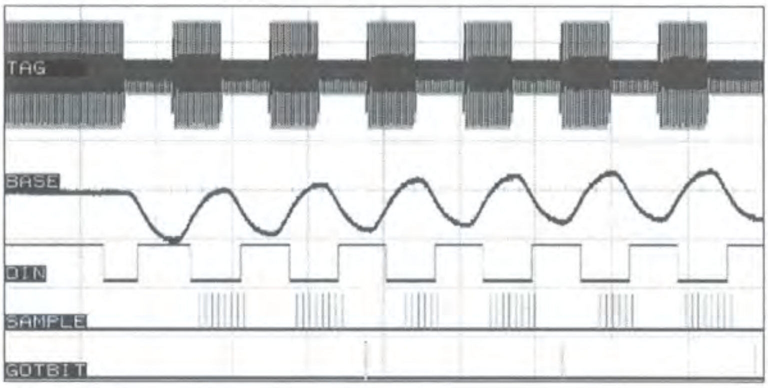

(b)

Figure 7.4 Waveforms showing sampling and decoding of transponder identification number. (a) non-inverted Signal, (b) inverted signal (achieved by adding 180° to demodulator phase). Waveforms in each window are (from top to bottom): transponder coil voltage, analogue baseband signal, digitised baseband signal, *GOT_SAMPLES* flag; and *BIT_FOUND* flag.

7.4.2 Improvements

Using the above method, the sample rate achieved was 59 kHz. To achieve higher resolution, the *DelayUs()* call was removed from the sampling loop, in which case the sample rate is determined by the instruction execution rate and the number of instructions per loop iteration. This gave a maximum possible sample rate of 77 kHz. However this approach could result in ill-defined sample rates on a different target PIC microcontroller, thus requiring re-adjustment of the sample bins. Note that the sample rate is actually dominated by the total instruction time per cycle, rather than *DelayUs()*, a consequence of using compiled C code rather than assembly code.

An alternative approach to the software-based sample and decode method would be to utilise hardware timer-capture blocks available on the PIC16C63A. This method would use a hardware interrupt that is configured to halt a timer following a transition of *DIN*. The pulse width would be determined from the timer value at a sample rate determined by the timer frequency which, for the 16C63A, can be set to a maximum frequency of 1 MHz assuming a 4 MHz oscillator crystal. Higher sample rates could be achieved by using a faster clock, but note that this would also require alteration of the HTRC110 clock frequency, on the assumption that a single crystal resonator is to be used in the design. Hardware sampling was not implemented for two reasons, the first being that increased sample resolution was not required, and second being that software portability is reduced.

7.5 Performance Evaluation

Transmitter performance is assessed by available field strength, susceptibility to de-tuning and the quality of field-gap modulation. The most critical receiver performance factor is the available signal to noise ratio appearing at the demodulator output, which places special emphasis on transmitter-receiver isolation.

7.5.1 Transmitter Parameters

The HTRC digital driver was found to be cable of sustaining 100 –200 mA of continuous current, though self-induced noise increased above 100 mA (see section 7.5.2.2.). Transmitter voltage was 5 V p-p which complies with low voltage regulations when using the interrogator in cable RFID applications. IEC 1010 limitations for hazardous voltage limits under normal operating conditions are defined as 30 V RMS. The current-driven nature of the inductive coupled transponder permits high current / low voltage operating conditions.

7.5.2 Factors Influencing Receiver Performance

Sources of noise manifest primarily from the transceiver itself in the form of switching noise caused by the digital drivers. External noise sources are less likely to couple to the interrogator or transponder coils in this system, since the quasi-static near-field region is used.

7.5.2.1 SNR: External Noise Sources

External noise sources couple either to the inductive antenna or directly to tracks on the PCB. Coupling via the inductive antenna is primarily inductive due to the low circuit impedance and is therefore dominated by flux coupling to the antenna. The interrogator and transponder coils posses very low radiation resistance because they are small in comparison with electrical wavelength and therefore receive very small amounts of radiating energy. Antenna radiation resistance is used to quantify the energy radiated by an electrically large antenna (whose size is of the same order as the electrical wavelength) and also quantifies energy scattered by receiving antennas. In [Balanis] Balanis derives an expression for the radiation resistance of electrically small loops (for which the current density is assumed constant around the loop circumference):

$$R_r = 31171 \cdot N^2 \left(\frac{C}{\lambda} \right)^4 \qquad (5)$$

where R_r is the radiation resistance, N the number of loop turns, C the loop circumference and λ the electrical wavelength. For Coil A, described in table 4.2 of chapter 4, this would equate to 3.65×10^{-8} Ω at the operating frequency of 125 kHz, which is negligible in comparison to copper resistance (12.7 Ω). Furthermore, out of band electromagnetic radiation has reduced influence because the transponder and interrogator both employ forced-resonance. Therefore prime sources of external interference are limited in-band sources placed sufficiently close to the interrogator antenna that near-field interaction occurs. Such interferers include other Short Range Devices (SRDs) operating in the same band and may include other RFID interrogators. The specific problem of co-interference between multiple RFID interrogators has been considered by Engels in [Engels]. Engels proposed a frequency assignment problem similar to that used in cellular systems, with the difference that little or no functionality is provided by the transponder to assist in the allocation process. However it is assumed that interrogators radiate omnidirectionally, which is not generally true of inductive RFID systems and so it is difficult to define interference zones for these devices. For the system under consideration interference characteristics of a co-channel interferer were observed by placing a second interrogator (simulated by a coil connected to a signal generator) close to the original interrogator coil. This produced the effect of causing strong disturbance to the transponder voltage and interrogator tap point voltage, particularly when A.M. modulation was applied to the interferer signal. Additional modulation products appear in the carrier, disturbing the transponder reply message. In addition, the interferer effectively "jammed" field-gap modulation by exciting the transponder between field gaps. Determination of the exact limitations of interrogator spacing will be critical in high volume applications such as product chain tagging.

7.5.2.2 Inherent (Self-Induced) Noise Sources

The principal source of self-induced noise can be attributed to coupling between the digital transmitter and demodulator input pin. The RFID radio system is unusual in that a small portion of the transmitted signal is directly coupled into the receiver in order to detect the received message and that signal transmission and reception must occur synchronously for passive operation. Due to the use of digital drivers in the transmitter, harmonics of the (filtered) transmit signal inevitably couple to the receiver during switching, albeit with high attenuation,. This coupling mechanism is capacitive due to the impedance of the demodulator input, which must be high impedance to isolate the receiver from the high transmission line current and to reduce the tap point voltage. It was found that for proximity and cable RFID applications switching noise must be minimised to reduce the likelihood of bit errors produced by the digitiser. In figure 7.5 the switching noise can be seen, which manifests as damped oscillations that are synchronous with the transmission driver switching. Reduction of switching noise was achieved by placing the RF transceiver on a PCB with appropriate track routing.

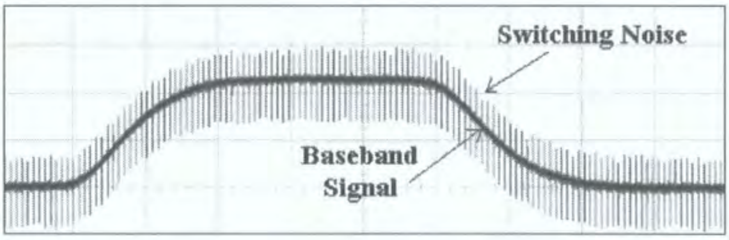

Figure 7.5 Switching noise at analogue demodulator output due to coupling of digital transmitter signal.

7.6 Transponder "Energy Range"

The "energy range" of a proximity RFID system may be estimated by considering the available transmit power, the transponder power consumption and system geometry. Finkenzeller derived the relevant equation from the transponder equivalent circuit [Finkenzeller], so a derivation is not given here. The minimum field strength, H_{min}, required by a transponder having coil area, A_{tag}, N_{tag} turns and minimum peak activation voltage, V_{tag_min}, is given by:

$$H_{\min} = \frac{V_{tag\_\min}\sqrt{\left(\frac{\omega L_2}{R_L}+\omega R_2 C_2\right)^2+\left(1-\omega^2 L_2 C_2+\frac{R_2}{R_L}\right)^2}}{\omega\mu_0 A_{tag} N_{tag}} \qquad (6)$$

where L_2 is the coil inductance, R_2 the coil resistance, R_L the chip resistance, C_2 the total secondary capacitance and ω the system frequency. The peak interrogator antenna current, I_{ant_peak} is defined as:

$$I_{ant\_peak} = \frac{\pi}{2}\left(I_{DC} - I_{chip}\right) \qquad (7)$$

where I_{DC} is the DC supply current and I_{chip} is the nominal chip current consumption. Equation 7 relates the DC current to the average of the oscillating resonant antenna current. It is then possible to rearrange equation 6 from section 3.2.1, chapter 3 to find the estimated achievable transponder/interrogator separation distance, d_{max}, for the given current and minimum field strength requirement:

$$d_{\max} = \sqrt{\sqrt[3]{\left(\frac{I_{ant\_peak} N_{reader} a_1^2}{2H_{\min}}\right)^2} - a_1^2} \qquad (8)$$

where a_1 is the interrogator radius and N_{reader} is the number of interrogator antenna turns. Using the parameters given in table 7.1 (which relates to the use of interrogator coil C as described in section 4.3.3, chapter 4 and a transponder constructed using coil D described in the same section), the approximate energy range was calculated to be 4.8 cm. This corresponds closely to the maximum range at which the transponder activated.

Parameter	Value
R_L	80 kΩ
R_2	210 Ω
C_2	210 pF
L_2	7.34 mH
A_{tag}	4.119×10^{-4} m^2
N_{tag}	460
Frequency	125 kHz
V_{tag_min}	4 V (peak)
a_l	0.8 cm
N_{reader}	230
I_{dc}	36 mA

Table 7.1 Proximity system parameters used for calculation of energy range

We may use equation 7 to investigate how d_{max} is dependent on the interrogator antenna radius by expressing equation 7 as a function of a_l to create the graph shown in figure 7.6. The achievable separation distance reaches a maximum when the interrogator antenna radius is approximately 1 m giving a range of 0.71 m. The relationship $d_{\max} = a_1/\sqrt{2}$ stated in section 3.2.2, chapter 3 is confirmed. To extend the range further, one or more of the following would have to occur (assuming fixed frequency):

1. increase transponder coil area or number of turns;
2. increase interrogator current;
3. reduce interrogator/transponder coil losses (increase quality factors);
4. reduce chip activation voltage.

The equations described here along with those in chapters 3 and 5 could be used to perform a sensitivity analysis to determine which parameters yield the greatest range benefits.

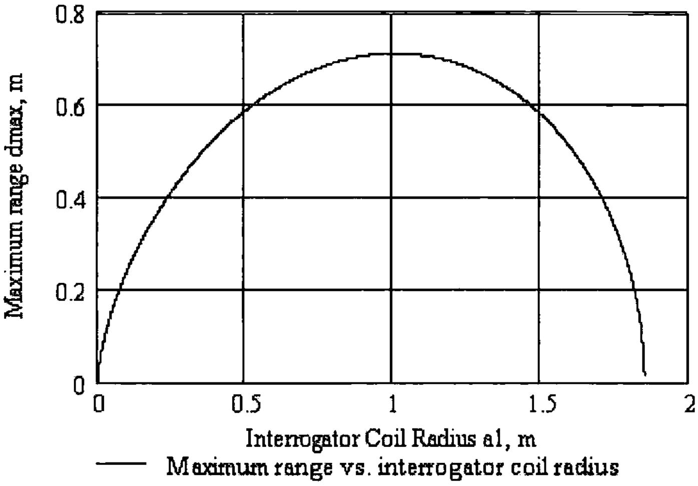

Figure 7.6 Energy range versus interrogator coil radius, showing maximum range when $d_{\max} = a_1 / \sqrt{2}$.

7.7 Compensation of Interrogator and Transponder Tuning Offset

The equations that describe the fundamental coupling mechanism were described in chapter 5. These equations are also applicable to situations in which the degree of coupling is variable allowing comparison between cable RFID and proximity RFID methods. The overriding characteristic of proximity RFID lies in the extreme variation of coupling coefficient which may vary between 0.01 % and close to 100 %. (One of the defining characteristics of cable RFID is the stability of the coupling coefficient, which typically takes the value of 90-97 % and remains comparatively constant.)

With this in mind, we repeat the process described in section 5.9, chapter 5, to calculate the effect of transponder and interrogator tuning on the demodulated signal given by equation 3:

$$e(t) = \frac{(m(t) + A)}{2} \cos(\theta)$$

We see that by varying *θ*, i.e., the detector sampling phase, a maximum baseband signal strength may be found by matching to the angle of load modulation.

7.8 Occurrence of Critical Coupling

When mutual inductance exists between two resonant circuits, a condition of critical coupling may occur. This effect was described by Terman [Terman] by finding the maximum possible secondary current as a function of coupling factor k and relating the condition to primary and secondary Q as follows:

$$k_{critical} = \frac{1}{\sqrt{Q_{primary} Q_{secondary}}} \tag{9}$$

where $k_{critical}$ is the critical coupling coefficient and $Q_{primary}$, $Q_{secondary}$ are the isolated primary and secondary circuit quality factors. This theory was originally developed to understand coupling mechanisms between valve-based radio frequency devices using large coils that could interfere when $k_{critical}$ is exceeded. When this occurs the secondary current are reduced. This effect is illustrated in figure 7.7 for a simulated proximity RFID system comprising interrogator coil inductance of 1 mH and transponder with open-circuit terminals and coil inductance 0.7 mH. Primary and secondary circuit losses were 26 Ω and 10 Ω respectively resulting in quality factors of 21 and 2.7 when tuned to 125 kHz. By equation 8 critical coupling occurs at 0.039, as indicated in figure 7.7. For $k \geq k_{critical}$, double peaks may occur at higher and lower frequencies than the intended resonant frequency which may cause interfere with other devices. The condition for occurrence of double humps is [Terman]:

$$k \geq k_{critical} \left[\frac{1}{2} \left(\frac{Q_{primary}}{Q_{secondary}} + \frac{Q_{secondary}}{Q_{primary}} \right) \right]^{\frac{1}{2}} \tag{10}$$

If $Q_{primary} = Q_{secondary}$ twin peaks always occur when $k \geq k_{critical}$, and when $Q_{primary} \neq Q_{secondary}$ occurrence of twin peaks is dependent on the Q ratio.

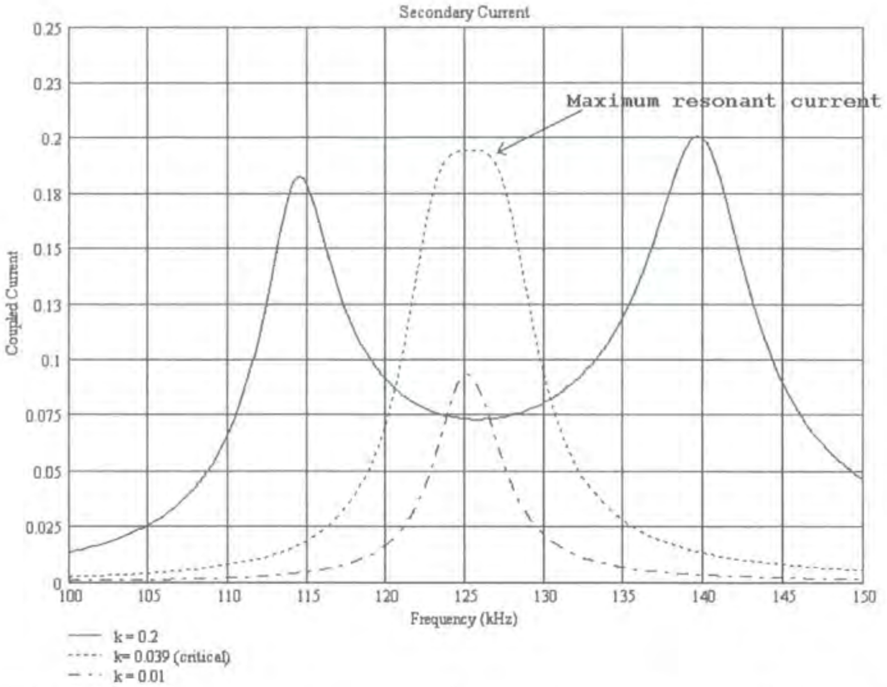

Figure 7.7 Proximity transponder current for various coupling coefficients showing maximum current at critical coupling coefficient

It is possible to show the variation of transponder current as a function of coupling coefficient at the intended resonant frequency, as shown in figure 7.8. It is seen that the point of maximum output is dependent on the transponder load because this determines secondary Q and therefore $k_{critical}$. Furthermore, for the simulated transponder considered (which is similar to actual 125 kHz transponder characteristics), critical coupling occurs at relatively weak coupling levels even when load modulation is active. These parameters must be carefully considered when planning an RFID system to avoid serious dampening when the transponder is located close to the interrogator.

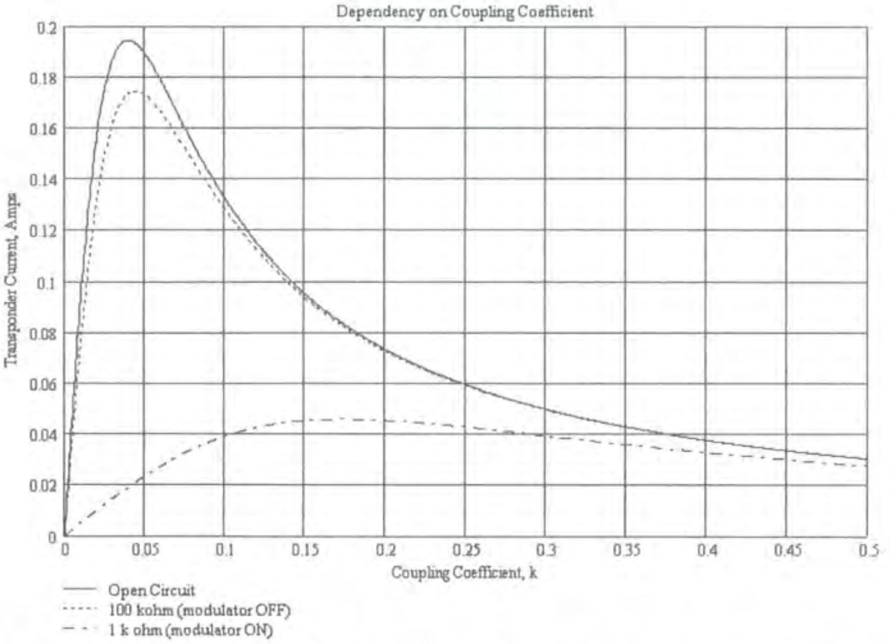

Figure 7.8 Variation of proximity transponder current with coupling coefficient showing maxima related to critical coupling.

The dampening phenomenon was encountered during evaluation of a commercial RFID interrogator[33] when a large transponder was used. The transponder voltage was measured for separation distances between 0 and 300 mm and revealed dampening of the transponder voltage due to exceeding critical coupling (figure 7.9). This was especially pronounced while the interrogator and transponder coils were coaxial and coplanar, and less so when the coils were orthogonally arranged.

---

[33] Interrogator manufactured by A&Z (Automatisierungs und Zeitsysteme), type ICR30.

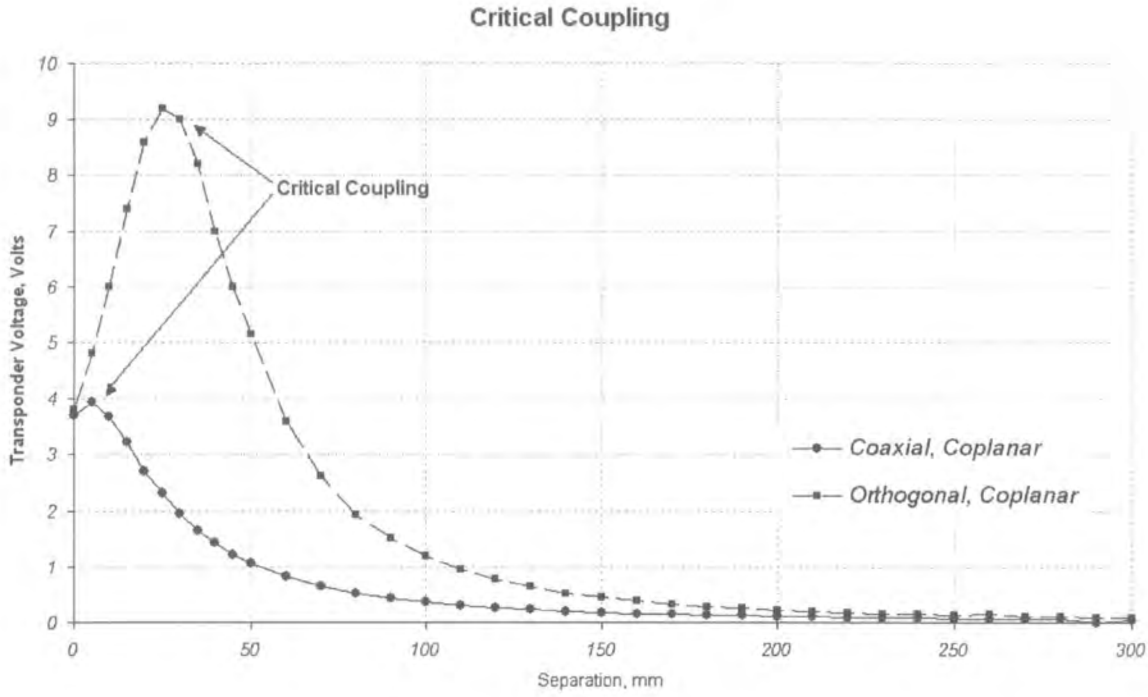

Figure 7.9 Demonstration of occurrence of critical coupling in commercial RFID interrogator and high-Q transponder.

7.8.1 Critical Coupling and Cable RFID

In chapter 5 a cable RFID concept was developed that uses a non-coupled primary resonant circuit (see section 5.8.2). To correctly analyse the onset of critical coupling the primary resonant circuit should *not* be included in calculating primary Q because there is no direct coupling between the primary resonance inductor (L_{prim}) and the coupler secondary. The only component of primary inductance that contributes toward critical coupling is the inductance, L_1, of the primary coupler. See figure 5.27 for an illustration of primary component positions. Since coupler primary inductance is generally very small, critical coupling is not reached even for the relatively high coupling coefficient present. The combination of self-losses of L_{prim}, quantified by R_{prim}, and current limiting resistance dominate primary losses and tend reduce overall primary Q such that critical coupling can *never occur*, that is, $k_{critical} \geq 1$.

The effect is illustrated by extending the example given in section 5.8.2., chapter 5. Considering the same parameter values, secondary Q values between 8.7 (load modulator OFF) and 2 (load modulator ON) occur. The primary Q is only 0.037 due to small primary inductance at the operating frequency of 125 kHz. The resulting critical coupling coefficient, $k_{critical}$, is found using equation 8 to be 3.8 which can never be achieved[34] and so reduction of secondary current does not occur provided primary losses do not decrease. We may calculate primary current using:

$$I_{primary} = \frac{V_{in}}{R_{prim} + j\left(\omega\left(L_{prim} + L_1\right) - \frac{1}{\omega C_{prim}}\right) + \frac{\left(\omega k\sqrt{L_1 L_2}\right)^2}{Z_{secondary}}} \qquad (11)$$

noting that coupled impedance is determined only by coupler inductance (L_1, L_2) and not by L_{prim}. Parameter values were defined in section 5.8.2., chapter 5. The characteristic is confirmed by graphing transponder current for various coupling coefficients and for each transponder load condition (figures 7.10 and 7.11), whereupon critical coupling is entirely absent.

---

[34] k must take a real value less than or equal to 1.

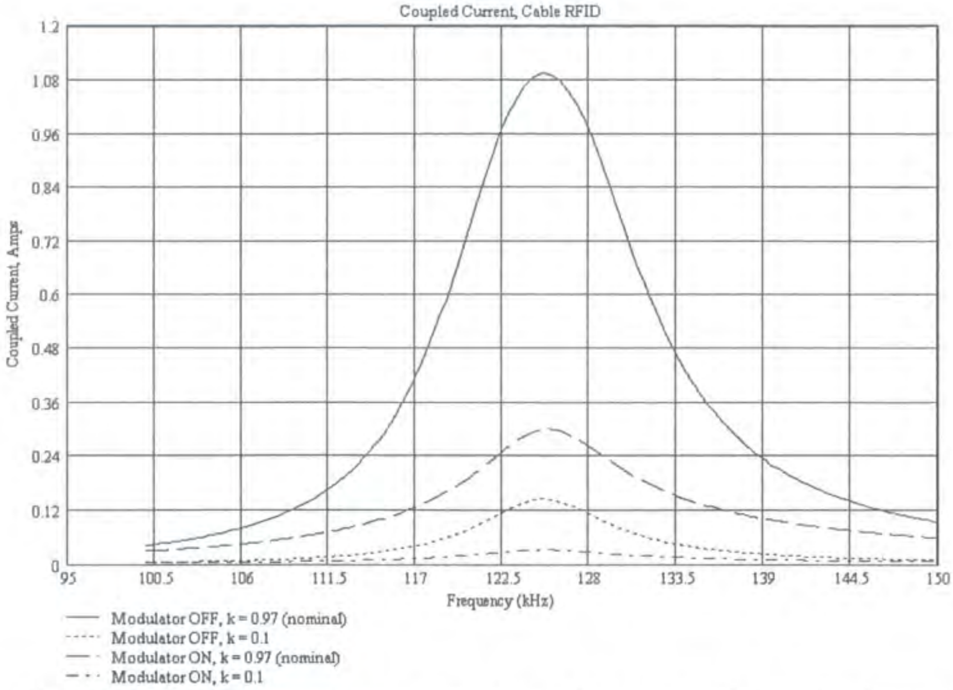

Figure 7.10 Cable RFID transponder current as a function of frequency for various *k* and transponder modulator behaviour. Modulator OFF/ON resistance is 100 kΩ / 1 kΩ respectively.

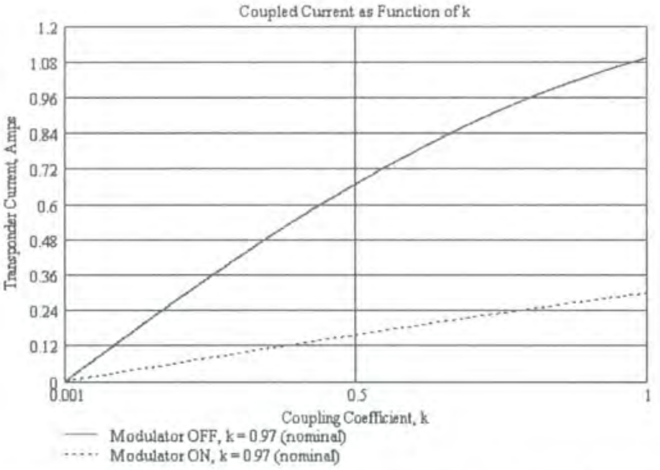

Figure 7.11 Direct variation of cable RFID transponder current as a function of coupling coefficient, showing absence of critical coupling.

The fact that critical coupling is less evident (or completely absent) in cable RFID configuration is beneficial because out-of-band emissions are minimised and design of the primary resonant circuit made easier in the knowledge that conditions for critical coupling are independent of inductance L_{prim}.

7.9 Summary

In this chapter a prototype RFID interrogator has been described that is suitable for proximity and cable RFID applications. The design was also used to signal across the live power-line as described in chapter 9. The signalling method was described along with the unusual nature of the RFID radio circuit. It was stated that external noise sources are generally confined to other proximity interrogators and in-band inductive sources since the interrogator and transponder form a direct near-field link and the inductive coils have very low radiation resistance that is far-outweighed by the copper loss thus rendering susceptibility to radiating waves negligible. Performance factors such as "energy range", tuning offsets and critical coupling were described from a theoretical perspective and validated by measurement. In particular it was shown that critical coupling generally does not occur when using cable RFID due to decoupling of the transponder and primary inductance.

8 *A Two Wire Coupler Design*

8.1 Introduction

As a practical solution, the common-mode coupler described in Chapter 4 has one principal disadvantage imposed by the magnetic circuit arrangement in that either live or neutral wire must be used exclusively during coupling; the transponder may not encircle both conductors. This limits scope of the potential embedded applications to those in which it is possible to separate the live and neutral wires. Applications that employ two or three-core insulated power cable (i.e., live, neutral and earth) require that the coupler is fitted either inside the appliance (during manufacture) or within part of the existing cable and plug assembly (e.g., within the fuse).

In this chapter we investigate a differential-mode coupler, that is, one which operates with live and neutral wires enclosed by the coupler core, thereby enabling it to fit around two or three-core power cabling. The concept was conceived from a patent held by Watson [Watson], who describes a device for "Sensing Electrical Currents". The arrangement was intended for use in a differential-mode current sensor and utilises a magnetic core placed around two current-carrying conductors. The currents are differential, i.e., in opposing directions. A highly sensitive detector circuit is connected to coils (comprising a few thousand turns) placed around the core that produce an output voltage representative of the current flowing through the conductors. The primary disadvantage encountered using this method lies in calibration; it is difficult to provide an accurate current measurement when variations in conductor spacing and orientation occur. In this chapter, an alternative embodiment of the design is investigated that aims to provide sufficient coupling for passive direct-load modulation.

This creates design constraints that contrast with Watson's active design, such as minimal winding loss leading to fewer winding turns and increased power output resulting from greater conductor separation. It will be shown that such an arrangement is possible and enables passive direct-load modulation signalling, provided certain criteria are met, including a suitable core geometry; minimum live and neutral wire spacing and suitable placement of the coupler windings.

8.2 Modelling a two-wire inductive coupler

8.2.1 Principle of operation

It is well known that two wires placed coaxially produce net zero magnetic flux field around the immediate external region[35]. If we place two wires close to each other, but not coaxial, and pass current in opposing directions through the wires, a net field exists close to the conductors, while at distance the field is nearly zero. The following equations can be used to describe the internal and external field produced by a single conductor [Dugdale]:

$$H_r(r) = \frac{I}{2\pi r} \quad (\mathrm{r} > \mathrm{a}) \quad (1) \qquad\qquad H_{cond}(r) = \frac{Ir}{2\pi a^2} \quad (\mathrm{r} \le \mathrm{a}) \qquad (2)$$

Where H_r is the external radial field strength, H_{cond} is the internal field strength, r is the radial distance from the conductor centre, I is the conductor current and a is the radius of the conductor. With constant radius the field holds for all positions around the conductor, so that the relationship is either $H \propto 1/r$ (external to the conductors) or $H \propto r$ (inside the conductors). The eddy current effect may be ignored for the frequencies of interest here (< 1 MHz).

---

[35] R.F. coaxial cable employs this arrangement: a small gap between the inner and outer conductor supports the propagating wave, the intention being that field components sum to zero outside the cable, preventing radiation.

Referring to figure 8.1, if the two wires separated by distance, *d*, carry differential currents of equal magnitude then for *r* much greater than *d* the net field will be approximately zero. In this situation the magnitude of the individual fields are approximately equal and opposing. In contrast the field vectors between conductors 1 and 2 sum. We can use equations 1 and 2 to construct a piece-wise graph of the field as a function of *r* in the plane intersecting both conductors. Shown in figure 8.2, the resulting profile of *H* has a strong region between the conductors, which falls at the mid-point between the conductors. Note that in the chosen plane *H* vectors simply add or subtract (an upward net vector is indicated by positive *H* values, downward net vectors by negative *H* values).

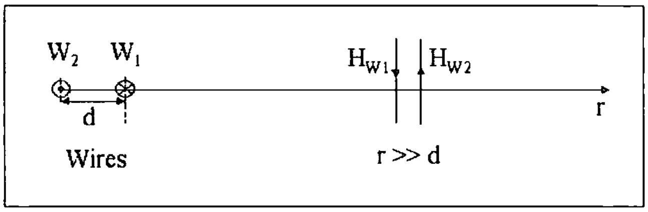

Figure 8.1 External field component due to wires 1 and 2, where each wire carries opposing currents. At distance, the combined field is close to zero.

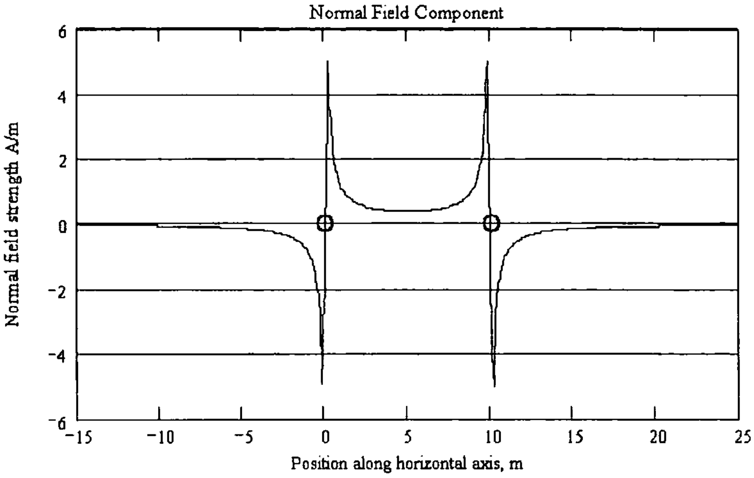

Figure 8.2 Resultant tangential magnetic field strength component along horizontal axis produced by two conducting wires along the horizontal axis. Conductor spacing is 10 cm and conductor radius 0.2 cm.

In figure 8.2 we also see the rapid decay of the field in regions not between the conductors. By considering the field equations it can be shown that the field strength at the mid-point between the conductors is inversely proportional to d and equal to $2I/\pi d$. Therefore when moving the conductors closer together, a stronger field is produced at mid-point, as illustrated in figures 8.3 and 8.4.

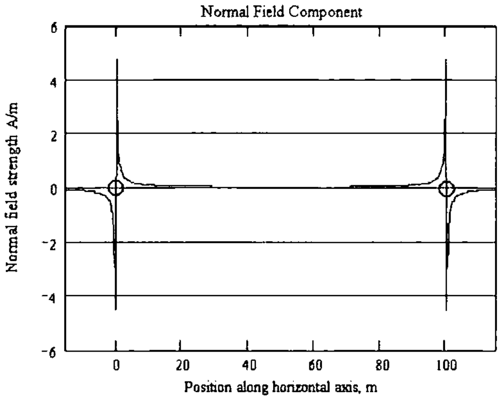

Figure 8.3 Magnetic field strength for
d = 100 cm, a = 0.2 cm

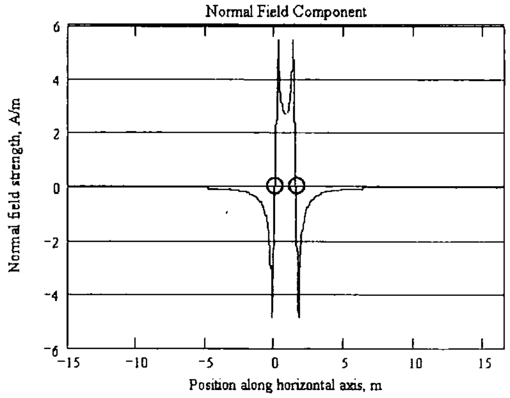

Figure 8.4 Magnetic field strength for
d = 1.5 cm, a = 0.2 cm

8.3 Field simulation for Symmetrical Winding Disposition

The field vectors do not sum in straightforward fashion for other planes in the region around the conductors, but it is possible to find the vector field in the region surrounding the conductors by field simulation. In figure 8.5, the result from a boundary field simulation is shown in which the flux pattern resulting from the two wires can be seen encircling the conductors. Each contour denotes a region of constant magnetic field strength. It shows the effect of placing a boundary condition such that the magnetic potential, A, is zero at the edges of the box. This is one possible boundary condition required to compute a solution. The horizontal bold line indicates the same plane as in figure 8.1, and the resulting flux density variation calculated by the simulation is shown in Figure 8.6. The profile agrees with that of that previously calculated.

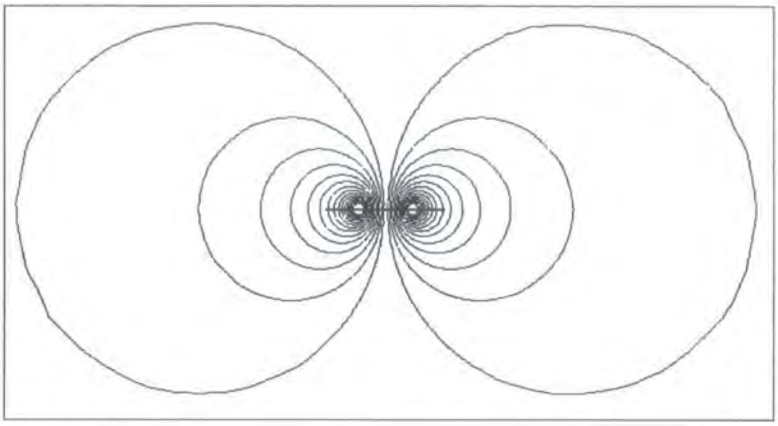

Figure 8.5 Magnetic flux surrounding a wire pair carrying opposite and equal current.

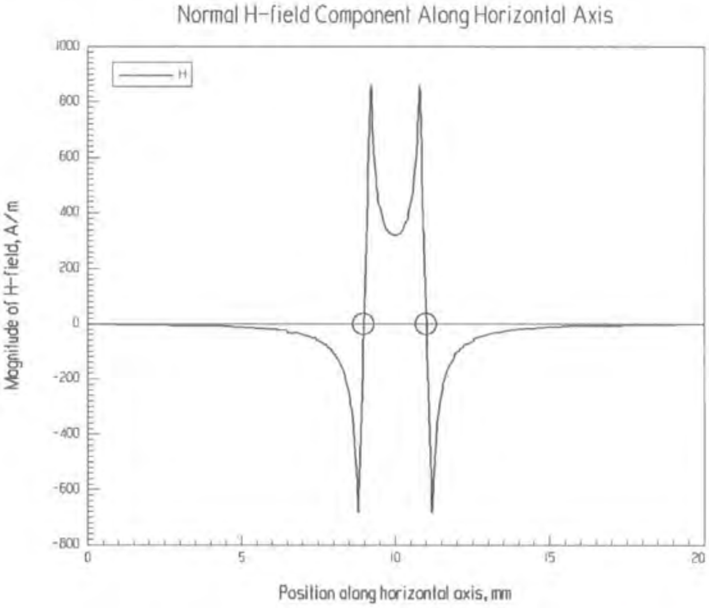

Figure 8.6 Simulated field strength variation along the line indicated in figure 8.5.

8.3.1 Variation of H field in the two wire coupler

In principle, a magnetic medium placed around the conductors should enhance the magnetic field strength at certain locations. By placing coils at in these regions, it would be possible to extract power from the current-carrying conductors. If a magnetic core with a relative permeability equal to 1000 is added to the region surrounding both conductors the field plot changes somewhat, as shown in figure 8.7, which shows the distribution of magnetic flux density surrounding the conductors and inside the core. The field pattern was generated using Maxwell 2D as a plane based simulation[36]. We see that the core influences the magnetic field such that it becomes drawn towards each end of the inner circumference of the core, concentrating the field next to the conductors. Flux must traverse an air path between the conductors, and this dominates path reluctance and hence the self-inductance of coils placed around the core. Geometrical symmetry forces this pattern. A profile of the flux density along the white line is shown in Figure 8.8, where the enhanced field in the core can be seen at the far extents of the graph. The fact that the flux density magnitude is significantly higher in the core than the region between the conductors highlights the useful effect of the magnetic core in bringing energy to the edge of the coupler. In comparison a single wire produces a considerably stronger peak field magnitude in the core, which explains why the single-wire coupler described earlier is favoured on the basis of performance, if not for practical reasons.

---

[36] Plane based simulations are conducted in the x-y plane and assume uniformity in the z axis.

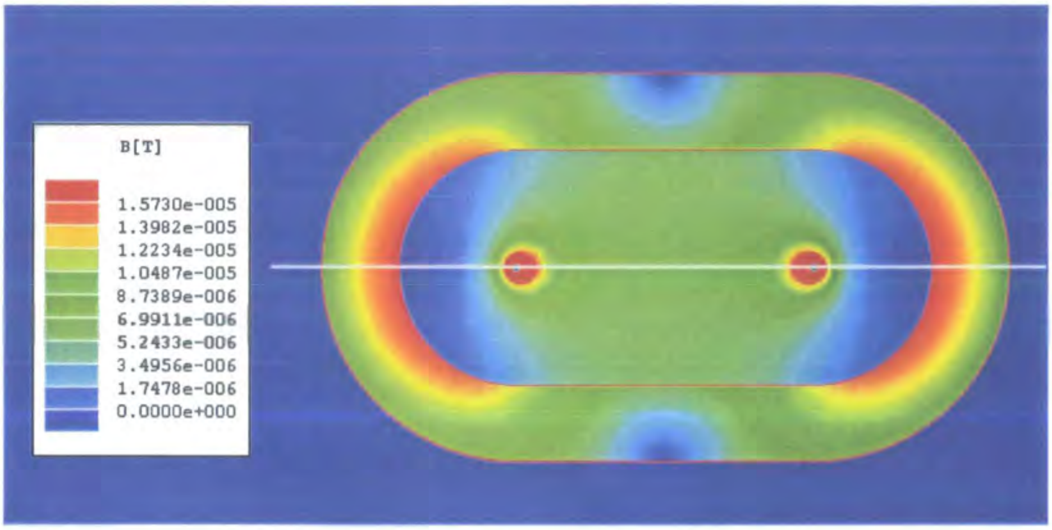

Figure 8.7 Magnetic flux density pattern produced by placing magnetic core around the differential wire pair. Relative permeability of core = 1000.

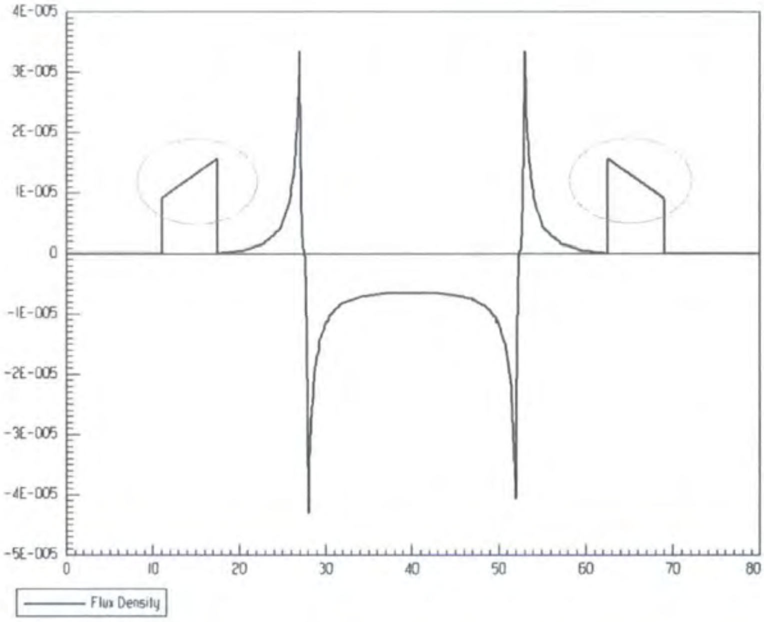

Figure 8.8 Variation of flux density along the white line indicated in figure 8.7 using two conductors. Circled regions show locations of strong flux within the core.

It is clear from figure 8.7 that windings should be placed around the core in the red regions where the B field is strongest, but only in those regions. Their placement is shown in Figure 8.9(a). It is important to realise that if a coil were placed around the entire core circumference, it would experience net zero flux. The reason for this lies in the magnetic flux paths surrounding the individual conductors (see figure 8.9(b)). This principle is used in so-called 'current compensated' toroidal windings employed for inductors used in line filters [Williams], the intention being to eliminate core saturation in the presence of differential balanced currents (i.e. the 50/60 Hz mains current) whilst presenting a high impedance to any common-mode current by via flux excitation in the core. Common mode signals are then attenuated by the combined inductive and resistive component of core permeability, whose loss tangent is chosen to be significant at higher frequencies, where noise signals tend to exist). In the present design, we should try to maximise the field produced by differential currents. Ampere's circuital law applied round the circumference of the magnetic core's cross-section (assuming static conditions) is:

$$\oint_{core} H.dl = \sum_{total} I \qquad (3)$$

A complete path around the core encloses net zero current since current through one wire opposes that through the other, thus we see that a coil placed around the circumference experiences net zero magnetic field.

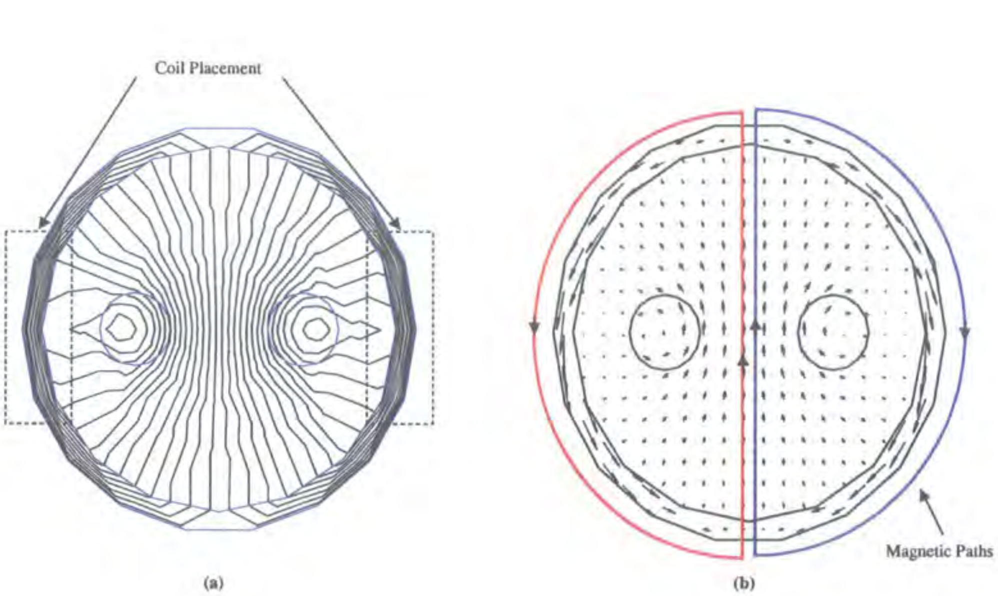

Figure 8.9 Two-wire coupler concept. (a) coil placement, (b) magnetic flux paths present in the design

8.3.2 Effect of permeability, conductor separation

In this section we investigate how flux in the core varies with core permeability and conductor spacing. A circular core is assumed with inner radius of 7.5 mm and outer radius of 11 mm. This is similar to the ferrite cores described in chapter 5. In figure 8.10 the relative core permeability is 1000 and is assumed to have infinite resistivity. The conductors each have a radius of 0.5 mm, pass 100 mA at a frequency of 125 kHz in opposing directions and are separated by 6 mm. The resulting flux pattern shows clear symmetry about the axis of vertical core symmetry. Flux is concentrated at each side of the core on the horizontal axis of symmetry, where transponder coils would be placed. The total peak flux passing through on leg of the core (see horizontal line marked on figure 8.10) was calculated by integrating the flux density over the cross section area. The nominal depth is 1 m giving flux units of Wb/m. Figures 8.11, 8.12

and 8.13 show examples of three combinations of core permeability and conductor spacing. It is interesting to note in figure 8.11 that the non-magnetic core (μ_r = 1) produces the same field pattern as seen in figure 8.5 where the core was absent. This procedure was repeated for various values of core permeability and conductor separation and the graph shown in figure 8.14 constructed that shows the variation of core flux. We see from the figure that increasing core permeability brings about an increase in flux until μ_r = 1000. Higher values of core permeability bring little benefit because the magnetic path is then dominated by the reluctance of the air path. Furthermore, core permeability brings about a similar increase of flux for each conductor spacing, although the relative benefit appears to increase as the conductor spacing increases. This assumption was tested by calculating, for each conductor spacing, the increase of core flux created by increasing relative core permeability from 1 to 10. The resulting graph (figure 8.15) shows that the relative benefit in fact *decreases* as the conductor spacing increases.

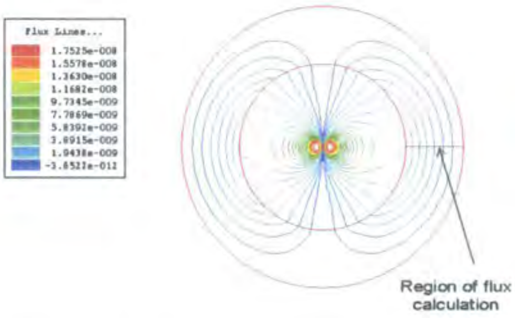

Figure 8.10 Flux pattern in circular core. Conductor spacing 6 mm, μ_r = 1000. Region of flux calculation shown by horizontal line at right side of core

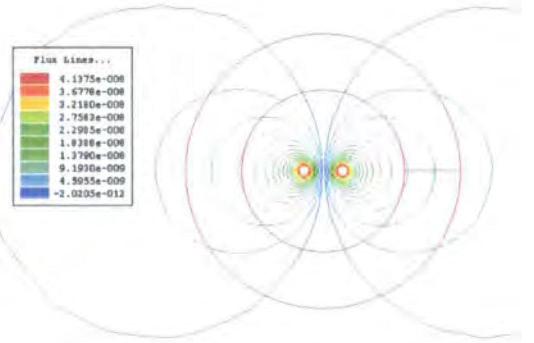

Figure 8.11 Flux pattern in circular core. Conductor spacing 6 mm, μ_r = 1.

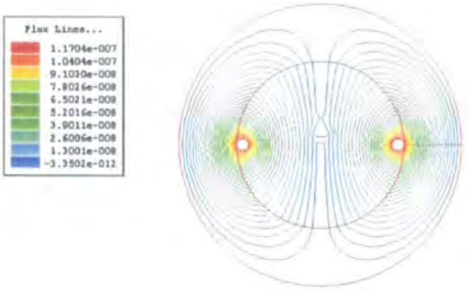

Figure 8.12 Flux pattern in circular core. Conductor spacing 12 mm, $\mu_r = 1000$.

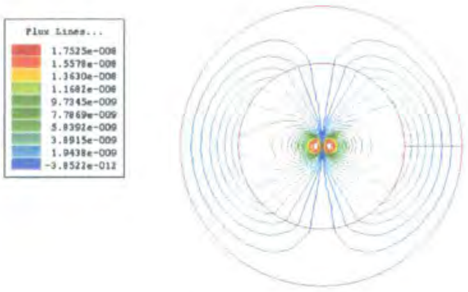

Figure 8.13 Flux pattern in circular core. Minimum conductor spacing, $\mu_r = 1000$.

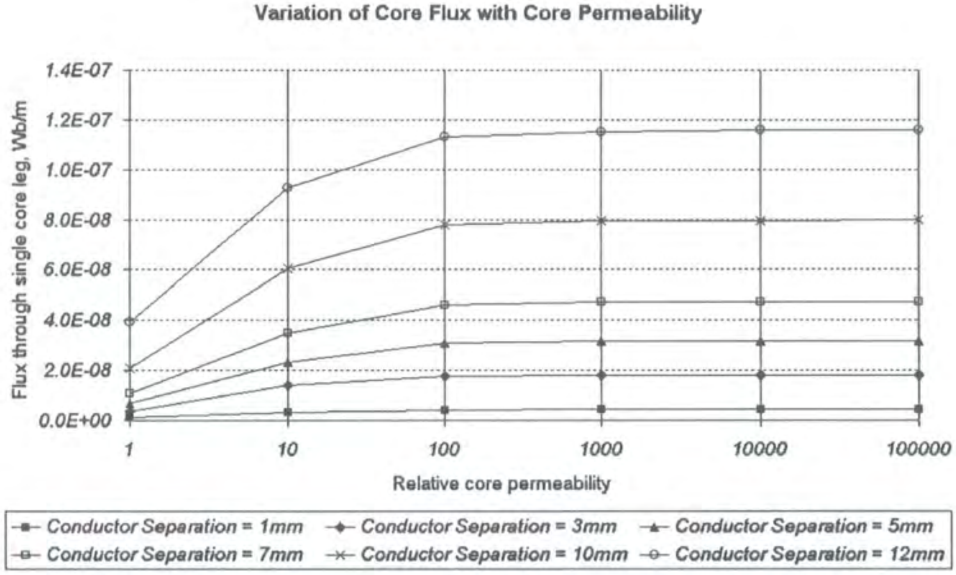

Figure 8.14 Variation of core flux with core permeability and conductor spacing for circular core described in the text.

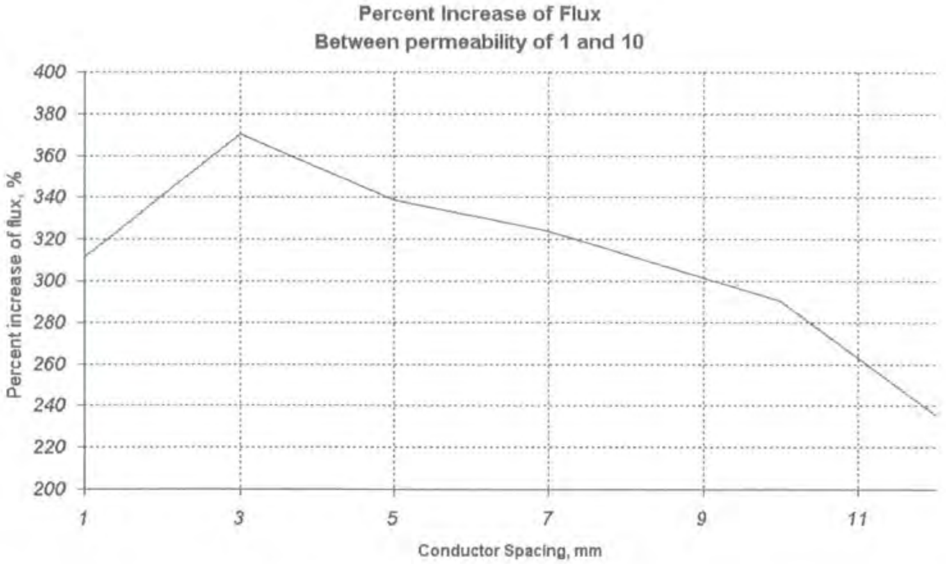

Figure 8.15 Percent increase in flux between relative core permeability 1 and 10, versus conductor spacing.

8.3.3 Energy distribution in the two wire coupler

Using two conductors causes energy to be stored between the conductors in the air gaps of the magnetic circuits. However, in order to convert the stored energy into electrical energy we now place coils around the core. In figure 8.16 we see the basic configuration of the two-wire coupler.

Storage of energy in the air gap may be demonstrated by referring to figure 8.17, which shows energy distribution from the computer simulation. The dark regions indicate areas of high energy. In the case of a single wire with no core, the field energy is strongest near the conductor figure 8.17(a), however with the presence of a core (figure 8.17(b)), energy is concentrated in the core. In figure 8.17(c), a wire pair with core results in energy appearing in the low permeability region between the wires.

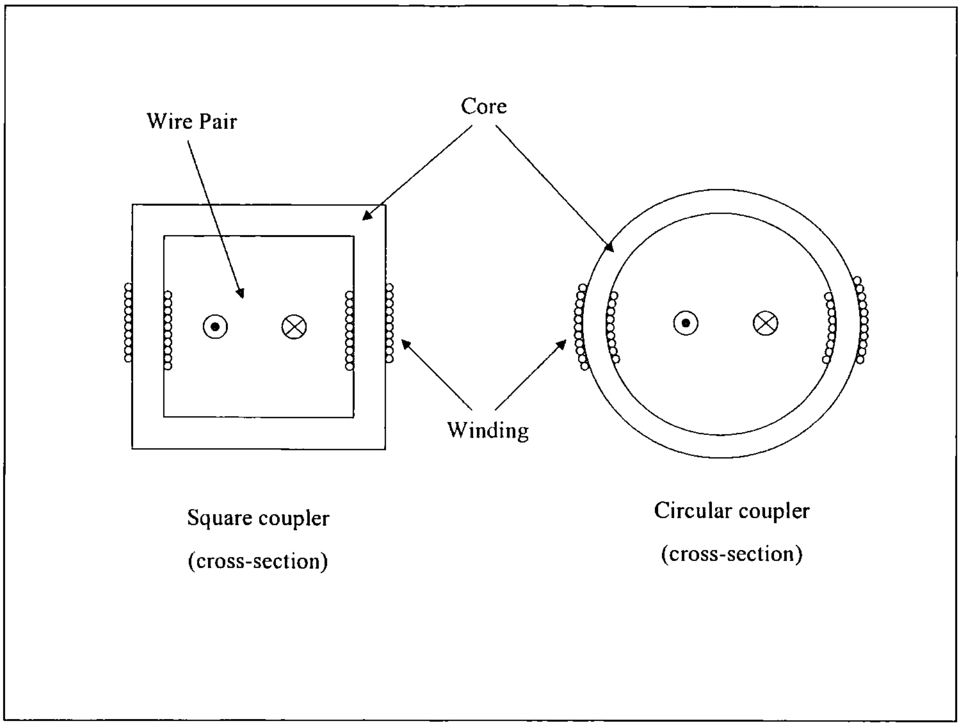

Figure 8.16 Basic layout of the two-wire coupler

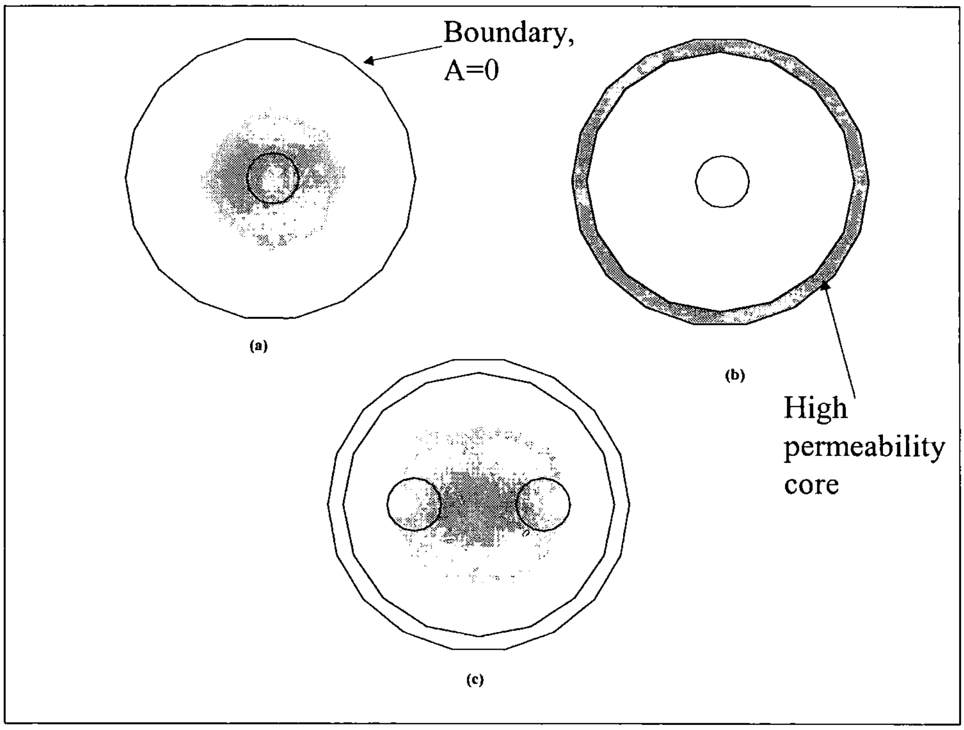

Figure 8.17 Energy stored in the coupler.
(a) single wire, (b) single wire with magnetic core,
(c) two wires with magnetic core

8.3.4 Conclusions from the simulation

System geometry creates a flux pattern that is forced to traverse the air gap between the two conductors along with the path around the magnetic core. Energy that was stored in the region between the wires can be accessed by coils placed around the core in the plane of the conductors. By this mechanism inductive coupling can, in theory, be achieved using the two-wire coupler design.

Given that inductance is defined as flux produced per unit current, we see that air gaps increase the magnetic circuit reluctance, leading to reduced flux and hence lower winding inductance. An alternative explanation is that air gaps reduce the effective permeability of magnetic core and hence the inductance of any copper windings placed around it. High winding inductance is desirable to reduce shunt inductance effects (see section 5.6.5, chapter 5), and to permit the use of smaller resonance capacitors, so we must quantify the reduction of coil inductance[37].

Related effects of the air gap problem comprise variation of mutual coupling with conductor separation and core shape. It was decided that conductor separation and core shape should be investigated experimentally, as this would also permit validation of the above simulation model.

8.4 Experimental Investigation of Two-wire Coupler

In this section the performance of a two-wire coupler is presented by means of inductance and induced voltage measurements.

---

[37] In addition, copper loss is minimised when fewer winding turns are required for a nominal inductance.

8.4.1 Test Coupler

To characterise coupler performance, test pieces were constructed. The most successful configuration is shown in figure 8.18. A useful degree of mutual coupling is possible using this coupler, due to large conductor separation and small effective air gap. The coupler was used during a series of measurements that aimed to find the optimal winding configuration and minimum conductor spacing required for actual transponder operation.

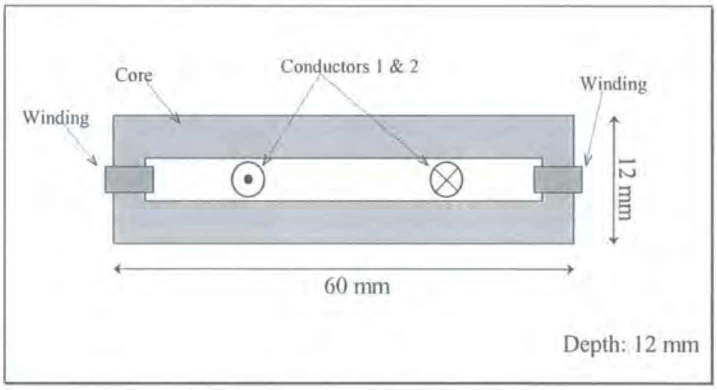

Figure 8.18: Test coupler diagram showing shape of core and location of conductors and windings.

The soft ferrite core has a relative permeability between 1000 and 2000, and is conventionally used in noise suppression applications. It exhibits minimal loss at the 125 kHz and 415 kHz test frequencies[38]. Two equal windings were placed around the ends of the test coupler, each comprising 10 turns of enamelled wire (40 AWG). Solid core 0.5 mm insulated wire was used for conductors 1 and 2. The Self Resonant Frequency (SRF) of the coils was measured and occur beyond 10 MHz; ensuring this did not affect measurements. This arrangement produces a more uniform field pattern

---

[38] I.e., $\tan(\delta) \cong 0$ at the frequencies of interest. In high frequency noise suppression applications $\tan(\delta)$ becomes appreciable, thus removing high frequency components by heat dissipation.

as shown in figure 8.19 that can be enhanced more effectively by the presence of the core.

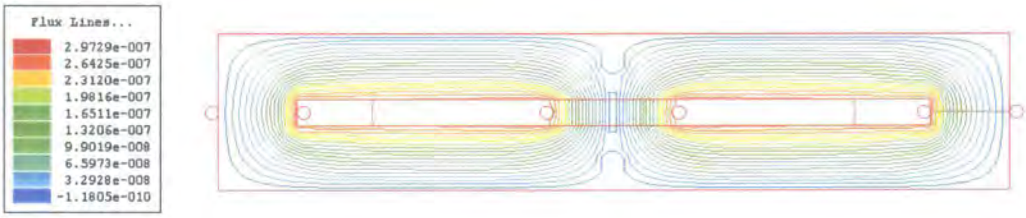

Figure 8.19 Magnetic flux pattern surrounding flat rectangular core. Excitation provided by conductors place near core centre. Outer conductors represent open-circuit coils. Conductor spacing 10 mm.

8.4.2 Characterisation by Inductance Measurement

Measurements were made in two categories: inductance measurements and voltage measurements. Inductance measurements were made by directly exciting the coils then measuring their complex impedance in various configurations. In contrast, voltage measurements were made in full coupler mode by feeding opposing currents to conductors 1 and 2 passing through the core, and then measuring the coil voltage. An impedance analyser (type Agilent 4294A) was used to record impedance data, and a digital storage oscilloscope (type Agilent 54622D) to record voltage data. An HP 8447D preamplifier with standard 50 Ω output resistance was used to excite conductors 1 and 2.

8.4.2.1 Inductance measurements using opposing fields

If we connect the coils such that the resulting flux around the core is in opposing fashion, we can inspect the effect of placing a 'magnetic shunt' at one point on the core.

The configuration is shown in figure 8.20, including the connection of coils and placement of the magnetic shunt.

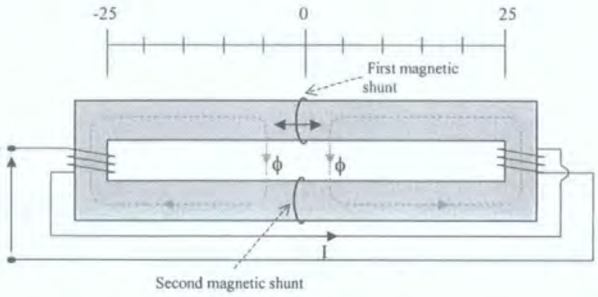

Figure 8.20 Coupler configuration for inductance measurements and opposing coils

A magnetic shunt consists of a low resistance wire loop placed around the core cross section as shown. By forcing the induced voltage in the wire to be zero, it has the effect of preventing any flux from flowing through that part of the core. Faraday's law of induction describes this:

$$\phi_{circuit} = -\int V_{shunt} dt \,|_{Vshunt \to 0} = 0$$

Since the wire has some resistance, flux will pass though the section, but it is sufficiently small to observe the desired effects. Either a single short or double short may be used as shown in the figure. This principle is used in the operation of ferro-resonant transformers, whereby multiple windings can be isolated by magnetic shunts in the sense that the flux paths linking the windings are separated. This is achieved by the alternative method of placing material of sufficient permeability in between legs of the core, causing a diversion of the flux towards the path of reduced reluctance. See [Kelly] for a detailed discussion of the operation.

By moving a single magnetic shunt along the core and recording the resulting inductance, the graph shown in figure 8.21 was produced. Inductance was measured at

125 kHz, using a 5 mA current source. A drop in inductance of 9.1% was recorded at the core edges (-25 mm and +25 mm) relative to the inductance recorded at mid-point, and a maximum value of 61.6 μH at the central position. As shown in figure 8.9(b), flux must flow though the air gap if a magnetic shunt is present, the net effect of which is to increase path reluctance by an amount dependent on the effective gap width. Proof of this assumption is found when we compare the inductance measured when the magnetic short is centrally positioned to that when the magnetic shunt is absent: there was no appreciable change in the measured inductance, indicating that this is the natural path for the flux in the opposing field arrangement. In addition, there was no appreciable change when using a double short. Thus, due to the opposing fields, inductance measured at the coil terminals results from two separate paths of flux.

The question remains as to why the inductance should decrease at -25 mm and +25 mm positions. An explanation can be found by investigating how the reluctance of the air gap changes with the short wire position. To do this, the experiment was repeated, but instead with only one coil connected to the impedance analyser, the other coil being electrically shorted so that it no longer contributed to circuit inductance. In figure 8.22 we see how inductance varies with magnetic short position. Around the mid-position (zero on the x-axis) the variation is linear, but near the far ends there is deviation from the linear profile. First of all, near the +25 mm position we see decreasing gradient as the inductance reaches its maximum value. Second of all, near the -25 mm position the gradient increases as the inductance reduces. If we apply this knowledge to the situation in which both coils are connected then we see that the coil whose inductance is increasing does so in small increments whilst the inductance of the other coil diminishes. The overall effect is reduced flux linkage, and hence inductance.

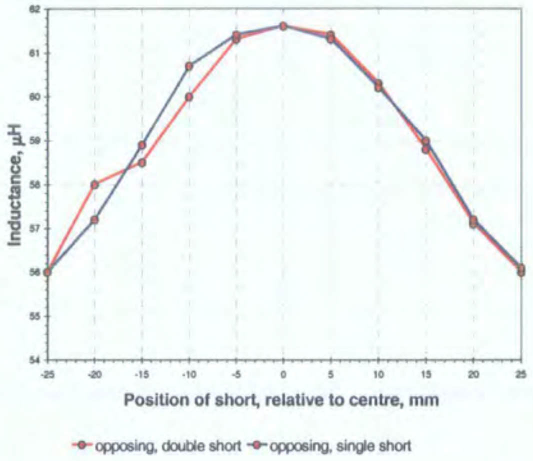

Figure 8.21 Measured inductance versus magnetic short position, showing both single and double short results.

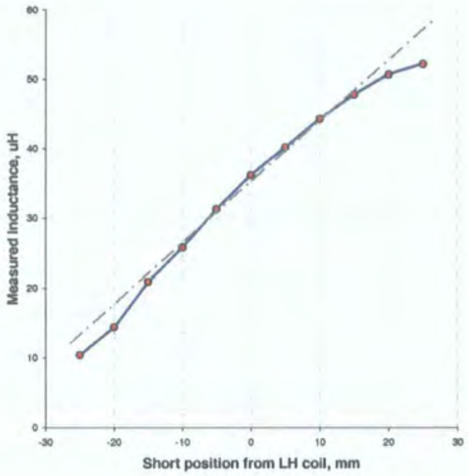

Figure 8.22 Effect of magnetic short on a single coil, showing deviation from a straight-line characteristic at extreme edges of the inner core cross-section.

8.4.2.2 Inductance measurement made using summing fields

We may connect the coils around the core such that flux flows in a single direction. Refer to figure 8.23 for the configuration. The measured inductance values as a function of magnetic the short-wire position are summarised in figure 8.24, which includes results from the previous section. Inductance now differs depending on the type of magnetic short used; the measured inductance is 67.7 μH with a single short-wire at mid-point, and 84.2 μH with a double short-wire. In addition, there is steeper fall-off when the single short-wire is near the core edges.

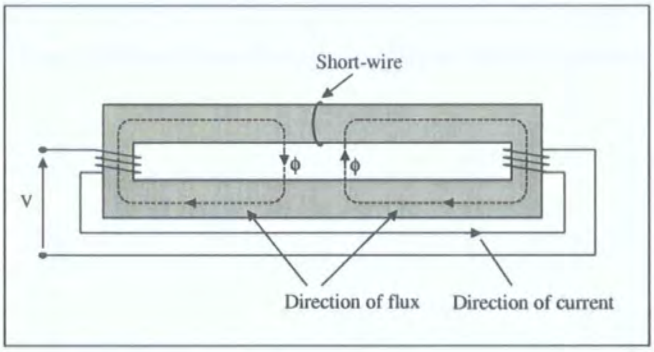

Figure 8.23 Coupler configuration for inductance measurements using summing coils.

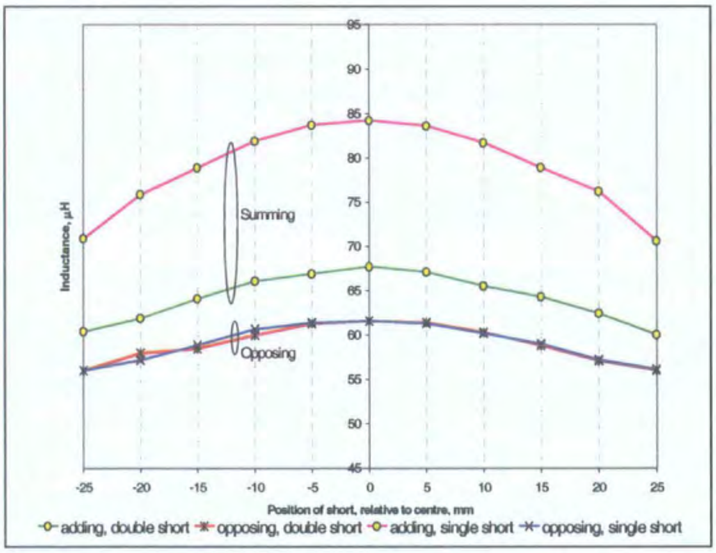

Figure 8.24 Adding and opposing coil inductance measurements, including single and double short.

Removing the magnetic short-wire completely when a summing field exists results in a measured inductance 387.1 μH, increasing coupler inductance more than four-fold.

8.4.3 Conclusion from inductance measurements

We may conclude that flux is forced across the central air gap, provided the coils are connected in opposing field configuration. If instead the summing configuration is employed, flux may travel around the core and no linkage is achieved in the region between the wires. We must therefore adopt an opposing field within the coupler.

8.4.4 Characterisation by Voltage measurements

In the previous section we considered paths of flux around the coupler produced by its own windings. In this section we consider the mutual inductance between current carrying wires passed through the core and the coupler windings. Capacitance is connected across the coil terminals to create parallel circuit resonance at the signal frequency, thereby giving each coil high dynamic impedance. This reduces current drawn by the windings and, if we neglect losses in the core, we may assume negligible current flow through the windings. Hence there is no appreciable loading of the primary circuit due to the presence of the coupler since the coupled current is approximately zero and so the voltage applied across the wires passing through the core remains constant. This allows us to use the output coil voltage as a direct indicator of mutual inductance between the current-carrying wires and the coupler coils without having to explicitly calculate mutual inductance. The voltage developed across each winding was recorded for various wire positions in an attempt to characterise its dependency on wire position, and so determine whether two-wire couplers are be suitable for use with a typical commercial load modulation transponder IC's.

8.4.4.1 Single Exciting wire

If a single exciting wire travels through the core we may connect the coils such that the induced EMFs sum (figure 8.25). This coupler operates in common-current mode, since the exciting current travels in one direction only.

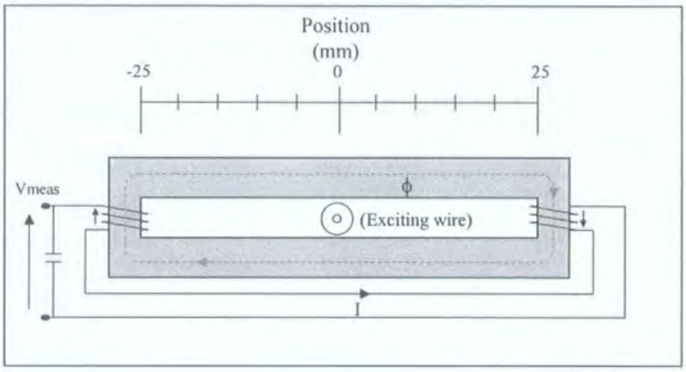

Figure 8.25 Configuration of common-mode coupler with summing coils

The resulting voltage, V_{meas}, may be approximated by the following equation:

$$V_{meas} = \frac{\frac{V_1}{CR}\sqrt{LpLs}\sqrt{1-\frac{ls}{Ls}}}{Rs + j\left(\omega L - \frac{1}{\omega C}\right)} \qquad (4)$$

This equation may be derived by combining equations for induced secondary EMF due to primary current, mutual inductance, coupling factor (derived from leakage inductance) and secondary circuit properties (see chapter 5). These were measured and summarised in table 8.1.

Variable	Description	Value
V_1	Voltage measured across a 10 Ω current sensing resistor placed in series with the exciting wire	500 mV

R	Current sensing resistor	10 Ω,
C	Capacitance added across the coil terminals	314 pF
L_p, L_s	Primary and secondary inductance respectively	1.2 μH, 379 μH
l_s	Secondary coil leakage inductance	166 μH
R_s	Coil ESR	53 Ω
ω	Operating frequency	2π*415 kHz

Table 8.1 Measured quantities used to calculate V_{meas}

All impedance values were measured at the precise signal frequency of 415 kHz using an impedance analyser. In table 8.2 the calculated and measured values of V_{meas} are compared, including a spice simulation constructed with the parameters in table 8.1.

Calculated Voltage	$10.7 \angle 77.2^{\circ}$
Measured Voltage	15.6
Simulation Voltage	15

Table 8.2 Calculated, measured and simulated values of V_{meas} (peak voltage)

The calculated value was lower than expected, mostly due to the difference between the operating frequency and secondary circuit natural resonant frequency, f_{res}. Using equations 5a and 5b we calculate f_{res} = 461 kHz and Q = 20.7, compared with the 415 kHz operating frequency. This results in lower V_{meas} and non-zero phase angle (the positive phase angle of 77.2 degrees indicates the circuit frequency is below resonance). However, the maximum measured voltage occurred at 415 kHz. This drop in resonant frequency was probably due to additional capacitance in the test circuit.

$$f_{res} = \frac{1}{2\pi\sqrt{LsC}} \qquad (5a) \qquad\qquad Q = \frac{1}{Rs}\sqrt{\frac{Ls}{C}} \qquad (5b)$$

The measured voltage does not depend on the position of the exciting wire when summing coils are used. In contrast, if the coils are connected such that the induced EMFs oppose, then the measured voltage is nearly zero volts for all exciting wire positions, except when it is placed directly next one coil, in which case a small voltage can be measured. This is due to a small portion of the total flux that traverses the air gap linking only with that coil, producing a complete magnetic circuit around the core and hence linking with the other coil.

8.4.4.2 Two exciting wires, summing coils

We now place two wires through the core carrying equal currents but in opposing directions, thereby creating the differential-mode coupler. By connecting the coupler coils such that induced EMFs sum, we may sense the balanced field pattern characteristics. Figure 8.26 shows the configuration used.

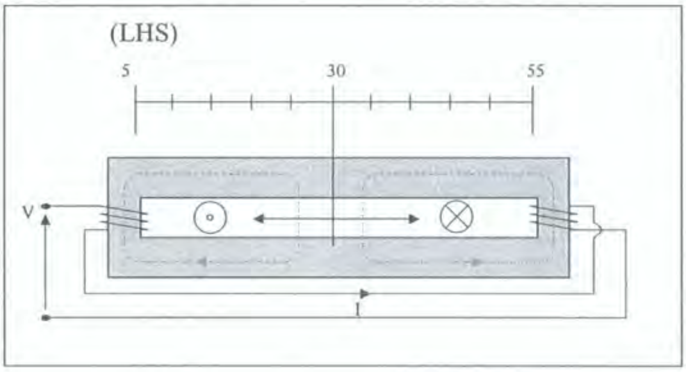

Figure 8.26 Coupler and two exciting wires: summing coils

Note that we may calculate the required terminal capacitance for a given frequency of resonance using equation 5a and the inductance measured from figure 8.24, giving 2 nF, which agreed with the actual amount required. Current through the exciting wires was set to 60 mA (peak) by measuring the voltage across a 10 Ω resistor in the primary circuit. This is similar to current requirements of the prototype cable transponder system.

The induced voltage was recorded as both wires were moved along the core, the position of each being referred to the left hand side of the core, as indicated in figure 8.20. The results are summarised in the contour plot of figure 8.27, where we see an output variation in the magnitude of the open-circuit voltage from –12 V to +12 V (peak-peak), where the minus sign indicates a phase reversal of 180 degrees. A null-region of zero output volts occurs whenever wire 1 and wire 2 are in the same position (i.e., directly next to one another), and the polarity changes when the wires are swapped about mid-position.

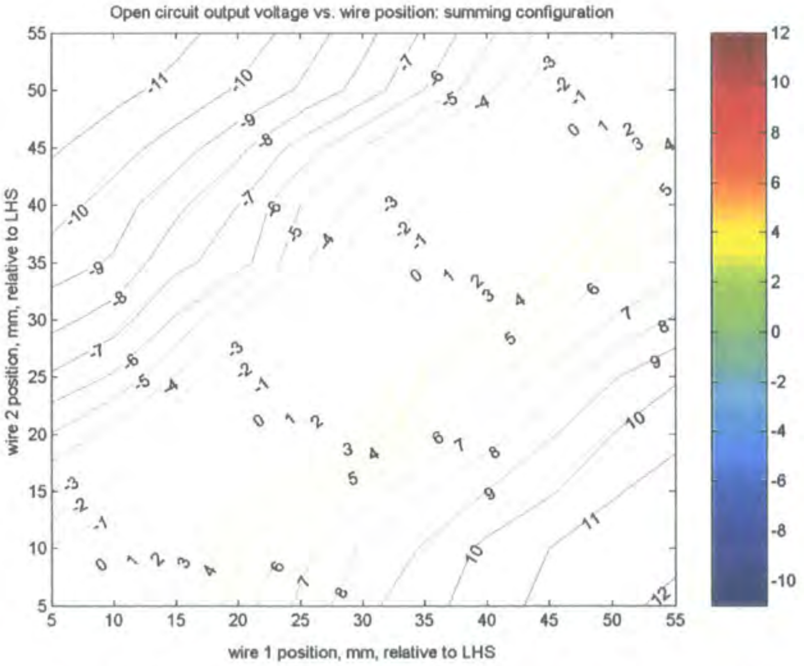

Figure 8.27 Contour map showing open-circuit voltage versus wire placement for summing coils

In figure 8.28, the open circuit voltage is shown for exciting wires separated symmetrically about the mid-position, extrapolated from a line section of the contour plot. Negative position values indicate when the wires are swapped about mid-position. For example, a 20 mm parting occurs when each wire is 10 mm from mid-position (i.e. one wire at 20 mm, the other at 40 mm). The voltage rises linearly about mid position until ±30 mm parting, beyond which it increases more gradually. Practical open circuit voltage (i.e., that which could support a low voltage, load modulation chip) appears at 6 V (peak–peak), for which a minimum 15 mm wire parting is required.

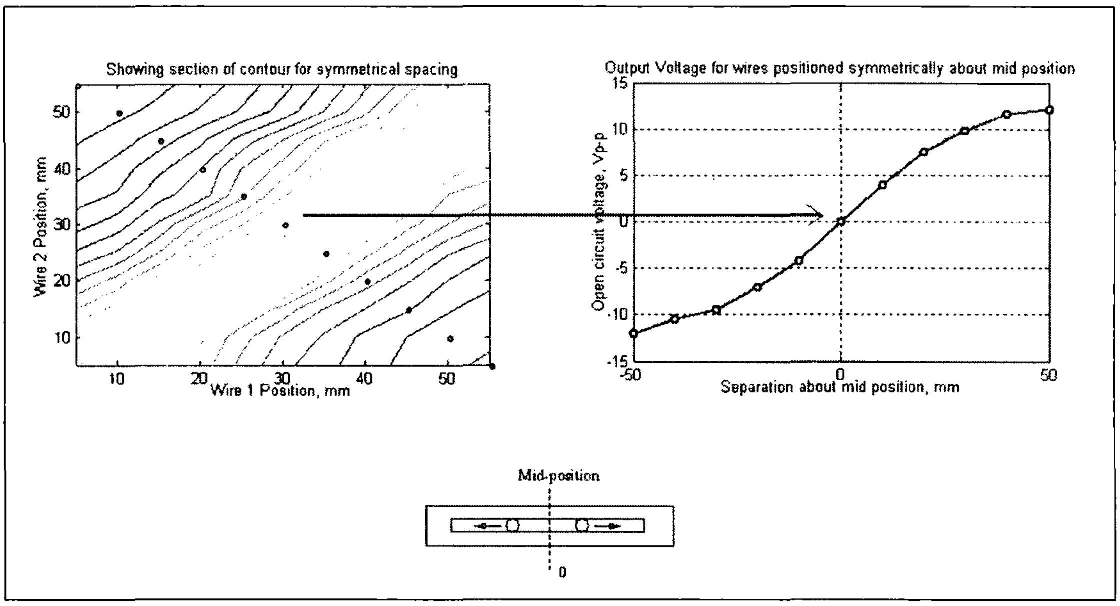

Figure 8.28 Open circuit voltage vs. symmetrical wire separation using two exciting wires, summing coil configuration

8.4.4.3 Two exciting wires, opposing coils

In the final configuration we investigate how open-circuit output voltage varies with wire separation when the coupler coils are connected in such a manner that the induced EMFs oppose, as depicted in figure 8.29. In this configuration, any voltage across the coils is due to an imbalance of the flux field; zero output volts occurs when the induced EMFs are exactly equal.

Measurements of open-circuit voltage were recorded under the same conditions used for the summing configuration, except that a capacitance of 200 pF was required for resonance at the same frequency of 450 kHz. (As before, we may calculate this value from figure 8.24 and equation 5a.) The position of each wire is measured from the left-hand side of the core, as before. By varying the position of each wire by 5 mm relative to this point, a contour plot of open-circuit voltage versus position was recorded (figure 8.30), where a minus sign indicates phase reversal of 180 degrees. Green lines indicate zero output volts which occurs when the wires are either in the same position (i.e., directly next to one another), or symmetrically spaced about mid-point. This contrasts with the result for symmetrical case with summing coils (figure 8.27). There are also regions of maximum positive or negative output, which occur when one wire is located mid-point and other at an edge, but at substantially lower levels than those recorded using a summing configuration (maximum of 0.36 V (opposing) versus 11.2 V (summing)). In general, output voltage is significantly higher for the summing configuration than for the opposing configuration.

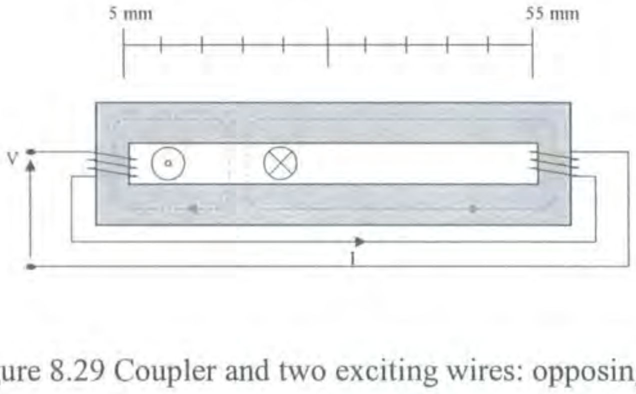

Figure 8.29 Coupler and two exciting wires: opposing coils

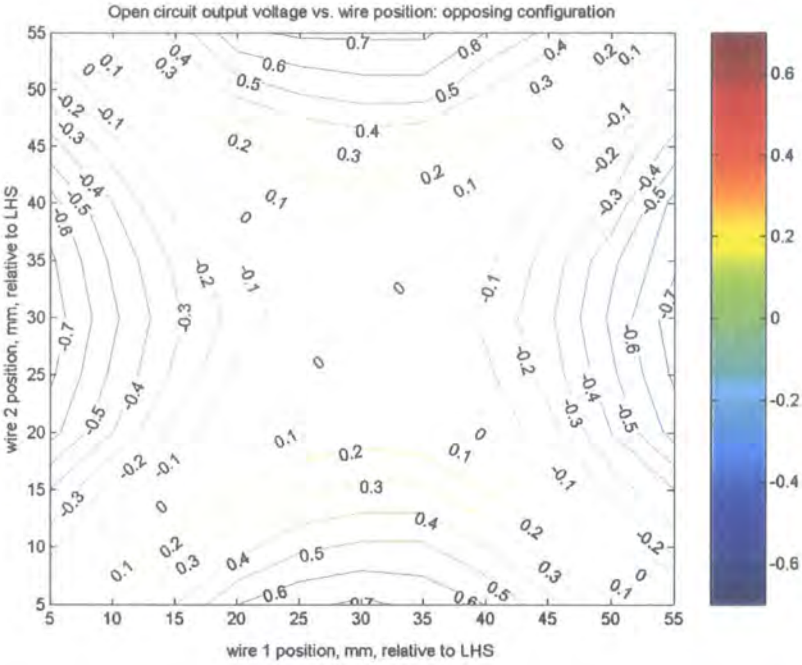

Figure 8.30 Contour plot showing variation of open circuit voltage with wire position for opposing coils

8.4.4.4 Conclusions from Voltage Measurements

The comparatively low output measured using opposing coils indicates lower mutual coupling, which is in agreement with the inductance measurements described earlier. The regions of strongest coupling occurred when one wire was placed at the centre, and the other wire at the far left or right end. This is less practical than the summing configuration, which produced good performance when the wires were spaced evenly from the mid-position. When configured in this way, the differential coupler achieves sufficient open-terminal voltage.

8.5 Two-wire Coupler Trial

To test actual performance, the above two-wire coupler was tested using the prototype interrogator described in chapter 7. The coupler was required to activate a HT1 transponder chip and support direct-load modulation.

8.5.1 Configuration

The two windings, each comprising 10 turns, were arranged in summing configuration as described in section 8.4.4.2. The capacitance was raised to 23.5 nF due to the lower operating frequency of 125 kHz, as required by the Hitag 1 transponder chip. Line current was 70.1 mA (peak). One wire was attached to the one end of the inner core, while the other was free to move along the core. For various wire positions the transponder terminal voltage was measured along with a record of whether communication could be established. The "*set_cc()*" ID request message was transmitted[39] and the analogue demodulator voltage signal inspected. The decoded ID string was displayed on the host PC to check for a valid response from the HT1 transponder.

8.5.2 Results

Communication was possible for wire separation greater than 30 mm, typically when the transponder terminal voltage exceeded 4.5 volts peak. This is the point at which the transponder begins to reply. Demodulation was always successful provided the transponder was operational. This means that circuit conditions permit sufficient load modulation when transponder voltage exceeds activation voltage. Figure 8.31 shows the voltage profile versus wire separation, where the dotted to solid line transition point indicates the minimum operational wire separation. In other respects this arrangement

---

[39] See section 7.4, chapter 7.

performs similarly to the single-wire coupler. This simple experiment demonstrates that a two-wire link can be successfully utilised in the cable tagging application.

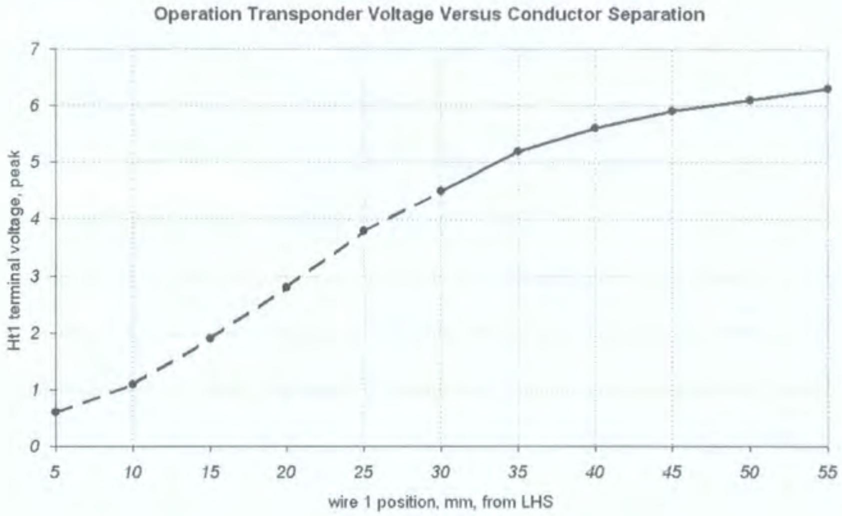

(a)

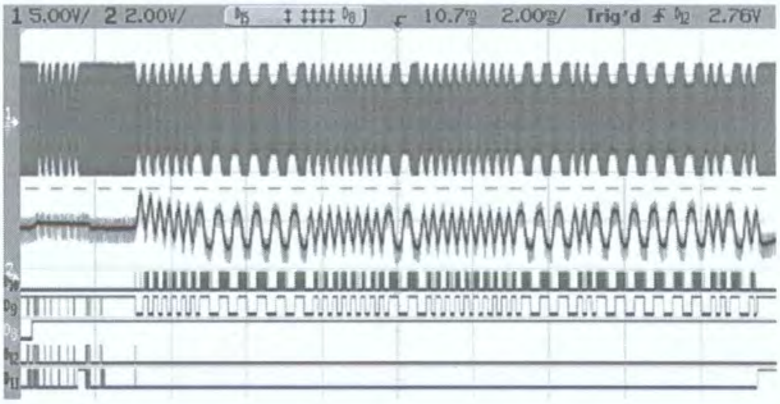

(b)

Figure 8.31 (a) Transponder voltage versus wire position during real communication test of the two-wire link. Dotted line section indicates non-operational region; solid line indicates operational region. (b) waveforms generated during SET_CC transaction. Top trace: transponder terminal voltage, second from top: demodulated receiver signal, third from top: controller sampling, fourth from top: digitised base band signal.

8.5.3 Discussion: minimum separation requirements

We see that when using this coupler shape, which is an extremely favourable one given the coupling arrangement, a minimum wire separation of 30 mm was required for the described configuration. In order to reduce the minimum separation one of the following steps would have to be taken: increase line current, increase the number of winding turns or reduce the effective air gap. High line current is possible when using cable RFID because the signalling system is confined to the PAT and appliance power cable, but not when signalling on the power-line due to regulations. The number of winding turns could be increased but this would be accompanied by higher winding loss, which would reduce circuit Q and therefore load modulation sensitivity.

8.6 Summary

In this chapter a two-wire coupler concept has been investigated. The aim was to provide a means of coupling between two current-carrying wires and secondary coils placed around the core without having to separate the wires. This requires a means to extract the magnetic field that is contained predominantly within the space between the two conductors. It was shown that a symmetrical arrangement of coils positioned at either side of the horizontal axis of symmetry wound on a permeable core that encircles the two conductors can force the path of magnetic flux to split along the vertical axis of symmetry. Mutual coupling then occurs and the induced EMF's across each coil sum to produce a terminal voltage.

Using finite-element simulation and measurement it was shown that the terminal voltage is strongly dependent on conductor spacing and core geometry. Circular cores are less suitable for this design because the proportion of air to magnetic path length is high. A flat rectangular core with relative permeability of around 1000 was found to give satisfactory coupling with a minimum conductor spacing of 30 mm. This arrangement produces a more uniform magnetic field that is more easily influenced by the magnetic core. For a given minimum terminal voltage, the minimum conductor spacing depends on core geometry. The flat rectangular geometry is not a practical arrangement for the application concerned (i.e., coupling to power-line cabling) and therefore a single wire coupling is considered to be the optimal arrangement.

8.7 Further work

Although this concept was shown to be unsuitable for typical appliance power cabling, it may be suitable for flat power-line cables. An example is shown in figure 8.32, where the line and neutral wires are separated by the earth wire. The appreciable live-neutral spacing may be utilised to provide sufficient coupling. The effect of earth wire on the magnetic field should be minimal due to its position; the magnetic field simply diverts around this conductor.

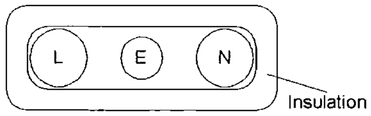

Figure 8.32 Typical flat power-line cabling showing spacing between line and neutral wires.

9 *Power-Line Signalling by Direct-Load Modulation*

9.1 Introduction

In this chapter we investigate the potential for passive direct-load modulation on the local power distribution system, referred to here as the power-line. This technique has two novel features: the absence of any power source at the remote (transponder) node, and direct modulation of the transmitted signal negating the need for active transmission at the remote node. The intention of this chapter is to find the limiting factors pertaining to the use of passive load modulation transponders described in chapter 5 and to assess the viability of such a system for appliance identification.

The concept of this system extends to tracking all active mains-powered devices within a specified range by using the power-line. The intention is to automate the process appliance identification to determine whether test dates have expired. This method would be particularly convenient for safety test markets because a device that is plugged into the power-line can be assumed to be in use and, through remote identification, can be brought to the attention of the safety engineer when the test date has expired. To extend the concept further, remote identification could allow monitoring of all appliances currently live on the power-line and the corresponding test dates of each appliance.

9.2 The Power-Line Channel (PLC)

The power-line is generally considered as a frequency, time dependent channel of which there are three principal classifications: the power distribution grid High–Voltage (HV) network, the local distribution system (MV) and the network residing within the building (LV). In this work we are concerned primarily with networks contained within a building or house, which may include commercial sites or ordinary homes.

A special power-line model is used in EMC applications to model the power-line consisting of an inductor and resistor connected in parallel between each node [Williams]. This is used to simulate the coupling of noise between source and victim and is implemented by an artificial mains network or Line Impedance Stabilization Network (LISN). This model is generally not representative of the wide variation of loads that may be connected to the power-line, all of which influence line impedance. Instead, its purpose is to present a known and repeatable impedance so that emissions and susceptibility measurements may be recorded and compared with allowable limits. It is also used according to standard EN 50065 [EN50065] to measure signal levels produced by power-line signalling devices operating between 3 kHz and 148.5 kHz.

Power-line impedance under operating conditions has been extensively measured in the United States by Nicholson et al. [Nicholson] and in some European countries by Malack et al. [Malak] using the current probe technique [Southwick], [Kwasniok1], [Kwasniok2]. This was initially performed to confirm the validity of the Line Impedance Stabilization Network (LISN), but included a measure of the variability of impedance. Important conclusions resulted: in the process of measuring the impedance presented by the power-line at power outlets in the United States, it was shown that the magnitude of power-line impedance varies from a few ohms to a few hundred ohms. Additionally, the mean of these measurements in the frequency range 150 kHz to 30 MHz was found to compare favourably with the standardised 50 Ω/50 μH LISN. However, there was significant divergence of LISN impedance and measured impedance below 150 kHz, since this is below the LISN compliance range. Nicholson measured power-line impedance from 20 kHz to 30 MHz and found the average impedance to range between 1 Ω and 100 Ω. Impedance at 100 kHz was found to range between a minimum of 3 Ω and maximum of 35 Ω. In [Nicholson], power-line impedance of European distribution systems was shown to be comparable to U.S. power-lines, including H.V. and L.V. distribution.

In a more recent study, Vines measured impedance characteristics of all typical power-line components including: distribution transformer, cable and loads [Vines85]. This work demonstrated that, for frequencies below 20 kHz, the power-line impedance "seen" by devices connected to a local power outlet tends to be dominated by the distribution transformer, unless electrically long cables, high power loads (low resistance) or power correction capacitors exist on the line. This dominant impedance tends to be of the *RL* type, that is, analogous to the series combination of inductance and resistance (having positive phase angle and magnitude that increases with frequency).

Power-line impedance and attenuation have been investigated by several others, including Chan et al. [Chan86], Hooijen [Hooijen] and Tanaka [Tanaka]. In [Chan86], Chan measured power-line attenuation in the frequency range 20-240 kHz on actual commercial and residential sites and found that attenuation was dependent on several factors, including topology (in-phase, cross-phase), distance and loads connected to the power-line. In-phase measurements typically yielded 0-20 dB attenuation when using identical transmitter and receiver line-line couplers, but could reach as high as 40 dB at higher frequencies depending on location and time of day. Short in-phase paths yielded 10 dB or less attenuation across the frequency range considered. The effect of typical household devices such as the television or electric kettle on attenuation was also considered, resulting in up to 10 dB further attenuation. Hooijen reports results collected during a survey of an urban low-voltage network in Amsterdam (comprising many under-ground lines) using the frequency range 9-95 kHz. In this case it was observed that channel impedance was very low, typically less than 1 Ω, due to the effect of many loads, each representing an entire house or street lamp, connected in parallel. Interestingly, standing wave effects could not be detected, most likely due to cable attenuation. A novel approach was taken by Forti to measure power-line impedance in which a capacitor was connected between live and neutral lines, causing ringing of the line voltage. This ringing is caused by line inductance and resistance forming a series LCR resonant circuit with the capacitor. The frequency and decay of the transient voltage allows calculation of line parameters L and R according to the damped oscillation equations:

$$L = \frac{1}{\omega_n^2 C}, \qquad R = 2\delta\sqrt{\frac{L}{C}}$$

where ω_n and δ are derived from the measured oscillation frequency, f_o and the ratio of successive peaks, ρ:

$$\omega_n = \frac{2\pi f_o}{\sqrt{1-\delta^2}}, \qquad \rho = \exp\left(-\frac{\pi\delta}{\sqrt{1-\delta^2}}\right)$$

This provides a one-port method for measuring power-line impedance but does not allow measurement of attenuation between two points in the power-line, which is also dependent on impedance.

9.2.1 Power-Line Noise Characterisation

The dependency of PLC signalling on power-line noise was illustrated in a paper by Chen et al. [Chen] who describes a system in which the power-line was used to transmit temperature measurements of an induction drive motor for condition monitoring purposes. Since such motors are commonly supplied by a PWM inverter power source, the communication system had to tolerate harmonics generated by the PWM signals which extend well into the 100 kHz range. FSK signalling was chosen at 3.5/6.5 MHz to avoid PWM switching noise, but it was found that switching noise easily coupled into the receiver circuit due to its high amplitude, causing strong interference of the baseband signal. Aided by the knowledge that the maximum switching noise interval was much less than the average data period, it was found that an impulse rejection circuit could be designed in the form of a low-pass filter to attenuate switching noise and increase receiver sensitivity. Although not generally possible, this example demonstrates how knowledge of the power-line channel characteristics would allow optimisation of the receiver.

Four main categories of power-line noise sources have been defined by Vines [Vines84] and others [O'Neal]:

1. Spectrally uniform noise that tends to decrease in amplitude at higher frequencies. This may be regarded as white noise for a band-limited communication system;
2. Impulsive noise, caused by single events such as switching a device on;
3. Noise synchronous with the power-line frequency, such as that caused by switching power supplies;
4. Noise that is non-synchronous with the power-line frequency, but having defined spectral features.

Considering the load modulation system described in this chapter the most important noise source was found to be other impedance modulators on the power-line. One of the most common forms of impedance modulator is the switching power supply as found in personal computers and similar DC electronic equipment. Load modulation was observed to occur mainly during the maxima and minima of the mains voltage i.e., at twice the mains voltage frequency, in agreement with [Chan86] and [O'Neal]. At each maxima and minima the line impedance varies as the power supply charges a capacitor across the power-line.

9.2.2 Strategies for Improvement

In [Chan86] and [Chan94], Chan suggests several means of improvement to power-line signalling:

1. Multi-channel communication that avoids poor channels;
2. Variable data rate adaptive to the current signal to noise ratio;
3. Avoid placement of receivers near "troublesome" sources;
4. High data rate with short-duration data blocks;
5. Low data rate with long-duration data blocks whilst ensuring sufficiently high bit energy to noise energy ratio.

9.3 Existing Power-Line Signalling Methods

Many systems have been developed and tested for power-line communication intended for one of the following markets: last mile "access" networks, industrial communications or "In-house" low-voltage networks. A common requirement of all methods encountered is powered receiving nodes that derive power from the mains voltage supply to sustain their radio circuits, which is not the case with passive load modulation. The most frequently used bands are currently 50-525 kHz and 1.6-30 MHz [Dalichau]. Interference dominates below 50 kHz and worldwide AM radio broadcasting occupies the band between 525 kHz and 1.6 MHz, which could be susceptible to interference from radiation produced power-line communication systems operating nearby.

In order to meet high performance "last mile" requirements following deregulation of telecommunication and energy markets [Brown], [Dostert01], sophisticated signalling methods have been developed that allow a degree of adaptation to the power-line channel characteristic by populating those frequency bands that have the most favourable transmission characteristics. Criteria for determining the most suitable transmission bands include signal attenuation, narrow-band noise sources and stability (i.e. how long the channel retains its current characteristics). The most recent (and highest performance) systems use Orthogonal Frequency Division Multiplexing (OFDM), which requires expensive multi-carrier transceivers and, most importantly, sophisticated receivers. It is claimed that secure and reliable communication is possible using this technique and transceiver cost is being reduced by developing system-on-chip solutions [Sanz].

Spread-spectrum signalling has been adopted in some commercial power-line systems [Radford], [Shwehdi], [Ochsner], [Dosdert90]. This has been adopted in the Consumer Electronics Bus (CEBus) standard, which is a communications protocol providing peer-to-peer communication in home and industrial networks. It defines similar CSMA/CD protocols to those used in the Ethernet protocol, but is of lower complexity and cost. Spread spectrum is a powerful method in power-line communication because it is inherently wideband—spreading the signal bandwidth over a considerably greater channel bandwidth thus creating process gain—and therefore offers a degree of immunity to narrow-band fading that is so prevalent in power-line channels. It also permits variable bit rates within a constant channel bandwidth by variation of the processing gain. Process gain is also useful in rejection of narrow-band noise sources that are also very common on the power-line. Two major spread-spectrum techniques are direct-sequence and frequency hopping, which require correlation or hopping sequence operations respectively at both transmitter and receiver. This would increase the cost of identification transponders considerably and would most likely require active nodes to provide the necessary RF functionality.

Less complex power-line signalling methods have appeared in the past twenty years for the in-house market, such as the X-10 [X10] protocol. This system communicates by 1 ms carrier bursts synchronised to the mains voltage zero-crossing points. The carrier frequency is 120 kHz, similar to the low frequency RFID channel frequency (125 kHz). Each transmission packet comprises nine data bits and four start bits and each is transmitted in true and complementary form, requiring 22 bit transmission per packet. Furthermore, to maximise robustness in the hostile power-line channel, each packet is transmitted twice. The resulting low data rates would not be problematic for a appliance detection system because speed of messaging is not critical in this application. However an active receiver is required, since the carrier bursts do not constitute an energising field capable of remote-powering of transponders.

Further low-complexity signalling systems have been developed in recent years such as direct ASK and FSK carrier modulation systems which are commonly referred to as "carrier-current" or "Power Line Carrier" (PLC) systems, although such methods have existed for at least thirty years [Jagoda]. These systems became commercially attractive after the introduction of low-voltage power-line signalling standards such as European

CENELEC standard EN 50065 [EN50065], approved in 1991. Examples of commercial implementations include National Semiconductor LM1983/2893 FSK carrier current transceivers [National], [Lee], [Monticelli], a Philips Semiconductor TDA5051 ASK home automation modem [Philips] and an ST Microelectronics ST7537 FSK Power-line Modem [Cappelleti]. Since channel impedance and noise variation can strongly disrupt such systems, applications were limited to those for which packet data loss is not critical to system integrity (e.g., voice transmission). The Philips and National Semiconductor products described above are now discontinued, most likely due to the lack of robust communication and the introduction of more sophisticated methods.

Techniques have been described that employ some form of load modulation at the transmitter (base station) in order to convey information to remote receivers on the power-line. Budek describes a method by which modulation of the power-line voltage is created by forcing a near-short circuit condition across the power-line conductors [Budek]. The near-zero condition would be sensed by remote receivers using a zero-crossing detector. Obviously switching must occur between the mains zero-crossing points and it is suggested that this is done during positive cycles. A more sophisticated approach is suggested by Baer [Baer] in which a load is switched rapidly on and off across the power-line in order to cause pulse modulation of the power-line voltage. The method described uses constant-width pulses switched at various intervals creating a combination of Pulse Amplitude Modulation (PAM), due to the mains voltage envelope, and Pulse Position Modulation (PPM) due to pulse spacing. With the correct manipulation, a desired modulated carrier may be approximated by this method.

9.3.1 Coupling Mechanisms

There are three main power-line coupling methods for communications signalling: current-line coupling, line-ground coupling and line-line coupling. These are illustrated in figure 9.1. Nomenclature is similar to that described by Cortina [Cortina] who considered each coupling mechanism for Medium Voltage (MV) power-line signalling. Current-line coupling is analogous to inductive coupling as described in chapter 5. Cortina remarked that current-line coupling is not suited to MV networks for communication purposes because the line impedance is high in MV networks[40]. The impression of a signal voltage upon the power-line is inefficient because the coupling impedance appears as a series element. For Low-Voltage (LV) signalling however, line impedance is lower and current-line (inductive) coupling is possible. Coupling loss was also investigated by Hooijen [Hooijen] who commented this can severely impact the range of urban power-line communication systems and that the coupler output impedance should be less than the power-line impedance.

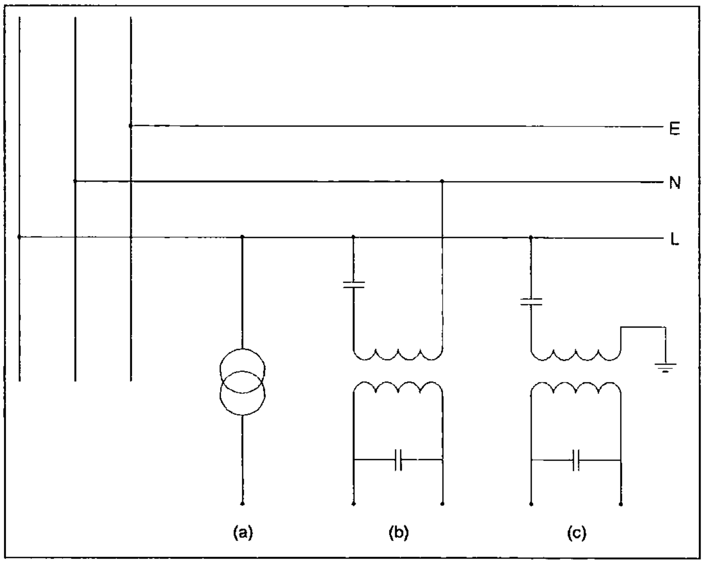

Figure 9.1 Power-line coupling mechanisms.
(a) current-line, (b) line-line, (c) Line- ground

---

[40] Current sensing using current transformers is suitable since accuracy, rather than signal strength, is most important.

It was decided to utilise line-line coupling for transmitter and receiver and to utilise the inductive couplers described in chapter 5 to maintain a non-galvanic link. This may increase the scope of embedded applications due to its non-evasive design. This also permitted the performance evaluation of inductive coupled transmitters in LV networks.

9.4 Modelling the Power-Line Channel

Characterisation of the power-line has been investigated by many authors in recent years due to the large market potential of high speed power-line communications. In most cases the channel parameters sought are the worst-case channel attenuation and fading. The channel is most often modelled by considering the network of wiring and loads connected to the distribution transformer.

Large theoretical studies have been conducted to characterise the power-line channel, for example [Esmailian], [Issa]. In [Esmailian] this is achieved by generating a random power network and calculating the attenuation between randomly chosen node pairs. Several thousand evaluations were carried out to build up a statistical model of the network and to estimate the channel capacity, which was reported to average 100 Mbps according to unspecified background noise and 1 mW transmit power.

Others have not attempted to generalise the channel, but instead have tried to show agreement between the calculated and measured characteristic for a specific example [tsuzuki02], [tsuzuki01], [Anastasiadou], [Assimakopoulos]. This has generally involved measuring the power line attenuation off-line i.e., with the mains supply disconnected. In [Tanaka] Tanaka recreated a section of power-line by constructing a copy and attenuation measurements compared with the (off-line) in-situ power line. Tanaka compared measured attenuation with the attenuation constant, α, and observed that actual attenuation was greater than the model above 100 MHz. He suggests that cable connections, which were crimped style, contribute to the cable inductance by up to 1.6 μH. This study illustrates the individuality of such power-line models: cable type, connection type, topology and loads connected, and that a compromise must be struck to avoid recording large amounts of data which may also be somewhat dependent on the networks used. Tsuzuki seems to acknowledge this in [Tsuzuki01] when he surveyed power-line and appliance impedance with dispersion data in an attempt to account for the variability seen across many channels and devices. Wide dispersion was seen in the impedance of both channels and appliances, often the order of several decades.

9.4.1 Hypothetical Power-line Channel

In this section no attempt is made to generalise characteristics of the power-line used for testing; the objective is to find whether direct-load modulation is possible on the power-line. Moreover, due to the passive operation, estimates of attenuation are important. A theoretical power-line that is similar to that described by Tsuzuki [Tsuzuki02] is used to show the possibility of load modulation. This approach has therefore been validated by power-line measurement by several authors.

We seek to find the attenuation between two points resident on a power-line channel and the change of input impedance perceived at the interrogator in response to load modulation at the interrogator. We adopt the ABCD transmission matrix approach described at detail in chapter 6 to find the desired quantities. The validity of the ABCD method applied to power-line modelling was discussed by Banwell et al. [Banwell1], [Banwell2], who showed that the model is valid for symmetrical cabling. The hypothetical power channel is shown in figure 9.2 which comprises several loads connected by IEC leads to the power sockets, which are separated by further power cabling. This forms a tree topology in contrast to the star topology[41]. For simplicity it is assumed that the interrogator and transponder are located at opposite ends of the channel. Note that the full coupled impedance and inlet filter are included at the transponder node as would occur in a cable RFID arrangement[42].

---

[41] Note that tree structures can be considered as single elements of the star topology. Star topologies have a single common connection point, which is normally the location of the distribution transformer.

[42] A type II inlet filter is assumed, see chapter 6.

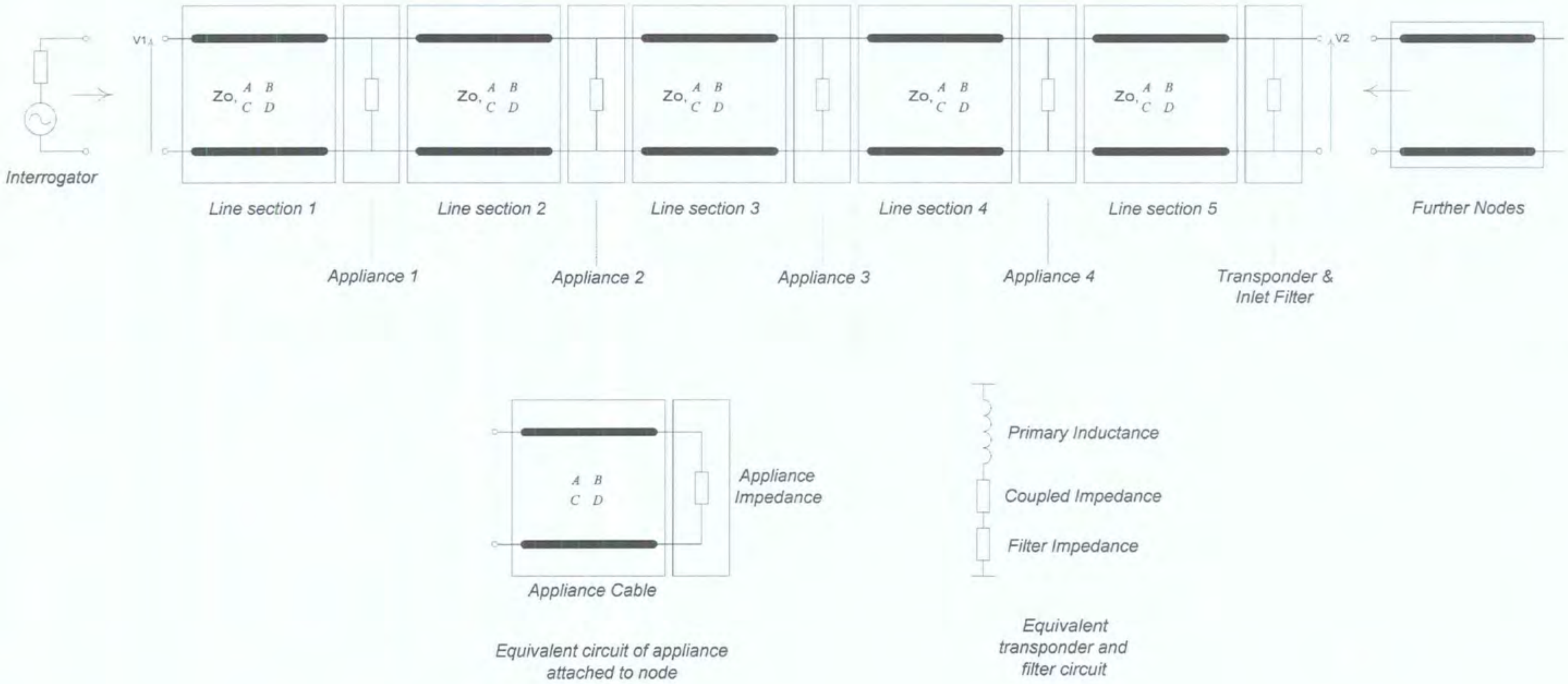

Figure 9.2 Transmission matrix model of a simulated power line channel comprising 5 nodes joined by power line sections. Also shown is equivalent model of each appliance, consisting of a power cable and inlet filter, along with equivalent circuit representing transponder attached to host appliance.

Impedance of the high-voltage power system connected to the distribution transformer is negligible along with the transformer secondary itself, which is considered to be high impedance for the frequencies of interest (see [Vines85] and [O'Neal], where transformer impedance was measured to be inductive up to 300 kHz). Note that if the transformer winding had significant capacitance this may have to be accounted for as it would shunt the channel at higher frequencies. Similarly, cabling between the first node (the interrogator) and the transformer could be included at higher frequencies.

To model cabling, the 6 A model described in section 6.5.4, chapter 6 was used. Results calculated using this model were compared to those suggested by Tsuzuki [Tsuzuki02], which applies for VVF[43] power cabling commonly used for in-door wiring in Japan, and were found to give very similar results across the frequency range 100 kHz – 100 MHz.

To find the attenuation between the interrogator node and transponder node, all transmission matrices representing intermediate nodes and cables are multiplied to give the overall ABCD parameters. The procedure is described more detail in appendix E. Note that intermediate nodes are represented by open or short circuit loads connected to IEC leads, thus representing the extreme extent of appliance loading. The input impedance of each intermediate node is calculated using:

$$Z_{input} = \frac{Z_{appliance} + Z_o \tanh(\gamma l_{cable})}{Z_o + Z_{appliance} \tanh(\gamma l_{cable})} \qquad (1)$$

where $Z_{appliance}$ is the appliance load, Z_o is the IEC lead characteristic impedance (modelled here as 6 A cabling), γ is the propagation constant and l_{cable} is the IEC cable

---

[43] VVF (Vinyl Flat) is a standard type of polyvinyl insulated electrical wiring used for Japanese domestic and office buildings.

length. The combined ABCD parameters are then used to find the open-circuit transfer function using:

$$\frac{V_{transponder}}{V_{\text{interrogator}}} = \left| \frac{1}{AZ_L + B + CZ_L Z_s + DZ_s} \right|_{ZL\to\infty, Zs\to 0} = \frac{1}{A} \qquad (2)$$

where Z_L represents the impedance of further nodes connected to the right of the transponder and Z_s represents the interrogator impedance. Assuming no further nodes exist beyond the transponder node and that the interrogator impedance is zero (a perfect source) then equation 2 simplifies as shown. Voltage attenuation can therefore be expressed as $20\log(1/A)$. We may also define the input impedance seen by the interrogator circuit by simplifying equation 10 in chapter 6, which was given as:

$$Z_{input} = \frac{A + Z_L B}{Z_L C + D}$$

Since the termination impedance is open-circuit this equation simplifies to:

$$Z_{input} = \frac{A}{C} \qquad (3)$$

Equation 3 represents input impedance presented to the interrogator circuit, which must vary by transponder load modulation if communication is to be established.

9.4.1.1 Simulation Results: Attenuation

Equation 2 was evaluated for various node separation distances and node impedances. In addition, the length of each appliance cable could be varied using equation 1. Evaluation of the most general power-line configurations are shown figure 9.3, including the following node impedances: open-circuit, short-circuit, matched impedance and appliance filter. The matched impedance load is approximate, since cable characteristic impedance is dependent on frequency. The chosen value was 120 Ω, giving good matching up to 3 MHz, and slight mismatch thereafter. Appliance filters were modelled as type II inlet filters as described in section 6.3, chapter 6. Open-circuit node conditions are obviously encountered when a power-line socket is unused. Short-circuit conditions should not occur unless a fault appears on the line, but was included to cover the worst-case load conditions. Clearly voltage attenuation varies considerably depending on frequency and node termination conditions. In some cases (below 100 kHz) *insertion gain* is seen due to resonance effects. A maximum attenuation of 139 dB occurs at 446 kHz when all nodes have inlet filters attached.

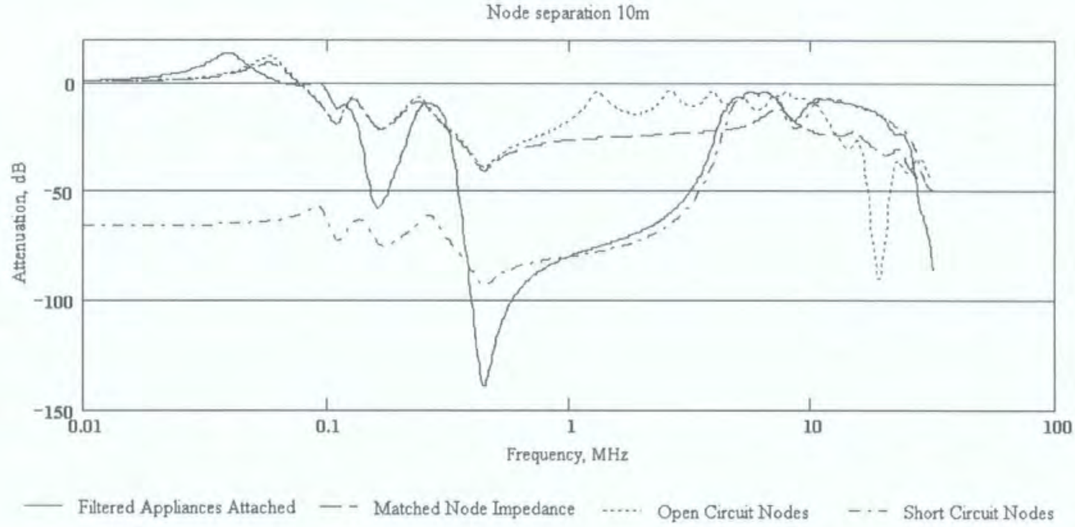

Figure 9.3 Attenuation of voltage between interrogator and transponder node versus frequency, showing dependency on node terminations. Nodes 1-5 spaced uniformly by 10 m, cable lengths attached to nodes were 2 m long.

At frequencies close to the cable RFID operational band (125 kHz) attenuation is still dominated by the combination of coupled impedance and inlet filter impedance (see section 6.5.6 for examples of their characteristic in the absence of the power-line) although the average value is determined by the channel characteristics. As would be expected, attenuation is higher for short-circuit nodes at low-frequency. At higher frequencies (above 1 MHz) appliance cable length begins to influence channel impedance, as reported by Tsuzuki [Tsuzuki01].

Further information is revealed by calculating the attenuation versus node separation distance. In figure 9.4 the length of line section 5 is varied between 1 and 1000 m, while nodes 1-4 have fixed lengths of 10 m. The frequency is 125 kHz and all nodes have inlet filters fitted. Attenuation increases rapidly as the transponder node is moved further from the interrogator, and the first line resonance effect takes place at around 800 m. The effect of reducing transponder chip impedance is also shown in figure 9.4, resulting in around 3 dB of additional attenuation. This would cause a drop in transponder node current and therefore transponder chip voltage for modulator ON periods during load modulation.

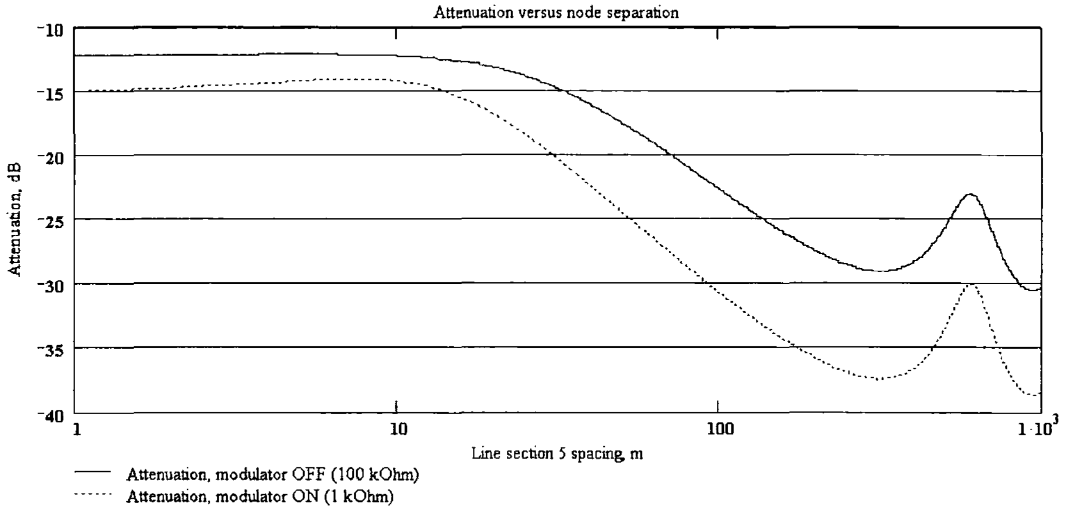

Figure 9.4 Attenuation between interrogator and transponder versus node separation at 125 kHz. Separation distance applies to nodes 1-4; separation between node 4 and 5 is fixed at 10 m. Filters attached to all nodes.

9.4.1.2 Load Modulation Sensitivity

The input impedance seen at the interrogator node must exhibit variations due to transponder load modulation if communication is to be established. Equation 3 was used to calculate the impedance of all components to the right of the interrogator node i.e., power cables, appliances and transponder. The simplified version of equation 3 may be used because the final termination impedance (Z_L) is assumed open-circuit (no further nodes beyond the transponder node); the transponder node is included in the evaluation of the *ABCD* system matrix. If further nodes are to be included beyond the transponder node, then these may be included as an equivalent input impedance, Z_L, which is then substituted into equation 6, chapter 10.

Input impedance was calculated at the fixed frequency of 125 kHz, which is the operating frequency of the transponder. In figure 9.5 input impedance is shown versus section 5 length, which is varied between 1 and 1000 m. The length of line sections 1-4 is fixed at 10 m. Appliance filters were modelled at each node. The graph shows that input impedance is dependent on node spacing, falling rapidly beyond 10 m spacing. The effect is more pronounced during the modulator OFF condition to the extent of becoming equal (in magnitude) to the impedance during modulator ON periods for around 20 m spacing. The modulator OFF condition emphasises the first resonance effect at around 30 m spacing causing a greater dip in the impedance. Main line resonance occurs at around 570 m spacing at this frequency in the form of a small increase in impedance, dampened by cable losses. The ability of the transponder to modulate system impedance deteriorates above node spacing of 100 m as cable losses increase, although some variation persists at the first resonant peak.

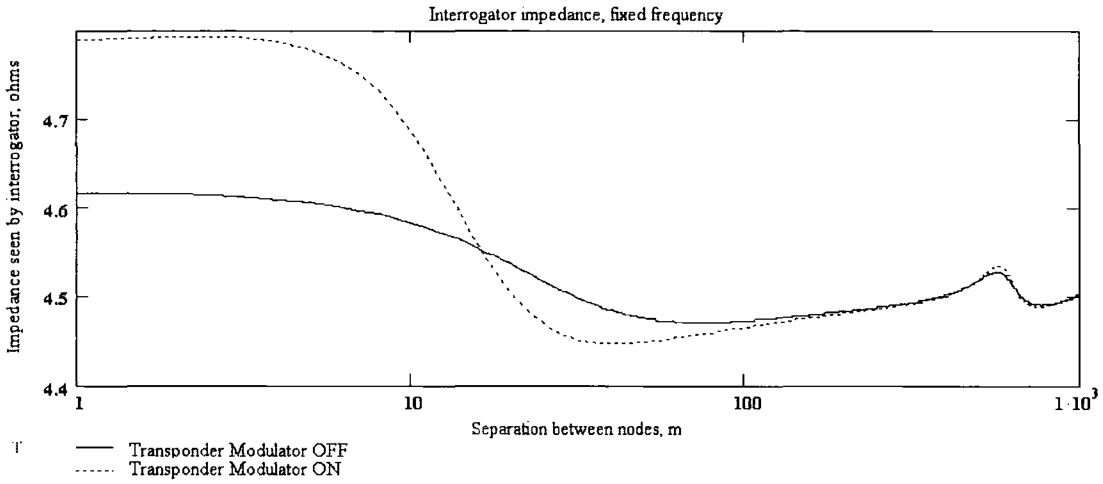

Figure 9.5 Variation of in magnitude of interrogator node impedance versus line section 5 length, including modulator OFF (100 kΩ) and ON (1 kΩ) conditions. Frequency is 125 kHz (transponder resonant frequency) and appliance filters are attached to each intermediate node. Line sections 1-4 have length 10 m.

Since the interrogator detector is capable of distinguishing between amplitude and phase modulation of the input impedance (see sections 5.9 and 7.7) we inspect the variation of real (resistive) and imaginary (reactive) components of the input impedance under different loading conditions. Results calculated using appliance filters attached to each node are shown in figure 9.6, where the variation of input impedance due to transition from modulator OFF to modulator ON are shown. Note for node separation less than 100 m, modulation of the input impedance always occurs as some combination of magnitude and phase variation. Complete failure only occurs if the change of phase and magnitude coincide at zero. Regions of zero magnitude or phase modulation do occur whenever the vector of input impedance is flipped about the real or imaginary axis of the Argand diagram. Further calculations were performed for open-circuit, short-circuit and matched-impedance node conditions (figures 9.7 – 9.9). Below 100m there is no evidence of zero impedance modulation; phase or magnitude (or both) modulation occurs. Note that modulation sensitivity is greatly reduced for short-circuit nodes (figure 9.8) and that open-circuit nodes resulted in reasonably consistent modulation of the real component of input impedance up to 100 m. The intention of matched-impedance nodes was to discourage the onset of resonance and has the effect of increasing load modulation sensitivity compared to the use of appliance filters. Load modulation sensitivity is generally increased as the impedance connected to each node increases, since the transponder is then able to dominate input impedance by its low line-line impedance.

By varying the length of line section 1-4 rather than section 5, a more drastic variation of input impedance can be seen (figure 9.10). Cable resonance strongly affects modulation of the interrogator impedance even when node spacing is less than 10 m. This is because standing waves are established along the whole power line as the node spacing is increased. In fact, the previous figures (9.6-9.9) are "snap-shots" of figure 9.10 at 10 m node spacing. There is always modulation of the input impedance until node spacing exceeds a given limit, which in this example is around 20 m. Beyond this point, two factors contribute towards the reduction of load modulation sensitivity. First, cable attenuation dominates system impedance. Second, shunting effects of the appliance filters causes further attenuation of the transponder signal. This second factor is confirmed by changing the node conditions to open-circuit (figure 9.11), which extends the useable range to around 100 m node spacing.

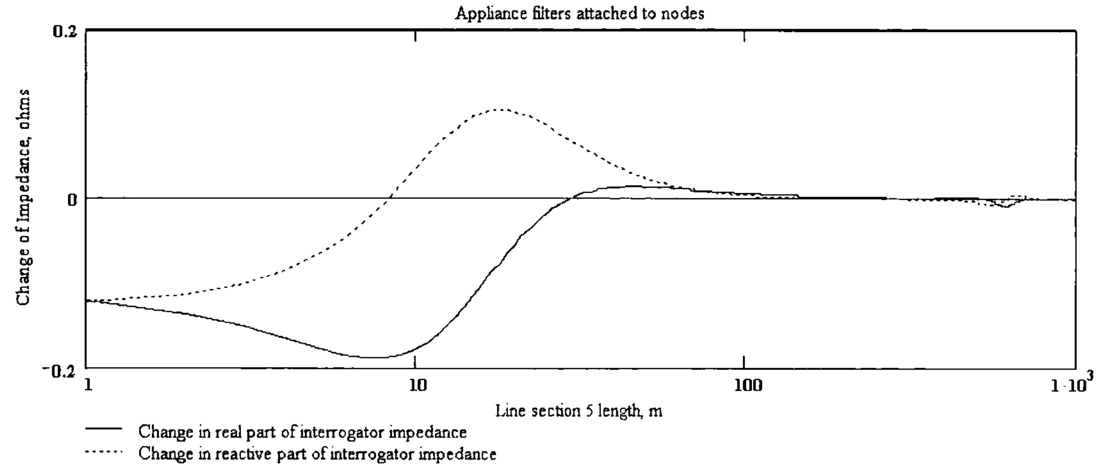

Figure 9.6 Modulation of input impedance by transponder, showing variation of real and imaginary components. Frequency = 125 kHz, appliance filter attached to each node.

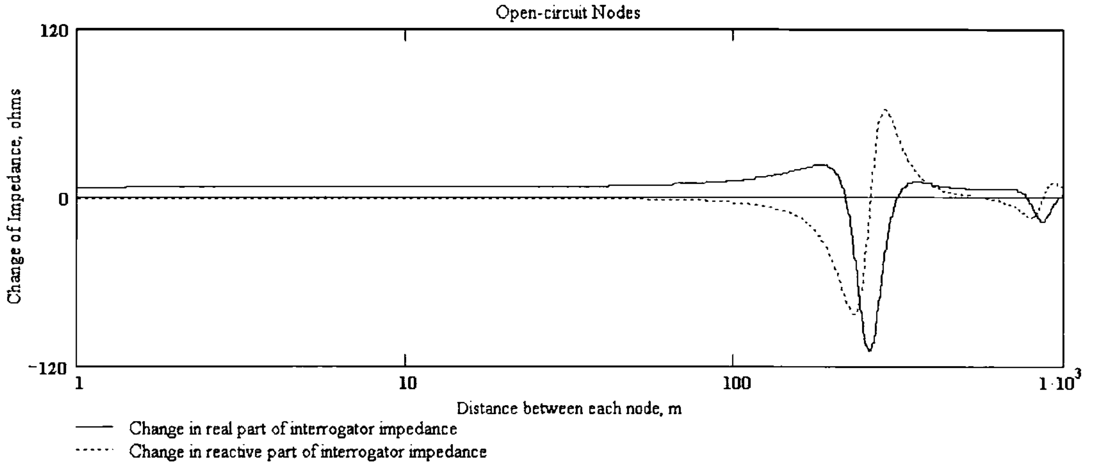

Figure 9.7 Input impedance modulation for open-circuit nodes.

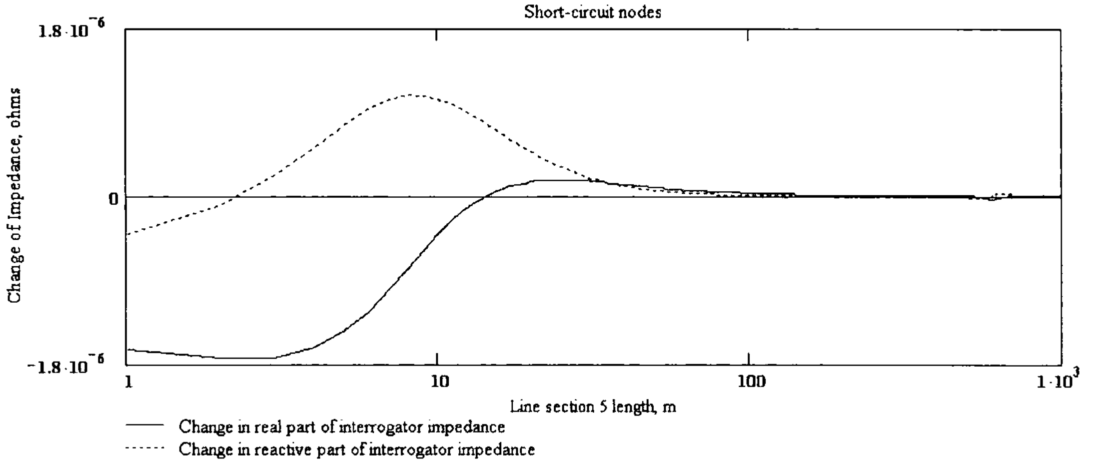

Figure 9.8 Input impedance modulation for short-circuit nodes.

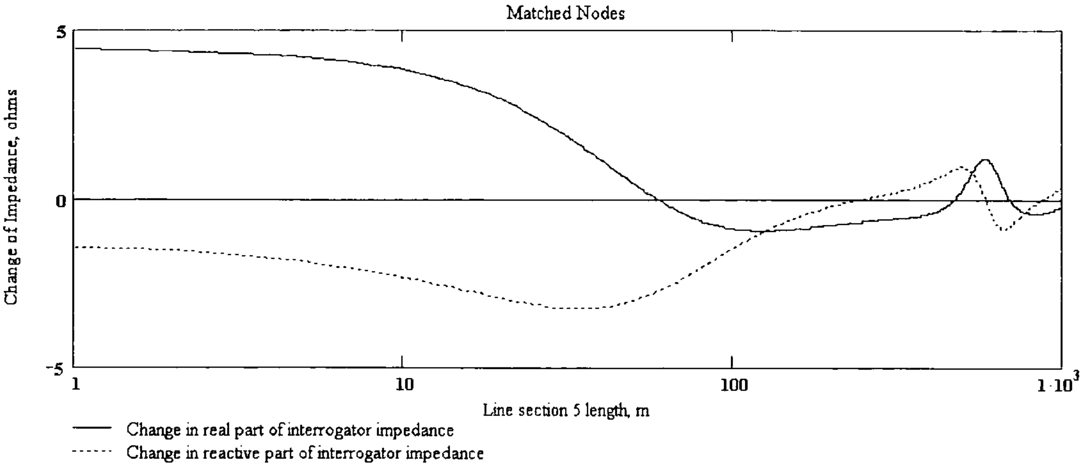

Figure 9.9 Input impedance modulation for impedance-matched nodes.

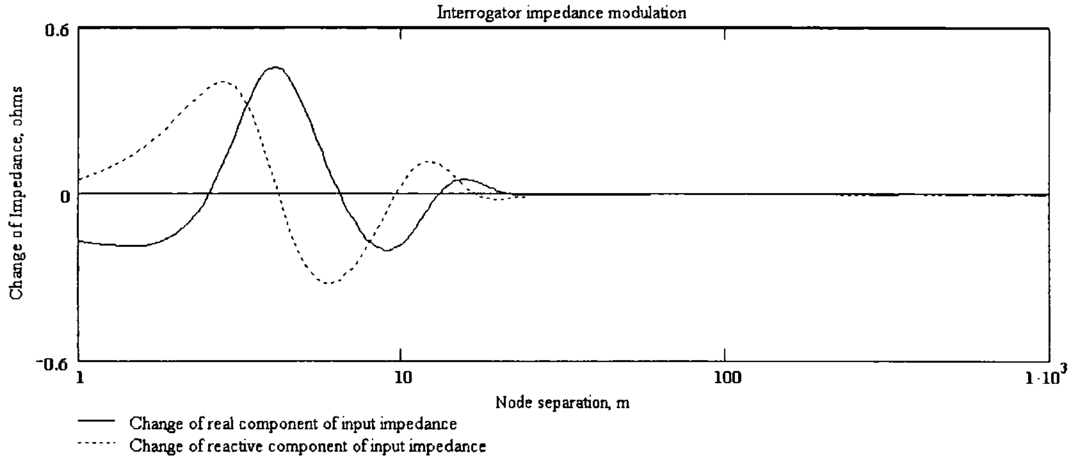

Figure 9.10 Input impedance modulation versus line section 1-4 length with appliance filters attached to nodes. Line section 5 has fixed length of 10 m.

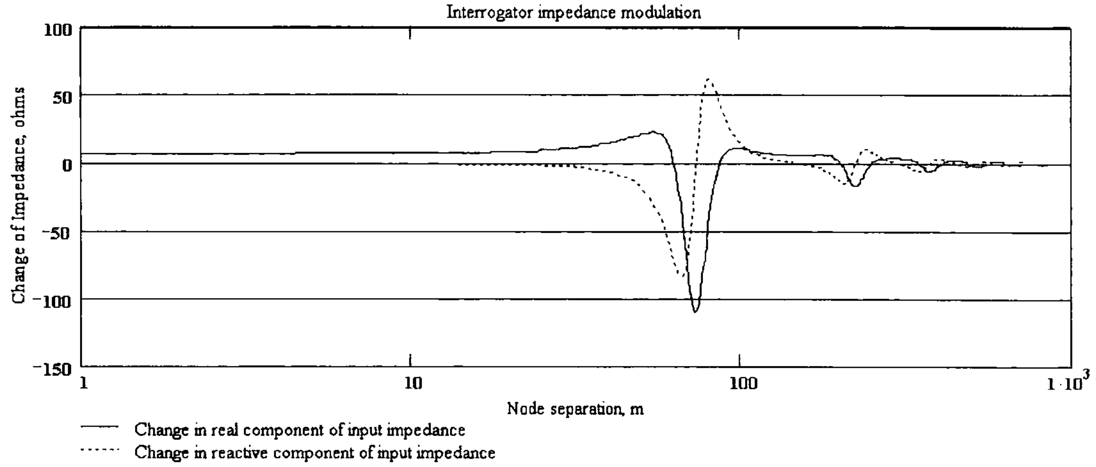

Figure 9.11 Input impedance modulation versus line section 1-4 length with open-circuit nodes. Line section 5 has fixed length of 10 m.

9.5 Prototype Power-line Interrogator System

A communication system was designed based on the interrogator described in chapter 7 and commercial RFID transponders to determine if passive direct-load modulation was possible across the power-line. As shown in figure 9.12, line-line coupling was used since this less sensitive to variation of line impedance (see section 9.3.1). The intention was to couple a modulated carrier to the power-line at point (a) which energises the remote transponder at point (b). An inductive coupler (having no galvanic connection to the power-line) is fixed to the live or neutral feed and a return path between line and neutral completed by the impedance of the appliance filter. As discussed in section 6.3, chapter 6, the impedance presented by the inlet filter is dominated by the inlet capacitor. If the transponder is activated load modulation takes place which causes small perturbations in the power-line impedance that must be detected by the interrogator.

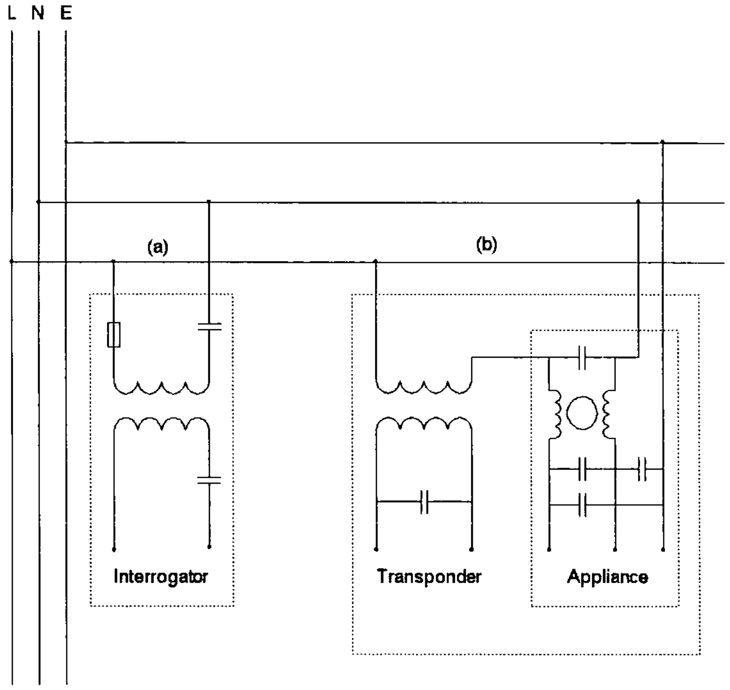

Figure 9.12 Experimental communication system showing coupling of interrogator and transponder to power-line.

An inductive coupler was used at point (a) having a turns ratio of 11:1 to maximise line current. The interrogator circuit features series resonance between capacitor C_{int} and the coupler inductance. This is necessary to allow the interrogator to sense small variations in line impedance caused by transponder load modulation but presents a dilemma, since line-line voltage is conventionally increased in power-line communication by parallel resonance. Transponder voltage is directly proportional to the current passing through its primary (see section 5.6.3, chapter 5), which is in turn proportional to line-line voltage when line-line coupling is used. Due to this compromise the transponder coupler turns-ratio arranged to be 40:1 to increase chip voltage. Preliminary results obtained using the test system were published in [McWilliam].

9.6 Measuring Load Modulation Sensitivity

The power-line communication system was connected to various mains sockets in an office located at the Durham University site. The electrical layout of part of this office is shown in figure 9.13. A populated power-line system was used to observe effects other mains appliances have on load modulation. The mains wiring in this office was scattered, i.e., having separate live, neutral and earth wiring that results in variation of line characteristic impedance and therefore cannot be modelled precisely. This type of wiring arrangement is very common in commercial offices due to its ease of fitment but has not been considered in the literature, since it cannot be modelled as a homogenous transmission line. A single transmit point and five transponder locations called receive points were used as indicated in figure 9.13. A cross-phase point, called receive point 4 was included.

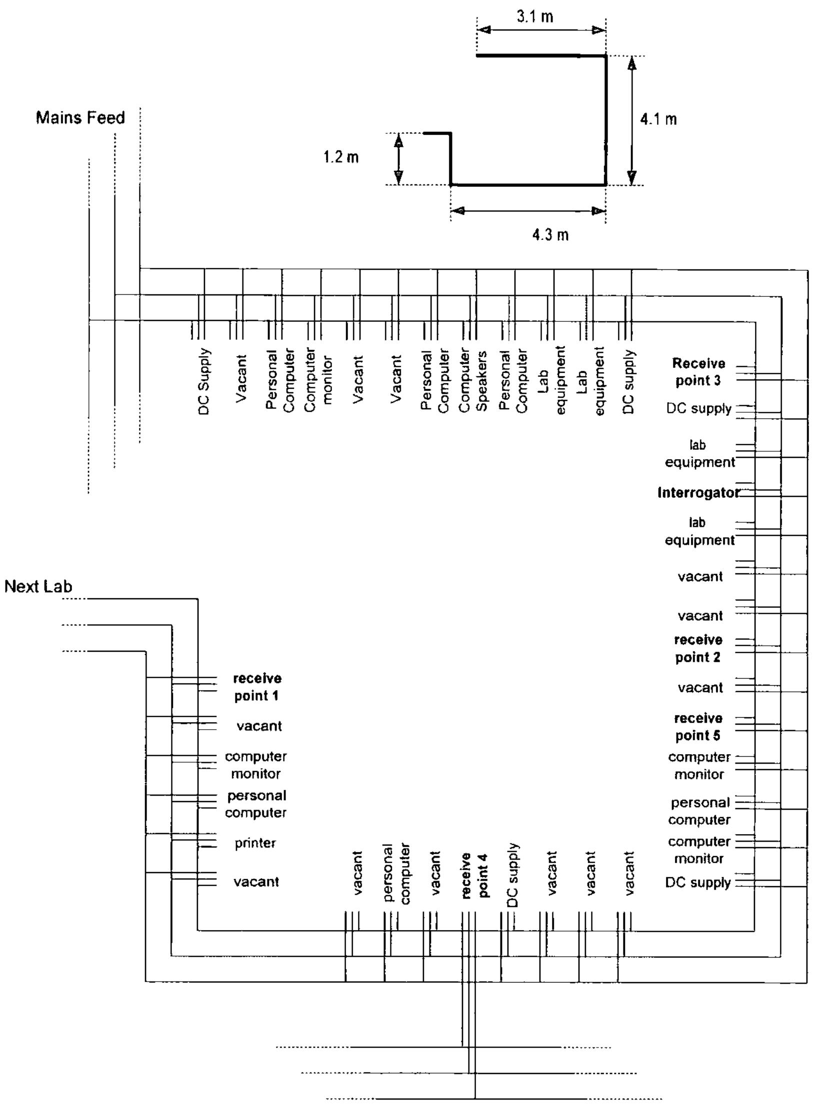

Figure 9.13 Schematic of power-line used for investigation.

To measure load modulation sensitivity the appliance filter was replaced by an 0.1μF X-class capacitor to maintain a consentient impedance in series with the transponder. The load connected to the coupler secondary terminals was switched between 1 kΩ and 100 kΩ. The corresponding change in tap point voltage at the interrogator circuit was measured (see section 5.8, chapter 5 for location of the tap point). The results are shown in table 9.1 including absolute and difference voltages.

Position	Transponder Voltage, Volts peak-peak ($R_{transponder}$ = 100 kΩ).	Transponder Voltage, Volts peak-peak ($R_{transponder}$ = 1 kΩ).	Difference in Transponder Voltage, Volts peak-peak.	Tap Point Voltage, Volts peak-peak ($R_{transponder}$ = 100 kΩ).	Tap Point Voltage, Volts peak-peak ($R_{transponder}$ = 1 kΩ).	Difference in Tap Point Voltage, Volts peak-peak.
Receive Point 1	22	2	20	18.48	18.26	0.22
Receive Point 2	21	2.4	18.6	18.55	18.42	0.13
Receive Point 3	5.85	0.64	5.21	18.18	18.17	0.01
Receive Point 4 (cross-phase)	0.5	0.04	0.46	18.15	18.15	0.00
Receive Point 5	12.2	1.1	11.1	18.15	18.07	0.08

Table 9.1 Load modulation sensitivity results.

The most striking result in table 9.1 was the transponder voltage at receive point 3 which is closer to the interrogator than receive point 5, yet shows weaker coupling. This is caused by fading of power-line channel possibly due to loading by a nearby appliance. Cross-phase coupling was very weak in this power system and is insufficient for passive communication. Receive point 1,2 and 5 exhibited sufficient coupling and load modulation sensitivity for passive load modulation and receive point 2 and 5 were used most often for communication. Note that load modulation sensitivity appears to increase with transponder voltage, which is consistent with the findings of section 5.8.2, chapter 5, where line resistance was found to affect load modulation sensitivity by altering primary and secondary Q. In power-line coupling, loading occurs between the interrogator and transponder inductive couplers due to power-line impedance as shown in figure 9.14, which causes attenuation of the transponder voltage and reduction of interrogator and transponder Q and therefore load modulation sensitivity. For a fixed frequency of 125 kHz the power-line impedance was assumed to be dominated by lumped resistance, *RPL*, and inductance, *LPL* as shown in figure 9.14.

The preliminary results show that load passive operation is possible for close range communication and that load modulation is simultaneously possible, in the absence of channel fading. In addition, load modulation sensitivity increases as the attenuation decreases.

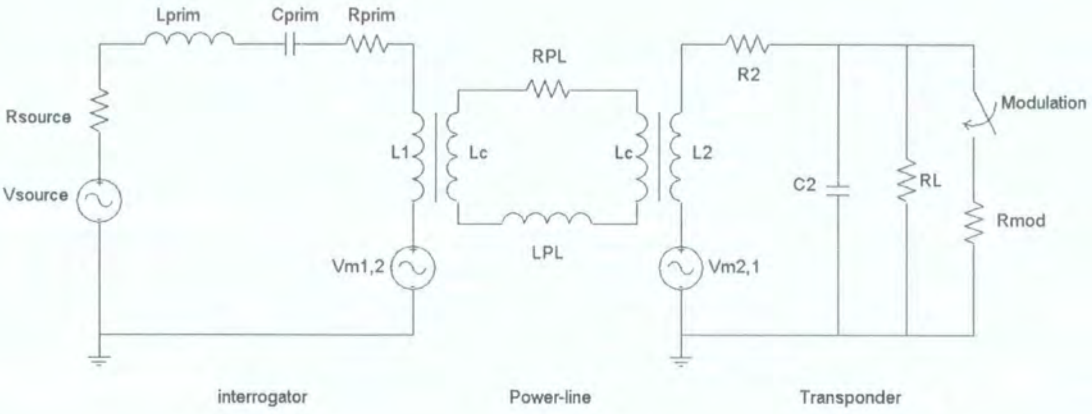

Figure 9.14 Equivalent circuit representing coupling between interrogator and transponder on the power-line. Power-line is represented by lumped inductance (*LPL*) and resistance (*RPL*).

9.6.1 Simulated Power-line Impedance

The power line impedance was simulated by finding the equivalent impedance $ZPL = |RPL + j\omega LPL|$ that gave similar interrogator and transponder voltage levels to those in table 9.1. This impedance was inserted in a cable connecting interrogator and transponder. The resulting impedance was around 60-70 Ω for receive points 2,3, and 5 which is within the range measured by Nicholson [Nicholson] and was found to be reasonably consistent over a number of weeks.

9.7 Effect of Channel Interference on Communication

Communication was established between interrogator and transponder in order to determine the effect of power-line noise sources such as those described in section 9.2.1. The interrogator software described in chapter 7 was modified to produce packet loss statistics to help quantify error rates.

9.7.1 Dominant Noise Sources

As discussed in chapter 7, self-induced receiver noise was reduced by placing the RF transceiver chip on a PCB providing isolation between the digital driver stage and the demodulator input. However switching noise was still present and contributed to received noise and bit error rate.

Channel noise was clearly evident in all forms described in section 9.2.1 i.e., synchronous, non-synchronous, wideband and impulsive. An obvious source of synchronous noise is the host appliance, whose inlet filter is used to complete the line-line circuit. An example of this type of noise is shown in figure 9.15, which was produced by a laptop computer power supply. Discontinuities in the line-line voltage occur at each maximum and minimum of the power line voltage i.e. at a rate of 100 Hz due to switching a capacitor between live and neutral. The noise waveform was recorded at the demodulator output of the interrogator RF chip (see chapter 7), which is highly sensitive to impedance modulation of this type since it is designed to detect load modulation of the interrogator circuit. Similar recordings were reported by Vines [Vines85] in relation to voltage noise sources, but in this context such noise sources constitute severe interdependence because the resulting impedance modulation dominates over transponder load modulation, and can "jam" the transponder signal. An example of such interference is shown in figure 9.16, where a switching power supply causes disturbance of the demodulator output during packet transmission.

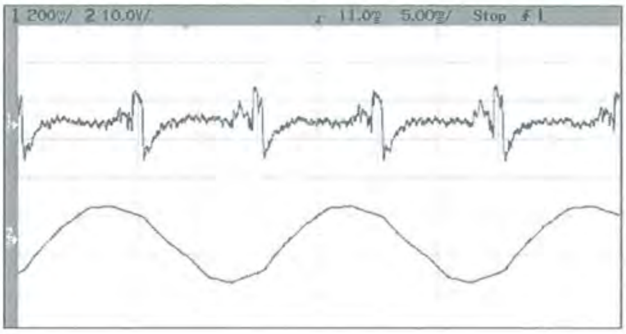

Figure 9.15 Synchronous noise generated by switching power supply of host appliance. Top trace: switching noise, bottom trace: 50 Hz mains waveform.

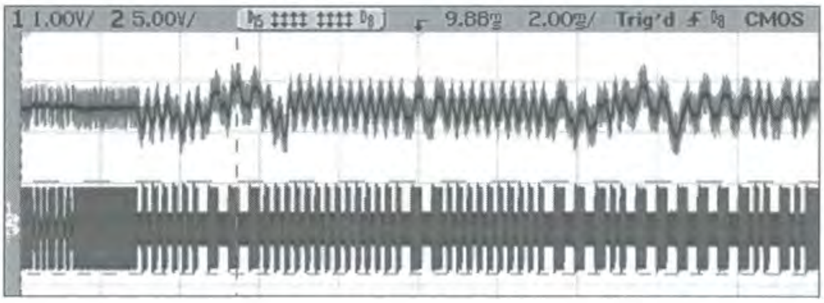

Figure 9.16 Interference caused at demodulator output due to nearby switching power supply. Top trace: demodulator output waveform, showing transponder message and two instances of interference, bottom trace: load modulation signal measured across transponder terminals.

9.7.2 Packet Analysis

To characterise the accumulative effects of channel noise, a large number of packets were transmitted from the transponder to the interrogator. The interrogator software described in chapter 7 was modified to monitor the number of correct, incorrect and dropped packets received. A packet comprises 32 bits that represent the unique transponder identification number. A channel test consisted of 256 read batches, each requiring 100 packet read operations. Each test required around 30 minutes to complete.

An example of the typical packet statistics gathered is shown in figure 9.17, which was recorded while the transponder was located at receive point 1 (figure 9.13). The figure shows that for each batch of 100 packet read operations, the majority of packets received were correctly detected, while a smaller number of packets were incorrectly detected or dropped.

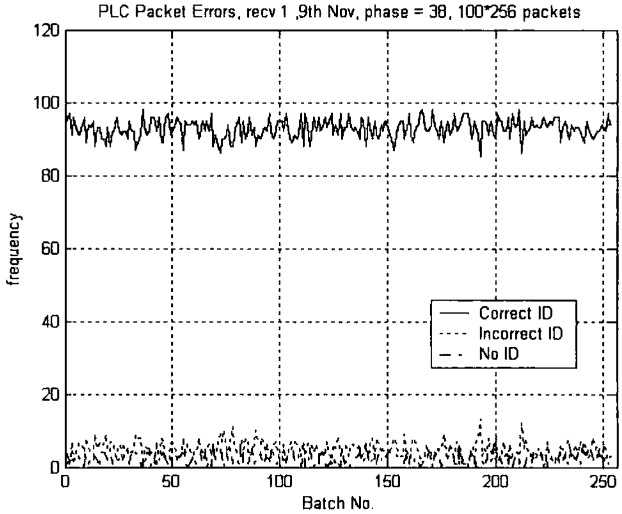

Figure 9.17 Example of power line channel test result, showing record of number of correct, incorrect and dropped packets per batch (one batch = 100 packet read operations).

Test results from receive locations 1,2 and 5 are summarised in tabular form in table 9.2, which represent the typical channel behaviour. As was stated in section 9.6 communication was not possible from receive points 3 and 4. Dropped packets indicate an illegal symbol transition (too long or too short) at the detector and are trapped by the sampling routine. Incorrect packets are the most undesirable result and are caused by one of two faults. The first is bit inversion due to foreign load modulators on the power-line, such as switching power supplies. The second is bit indecision by the detector caused by self-induced noise. The example results shown in table 9.2 show that errors were encountered least often from receive point 1, which is farthest from the interrogator. Dropped packets are dominant from receive point 2 while incorrect packets are dominant from receive point 5. Both receive points exhibited low sensitivity to load modulation in comparison with receive point 1 (table 9.1), which contributes to bit indecision in the detector.

Receive point	Correct packets	Incorrect packets	Dropped packets
1	23754 (92.79 %)	1195 (4.67 %)	651 (2.54 %)
2	6768 (26.43 %)	43 (0.17 %)	18789 (73.4 %)
5	3654 (14.27 %)	13779 (53.82 %)	8167 (31.91 %)
1 (low noise receiver)	25548 (99.8 %)	0 0 %)	52 (0.2 %)

Table 9.2 Prominent channel test results from three receive points.
Total packets per test = 25600.

As mentioned earlier. a low-noise implementation of the interrogator was designed using careful PCB layout that significantly reduced bit indecision due to self-induced noise. The design produced no errors while being used as a proximity RFID interrogator and it was therefore assumed that self-induced noise was rendered negligible and packet errors were then due to power-line noise sources. An example of the benefit of this design is shown in the last row of table 9.2, where no incorrect packets were detected at receive point 1 in comparison to 4.67 % using the original interrogator design. In many tests it was possible to record zero packet loss and incorrect packets by using the low-noise interrogator, but the occurrence of such results was not sufficiently repeatable. It is suggested that running tests with a greater number of batches would reveal packet errors that occur over longer periods due to power-line channel variations.

Power-line communication was tested using an actual appliance attached to the transponder node, rather than the X-type capacitor. The appliance used was a compact switched-mode power supply for a laptop computer. The mains inlet filter provided a path between live and neutral enabling current to flow, which energised the transponder.

In all cases studied it was found that the presence of the appliance filter *reduced* packet error rates due to increased signal to noise ratio at the detector output. This may be caused by the increased rejection of "noise" by the inlet filter which resulted in lower line-line impedance at the carrier frequency of 125 kHz, and hence higher primary current passing through the transponder primary. This increase in signal to noise power also aided in overcoming foreign load modulation caused by the power supply itself.

9.8 Conclusion

Under favourable conditions the method of passive direct-load modulation was found to be possible over the power-line. Load modulation sensitivity is a function of the instantaneous power-line impedance and is therefore influenced by variation of the power-line impedance. In some cases foreign impedance modulators pose a challenge for the power-line transponder, which must assert impedance modulation via the inductive coupling mechanism. In contrast, most foreign load modulators such as switching power supplies assert channel impedance modulation by direct connection to the power-line, and therefore constitute major interferers.

Passive transponder operation was possible within the limited sample power-line and was shown to be theoretically feasible across several tens of meters. However the biggest challenge in passive communication is the variation of attenuation depending on the frequency and distance of communication. The frequency response was found to vary widely even at the low operational frequency and exhibited strong dependencies on loads attached to the power-line and cable lengths.

A channel model was established using the transmission matrix approach which incorporated the coupled transponder impedance equivalent inlet filter model. The results indicate that load modulation sensitivity is dependent on the same parameters as attenuation, namely, channel loads and cabling. However for the combinations investigated it was shown that some combination of amplitude and phase modulation should always occur and that modulation nulls were not encountered.

9.9 Further Work

Characterisation by measurement could be extended in two ways. The first method would involve further measurements across a real power-line to construct a statistical model of channel impedance. Where this has been attempted elsewhere, many results were required before generalisations could be made . Furthermore, power-line load characterisation is still difficult due to the large range of appliances that exist, each with individual characteristics. The second method for measurement would involve building a virtual power-line that is off-line i.e., disconnected from the mains supply, as adopted by Tanaka [Tanaka]. This would permit direct measurement of impedance due to cabling and (non-active) appliances.

The channel model could be extended to create a probabilistic description of the power-line and its loads. At the simplest level, load impedances and cable lengths could be assigned a probability distribution that describes their likely variation.

10 A Minimal-Hardware RFID Interrogator Design

10.1 Introduction

In this chapter a novel approach to RFID interrogator design is investigated which uses a digital-domain implementation with the primary aim of increasing the flexibility of the radio device. In contrast to a recent flexible interrogator design described in [Reynolds], we take a minimal hardware approach, and in doing so identify fundamental hardware constraints placed on transmitter and receiver blocks. It is demonstrated that a minimal-hardware transmitter implemented in the digital domain can activate a passive low-frequency transponder, and that a simple detector attached to the transmit path can be used to produce a baseband signal which is then digitised. Subsequent data processing could then be performed to decode the packet data within the digital domain with the associated benefit of reconfigurable architecture. The device was implemented using an FPGA. Compromises made in the transmitter and receiver path are identified and evaluated.

10.2 The Need for an Adaptable Interrogator

During the last few years, manufacturers have focused their attention on reducing the cost of transponder production in order to meet the needs of high-volume markets. While transponder cost certainly forms one key requirement for successful uptake in the these markets, the impact of reader design should not be ignored because it brings a major influence to RFID by accommodating transponder-orientated design factors. The most prominent influencing factors are:

1. Several frequency bands are used in RFID;

2. For each frequency band, various transponder chips are available on the market, each with proprietary signal modulation and communication protocols;
3. Anti-collision methods are in still under development because the balance of cost effectiveness has not yet been met.

The need for interrogator flexibility became apparent during the development of a software-controlled interrogator module for Seaward Electronic (see chapter 7). The design lacked flexibility regarding frequency agility, alternative modulation protocols and anti-collision mechanism and the upgrade potential was limited. At the time when work on the module design commenced, state of the art low-cost transponders operated at 125 kHz and 13.56 MHz and employed simple anti-collision methods. Over the duration of the project several new developments in transponder technology have materialised, including new collision arbitration techniques, protocols and frequency bands. These changes were driven by the increasing RFID market and drafting of new standards for radio frequency identification[44]. Due to the lack of universal RFID standards, each transponder family adopts a proprietary protocol, coding and anti-collision mechanism. However since the inductive coupling mechanism is common to low frequency transponders, the development of "multi-tag" interrogators that use a single RF transceiver and software-controlled baseband processing is possible. Such readers currently operate at fixed frequency, limiting scope in multi-band transponder environments. The problem will be exasperated further when UHF (860-910 MHz) and even Microwave (2.45 GHz) transponders become widespread. The universal RFID interrogator would be capable of adapting to the three points listed above i.e., frequency band, modulation/protocol and anti-collision method.

---

[44] See Chapter 2

10.3 A Software-Defined Approach

A potential solution is to define radio functionality in the digital domain such that its functionality is under software control and therefore reconfigurable. This type of radio is often called *Software Defined Radio* (SDR), a term adopted by Mitola [Mitola] and subsequently others [Finlay], [Bing], [Hentschel], [Buraccini]. SDR is fundamentally different from *Software Controlled Radios*, which employ fixed RF circuits connected to microcontrollers. Although microcontroller code drives system events and controls timing, the radio architecture is essentially fixed. Buracchini states in [Buracchini] that SDR should be "*multistandard, multiband and reprogrammable by software*". Mitola identifies the idealised SDR as having all radio functions defined in the digital domain, requiring direct conversion at the RF input. In such an architecture, the only remaining analogue components would be the antenna, high quality band-pass filter and low-noise amplifier. Such a radio design is technically challenging however because very high ADC sample rates are required to digitise the RF signal [Bing]. A more realistic implementation involves digitising the IF signal, which typically operates under 100 MHz, and has been implemented in various architectures [Lackey], [Blust], [Pérez], [Kennedy]. An alterative method is direct down-conversion in which a band limited signal is sampled at a rate greater than the bandwidth, but less than the carrier frequency [Wepman], [Bringham]. This generates multiple replicas of the original band pass signal, some of which are centred about frequencies lower than the original carrier frequency. In [Laddomada] a high-speed ADC is used to convert RF signals with a maximum bandwidth of 100 MHz and carrier frequency of 2 GHz. The resulting down-converted signal comprises the pass-band signal converted directly to baseband frequency that can be processed by a workstation PC. In general the ADC forms a critical element in any SDR because its sample rate, resolution and linearity place constraints on the overall system performance. In addition, the digital hardware must be capable of processing very large amounts of data [Baines]. For example, Bing [Bing] estimates that around 100 billon instructions per second would have to be executed in order to process the IF stage of a GSM mobile phone in the digital domain. A final challenge to be overcome by SDR is regulation, which at present does not favour agile radio systems due to issues regarding uniformity, spectrum allocation and spurious emissions [Bishop].

10.3.1 Potential Advantages for RFID Interrogator Design

The benefits of reconfigurability, multi-standard compatibility and multi-band capability are potentially great for RFID interrogator design. Reconfigurability brings the benefit of future adaptation; new transponder protocols, coding and modulation methods may be incorporated without hardware changes. This is especially true for RFID interrogators because the fundamental physical signalling methods (i.e., inductive coupling, direct-load modulation and back scatter) are unlikely to change radically due to limitation of transponder chip complexity. A possible exception could be active transponders, which can afford to adopt more complex signalling methods with a corresponding larger variation of methods used.

Multi-standard compatibility would bring benefits to RFID technology for two main reasons. The first reason is that global standards such as ePC, GTAG and ISO 18000 are still in development (see chapter 2) and therefore an interrogator purchased today may be non-compliant in the future when standards are ratified. The second reason is that many RFID applications are global (e.g., tagging of goods in global supply chains) and it is often necessary to read a transponder in more than one country. RFID systems must comply with the national regulations regarding signal power, band and spurious emissions. Such regulations can vary considerably between regions. Rather than specify different interrogators for each region, a single multi-standard interrogator design could be purchased that is capable of complying with all international EMC and telecommunications standards.

The third benefit, multi-band capability, would bring obvious benefits to the RFID field, since four bands (125 kHz, 13.56 MHz, 860/910 MHz and 2.45 GHz) are most commonly used at present, spanning four decades of the frequency domain. However with current technology, it is difficult to construct analogue front-ends and antennas that span such a wide range of frequencies. To compound the problem, two distinct physical mechanisms are used in RFID (near-field and far-field) which require different antenna configurations. To date, this issue has been managed using multiple analogue front-ends/antennas. For example, the Speakeasy military software radio architecture [Lackey] utilises multi-band processing at baseband and requires interchangeable RF modules to support different radio bands. Special requirements of antennas for multi-band RFID were considered in [Reynolds], where a dual 125 kHz / 13.56 MHz design was achieved by using two front-end sets each having an antenna, filtering / down-conversion circuitry and sampling circuit.

10.4 Reconfigurable RFID Interrogator Concept

In this section implementation of a simple RFID interrogator in the digital domain is described. In addition to reconfigurability, emphasis was placed on low-complexity to achieve a minimal hardware design. The concept and hardware is described then detailed aspects of the transmitting and receiving blocks are investigated.

10.4.1 Design Concept

A reduced form of the canonical software radio architecture is illustrated in figure 10.1, showing the components most important for interrogator functionality[45]. The single inductive antenna shown in figure 10.1 is required to support simultaneous transmission and reception since transponder → interrogator communication takes place by direct-load modulation of the carrier current. The demonstration system has a sufficiently low frequency of operation (125 kHz) to permit direct conversion of transmit / receive signals.

The minimal transmitter hardware design is expanded in figure 10.2, showing the direct synthesis blocks that drive the resonant antenna circuit by digital signalling. No DAC is required in this design.

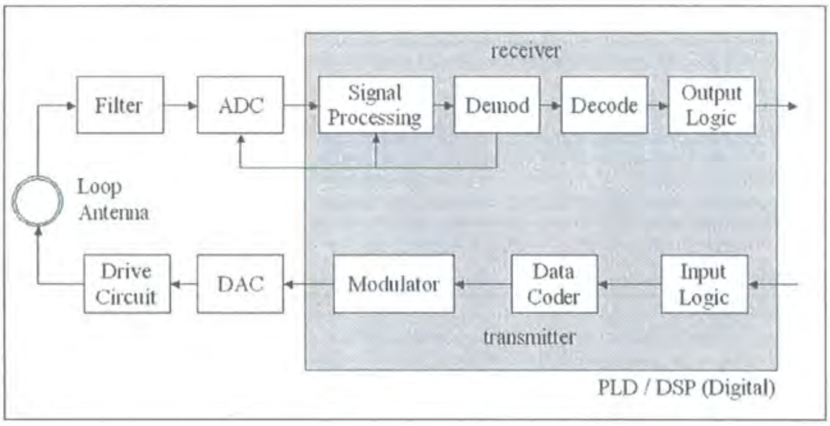

Figure 10.1 Adapted form of canonical SDR architecture.

---

[45] See Mitola [mitola] for a discussion of the canonical software radio architecture.

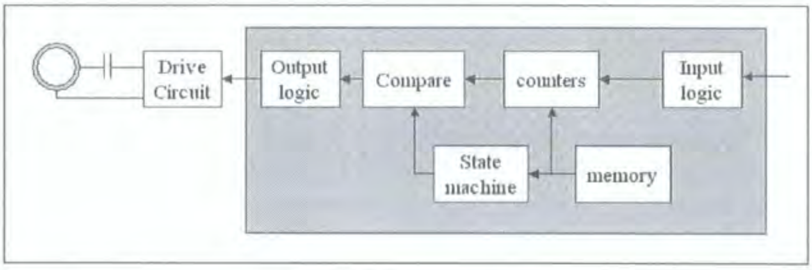

Figure 10.2 Expanded view of transmitter.

10.4.2 Hardware

The digital design was implemented using an FPGA[46]. A combination of schematic entry[47] and hardware description language (VHDL) was used to create the software design. As an alternative this design could also have been implemented using a DSP processor. Analogue-to-digital conversion was carried out by an AD9203 device, which has a maximum sample rate of 40 MSPS at 10 bit resolution.

The receiver currently consists of a simple envelope detector as illustrated in figure 10.3. An impedance buffer was used to avoid loading effects between the detector output and ADC input impedance, which can be as low as 100 Ω [ADdata].

---

[46] The device used was an Altera Apex™ 20KE FPGA with 200 available logic elements.

[47] Using Altera Quartus™ Design Software.

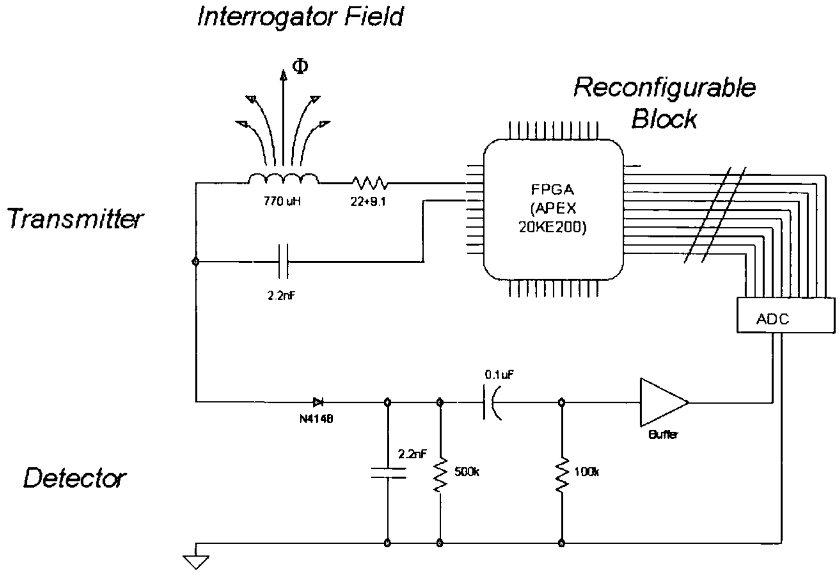

Figure 10.3 Demonstration of a digital transmitter and analogue detector. Baseband signal is then digitised for thresholding and decoding.

10.4.3 Transmitter

As mentioned earlier, it is possible to implement the transmit functionality entirely within the digital domain. A differential square wave driver is fed into the transmit LCR circuit, which contains the inductive antenna. The band pass characteristic of the transmitter circuit accentuates the fundamental component of the square pulse train which is equal to the first term of its Fourier series, $4\sin(\omega_c t)/\pi$, where ω_c is the carrier frequency. Higher harmonics are attenuated according to the Q factor of the transmit circuit. The resulting resonant voltage waveform is shown in figure 10.4, where the complementary digital driver may be seen. Due to the output resistance of each driver output and losses in the transmitter circuit, switching losses occur at each positive and negative peak of the waveform (i.e., between capacitive and inductive half-cycles). A larger voltage drop at the switching point indicates higher transmitter circuit losses. Switching noise is not critical from the perspective of transmission; the tuned circuit present in the transponder removes such discontinuities. However since the receiver must be attached to the transmit circuit to sense load modulation, switching noise is coupled to the receive signal path and manifests as synchronous noise in the demodulated signal[48]. This can increase the likelihood of threshold decision errors during decoding. Switching loss should therefore be minimised by reducing losses in the transmit circuit.

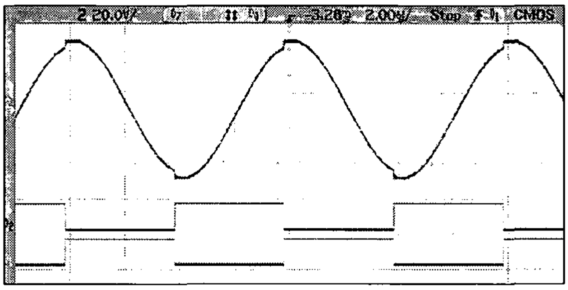

Figure 10.4 Direct digital drive circuit for interrogator transmitter.
Bottom and middle traces: complementary digital drive signal.
Top trace: resulting resonant voltage, which is representative of the line current.

Inductor current is sourced directly from the FPGA digital pins, which are capable of supplying a combined 50 mA (RMS) at CMOS voltages at the fundamental frequency. Primary current is limited by a 22 Ω resistor to prevent excessive distortion or damage.

Field pulsing is generated to communicate with the transponder. Field pulsing in the demonstration unit is illustrated in figure 10.5, where pulsing of the tap point and transponder voltage is shown. Field pulsing is coordinated by a state machine defined in HDL that controls various logic blocks comprising counters, timers and compare units. The demonstration unit produces pulse patterns compatible with Philips Hitag 1 transponders, but any field-gap pattern could be generated by reprogramming the logic. Currently the transmitter repeatedly issues a programmed command to the transponder.

---

[48] See section 7.5.2.2, chapter 7 for an example of switching noise in the baseband signal.

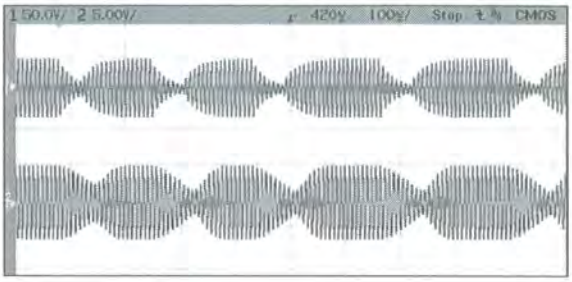

Figure 10.5 Illustration of field pulsing in demonstration unit.
Top trace: pulsing of the resonant tap point voltage (transmitter).
Bottom trace: resulting field gap modulation at transponder terminals.

10.4.4 Receiver

The receiver has not yet been fully implemented, but demonstrates that the RF or base band signal can be digitised for further process in the digital domain. Conversion of the demodulated (baseband) signal is shown in figure 10.6, where the digitised signal has been piped through the FPGA to a high-resolution DAC (not shown in figure 10.3) for displaying on the oscilloscope. Note that due to the strong pass band characteristic of the interrogator circuit, low-pass or band-pass filtering is less critical here than for traditional radio systems. Demodulation was achieved by a simple envelope detector[49].

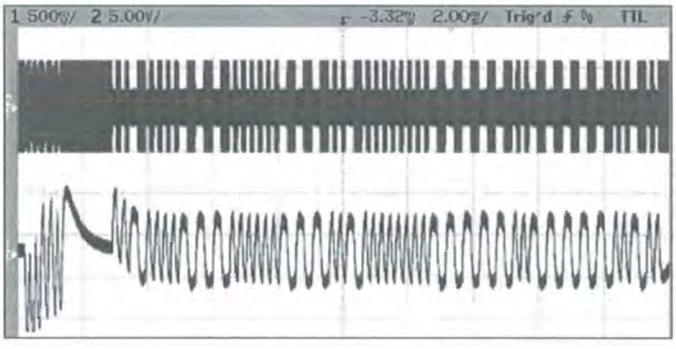

Figure 10.6 Example of digitised base band signal, using analogue detector.
Top trace: transponder terminal voltage, showing load modulation.
Bottom trace: resulting digitised base band signal prepared for decoding
(ADC and DAC sample rate: 40 MSPS).

---

[49] See section 7.3.1, chapter 7 for a description of the modulation scheme used.

10.4.4.1 Direct Carrier Conversion

As mentioned earlier, it is possible to digitise the complete 125 kHz RF carrier without requiring an expensive ADC. To implement carrier-conversion at higher bands (e.g., 13.56 MHz) would require a significantly faster ADC and correspondingly higher processing rate, but is under development in more expensive designs [Reynolds]. An example of the basic procedure is illustrated in figure 10.7. A passive voltage divider and impedance buffer is used to prepare the signal for digital conversion. Voltage division must be carried out using a passive divider due to the large magnitude of the tap point voltage, which can exceed 100 V (peak-peak).

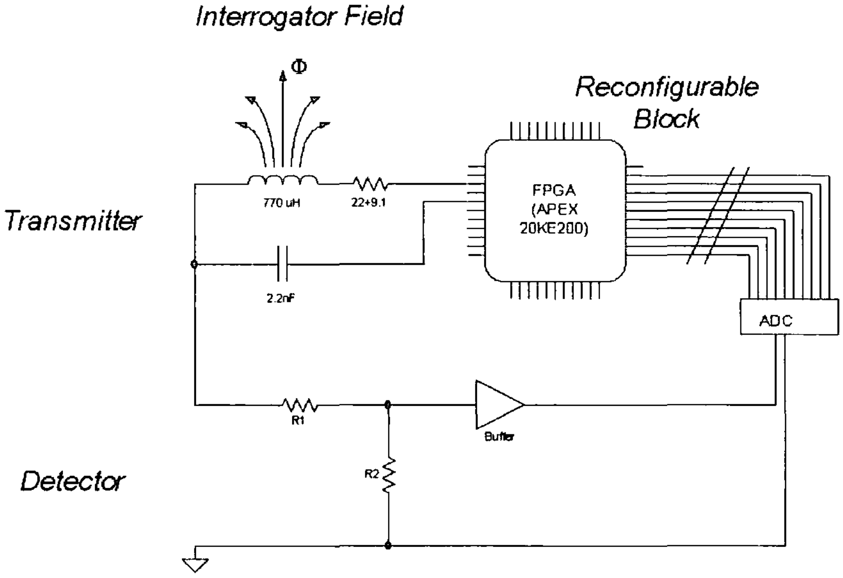

Figure 10.7 Simplification of receiver by direct conversion of RF carrier.

By digitising the entire carrier any demodulation technique may be implemented directly in the FPGA. A trivial example is signal rectification by a digital modulus operator to imitate envelope detection followed by filtering, scaling and thresholding. As this design in still in early development the full receiver is not yet implemented and a simple illustration of the demodulated signal is shown in figure 10.8 where the digitised carrier has been digitally rectified by appropriate logic, revealing the baseband signal that corresponds with transponder load modulation. Digital filtering and detection are now required to recover the message.

Figure 10.8 Digital demodulation of the sampled RF carrier.
Top trace: Transponder terminal voltage, showing load modulation of the field.
Bottom trace: Base band signal recovered by rectification in digital domain.

10.4.5 Performance

The demonstration unit uses current directly sourced from the FPGA drivers and is thus not intended for long range proximity sensing. The activation range is comparable to the software controlled interrogator described in chapter 7. As the receiver section has not yet been completed receiver performance cannot yet be properly evaluated. Sensitivity to direct-load modulation was however observed in the digital domain which should allow detection of the transmitted packet.

10.4.6 Summary

In this chapter a new approach to RFID interrogator design is introduced that adopts a minimal hardware design by implementing as many functions as possible in the digital domain. The directly digital transmitter can be operated using any digital CMOS device that provides sufficient output current with the addition of a few passive components. As more receiver functionality is defined in the digital hardware, the design will become reconfigurable and more suited to the changing RFID industry. The most important component that defines reconfigurability in this design is the placement of the ADC, which is a common dependency of software-defined radios. It is possible to convert the entire carrier for low frequency transponder systems and work is ongoing to investigate the possibility of direct conversion to higher RFID frequency bands.

11 Conclusion

The proliferation of electronic identification technologies has increased rapidly over the past three years to include high-volume global tracking applications. Upon the successful adoption of emerging global standards such as the Electronic Product Code (ePC), Global Tag (GTAG) and ISO 18000 physical specification, the market is expected to increase dramatically in both size and diversity during the next few years. The cost of high-volume transponders will fall accordingly with the introduction of new assembly processes. This evolution will also directly benefit specialist low-volume markets.

It has been shown that the benefits of automatic identification and electronic data storage can be brought to the application of electrical safety testing. The intention has been to enable automatic identification of mains-powered appliances prior to the testing phase with minimum user intervention. This document has focused on the following electronic identification techniques: proximity Radio Frequency Identification (RFID), cable RFID and power-line signalling.

Proximity RFID enables rapid electronic identification by proximity detection of inductive transponders that have been fixed to electrical appliances. It was necessary to maintain performance in substantially metallic environments in which transponders are sometimes mounted directly on metal surfaces and interrogators are moved close to metallic objects. An interrogator coil design is described that provides stable operational impedance at a frequency of 125 kHz when placed in close proximity to various metallic surfaces. This was achieved firstly by minimising coil area to the extent that the radius is comparable to that of the transponder coil, and secondly by limiting the minimum shield-coil separation distance. A ferrite core was used to allow reduction of winding turns and therefore copper loss. Proximity RFID interrogators have been manufactured using this arrangement.

The problem of source-sensor position and orientation was generalised by visualising the degree of coupling on a unit sphere. Field nulls always exist between single source and sensor coils. It was shown that nulls may be eliminated by using orthogonal source and sensor arrangements, comprising three coils aligned to the x,y and z planes. Provided a suitable signal generation or recombination method is used, coupling nulls may be removed. The prospect of orthogonal sensor coils in RFID applications is unattractive due primarily to cost. Therefore it is suggested that an arrangement of orthogonal interrogator coils could be employed to remove dependency on orientation, perhaps using time-multiplexed signal generation.

A novel automatic identification method called cable RFID is described that uses the appliance power cable as a communication channel. This method enables automatic identification using the Portable Appliance Tester (PAT) before testing commences. Upon plugging the appliance into the test port, an embedded interrogator retrieves data from a transponder fixed to the power cabling. Typical data gathered includes the unique identification number, test codes and previous test history. Data may be read from and written to the transponder, which, in the current embodiment, offers 2 kilobits of storage space. Inductive coupling is achieved by a single-wire coupler comprising ferrite core, winding capacitor and low-power IC. A complete electrical path for the carrier-current exists, consisting of the transponder coupled impedance, power cable and inlet filter. A decoupled primary resonant circuit was employed to produce a detection signal that contains direct-load modulation information. It was shown that sensitivity to load modulation is then dependent on primary and secondary Q-factors and that nulls can occur in the amplitude modulation signal due to tuning errors in the primary and secondary resonant circuits. An adaptive synchronous detector having adjustable sample phase was used to recover the baseband signal by following the complex modulation produced (i.e., amplitude and phase) by the non-ideal cable RFID system. Possible locations for the cable RFID transponder include placement within the appliance casing (fitted during manufacture) or within the standard electrical fuse casing.

The cable RFID method was shown to be possible over long cable sections and even during the occurrence of standing waves. In practice standing waves are induced by the low impedance presented by the inlet filter, which approaches a short-circuit condition at the frequency of operation. An analytical approach was developed that allowed calculation of transponder voltage as a function of position along the cable.

An alternative to the single-wire coupler is described that utilises both conducting wires, thus forming a two-wire coupler arrangement. Field simulation was used to find the optimum placement of coupler windings and to show that the split flux path is dominated by a central air gap between the conductors. It was shown that core permeability and conductor spacing largely determine the coupled flux in each winding. For a given winding configuration and core geometry, the minimum conductor separation can be determined that achieves the required transponder IC voltage. Transponder voltage is strongly dependent on secondary Q, precluding the use of many secondary turns due to the copper loss incurred. Flat rectangular core shapes were found most suitable for coupling between the conductors and windings and were demonstrated to support passive load modulation communication. However the minimum required conductor separation (30 mm for the test coupler considered) typically requires an excessively wide core geometry that would require separation of the conductors at some point along the power cable.

The feasibility of passive direct-load modulation on the mains power-line was investigated with the aim of enabling automatic device identification across the local power-line. This signalling method was shown to be possible due to sufficiently low channel impedance at the operational frequency. However the channel exhibits narrow fading caused by interaction between cabling and loads attached to the power-line, even for frequencies below one megahertz. A simulation was devised that allows prediction of attenuation and load modulation sensitivity and includes the influence of cabling, loads and transponder impedance. The results indicate that attenuation becomes a limiting factor beyond a few tens of meters on the simulated power-line section. Load modulation sensitivity could be maintained at this range. Power-line signalling by passive load modulation was demonstrated across a sample power-line and some locations of satisfactory and unsatisfactory performance identified.

Finally, two electronic interrogator designs were presented. The first takes the form of an embeddable module designed for integration with safety test products manufactured by Seaward Electronic Ltd. This device was also used to research cable RFID and power-line signalling. Assessment of the performance showed that self-induced noise is dominant in determining detector error rates. Self-induced noise is especially prominent in this design due to coupling between transmitter and receiver and the need for simultaneous transmission and reception. A second interrogator device was described that is made reconfigurable by applying the canonical Software Defined Radio (SDR) architecture defined by Mitola [Mitola]. Implementation was by FPGA. A novel transmitter is employed having a minimum level of hardware and which is driven directly by the digital device. It is suggested that direct-conversion of the carrier is possible at lower RFID frequency bands and that this would render the receiver reconfigurable. Such a device will permit software adaptation of the interrogator to accommodate the latest RFID protocols, frequency bands and modulation schemes defined by emerging standards.

List of References

[Alexander]	Alexander K., et al., "Focus on the Supply Chain: Applying Auto-ID within the Distribution Center", Auto-ID Center, MIT and IBM Business Consulting Services, June, 2001. http://www.autoidcentre.org/.
[ADdata]	Data sheet: "AD9203 10-bit, 40 MSPS, 3V, 74 mW A/D Converter" Analog Devices. Rev. A.
[Alston]	Alston I., Madahar B., "From C to Netlists: Hardware Engineering for Software Engineers?", IEEE Electronics & Communications Engineering Journal, August, 2001, pp. 165-173.
[Anastasiadou]	Anastasiadou D., Antonakopoulos T., "An Experimental Setup for Characterising Residential Power Grid Variable Behaviour", Proc. 6th International Symposium on Power-Line Communications and its Applications (ISPLC), March, 2002.
[Assimakopoulos]	Assimakopoulos, C., Pavlidou F.N., "Measurements and Modelling on In-house Power Lines Installation for Broadband Communications", Proc 5th International Symposium on Power-line Communications and its Applications, April, 2001, pp. 73-78.
[Aston]	Aston K., "The Electronic Product Code – The Next Wave of the Computer Revolution?", Proc. Smart Labels Conference, Cambridge, 24 Sept, 2001.
[Baer]	Baer H., "Method for Transmitting Data Via a Line of an Alternating Current Distribution Network, and a Transmitter for Carrying out the Method", U.S. Patent 4,642,637, February, 1987.
[Baines]	Baines R., "The DSP Bottleneck", IEEE Communications Magazine, May, 1995, pp. 46-54.
[Balanis]	Balanis, C.A., *Antenna Theory*, 2nd ed., New York: Wiley, 1997, Chapter 5.
[Balanis]	Balanis C.A., *Antenna Theory, Analysis and Design*, 2nd Ed., Wiley, NY, 1997.
[Ball]	Ball E., Staniforth J.A., "Transfer impedance Between Circular Coils Separated by Thick Nonferrous Metal Sheets", IEE Proceedings, Vol. 128, Pt. A, No. 1, January, 1981.
[Banwell1]	Banwell T.C., Galli S., "A New Approach to the Modelling of the Transfer Function of the Power Line Channel", Proc 5th International Symposium on Power-line Communications and its Applications, April, 2001, pp. 319-324.
[Banwell2]	Banwell T.C., Galli S., "On the Symmetry of the Power Line Channel", Proc 5th International Symposium on Power-line Communications and its Applications, April, 2001, pp. 325-330.
[Bing]	Bing B., Jayant N., "A Cellphone for all Standards", IEEE Spectrum, May, 2002, pp.34-39.

[Bingeman] Bingeman, G., "Transmission Lines as Antennas", RF Design, Jan 1, 2001, pp. 74-82.

[Bishop] Bishop D., "Software is All", RF Design, September, 2000. www.rfdesign.com.

[Bluespec] "Specification of the Bluetooth System", Volume 1 (Core Specification), Version 1.1, February 22, 2001. http://www.bluetooth.org.

[Blust] Blust S., Murotake D., "Software-Defined Radio Moves Into Base-Station Designs", Wireless Systems Design, November, 1999, 31-40.

[Boys] Boys J.T., Covic G.A., Green A.W., "Stability and Control of Inductively Coupling Power Transfer Systems", IEE Proc. Electr. Power Appl., Vol. 147, No. 1, January, 2000, pp.37-43.

[Bray] Bray J., Sturman C.F., *Bluetooth, Connect Without Cables*, Prentice Hall PTR, NJ, 2001.

[Brigham] Brigham E.O., *The Fast Fourier Transform and its Applications*, Prentic-Hall, NJ, 1988.

[Brown] Brown P.A., "Broadband PLT Access Solutions – Assessing Developments", Proc. ISPLC (Malmö, Sweden), April, 2001, pp. 169-174.

[Budek] Budek, J.A., "Communication Via an Electricity Supply Chain", U.S. Patent 4,348,582, September, 1982.

[Bunszel] Bunszel, C., "Magnetic Induction and RF", Aura Communications, Wilmington, Mass. www.auracomm.com.

[Bunszel01] Bunszel C., "Magnetic Induction: A Low-Power Wireless Alternative", RF Design, November, 2001, www.rfdesign.com.

[Buracchini] Buracchini E., "The Software Radio Concept", IEEE Communications Magazine, September, 2000, pp.138-143.

[Bursky] Bursky, D., "Miniature Embeddable Antenna Targets Bluetooth Systems, Weighs in at 1 g", Electronic Design, Volume 47, No. 22, October 1999.

[Butler] Butler, N.R, Palmero V., Cobler P.J., "Short-Range Magnetic Communication System", US Patent 9,637,052, November, 1996.

[Calderbank] Calderbank P., "Successful use of RFID on Metal Gas Cylinders", Proc. Smart Labels 2001 Conference, Cambridge, 24-25 September, 2001.

[Cappelletti] Cappelletti R., Baschirotto A., "A Power Line FSK Transceiver with Reduced Power Consumption", IEEE Transactions on Consumer Electronics, Volume 47, No. 2, May, 2001, pp. 207-213.

[Chan86] Chan H.L., Donaldson W., "Attenuation of Communication Signals on Residential and Commercial Intrabuilding Power-Distribution Circuits", IEEE Transactions on Electromagnetic Compatibility, Volume EMC-28, No. 4, November, 1986, pp. 220-230.

[Chan94] Chan H.L., Friedman D., Donaldson R.W., "Performance Enhancement using Forward Error Correction on Power Line Communication Channels", IEEE Transactions on Power Delivery, Volume 9, No. 2, April, 1994, pp. 645-653.

[Chartier] Chartier, P., Furness, A., "A Study of Data Carrier Issues for the Next Generation of Integrated ADIC Technology", Praxis Consultants, 1998 (distributed by Aimglobal, www.aimglobal.org)

[Chen] Chen S., Zhong E., Lipo T.A., "A New Approach to Motor Condition Monitoring in Induction Motor Drives", IEEE Transactions on Industry Applications, Volume 30, No. 4, July, 1994, pp. 905-910.

[Christopoulos] Christopoulos, C., *The Transmission-Line Modelling Method*, IEEE Press, New York, 1995.

[Chu] Chu, L.J., "Physical Limitations of Omni-Directional Antennas", Journal of Applied Physics, Volume 19, December, 1948, pp. 1163-1175.

[CIE00] Anon., "Industrial Sensor Networks go Wireless", Components in Electronics, September, 2000, pp. 79-80.

[CIE01] "Soc makes Ordinary Sensors Smart", Components in Electronics, October, 2001. p. 6.

[Cortina] Cortina R., "Telecommunication Systems on Power Distribution Networks: High Frequency Performance of Carrier Channels", IEEE Transactions on Power Delivery, Volume 9., No. 2, April, 1994, pp. 654-660.

[Dalichau] Dalichau H., "Evaluation of Different Frequency Bands Regarding their Qualification for Inhouse Powerline Communicaion", Proc. ISPLC (Malmö, Sweden) , April, 2001, pp. 203-210.

[Davie] Davie A., "Intelligent Tagging for Transport and Logistics: the ParcelCall Approach", Electronics & Communication Engineering Journal, June, 2002, pp. 122-128.

[DeLeon] De Leon F., Semlyen A., "Efficient Calculation of Elementary Parameters of Transformers", IEEE Transactions on Power Delivery, Vol. 7, No. 1, January, 1992.

[Dettmer] Dettmer R., "Getting Smarter", IEE Review, May, 1998, pp. 123-126.

[Dezuari] Dezuari O., Gilbert S.E., Belloy E., Gijs M.A.M., "High Inductance Planar Transformers", Sensors and Actuators, Vol. 81 (2000), pp. 355-358.

[Domingo] Domingo-Ferrer J., Hartel P., "Current Directions in Smart Cards", Computer Networks, Volume 36, 2001, pp. 377-379.

[Dostert01] Dostert K., *Powerline Communications*, Prentice Hall PTR, 2001.

[Dostert90] Dostert K.M., "Frequency-Hopping Spread-Spectrum Modulation for Digital Communications Over Electrical Power Lines", IEEE Journal on Selected Areas in Communications, Vol. 8, No. 4, May, 1990.

[Dreifus] Dreifus H., Monk T.J., *Smart Cards*, Wiley, London.

[Dugdale] Dugdale, D., *Essentials of Electromagnetism*, Hampshire: Macmillan Press Ltd., 1993, pp. 119-121.

[Ealing] Ealing M., "World's Largest System Integration of Smart Baggage Tags at San Francisco Airport", Proc. Smart Labels Conference, Cambridge, 24 Sept, 2001.

[EN50065] BS EN 50065-1 : 1992, "Specification for Signalling on Low-Voltage Electrical Installations in the Frequency Range 3 kHz to 148.5 kHz", British Standards Institute.

[EN50081] EN 50081 part 1: 1992, "Generic Emission Standard, part 1: residential, commercial and light industry environment".

[EN50082] EN 50082 Part 1: 1992. "Generic Immunity Standard, part 1: residential, commercial and light industry environment".

[EN55022] EN 55022 : 1994, "Limits and Methods of measurement of radio disturbance characteristics of information technology equipment. 1994".

[Engels] Engels D., "The Reader Collision Problem", White Paper, The Auto-ID Centre, MIT, Cambridge, MA, www.autoidcenter.org.

[Esmailian] Esmailian T., Kschischang F.R., Gulak P.G., "An In-building Power Line Channel Simulator", Proc. 6th International Symposium on Power-Line Communications and its Applications, Athens, March, 2002 pp.31-35.

[ETSI300] ETSI EN 300 330 "ElectroMagnetic Compatibility and Radio Spectrum Matters (ERM);Short Range Devices (SRD);Technical characteristics and test methods for radio equipment in the frequency range 9 kHz to 25 MHz and inductive loop systems in the frequency range 9 kHz to 30 MHz"

[Fancher] Fancher C.H., "In your Pocket Smartcards", IEEE Spectrum, Feburary, 1997, pp. 47-53.

[Fink] Fink D.G., *Standard Handbook for Electrical Engineers*, 10th Ed. McGraw-Hill, NY, 1968.

[Finkenzeller] Finkenzeller, K., *RFID Handbook*, Wiley, 1999, p 64.

[Finlay] Finlay G., "Understanding SDR Requirements", Wireless Systems Design, July, 2001, 43-50.

[Forti] Forti M.M., Millanta L.M., "Power-Line Impedance and the Origin of Low-Frequency Oscillatory Transients", IEEE Transactions on Electromagnetic Compatibility, Volume 32, No. 2, May, 1990, pp. 87-97.

[Fraden] Fraden J., *Handbook of Modern Sensors: Physics, Designs and Applications*, 2nd ed., Sprimger-Verlag, NY, 1996, page 56.

[Frenzel] Frenzel L., "An Evolving ITS Paves the Way for Intelligent Highways", Electronic Design, January 8.

[Friedman] Friedman D., Heinrich H., Duan D.W., "A Low-Power CMOS Integrated Circuit for Field-Powered Radio Frequency Identification Tags", IEEE International Solid-State Circuits Conference, 1997, pp. 294-295.

[Gengel] Gengel G.W., "Integrated circuit packages assembled utilizing fluidic self-assembly", U.S. Patent 6,417,025, July 9, 2002.

[Giunta] Giunta J.M, "System for Controlling the Movement of an Animal", U.S. Patent 4,967,695, November 6, 1990.

[Goldstein] Goldstein H., *Classical Mechanics*, 2nd Ed., Student World Series Ed., Addison-Wesley, Reading, Mass., 1980.

[Grover] Grover F.W., *Inductance Calculations*, Van Norstrand, Princeton, N.J., 1946, reprinted by Dover Publications, New York, 1962.

[GTAG] "EAN•UCC Global Tag GTAG™ Technical Specification", V0.2 for Industry Reference, Uniform Code Council, August, 2002. http://www.uc-council.org/.

[Hansen] Hansen, R.C., "Fundamental Limitations in Antennas", Proc. IEEE, Vol. 69, No. 2, February, 1981, pp. 170-181.

[Hasselgran] Hasselgran L., "Geometrical Aspects of Magnetic Shielding at Extremely Low Frequencies", IEEE Transactions on Electromagnetic Compatibility, Vol. 37, No. 3, August, 1995.

[Hentschel] Hentschel T., Henker M., Fettweis G., "The Digital Front-End of Software Radio Terminals", IEEE Personal Communications, August, 1999, pp. 6-12.

[Hitagcom] Product Specification, "HT1 Transponder Family Communication Protocol", Rev 2.2, Philips Semiconductors, January, 1999.

[Hitagic] Product Specification, "HT1 ICS30 02 Family, HITAG™ 1 Transponder IC", Rev. 1.4, October 1997.

[Hitagre] Product Specification, "HTRC110 Hitag Reader Chip", Rev. 1.1, Philips Semiconductors, December, 1997.

[Hooijen] Hooijen O.G., "A Channel Model for the Residential Power Circuit Used as a Digital Communications Medium", IEEE Transactions on Electromagnetic Compatibility, Volume 40, No. 4., November, 1998, pp. 331-336.

[Hurley] Hurley W., Wilcox D.J., "Calculation of Leakage Inductance in Transformer Windings", IEEE Transactions on Power Electronics, Vol. 9, No. 1, January, 1994.

[IDtech] *Smart Labels Analyst*, IDTechEx Web Journal, Issue 11, December, 2001, www.idtechex.com.

[ISO18000] ISO/IEC 18000-6 (draft) "Information Technology — Radio Frequency Identification (RFID) for Item Management — Part 6:

Parameters for Air Interface Communications at 860-930 MHz", ISO/IEC JTC 1/SC 31/WG 4/SG 3 N311, April 2002.

[Issa] Issa, F., Abdouss A., "Indoor PLC Network Simulator", Proc. 6th International Symposium on Power-Line Communications and its Applications", Athens, March, 2001, pp. 36-39.

[Jagoda] Jagoda et al., "Communicating Over Power Lines", U.S. Patent 3,909,821, Sept., 1975.

[Jones] Jones, C.E., Sivalingham, K.M., Agrawal, P., Chen, J.C., "A Survey of Energy Efficient Protocols for Wireless Networks", Wireless Networks, Vol. 7, 2001, pp. 343-358.

[Kaiser] Kaiser U., Steinhagen W., "A Low-Power Transponder for High-Performance Identification Systems", IEEE Journal of Sold-State Circuits, Vol. 30, No. 3, March, 1995.

[Kalmus62] Kalmus H.P., "Short Range Tracking System", U.S. Patent 3,046,549, July 24, 1962.

[Kalmus64] Kalmus H.P., "Direction Indicatior", U.S. Patent 3,121,228, February, 1964.

[Kelley] Kelley A.W., Wilson T.G., Owens H.A., "Analysis of the Ferroresonant Transformer With a Rectified output in the Low-Line-Voltage Minimum-Line-Frequency Full-Load Condition", IEEE Transactions on Power Electronics, Vol. 9, No. 3, May, 1994.

[Kennedy] Kennedy J., Sullivan M., "Direction Finding and "Smart Antennas" Using Software Radio Architectures", IEEE Communications Magazine, May, 1995, pp. 62-68.

[Kwasniok1] Kwasniok P.J., Kozlowski J., Stuchly S.S., "An Improved Method of Measuring Power-Line Impedances Using Two Current Probes", IEEE Transactions on Electromagnetic Compatibility, Volume 35, No. 4, November, 1993, pp. 473-475.

[Kwasniok2] Kwasniok P.J., Kozlowski J., Stuchly S.S., "Technique for Measurement of Powerline Impedances in the Frequency Range from 500 kHz to 500 MHz", IEEE Transactions on Electromagnetic Compatibility, Volume 35, No. 1, February, 1993, pp. 87-90.

[Lackey] Lackey R., J., Upmal D., W., "Speakeasy: The Military Software Radio", IEEE Communications Magazine, May, 1995, pp. 56-61.

[Laddomada] Laddomada M., *et al*, "A PC-Based Software Receiver Using a Novel Front-End Technology", IEEE Communications Magazine, August, 2001, pp. 136-145.

[Lee] Lee M., "A New Carrier Current Transceiver I.C.", IEEE Transactions on Consumer Electronics, Volume CE-28, No. 3, August, 1982, pp. 409-413.

[Leen] Leen G., Heffernan D., "Vehicles without Wires", IEE Computing & Control Engineering Journal, October, 2001, pp. 205-211.

[Levy] Levy S., "Electromagnetic Shielding Effect of an Infinite Plane Conducting Sheet Placed Between Circular Coaxial Coils", Proceedings of IRE, Vol. 24, No. 6, June, 1936.

[Liard1] Liard M.J., “The Global Markets and Applications for Radio Frequency Identification and Contactless Smartcard Systems, 4th Edition, Volume I”, VDC Executive White Paper, January 2003.

[Liard2] Liard M.J., “The Global Markets and Applications for Radio Frequency Identification and Contactless Smartcard Systems, 4th Edition, Volume II: RFID Transponder ICs”, VDC Executive White Paper, February 2003.

[MacFayden] MacFayden K.A., *Small Transformers and Inductors*, Chapman & Hall, London, 1953.

[Malack] Malack J., Engstrom J.R., “RF Impedance of United States and European Power Lines”, IEEE Transactions on Electromagnetic Compatibility, February 1976, pp. 36-38.

[Matsuki] Matsuki, H., “Energy Transfer System Utilizing Amorphous Wires for Implantable Devices”, IEEE Transactions on Magnetics, Vol. 31, No. 2, March, 1995, pp. 1276-1282.

[McWilliam] McWilliam R.P., Purvis A., “Mains Appliance Identification for Safety Test System”, Proc. 6th International Symposium on Power-Line Communications and its Applications”, Athens, March, 2001, pp. 147-151.

[Meys] Meys, Renè P., “A Summary of the Transmitting and Receiving Properties of Antennas”, IEEE Antennas and Propagation Magazine, Vol. 42, No. 3, June, 2000.

[Mino] Mino, M., “A Planar Microtransformer for Use in Micro-Switching Converters”, IEEE Transactions on Magnetics, Vol. 28, No. 4, JULY, 1992, pp. 1969-1972.

[Mitola] Mitola J., “The Software Radio Architecture”, IEEE Communications Magazine, May, 1995, pp. 26-38.

[Monticelli] Monticelli D., Wright M., “A Carrier Current Transceiver IC for Data Transmission Over the AC Power Lines”, IEEE Journal of Solid-State Circuits, Volume SC-17, No. 6, December 1982, pp. 1158-1165.

[Morgan] Morgan D., *A Handbook for EMC Testing and Measurement*, Peter Peregrinus Ltd. On behalf of the Institution of Electrical Engineers, Exeter, UK, 1994.

[Moser] Moser J.R., “Low-Frequency Low-Impedance Electromagnetic Shielding”, IEEE Transactions on Electromagnetic Compatability, Vol. 30, No. 3, August, 1988.

[Murphy] Murphy J.H., Parkinson H.E., “Underground mine communications”, Proc. IEEEE, Vol. 66, pp. 26-50, January, 1978.

[National] Data Sheet, “LM1893/LM2893 Carrier-Current Transceiver”, National Semiconductor, April 1995. Available at http://www.national.com.

[Neaves] Neaves P., “Dynamic Connection of Wearable Computers to

Companion Devices using Near-field Radio", Proceedings of The Second International Symposium on Wearable Computers, October 1998, pp. 156-157. http://citeseer.nj.nec.com/neaves98dynamic.html.

[Nicholson] Nicholson J.R., Malack J.A., "RF Impedance of Power Lines and Line Impedance Stabilization Networks in Conducted Interference Measurements", IEEE Transactions on Electromagnetic Compatibility, May, 1973, pp. 84-86.

[Noore] Noore A., "Highly Robust Biometric Smart Card Design", IEEE Transactions on Consumer Electronics", Volume 46, No. 4, November, 2000, pp. 1059-1063.

[Nowottnick] Nowottnick J., "Read/Write Devices based on the HITAG Read/Write IC HTRC110", Application Note AN 98080, Philips Semiconductors, 21 Sept. 1998.

[O'Neal] O'Neal J.B., "The Residential Power Circuit as a Communication Medium", IEEE Transactions on Consumer Electronics, Volume CE-32, No. 3, August, 1986, pp. 567-577.

[Ochsner] Ochsner H., "Data Transmission on Low Voltage Power Distribution Lines Using Spread Spectrum Techniques", Proc. Can. Commun. Power Conf. (Montreal, P.Q., Canada), Oct 15-17, 1980, pp. 236-239.

[Olsen] Olsen R.G., Farstad A.J., "Electromagnetic direction finding experiments for location of trapped miners", IEEE Transactions on Geoscience Electronics, Vol. GE-11, pp. 178-185, October, 1973.

[Olsen] Olsen R.G., "Some Observations About Shielding Extremely Low-Frequency Magnetic Fields by Finite Width Shields", Vol. 38, No. 3, August, 1996.

[Owschewski] Owschewski, W.W., "The Hybrid Compatible Transformer", IEEE Transactions on Components, Hybrids and Manufacturing Technology, Vol. 32, CHMT-2, No. 4, December, 1979, pp. 487-490.

[Palmero02] Palmero V., *et al*, "Inductive Communication System and Method", Aura Communications, U.S. Patent 6,459,882, October 1, 2002.

[Palmero99] Palmero V., *et al*, "Diversity Circuit for Magnetic Communication System", U.S. Patent 5,912,925, June 15, 1999.

[Pérez] Pérez-Neira A., Mestre X., Fonollosa J.R., "Smart Antennas in Software Radio Base Stations", IEEE Communications Magazine., February, 2001, pp. 166-173.

[Philips] Data Sheet, "TDA5051 Home Automation Modem", Philips Semiconductors, May, 1999. Available at http://www.semiconductors.philips.com.

[PIC63] Product Specification, "PIC16C63A/65B/73B/74B; 8-bit CMOS Microcontroller with A/D Converter", document number DS30605C, Microchip, 2000.

[Praca] Praca D., Barral C., "From Smart Cards to Smart Objects: the Road to New Smart Technologies", Computer Networks, Volume 36, 2001, pp. 381-389.

[Raab] Raab F.H., Blood E.B., Steiner T.O., Jones H.R., "Magnetic Position and Orientation Tracking system", IEEE Transactions on Aerospace and Electronic Systems, Vol 15, No. 5, September, 1979.

[Radford] Radford D., "Spread-spectrum data leap through ac power wiring", IEEE Spectrum, November, 1996, pp. 48-53.

[Rankl] Rankl W., Effing W., *Smart Card Handbook*, Wiley, London.

[Rappaport] Rappaport T., S., *Wireless Communications, Principles and Practice*, 2nd Ed. Prentice Hall, NJ, 2002.

[Refdat] *Reference Data for Radio Engineers*, Indianapolis: Sams,, 1968, 5th edition.

[Reynolds] Reynolds M., *et al*, " Multi-Band, Low-Cost EPC Tag Reader", Auto-ID Centre, MIT, September, 2001.

[Rizzi] Rizzi, P.A., *Microwave Engineering, Passive Circuits*, Prentice-Hall, NJ, 1988.

[Roesner] Roesner B.R., "Apparatus and Method for Detuning of RFID Tag to Regulate Voltage", U.S. Patent 6,229,443, May 8, 2001.

[Sanz] Sanz A, Garcia Nicolas J.I., Urriza I., "A Broadband model Mixed-Signal Front end for Power Line Communications", Proc. ISPLC (Athens, Greece), March, 2002, pp. 302-306.

[Schuermann] Schuermann at al., "Transponder Arrangement", U.S. Patent No. 5,053,774.

[Seshadri] Seshadri S.R., *Fundamentals of transmission lines and electromagnetic fields*, Addison-Wesley Pub. Co., Reading, Mass, 1971.

[Shwehdi] Shwehdi M.H., Khan A.Z., "A Power Line Data Communication Interface Using Spread Spectrum Technology in Home Automation", IEEE Transactions on Power Delivery, Vol. 11, No. 3, July 1996, pp. 1232-1237.

[Snelling] Snelling E.C., *Soft Ferrites, Properties and Applications*, Mullards Research Laboratories, London, 1969.

[Soloman] Soloman, S., *Sensors Handbook*, McGraw-Hill, NY, 1998, pages 1.23-1.33.

[Southwick] Southwick R.A., "Line Impedance Measuring Instrumentation Utilizing Current Probe Coupling", IEEE Transactions on Electromagnetic Compatability, Vol. 13, No. 4, November, 1971, pp. 30-36.

[Sowell] Sowell, B.F., Bowman, J.G.P., Branine, M.E., Hubbert, M.E., "Radio Frequency Technology to Measure Feeding Behaviour and Health of Feedlot Steers", Applied Animal Behaviour Science, Vol. 59, 1998, pp. 277-284.

[Stajano] Stajano F., *Security for Ubiquitous Computing*, John Wiley & Sons, 1st ed, 2002.

[Stremler] Stremler F.G., *Introduction to Communication Systems*, 3rd Edition, Addison-Wesley, Reading, 1990.

[Tanaka] Tanaka M., Transmission Characteristics of a Power Line used for Data Communications at Higher Frequencies", pp. 37-42.

[Terman] Terman F.E., *Radio Engineer's Handbook*, First Ed., McGraw-Hill, New York, 1943.

[Tsuzuki01] Tsuzuki S., Yamamoto S., Takamatsu T., Yamada Y., "Measurement of Japanese Indoor Power-line Channel", Proc. 5th International Symposium on Power-Line Communications and its Applications (ISPLC), April, 2001.

[Tsuzuki02] Tsuzuki S., Takamatsu. T, Nishio H., Yamada Y., "Estimation Method of the Transfer Function of Indoor Power-line Channels for Japanese Houses", Proc. 6th International Symposium on Power-Line Communications and its Applications (ISPLC), March, 2002.

[Vines84] Vines R.M., Trussell H.J., Gale L.J., O'Neal J.R., "Noise on Residential Power Distribution Circuits", IEEE Transactions on Electromagnetic Compatability, Vol. 26, No. 4, November, 1984, pp. 161-168.

[Vines85] Vines R.M., Trussell H.J., Shuey K.C., O'Neal J.R., "Impedance of the Residential Power-Distribution Circuit", IEEE Transactions on Electromagnetic Compatibility, Vol. 27, No. 1, February, 1985, pp. 6-12.

[Watson] Watson M.B., "Sensing Electrical Current", G.B. Patent 2,259,780, March 24 1993.

[Wepman] Wepman J.A., "Analog-to-Ditial Converters and Their Applications in Radio Receivers", IEEE Communication Magazine, May, 1995, pp. 39-45.

[Westman] Westman H.P. (Editor), *Reference Data for Radio Engineers*, 5th Ed., Howard W. Sams & Co., Inc., Indianapolis, 1970.

[Wheeler] Wheeler, Harold. A., "Small Antennas", IEEE Transactions on Antennas and Propagation, Vol AP-23, No. 4, July, 1975, pp. 462-469.

[Williams] Williams, T., *EMC for Product Designers*, 2nd Ed., Newnes, Oxford, 1996.

[X10] X-10 homepage. http://www.x10.com.

Appendix A - Survey of Transponder ASIC's

A survey of popular transponder ICs was conducted in order to identify the most appropriate IC for the application described in chapter 2. The data collected is summarised in the table below.

Manufacturer	**Model Number(s)**	**Frequency**	**Tag or Chip**	**Mount-on-metal Ready?**	**Memory**	**Memory Pages**	**Anti-collision**	**Memory Type**
Texas Instruments TIRIS	RI-TRP-R9VS RI-TRP-W9VS	134.2KHz	Tag	YES	64 bit	1		Read Only or R/W
Gemplus	GemFly family	125KHz	Tag/Chip	No	64 bit			Read Only or R/W
Gemplus	C210	13.56MHz	Chip (only available as a label from Gemplus)	No	80 bit			Factory-programmable
Gemplus	C220	13.56MHz	Chip (only available as a label from Gemplus)	no	73 bit (40 of which lockable)		YES	R/W
Microchip	MCRF200	125KHz	Chip	no	128 bits		no	R/W contactless prog, but OTP only
Microchip	MCRF202	125KHz	Chip	no	128 bits		yes	Read Only
Microchip	MCRF250	125KHz	Chip	no	128 bits		yes	R/W contactless prog, but OTP only (WORM)
Microchip	MCRF355	13.56MHz	Chip	no	154 bits		yes	Contact write
Microchip	MCRF360	13.56MHz	Chip	no	154 bits		yes	Contact write
Microchip	MCRF450	13.56MHz	Chip	no	1 kbit		yes	contactless R/W
Silway	SWO27	125KHz	Chip	no	64 bits		no	Factory programmed
Silway	SWO17	134KHz	chip	no	128 bits		no	Factory programmed

Atmel	T5554	125KHz	chip	no	224 bits	7 block of 32 bits	yes 'Answer-On-Request'	Contactless R/W
Atmel	T5556	125KHz	chip	no	224 bits	7 block of 32 bits	no	WORM, contactless OTP
Atmel	e5530	100-450KHz	chip	no	32,64,96 or 128 bits		no	factory programmed
Atmel	e5551	125KHz	chip	no	224 bits	7 block of 32 bits	yes 'Answer-On-Request'	contactless R/W
Atmel	e5561	125KHz	chip	no	320 bits	10 blocks of 32 bits	no	contactless R/W
EM Marin	P4150	125KHz	chip	no	1 kbit	32 * 32 bits	no	contactless R/W
EM Marin	P4069	125KHz	chip	no	128 bit	8 * 16 bit	no	contactless R/W
EM Marin	H4003	125KHz	chip	no	64 bit		no	Factory programmed
EM Marin	H4005	125KHz	chip	no	128 bit		no	Factory programmed
EM Marin	H4006	13.56MHz	chip	no	64 bit		no	Factory programmed
EM Marin	H4100	125KHz	chip	no	64 bit		no	Factory programmed
ER Marin	P4022	any	chip	no	64 bit		YES	Factory programmed
EM Marin	H4102	125KHz	chip	no	64 bit		no	Factory programmed
Philips	Hitag 1	125KHz	chip	no	2 kbit	64 pages, each 4 bytes	YES	contactless R/W
Philips	Hitag 2	125KHz	chip	no	256 bit	8 * 32 bits	no	contactless R/W
Philips	I-Code 1	13.56Mhz	chip	no	512 bit		YES	contactless R/W
Philips	I-Code SLI	13.56Mhz	chip	no	1042 bit		YES	contactless R/W

Appendix B - An expression for the coupling coefficient

Introduction

We consider a derivation for the coefficient of coupling between coaxial, coplanar coils. The derivation includes assumptions.

Assumptions

The radial component of the magnetostatic flux density produced by a coil aligned to the z-axis is:

$$B_z = \frac{\mu_0 N_1 I_1}{2\pi} \frac{a_1^2}{\left(d^2 + a_1^2\right)^{3/2}} \qquad \text{B1}$$

where B_z is the field component along the z-axis, N_1 the number of turns, I_1 the current, a_1 the radius of the coil and d the point of observation along the z axis. An EMF is induced across the terminal of a nearby magnetic sensor placed coaxially with the first coil:

$$V_{2_{o/c}} = j\omega N_2 A_2 B_z \cos(\theta) \qquad \text{B2}$$

Where $V_{2\,o/c}$ is the measured voltage with open circuit terminals, N_2 the number of turns comprising the second coil, A_2 the cross sectional area of the second coil and θ the angle of incidence. If we allow current to flow from the terminals of the sensor coil then the following electrical equations can be formed:

$$V_1 = j\omega L_1 I_1 + j\omega M I_2 \qquad \text{B3}$$

$$V_2 = j\omega M I_1 + j\omega L_2 I_2 \qquad \text{B4}$$

Where V_x, I_x are the voltage and current at the terminals of coil x, L_x the respective coil inductance and M the mutual inductance.

Derivation

We now find an expression for M, given the condition that the sensor current, I_2 is zero. Equation B4 becomes:

$$V_2 = j\omega M I_1 \Rightarrow M = \frac{V_2}{j\omega I_1} = \frac{\mu_0 N_1 N_2 A_2}{2\pi}\cos(\theta)\frac{a_1^2}{\left(d^2 + a_1^2\right)^{3/2}} \qquad \text{B5}$$

by substitution of equation B2 and B1. This is an expression involving only system geometry. To find k, we use the following definition:

$$k = \frac{M}{\sqrt{L_1 L_2}} \qquad \text{B6}$$

Using the fundamental definition of inductance we can express the denominator of equation B6 as:

$$\sqrt{L_1 L_2} = \sqrt{\frac{N_1\phi_1}{I_1}\frac{N_2\phi_2}{I_2}} = \left(\frac{N_1^2 A_1 \mu_0}{2\pi}\frac{a_1^2}{\left(d^2 + a_1^2\right)^{3/2}}\frac{N_2^2 A_2 \mu_0}{2\pi}\frac{a_2^2}{\left(d^2 + a_2^2\right)^{3/2}}\right)^{1/2}$$

where equation B1 has been substituted. It was also assumed that the field is uniform across the coil area. Setting $d = 0$ (since we are calculating self-inductance):

$$\sqrt{L_1 L_2} = \frac{\mu_0 N_1 N_2}{2\mu}\sqrt{\frac{A_1 A_2}{a_1 a_2}} \qquad \text{B7}$$

Substituting equations B5 and B7 into equation B6 gives a general expression for k:

$$k = A_2\sqrt{\frac{a_1 a_2}{A_1 A_2}}\frac{a_1^2}{\left(d^2 + a_1^2\right)^{3/2}}\cos(\theta) \qquad \text{B8}$$

The most common coil geometry is circular, where source and sensor coil areas are given by $A_1 = \pi a_1^2$ and $A_2 = \pi a_2^2$ respectively. Accounting for this in equation B8 gives the final expression for k:

$$k = \frac{a_1^2 a_2^2}{\sqrt{a_1 a_2}\left(d^2 + a_1^2\right)^{3/2}}\cos(\theta) \qquad \text{B9}$$

where a_l is the radius of the largest coil.

Simplifications

In deriving equation B9 the following simplifications were made

- We considered only the radial field component of B; the tangential component has little effect when considering coaxial coils.
- Ignored effects of winding geometry; the result is valid only when the coil's winding height and depth is small compared to the radius.
- The field is uniform across coil areas A_1 and A_2.
- Copper loss in the coil windings was ignored. By making L_1 and L_2 complex quantities that represent the inductance and ESR (Equivalent Series Resistance) of the coil, the copper loss could be included.

Equations B5, B8 and B9 can be used to describe the behaviour of inductively coupled coils when they are coaxial and coplanar.

Appendix C – Simulation of arbitrary source-sensor coupling

Introduction

This method is based on a technique described by Raab [Raab] for calculating normalised coupling between two ideal magnetic loops. Field equations were solved in Mathcad software and the results processed in a Matlab script for visualisation. This appendix describes the method used to produce the spherical plots illustrated in chapter 3.

Solution

The source vector, f_l, describes excitation of three orthogonal coils. For example, assuming excitation of only the x-orientated source coil:

$$f_1 := (1 \quad 0 \quad 0)^T \qquad \text{C1}$$

The actual field component produced by each coil comprise radial and tangential elements, defined by:

$$H_r(\theta) = \frac{C}{r^2}\cdot\cos(\theta) \qquad H_t(\theta) = \frac{C}{2r^2}\cdot\sin(\theta) \qquad C = \frac{N\cdot A\cdot G}{2\cdot\pi} \qquad \text{C2}$$

where H_r and H_t are the radial and tangential field components respectively. C is a constant that accounts for coil area, number of turns and is assumed to be unity. Raab showed that general source-sensor coupling can be calculated by using a series of transform matrices. These are described in detail by Goldstein [Goldstein]. The general transform matrices are:

$$T_\alpha(\alpha) := \begin{pmatrix} \cos(\alpha) & \sin(\alpha) & 0 \\ -\sin(\alpha) & \cos(\alpha) & 0 \\ 0 & 0 & 1 \end{pmatrix} \qquad T_\psi(\psi) := \begin{pmatrix} \cos(\psi) & \sin(\psi) & 0 \\ -\sin(\psi) & \cos(\psi) & 0 \\ 0 & 0 & 1 \end{pmatrix}$$

$$T_\beta(\beta) := \begin{pmatrix} \cos(\beta) & 0 & -\sin(\beta) \\ 0 & 1 & 0 \\ \sin(\beta) & 0 & \cos(\beta) \end{pmatrix} \qquad T_\theta(\theta) := \begin{pmatrix} \cos(\theta) & 0 & -\sin(\theta) \\ 0 & 1 & 0 \\ \sin(\theta) & 0 & \cos(\theta) \end{pmatrix}$$

$$S := \begin{pmatrix} 1 & 0 & 0 \\ 0 & -\frac{1}{2} & 0 \\ 0 & 0 & -\frac{1}{2} \end{pmatrix} \qquad T_\phi(\phi) := \begin{pmatrix} 1 & 0 & 0 \\ 0 & \cos(\phi) & \sin(\phi) \\ 0 & -\sin(\phi) & \cos(\phi) \end{pmatrix}$$

Matrix S is used to compute the combination of radial and tangential field components coupled between zero-orientation orthogonal source and sensor coils. Angles α and β are azimuthal and elevation position angles respectively. Sensor orientation is described by azimuthal, elevation and roll angles, Ψ, θ and ϕ respectively. Raab derives the general coupling equation as:

$$f_5(\alpha,\beta,\theta,\phi,\psi) := \left(\frac{C}{r^3}\right)\cdot T_\phi(\phi)\cdot T_\theta(\theta)\cdot T_\psi(\psi)\cdot T_\alpha(-\alpha)\cdot T_\beta(-\beta)\cdot S\cdot T_\beta(\beta)\cdot T_\alpha(\alpha)\cdot f_1 \tag{C3}$$

Equation C4 describes the sensor output for the sources defined in S and for the position/orientation angles described above. It is solved for a set of azimuthal and elevation position angles for a given sensor orientation.

Equation C3 was used to calculate the sensor output when a single source is used and signals produced by three orthogonal sensor coils are recombined by various methods (see section 3.5.1, chapter 3). The methods included: rectify and sum; RMS and sum; blind sum; and strongest source. Calculation of each recombination method is described by the following equations implemented in Mathcad:

Magnitude (rectifier) type:

$$\mathrm{rectifier}\left(\alpha,\beta_{\mathrm{incline}},\theta,\phi,\Psi\right) := \left|f_5\left(\alpha,\beta_{\mathrm{incline}},\theta,\phi,\Psi\right)_0\right| + \left|f_5\left(\alpha,\beta_{\mathrm{incline}},\theta,\phi,\Psi\right)_1\right| + \left|f_5\left(\alpha,\beta_{\mathrm{incline}},\theta,\phi,\Psi\right)_2\right|$$

RMS Recombiner

$$\mathrm{rms}\left(\alpha,\beta_{\mathrm{incline}},\theta,\phi,\Psi\right) := \sqrt{\left(f_5\left(\alpha,\beta_{\mathrm{incline}},\theta,\phi,\Psi\right)_0\right)^2 + \left(f_5\left(\alpha,\beta_{\mathrm{incline}},\theta,\phi,\Psi\right)_1\right)^2 + \left(f_5\left(\alpha,\beta_{\mathrm{incline}},\theta,\phi,\Psi\right)_2\right)^2}$$

"Blind" Recombination

$$\mathrm{sum}\left(\alpha,\beta_{\mathrm{incline}},\theta,\phi,\Psi\right) := f_5\left(\alpha,\beta_{\mathrm{incline}},\theta,\phi,\Psi\right)_0 + f_5\left(\alpha,\beta_{\mathrm{incline}},\theta,\phi,\Psi\right)_1 + f_5\left(\alpha,\beta_{\mathrm{incline}},\theta,\phi,\Psi\right)_2$$

Decision including Rectifier

$$\mathrm{advanced\_decision}\left(\alpha,\beta_{\mathrm{incline}},\theta,\phi,\Psi\right) := \left|\begin{array}{ll} \left|f_5\left(\alpha,\beta_{\mathrm{incline}},\theta,\phi,\Psi\right)_0\right| & \text{if } \left(\left|f_5\left(\alpha,\beta_{\mathrm{incline}},\theta,\phi,\Psi\right)_0\right| \ge \left|f_5\left(\alpha,\beta_{\mathrm{incline}},\theta,\phi,\Psi\right)_1\right|\right) \wedge \left(\left|f_5\left(\alpha,\beta_{\mathrm{incline}},\theta,\phi,\Psi\right)_0\right| \ge \left|f_5\left(\alpha,\beta_{\mathrm{incline}},\theta,\phi,\Psi\right)_2\right|\right) \\ \left|f_5\left(\alpha,\beta_{\mathrm{incline}},\theta,\phi,\Psi\right)_1\right| & \text{if } \left(\left|f_5\left(\alpha,\beta_{\mathrm{incline}},\theta,\phi,\Psi\right)_1\right| \ge \left|f_5\left(\alpha,\beta_{\mathrm{incline}},\theta,\phi,\Psi\right)_0\right|\right) \wedge \left(\left|f_5\left(\alpha,\beta_{\mathrm{incline}},\theta,\phi,\Psi\right)_1\right| \ge \left|f_5\left(\alpha,\beta_{\mathrm{incline}},\theta,\phi,\Psi\right)_2\right|\right) \\ \left|f_5\left(\alpha,\beta_{\mathrm{incline}},\theta,\phi,\Psi\right)_2\right| & \text{if } \left(\left|f_5\left(\alpha,\beta_{\mathrm{incline}},\theta,\phi,\Psi\right)_2\right| \ge \left|f_5\left(\alpha,\beta_{\mathrm{incline}},\theta,\phi,\Psi\right)_0\right|\right) \wedge \left(\left|f_5\left(\alpha,\beta_{\mathrm{incline}},\theta,\phi,\Psi\right)_2\right| \ge \left|f_5\left(\alpha,\beta_{\mathrm{incline}},\theta,\phi,\Psi\right)_1\right|\right) \end{array}\right.$$

These equations were evaluated as a function of azimuthal position (*α*) for a given elevation ($\beta_{incline}$ = 0 degrees) and zero orientation ($\alpha = \beta = \theta = \phi = \psi = 0$) to produce the graph shown in figure 3.14, section 3.5.1.

Equation C4 was also evaluated for general *α* and *β* to construct a picture of sensor output versus position around the unit sphere. The following Mathcad sheet extract shows preparation of the data for processing in Matlab:

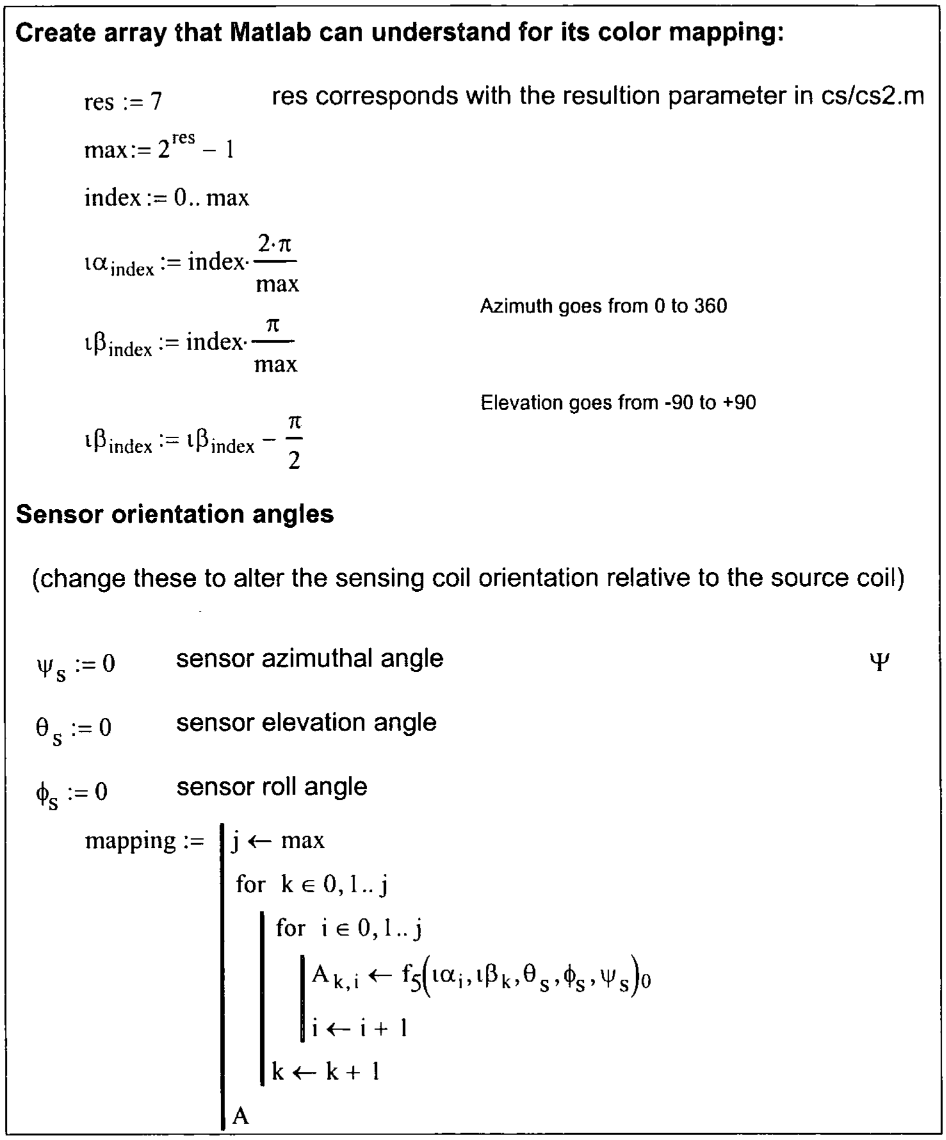

Create array that Matlab can understand for its color mapping:

$res := 7$ res corresponds with the resultion parameter in cs/cs2.m

$max := 2^{res} - 1$

$index := 0 .. max$

$\iota\alpha_{index} := index \cdot \frac{2 \cdot \pi}{max}$

Azimuth goes from 0 to 360

$\iota\beta_{index} := index \cdot \frac{\pi}{max}$

Elevation goes from -90 to +90

$\iota\beta_{index} := \iota\beta_{index} - \frac{\pi}{2}$

Sensor orientation angles

(change these to alter the sensing coil orientation relative to the source coil)

$\psi_s := 0$ sensor azimuthal angle Ψ

$\theta_s := 0$ sensor elevation angle

$\phi_s := 0$ sensor roll angle

```
mapping := | j ← max
           | for k ∈ 0, 1 .. j
           |     | for i ∈ 0, 1 .. j
           |     |     | $A_{k,i} \leftarrow f_5(\iota\alpha_i, \iota\beta_k, \theta_s, \phi_s, \psi_s)_0$
           |     |     | i ← i + 1
           |     | k ← k + 1
           | A
```

The loop evaluates equation C4 for every discrete value of *α* and *β*. The resulting vector *mapping* is passed to a data file that is loaded into the Matlab workspace. Matlab was then used to construct a spherical plot whose surface was coloured using a custom colour map defined according to the discrete values of vector *mapping*. The following is a code extract from the Matlab script:

```
function [H]=cs2(a,A)
%[H]cs2(a,A)
%This function generates the spherical color plot of the
%normalised field strength for inductive loops.
%The color map data comes from a mathcad worksheet called
%"inductor loop positioning.mcd".
%-----------------------------
%a is the resolution (must correspond with data.mat size)
%A is the colormap data
%H is a handle to the figure
%-----------------------------
%
figure
k=a;whos
n=2^k-1;
theta=pi*(-n:2:n)/n;
phi=(pi/2)*(-n:2:n)'/n;
X=cos(phi)*cos(theta);
Y=cos(phi)*sin(theta);
Z=sin(phi)*ones(size(theta));
colormap('default');
map=colormap;
C=A;
hidden ON

%draw and get handle
H=surf(X,Y,Z,C)

%Graphics formatting:
axis square;
colormap(map);
colormap hot;
set(H,'edgecolor','none');
```

Function cs2 creates a unit sphere by mapping the spherical coordinates, r and ϕ from Cartesian coordinates, x, y and z. A surface plot is created using the function *surf* to which the custom colour map is passed. Variable a specifies the colour map resolution.

Example

An example of the source-sensor coupling calculated by the above method is illustrated in figure C1. In this example, the source vector is:

$$f_1 := (1\ \ 0\ \ -1)^T$$

which specifies positive *x* and negative *z* source coils, and no *y* coil. Sensor orientation angles were: 60º (azimuthal), -30º (elevation) and 0º (roll). The colorbar represents relative source signal output. Note the regions of zero sensor output (light grey) that occur in the example.

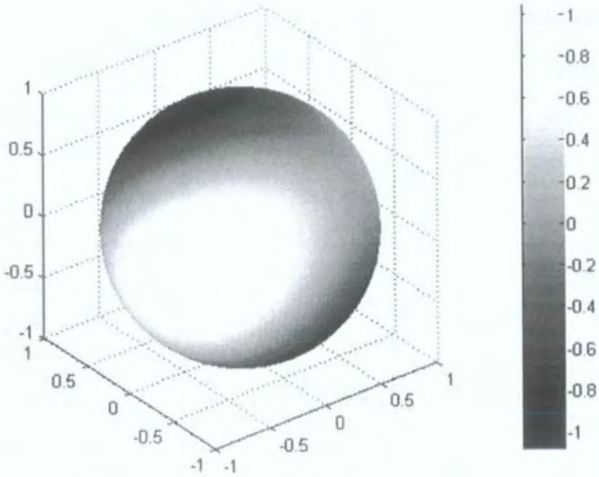

Figure C1 Source-sensor coupling for sample source configuration and source orientation.

Appendix D – Discretised Transmission Line Model Solution

This appendix provides a brief overview of a Matlab-based solution to the discrete transmission line model described in chapter 6. A detailed description of the transmission line model implemented is given by Christopoulos in [Christopoulos]. Referring to figure 6.23, section 6.5.4. and table D1, the distributed line parameters are:

$$L = \Delta x L_d\,,\ C = \Delta x C_d\,,\ R = \Delta x R_d\,, G = \Delta x G_d$$

Z_0	Characteristic Impedance
$R_{transponder}$	Resistance representing transponder at resonance
R	Cable resistance
G	Cable admittance representing dielectric loss
L	Cable Inductance, per unit *Δx*
C	Cable capacitance, per unit *Δx*

Table D1 Discrete transmission line parameters.

The decoupled discretised transmission line model equations are expressed by Christopoulos:

$$\frac{\partial^2 i}{\partial x^2} = \frac{GR}{(\Delta x)^2} i + \frac{1}{(\Delta x)^2}(GL + RC)\frac{\partial i}{\partial t} + \frac{LC}{(\Delta x)^2}\frac{\partial^2 i}{\partial t^2}\,,$$

$$\frac{\partial^2 v}{\partial x^2} = \frac{GR}{(\Delta x)^2} v + \frac{1}{(\Delta x)^2}(GL + RC)\frac{\partial v}{\partial t} + \frac{LC}{(\Delta x)^2}\frac{\partial^2 v}{\partial t^2}$$

Considering reactive components (*L*,*C*) as equivalent stubs:

$$Z_o = \sqrt{\frac{L}{C}}\,,\ \Delta t = \frac{\Delta x}{propagation\_speed} = \Delta x\sqrt{L_d C_d} = \Delta x\sqrt{\frac{LC}{(\Delta x)^2}} = \sqrt{LC}$$

The notation adopted for the discrete solution method is summarised in table D2. The solution proceeds by calculating the voltages and currents at each node along the transmission line including incident and reflected voltages. The time step is then incremented and the solution updated. The procedure is summarised below (the full method is derived by Christopoulos).

Symbol	Meaning
${}_kVR^i_n, {}_kVR^r_n$	Incident and reflected voltage waveforms travelling right at node *n*
${}_kVL^i_n, {}_kVL^r_n$	Incident and reflected current waveform travelling right at node *n*
${}_kI_n$	Current flowing through node *n*
R_S	Source resistance
${}_kV_s$	Source voltage
Z_{ind}	Impedance of inductor stub
Z_{cap}	Impedance of capacitor stub
${}_kV_{ind}$	Inductor stub equivalent Thevenin voltage
${}_kV_{cap}$	Capacitor stub equivalent Thevenin voltage
${}_kV^i_{ind}, {}_kV^r_{ind}$	Incident and reflected voltages at inductor stub
${}_kV^i_{cap}, {}_kV^r_{cap}$	Incident and reflected voltages at capacitor stub
${}_kVR^r_{L-1}$	Reflected voltage travelling right at node next to termination node
${}_kVL^i_L, {}_kVL^r_L$	Incident and reflected voltage waveforms travelling left at termination node

Table D2 Notation used for discrete solution

At each new time step, calculate new node voltages and currents at intermediate nodes:

$$
{}_kV_n = \frac{\dfrac{2\,{}_kVL^i_n}{Z_o} + \dfrac{2\,{}_kVR^i_n}{Z_o + R}}{\dfrac{1}{Z_o} + \dfrac{1}{R + Z_o} + G} \qquad {}_kI_n = \frac{{}_kV_n - 2\,{}_kVR^i_n}{R + Z_o}
$$

Calculate new voltages representing left and right waveforms:

$$
{}_kVL_n = {}_kV_n \qquad {}_kVR_n = 2\,{}_kVR^i_n + {}_kI_n Z_o
$$

Calculate scatter (reflection) voltages:

$$
{}_kVL^r_n = {}_kVL_n - {}_kVL^i_n \qquad {}_kVR^r_n = {}_kVR_n - {}_kVR^i_n
$$

Find new incident voltages (for next time step):

$$
{}_{k+1}VL^i_n = {}_kVR^r_{n-1} \qquad {}_{k+1}VR^i_n = {}_kVL^r_{n+1}
$$

In this model, the midsection of the transmission line contains the transponder resistance in the form of a series resistance, $R_{transponder}$:

$$ {}_kV_n = \frac{\dfrac{2\,{}_kVL_n^i}{Z_o} + \dfrac{2\,{}_kVR_n^i}{Z_o + R_{transponder}}}{\dfrac{1}{Z_o} + \dfrac{1}{R_{transponder} + Z_o} + G} \qquad {}_kI_n = \frac{{}_kV_n - 2\,{}_kVR_n^i}{R_{transponder} + Z_o} $$

Scatter and incident voltages for this node are calculated as above.

Voltage and current conditions at the source are calculated using:

$$ {}_kV_1 = \frac{\dfrac{{}_kV_s}{R_s} + \dfrac{2\,{}_kVR_1^i}{R + Z_o}}{\dfrac{1}{R_s} + \dfrac{1}{R + Z_o}} \qquad {}_kI_1 = \frac{{}_kV_1 - 2\,{}_kVR_1^i}{R + Z_o} $$

Source scatter equations:

$$ {}_kVR_1 = 2\,{}_kVR_1^i + {}_kI_1Z_o \qquad {}_kVR_1^r = {}_kVR_1 - {}_kVR_1^i $$

The new incident voltages appearing at the source for the next time step are:

$$ {}_{k+1}VR_1^i = {}_kVL_2^r $$

The line termination impedance comprises the series combination of resistance, inductance and capacitance:

$$ {}_kV_{11} = \frac{\dfrac{2\,{}_kVL_{11}^i}{Z_o} + \dfrac{2\left({}_kV_{cap}^i + {}_kV_{ind}^i\right)}{R_L + Z_{cap} + Z_{ind}}}{\dfrac{1}{Z_o} + \dfrac{1}{R_L + Z_{cap} + Z_{ind}} + G} \qquad {}_kI_L = \frac{{}_kV_{11} - 2\left({}_kV_{cap}^i + {}_kV_{ind}^i\right)}{R_L + Z_{cap} + Z_{ind}} $$

$$ {}_kV_{cap} = 2V_{cap}^i + {}_kI_LZ_{cap} \qquad {}_kV_{ind} = 2V_{ind}^i + {}_kI_LZ_{ind} $$

Scatter voltages are defined at node L:

$$ {}_kVL_L^r = {}_kV_L - {}_kVL_L^i \qquad {}_kV_{ind}^r = {}_kV_{ind} - {}_kV_{ind}^i \qquad {}_kV_{cap}^r = {}_kV_{cap} - {}_kV_{cap}^i $$

New incident voltages for next time step are:

$$ {}_{k+1}VL_L^i = {}_kVR_{L-1}^r \qquad {}_kV_{ind}^i = -{}_kV_{ind}^r \qquad {}_kV_{cap}^i = {}_kV_{cap}^r $$

Matlab Code

A Matlab script was written to implement the above method for a specified transmission line, transponder and termination impedance. For the final five percent of total time steps voltage and current profiles along the transmission line are plotted. A standing wave pattern appears as lines are superimposed on the graphs. The code is listed below:

```
function
tlm3(Ld,Cd,Rd,Gd,Rs,Rload,Lload,Cload,Rtag,length,num_sections,time_end,frequenc
y,source_magnitude)
%
tlm(Ld,Cd,Rd,Gd,Rs,Rload,Lload,Cload,Rtag,length,num_sections,time_end,frequency,source_magnitud
e)
% Returns [Vnode]
%
% This routine solves the Transmission Line Model (TLM) for a
% homogeneous transmission line. It gives the voltage variation along
% the line at disctrete points along the line at discrete steps in time
%
% Line parameters are:
%
%   Ld line inductance /m
%   Cd Line capacitance /m
%   Rd Line resistance /m
%   Gd line conductance /m
%   (Note: all per unit meter)
%
%   Rload is the load connected to the end of the line [ohms]
%   Lload is load inductance [Hendrys]
%   Cload is load capacitance [Farads]
%   Rtag is a typical tag load [ohms]
%   length is the length of the transmission line [m]
%   num_sections is the number of sections to be used in modelling the trannsmission line. should be an
odd number in this version
%   time_end is the duration of the simulation [s]
%   frequency is the frequency of the signal from the generator [Hz]
%   source_magnitude is the magnitude of the generator voltage [V]
%
%   Time step is dt = dx / u  (u = phase velocity) = sqrt(LC)
%
% rm (17/02/01)
%
time = cputime;
small = 1e-6;

Ld=0.6e-6;
Cd=73e-12;
Rd=0;
Gd=0;
Rs=50;
Rload=small;
Lload=0;
Cload=inf;
Rtag=10;
```

```
length=75;
num_sections=561; %1601
frequency=1e6;
time_end=100/frequency;
source_magnitude=0.5/2;

k=0; m = 1;
indicator=0;

% Initialise matrices
%Current & voltage at nodes
Vnode=zeros(1,num_sections+1);
Inode=zeros(1,num_sections+1);
Vright=zeros(1,num_sections+1);
Vleft=zeros(1,num_sections+1);
Vload=zeros(1,k+1);
Vind=zeros(1,1);
Vcap=zeros(1,1);
%voltage reflections at node
Vright_ref=zeros(1,num_sections+1);
Vleft_ref=zeros(1,num_sections+1);
Vload_ref=zeros(1,1);
Vind_ref=zeros(1,1);
Vcap_ind=zeros(1,1);
%incident voltages (for next time step)
%this is the initial condition (all incidient voltages are zero)
Vright_incid=zeros(1,num_sections+1);
Vleft_incid=zeros(1,num_sections+1);
Vload_incid=zeros(1,1);
Vind_incid=zeros(1,1);
Vcap_incid=zeros(1,1);

distance=[0:length/num_sections:length];
%set up line parameters and time step
nmax=num_sections+1;
dx=length/num_sections; %this MUST be much less than electrical wavelength
C=dx*Cd; %capacitance per section
L=dx*Ld; %inductance per section
Zo=sqrt(L/C) %characteristic impedance of each section
dt=sqrt(L*C); %determine step time ( dt=dx/u = sqrt(LC) )

R=dx*Rd; %loss per section
G=dx*Gd; %shunt loss per section

ZLind = (2*Lload/dt);
ZLcap = (dt/(2*Cload));

% find nodes around the mid section
n_mid_1 = nmax/2;
n_mid_2 = n_mid_1 + 1;

%set up plot windows
%close
figure('position', [1100,200,600,400]) %left,bottom,width,height
subplot(2,1,1)
%axis([1 (num_sections+1) -1 1])exit
title('tlm');
xlabel('line section');
ylabel('voltage');
grid on
```

```
hold on

subplot(2,1,2)
%axis([1 (num_sections+1) -10e-3 10e-3])
xlabel('line section');
ylabel('current');
grid on
hold on

%main loop
while k*dt <= time_end
  %Calculate node voltages and currents
  % node 1 (next to generator)
  Vs = source_magnitude*cos(2*pi*frequency*k*dt); %lookup source voltage at time current time step
  Vnode(1) = ((Vs/Rs)+(2*Vright_incid(1)/(R+Zo)))/((1/Rs)+(1/(R+Zo)));
  Inode(1) = (Vnode(1)-2*Vright_incid(1))/(R+Zo);
  Vright(1) = 2*Vright_incid(1)+Inode(1)*Zo;

  %intermediate nodes
  for n = 2:(nmax-1)
    if n == n_mid_1
      Vnode(n) = ((2*Vleft_incid(n)/Zo)+(2*Vright_incid(n)/(Zo+Rtag)))/((1/Zo)+(1/(Rtag+Zo))+G);
      Inode(n) = (Vnode(n)-2*Vright_incid(n))/(Rtag+Zo);

    else
      Vnode(n) = ((2*Vleft_incid(n)/Zo)+(2*Vright_incid(n)/(Zo+R)))/((1/Zo)+(1/(R+Zo))+G);
      Inode(n) = (Vnode(n)-2*Vright_incid(n))/(R+Zo);
    end

    Vleft(n) = Vnode(n);
    Vright(n) = 2*Vright_incid(n)+Inode(n)*Zo;
  end

  %right most node (next to load)
  Vnode(nmax) =
((2*Vleft_incid(nmax)/Zo)+(2*(Vcap_incid+Vind_incid)/(Rload+ZLind+ZLcap)))/((1/Zo)+(1/(Rload+Z
Lind+ZLcap))+G);
  Inode(nmax) = (Vnode(nmax)-2*(Vcap_incid+Vind_incid)) / (Rload+ZLind+ZLcap);
  Vcap = 2*Vcap_incid + Inode(nmax)*ZLcap;
  Vind = 2*Vind_incid + Inode(nmax)*ZLind;
  %not really needed:
  Vload(m) = Vcap + Vind;

  %Calculate reflected voltages
  %node 1 (next to generator)
  Vright_ref(1) = Vright(1) - Vright_incid(1);

  %intermediate nodes
  for n = 2:(nmax-1)
    Vright_ref(n) = Vright(n) - Vright_incid(n);
    Vleft_ref(n) = Vleft(n) - Vleft_incid(n);
  end

  %right most node (next to load)
  Vleft_ref(nmax) = Vnode(nmax)- Vleft_incid(nmax);
  %Load reflection conditions
  Vind_ref = Vind - Vind_incid;
  Vcap_ref = Vcap - Vcap_incid;
  %Vload_ref = Vload - Vload_incid;
```

```
  %Calculate new incident voltages (used in next time step)
  %node 1 (next to generator)
  Vright_incid(1) = Vleft_ref(2);

  %intermediate nodes
  for n=2:(nmax-1)
    Vright_incid(n) = Vleft_ref(n+1);
    Vleft_incid(n) = Vright_ref(n-1);
  end

  %right most node (next to load)
  Vleft_incid(nmax) = Vright_ref(nmax-1);
  %Load incident conditions
  Vcap_incid = Vcap_ref;
  Vind_incid = -Vind_ref;

  if (k*dt+dt) > (time_end*0.95)
    subplot(2,1,1);
    plot(distance,Vnode,'k');
    subplot(2,1,2);
    plot(distance,Inode,'b');
    %-------------
  end

  if( (k*dt) > (indicator*time_end) )
      sprintf('>> %2.0f percent complete...',indicator*100)
      indicator = indicator + 0.01;
  end

  %if(indicator < 0.01)
   %   sprintf('First 1 percent took %5.2f seconds, continue?\n (estimated completion time: %5.1f
s.)',cputime-time,(cputime-time)*100)
    %  response = input('>','s')
     % if(response == 'n')
      %   close
       %  error('quit')
       %end
       %   end

  k = k+1; m = m+1;
end
subplot(2,1,1);
plot(distance,Vnode,'c');
subplot(2,1,2);
plot(distance,Inode,'c');
result = Vnode;

%output result (voltage along the line) if required
zoom ON;
sprintf('Time is %5.2f seconds, %d time iterations,\nZo is %2.2f Ohms,\ndt was %e, dx was %f.',cputime-
time,k,sqrt(Ld/Cd),dt,dx)
```

Appendix E - Transmission Matrix (ABCD) Approach

Introduction

In this appendix a method for calculating power-line attenuation and input impedance is described. The transmission matrix method is a convenient method for solving circuits composed of several two-port networks connected in series. This solution was implemented using Mathcad software. Referring to figure 9.2 in section 9.4.1, the power-line was modelled as a series of cable sections and nodes. The impedance at each node represents one of the following: an appliance (simulated by the inlet filter impedance), an open-circuit (not in use) or a short-circuit (fault condition or approximation to heavy load).

Solution

Transmission line parameters *R* (copper loss), *L* (cable inductance), *C* (cable capacitance) and *G* (dielectric loss) are calculated using the following equations:

$$R(f) := \frac{k}{r}\sqrt{\frac{\mu\cdot f}{\pi\cdot\sigma}} \qquad L(f) := \frac{\mu 0}{\pi}\cdot \operatorname{acosh}\left(\frac{d}{2r}\right) \qquad C(f) := \frac{\pi\cdot\varepsilon_0\cdot\varepsilon r(f)}{\operatorname{acosh}\left(\frac{d}{2\cdot r}\right)} \qquad G(f) := 2\cdot\pi\cdot f\cdot C(f)\cdot\Lambda(f)$$

where σ is the conductivity of the conductor, *d* the conductor separation, *a* the conductor radius. *A(f)* is a linear function of frequency representing the loss tangent of the dielectric insulator. It is given by [Tsuzuki02]:

$$\Lambda(f) \equiv -5.7257\cdot 10^{-10}\cdot f + 0.06$$

Cable characteristic impedance can then be found using:

$$Zo(f) := \sqrt{\frac{R(f) + 2\cdot\pi\cdot f\cdot L(f)\cdot 1i}{G(f) + 2\cdot\pi\cdot f\cdot C(f)\cdot 1i}}$$

and the propagation constant:

$$\gamma(f) := \sqrt{(R(f) + 2\cdot\pi\cdot f\cdot L(f)\cdot 1i)\cdot(G(f) + 2\cdot\pi\cdot f\cdot C(f)\cdot 1i)}$$

If node has an appliance lead attached of length 2m. The equivalent input impedance presented to the node is therefore:

$$\mathrm{Zloadn}(f) = \mathrm{Zo}(f)\cdot\left(\frac{\mathrm{Zn}(f) + \mathrm{Zo}(f)\cdot\tanh(\gamma(f)\cdot\mathrm{lloadn})}{\mathrm{Zo}(f) + \mathrm{Zn}(f)\cdot\tanh(\gamma(f)\cdot\mathrm{lloadn})}\right)$$

where *Zn(f)* is the n^{th} load attached to the appliance cable and *lloadn* is the length of the n^{th} appliance cable. An appliance is represented by the its inlet filter impedance, which was given in section 6.3. For the type II filter considered in chapter 9 we may derive the input impedance of the filter:

$$Z_{b1}(f) := R_{choke} + R_{x2} + 1\mathrm{j}\cdot\left[2\cdot\pi\cdot f\cdot(L_{leak} + L_{x2}) - \frac{1}{2\cdot\pi\cdot f\cdot C_{x2}}\right]$$

$$Z_{b2}(f) := R_{x1} + 1\mathrm{j}\cdot\left(2\cdot\pi\cdot f\cdot L_{x1} - \frac{1}{2\cdot\pi\cdot f\cdot C_{x1}}\right)$$

$$Z_{filter}(f) := \frac{Z_{b1}(f)\cdot Z_{b2}(f)}{Z_{b1}(f) + Z_{b2}(f)}$$

where $Z_{b1}(f)$ and $Z_{b2}(f)$ are load-side and mains-side filter branches respectively. Referring to figures 6.9(c) and 6.12, the parameters are: choke loss (R_{choke}), choke leakage inductance (L_{leak}), load-side capacitance (C_{x2}), load-side capacitor loss (R_{x2}), load-side capacitor lead inductance (L_{x2}), mains-side capacitance (C_{x1}), mains-side capacitor loss (R_{x1}) and mains-side capacitor lead inductance (L_{x1}).

At the transponder node the impedance consists of an appliance (comprising appliance cable and inlet filter) and transponder coupled impedance. It is assumed that the transponder is located at the far end of the appliance cable (i.e., nearest to the appliance). The series combination of coupled and filter impedance is:

$$Z_L(f, R_L) := Z_{tr\_prim}(f, R_L) + Z_{filter}(f)$$

where R_L is the transponder chip load and $Z_{tr\_prim}(f,R_L)$ is the transponder coupled impedance given by:

$$Z_{tr\_prim}(f, R_L) := 1\mathrm{j}\cdot 2\cdot\pi\cdot f\cdot L_{tr\_prim} + \frac{\left(2\cdot\pi\cdot f\cdot k\cdot\sqrt{L_{tr\_prim}\cdot L_{tr\_sec}}\right)^2}{Z_{tr\_sec}(f, R_L)}$$

see section 5.6.3, chapter 5 for a derivation of this expression and a description of the transponder parameters.

Having defined cable and node impedances the ABCD transmission matrix solution may be calculated. See appendix C in [Rizzi] for detailed description of the method. The combined ABCD matrix solution for five nodes and five cable section is given by:

$$\mathrm{TM}\left(f, \mathrm{length\_end}, \mathrm{length\_others}, R_L\right) = \begin{pmatrix} \cosh(\gamma(f)\cdot \mathrm{length\_others}) & \mathrm{Zo}(f)\cdot \sinh(\gamma(f)\cdot \mathrm{length\_others}) \\ \frac{1}{\mathrm{Zo}(f)}\cdot \sinh(\gamma(f)\cdot \mathrm{length\_others}) & \cosh(\gamma(f)\cdot \mathrm{length\_others}) \end{pmatrix} \cdot \begin{pmatrix} 1 & 0 \\ \frac{1}{\mathrm{Zload1}(f)} & 1 \end{pmatrix} \cdots$$

$$\cdots \begin{pmatrix} \cosh(\gamma(f)\cdot \mathrm{length\_others}) & \mathrm{Zo}(f)\cdot \sinh(\gamma(f)\cdot \mathrm{length\_others}) \\ \frac{1}{\mathrm{Zo}(f)}\cdot \sinh(\gamma(f)\cdot \mathrm{length\_others}) & \cosh(\gamma(f)\cdot \mathrm{length\_others}) \end{pmatrix} \cdot \begin{pmatrix} 1 & 0 \\ \frac{1}{\mathrm{Zload2}(f)} & 1 \end{pmatrix} \cdots$$

$$\cdots \begin{pmatrix} \cosh(\gamma(f)\cdot \mathrm{length\_others}) & \mathrm{Zo}(f)\cdot \sinh(\gamma(f)\cdot \mathrm{length\_others}) \\ \frac{1}{\mathrm{Zo}(f)}\cdot \sinh(\gamma(f)\cdot \mathrm{length\_others}) & \cosh(\gamma(f)\cdot \mathrm{length\_others}) \end{pmatrix} \cdot \begin{pmatrix} 1 & 0 \\ \frac{1}{\mathrm{Zload3}(f)} & 1 \end{pmatrix} \cdots$$

$$\cdots \begin{pmatrix} 1 & 0 \\ \frac{1}{\mathrm{Zload4}(f)} & 1 \end{pmatrix} \cdot \begin{pmatrix} \cosh(\gamma(f)\cdot \mathrm{length\_end}) & \mathrm{Zo}(f)\cdot \sinh(\gamma(f)\cdot \mathrm{length\_end}) \\ \frac{1}{\mathrm{Zo}(f)}\cdot \sinh(\gamma(f)\cdot \mathrm{length\_end}) & \cosh(\gamma(f)\cdot \mathrm{length\_end}) \end{pmatrix} \cdots$$

$$\cdots \begin{pmatrix} 1 & 0 \\ \frac{1}{\mathrm{Zload5}\left(f, R_L\right)} & 1 \end{pmatrix}$$

where *length_end* is the length of the final cable section and *length_others* is the length of each intermediate cable section. Matrix *TM* contains the four ABCD parameters representing the complete electrical system. They are defined by accessing each element of *TM*:

$$\mathrm{TA}\left(f, \mathrm{length\_end}, \mathrm{length\_others}, R_L\right) := \mathrm{TM}\left(f, \mathrm{length\_end}, \mathrm{length\_others}, R_L\right)_{0,0}$$

$$\mathrm{TB}\left(f, \mathrm{length\_end}, \mathrm{length\_others}, R_L\right) := \mathrm{TM}\left(f, \mathrm{length\_end}, \mathrm{length\_others}, R_L\right)_{0,1}$$

$$\mathrm{TC}\left(f, \mathrm{length\_end}, \mathrm{length\_others}, R_L\right) := \mathrm{TM}\left(f, \mathrm{length\_end}, \mathrm{length\_others}, R_L\right)_{1,0}$$

$$\mathrm{TD}\left(f, \mathrm{length\_end}, \mathrm{length\_others}, R_L\right) := \mathrm{TM}\left(f, \mathrm{length\_end}, \mathrm{length\_others}, R_L\right)_{1,1}$$

Assuming zero generator loss and zero termination impedance, power-line attenuation may then be calculated using [Tsuzuki02]:

$$\mathrm{attenuation}\left(f, \mathrm{length\_end}, \mathrm{length\_others}, R_L\right) := 20\cdot \log\left(\frac{1}{\left|\mathrm{TA}\left(f, \mathrm{length\_end}, \mathrm{length\_others}, R_L\right)\right|}\right)$$

Finally, the input impedance, *interrog_Z()*, at the interrogator node (node 1) can be calculated using [Rizzi]:

$$\text{interog\_Z}\left(f, \text{length\_end}, \text{length\_others}, R_L\right) := \frac{\text{TA}\left(f, \text{length\_end}, \text{length\_others}, R_L\right)}{\text{TC}\left(f, \text{length\_end}, \text{length\_others}, R_L\right)}$$

This equation was used to find the load modulation sensitivity at the interrogator node.

Appendix F - Publications and Presentations

McWilliam R.P., Purvis, A., "Mains Appliance Identification for Electrical Safety Test System", Proc. 6th International Symposium on Power-Line Communications and its Applications, Greece, March, 2002.

McWilliam R.P., Purvis, A., "The Potential for Software Radio Techniques in Radio Frequency Identification (RFID) Technology", PREP 2002 Conference.